ELECTRICAL TRANSFER FUNCTION AND POLING MECHANISMS FOR NONLINEAR OPTICAL POLYMER MODULATORS

by

MICHAEL DALE WATSON

A DISSERTATION

Submitted in partial fulfillment of the requirements
For the degree of Doctor of Philosophy
in
The Department of Electrical and Computer Engineering
of
The School of Graduate Studies
of
The University of Alabama in Huntsville

HUNTSVILLE, ALABAMA

2005

In presenting this dissertation in partial fulfillment of the requirements for a doctoral degree from The University of Alabama in Huntsville, I agree that the Library of this University shall make it freely available for inspection. I further agree that permission for extensive copying for scholarly purposes may be granted by my advisor or, in his absence, by the Chair of the Department of Electrical and Computer Engineering or the Dean of the School of Graduate Studies. It is also understood that due recognition shall be given to me and to the University of Alabama in Huntsville in any scholarly use which may be made of any material in this dissertation.

_____ _____

Michael D. Watson (date)

DISSERTATION APPROVAL FORM

Submitted by Michael D. Watson in partial fulfillment of the requirements for the degree of Doctor of Philosophy in Electrical Engineering and accepted on behalf of the Faculty of the School of Graduate Studies by the dissertation committee.

We, the undersigned members of the Graduate Faculty of the University of Alabama in Huntsville, certify that we have advised and/or supervised the candidate on the work describe in this dissertation. We further certify that we have reviewed the dissertation manuscript and approve it in partial fulfillment of the requirements of the degree of Doctor of Philosophy in Electrical Engineering.

_____ Committee Chair
(Date)

_____ Advisor

_____

_____

_____

_____

_____ Department Chair

_____ College Dean

_____ Graduate Dean

ABSTRACT

School of Graduate Studies
The University of Alabama in Huntsville

Degree Doctor of Philosophy College/Dept. Engineering/Electrical and Computer Engineering

Name of Candidate Michael Dale Watson

Title Electrical Transfer Function and Poling Mechanisms for Nonlinear Optical Modulators.

Electro-Optic Polymers hold great promise in increased electro-optic coefficients as compared to their inorganic corollaries. Many researchers have focused on quantum chemistry to describe how the dipoles respond to temperature and electric fields. Much work has also been done for single layer films to confirm these results. For optical applications, waveguide structures are utilized to guide the optical waves in 3 layer stacks. Electrode poling is the only practical poling method for these structures. This research takes an electrical engineering approach to develop poling models and electrical and optical transfer functions of the waveguide structure. The key aspect of the poling model is the large boundary charge density deposited during the poling process. The boundary charge density also has a large effect on the electrical transfer function which is used to explain the transient response of the system. These models are experimentally verified. Exploratory experiment design is used to study poling parameters including time, temperature, and voltage. These studies verify the poling conditions for CLDX/APC and CLDZ/APEC guest host electro optic polymer films in waveguide stacks predicted by the theoretical developments.

Abstract Approval: Committee Chair _____

Department Chair _____

Graduate Dean _____

ACKNOWLEDGEMENTS

I give glory to my Lord and Savior, Jesus Christ, for the blessing of being able to conduct this research and interact with the many professionals who have guided or supported this work. I gratefully acknowledgement my committee for their guidance in the accomplishment of the work. In particular I owe special gratitude to Dr. Abushagur who has been my advisor and friend through out my graduate career. Special thanks are due to Dr. Ashley who has provided outstanding guidance on this work and who has provided the opportunity and the direction to accomplish this work. I also greatly appreciate Dr. Lindquist accepting the role of Chairman shortly before my Qualification Exam and assisting in completing my degree requirements.

I acknowledge the support I have received from the National Aeronautics and Space Administration (NASA) Marshall Space Flight Center (MSFC) through the Part Time and Full Time Studies Programs and the Center Director's Discretionary Fund. I greatly appreciate the support and encouragement I have received to complete this work by my management, Joe Zimmerman, Kurt Jackson, Fred Roe, and Jack Bullman, during this period. I am grateful to the United States Army Aviation and Missile Research, Development, and Engineering Center (AMRDEC) for their support in providing laboratory space and equipment and producing the test wafers for this work. I am also grateful to the United States Navy Air Warfare Center at China Lake for producing the materials used in this research.

Finally I am most grateful to the loving and patient support of my wife, Lisa, and my children, Brandon, Zachary, Olivia, Micah, and Elizabeth. Thank you for your love and understanding through this long process.

TABLE OF CONTENTS

LIST OF FIGURES

LIST OF TABLES

CHAPTER 1

Introduction

Over the past 15 years, electro-optic (EO) polymers have been investigated for various integrated optics applications. These applications have ranged from second harmonic generation devices to polarization mode converters to EO modulators.[1] Of these applications, EO modulators currently show great promise in terrestrial applications for GHz telecommunications modulators and fiber optic gyroscope (FOG) modulators operating at wavelengths of 1.3 microns and 1.55 microns. For FOG applications, EO polymers offer the advantage of simple integration with other waveguide components and excellent modulation bandwidth for this low frequency application (approximately 100 KHz) [2].

Although these EO polymers offer great potential benefits in these applications, the electrical properties of 3 layer polymer stacks are not well understood or defined. A good definition of the waveguide electrical transfer function is important to understand the modulation characteristics of electro optical modulators. The alignment mechanisms of dipoles in the core material, accomplished by electrical poling, is also crucial to defining the maximum achievable electro optical response for a given waveguide structure. Understanding the poling factors that lead to the measured V_π and optical losses related to poling are essential to the fabrication of practical devices.

This dissertation defines the electrical transfer function for a 3 layer waveguide stack. The basic theory is defined including the physical properties that correspond to the

electrical model. Following this, the poling process is described for the 3 layer stack. The charge transport mechanisms and charge densities of the electro optic stack are derived. The measurable macroscopic poling properties of these stacks are related to the molecular alignment mechanisms. The charge densities are found to have a significant effect in not only the dipole alignments but also contribute to electrostriction which increases optical losses in poled waveguides. These charge densities are related to poling time, temperature, and voltage. A detailed set of experiments is defined and performed to verify the theoretical results. These experiments show that the theory describes the electrical poling and transfer function very well.

EO polymers are formed by introducing a chromophore with nonlinear optical properties into a polymer matrix. There are 3 approaches to incorporating the chromophore into the polymer matrix. 1) The chromophore may be added as a quest molecule in a polymer host. Typical hosts included PMMA (Poly (Methyl MethAcrylate), polycarbonate (PC), polysolfone (PSF), and polystyrene (PS). 2) The chromophore may be attached as a side chain molecule to a polymer backbone. 3) The chromophore may be incorporated as a main chain molecule directly into the polymer backbone.

Various chromophores have been evaluated over the last few years. A good nonlinear optical chromophore is characterized by a large r_{33} electro-optic coefficient. The r_{33} coefficient is directly related to the material dipole mobility, μ, and the hyperpolarizability, β. Thus, good EO chromophores are often termed high $\mu\beta$ chromophores. A good measure of EO polymer nonlinear optical characteristics is that of LiNbO3. LiNbO3 has an r_{33} of 8.7 pm/V [3]and excellent thermal stability up to 1145 °C (Currie Temperature) [4]. Current NLO polymers have theoretical r_{33} values ranging

from 75 - 150 pm/V [3]. Other important features of a good chromophore include long-term thermal stability, low optical losses at the desired wavelengths, and solubility with polymer (for quest/host materials). The most prominent chromophores include Disperse Red 1 (DR1), DANS (4-N,N-dimethylamino-4'-nitrostilbene), and CLD.

EO polymers are typically applied as thin films by spinning and drying the material on a substrate or lower cladding. The spinning process leaves the chromophore molecules in a random orientation, and thus the polymer films have a centrosymmetric orientation and no nonlinear optical properties. To achieve the EO effects in polymers, poling is required to orient the molecules in a preferred direction, creating a noncentrosymmetric structure. The poling is typically performed by application of an electric field while heating the device to the glass transition temperature (Tg) of the EO polymer material. This heating creates space in the polymer matrix to allow the non-linear optical chromophores to orient themselves along the electric field. By maintaining the electrical field while cooling the sample freezes the chromophore orientation into the polymer matrix creating a birefringence in the polymer. Studies have shown that the chromophore orientation will relax over time. This relaxation time decreases with increasing temperature, dropping off very quickly as the polymer T_g is approached. Poling temperature profiles have a large effect on thermal stability of EO polymers. These studies indicate that aging of polymers during poling can reduce the space for the chromophores reorientation and substantially increase relaxation times.[1] Thus, the poling technique is of fundamental importance to not only EO effects, but to thermal stability as well.

Many of the early EO polymers based on PMMA, Polycarbonate, and Polystyrene host systems had low Tg's (approximately 90 - 120 °C). [1] Thus their relaxation times

degraded quickly as device temperatures increased. To provide better stability at higher temperatures, high T_g materials are needed to enable EO polymer device operation at 120 – 155 °C temperatures while maintaining long relaxation times. One of the most promising materials is the CLD family of EO polymers. These materials use the CLD chromophore as a guest/host. In these guest/host materials, CLD has been mixed with amorphous polycarbonate (APC), polyimides, and polysolfones. Tg's for these materials range from 145 °C to 193 C depending primarily on the host material or polymer backbone chemistry.

Much work has been done in studying optical losses and low modulation voltages for these materials. CLD1/APC has been reported to have an r_{33} of 43 pm/V leading to a V_π of 4.2 V at a wavelength of 1.55 microns. Optical losses have also been reported for rib waveguides at 1.7 dB/cm at 1.55 microns. [5] While basic poling techniques have been reported, little work has been reported on the poling mechanisms of CLD based materials. [6,7,8,9] One of the objectives of this dissertation is to determine the basic poling mechanisms for CLD materials and determine poling conditions that improve modulation voltage of a CLD based high temperature polymer modulator.

To determine efficient poling methods, an understanding of the poling mechanisms in a 3 layer waveguide structure is required. Past and current research has focused on single polymer layers and has not considered effects of the waveguide structure such as the boundary interface. [10,11,12] Basic charge models have been developed for single layer and 2 layer non-polar films [10,13] and some experimental work has been reported for 2 layer films using a Teflon AF upper layer and a DR1/PMMA lower layer. [14] The charge distribution and motion induced by ion beam poling and corona poling across air gaps have been studied extensively. [15,16]

Investigations based on dielectric constant measurements have also been conducted. [17] Polymer films characteristics have been studied by a variety of methods including Thermally Stimulated Discharge (TSD) [13], Second Harmonic Generation (SHG), pyro-electric currents, [1] and thermal and acoustic waves. [18,19] Work has been reported on single layer guest/host systems, [20], and for single layer polyamide film irradiation influence, [21], using TSD for experimental analysis. Some limited work has been done on 3 layer planar film TSD currents. [22] SHG studies have also been conducted for UV bleached glass doped waveguide structures, but these studies have focused on the molecular orientation symmetries of the waveguide boundaries.[23,24,25] Space charge theories have also been used to describe diffraction grating formation in single layer films of photorefractive materials. [26] Investigations of waveguide structures have recently addressed the conductivity of the cladding layers [27], but these studies have not considered the boundary and polarization charge layers formed in a waveguide structure.

The molecular theory development, single layer charge models, and measurement techniques have provided a tremendous amount of knowledge on polymer films but are often difficult to employ in standard fabrication processes. Poling currents offer a straight forward macroscopic quantity that is easily measured during device fabrication. Poling and TSD current techniques offer a method to study material poling mechanisms including the activation energy, E_A, and the natural frequency, α_r, of the material dipoles. These currents are caused by the flow of charges in the waveguide structure and thus a model has been developed to investigate the charge distribution and induced currents during the poling process.

Considering device operation, electrical performance of electro optic modulators is key to their application in high speed communications and gyroscope systems.

Traditionally, waveguide electrical models have focused on the design of the electrodes for microwave frequencies. Some of the first models viewed the polymer waveguide structure as a series stack of RC circuits modeling the bulk resistance and capacitance of each layer. [10] More recent models have defined the waveguide stack as a series combination of bulk capacitances, but have not addressed the stack resistance.[28] Models have also been generated which consider the second order hyperpolarizability response to poling field transients but did not address a waveguide structure or the reduction in poling field due to the 3 layer stack.[29] Some work has also been performed to match microwave impedance for a polymer waveguide based on models developed for lithium niobate. [30] Investigations of waveguide structures have addressed the conductivity of the cladding layers [27], but these studies have not considered the total stack electrical properties.

Various groups have reported results for microwave modulation of electro optic polymer modulators. 39 GHz modulation was reported with a UFC170-CLD1/APC-UV15 waveguide structure. [31] Time stretching applications has also used CLD1/APC mach zehnder modulators operating up to 101.7 GHz. [32] The highest frequency reported has been 110 GHz. [33] Much attention has been paid in these developments to the design of microwave electrodes [34,35], but not to the electrical characteristics of the polymer stack.

To investigate poling methods, a series of experiments were conducted to explore poling mechanisms. To measure the poling effectiveness predicted by the theories defined by this dissertation, modulator half wave voltages are determined through experimental measurements. Modulators were constructed of two CLD variations, CLDZ and CLDX. A statistical Design of Experiment approach was used to define the poling

parameter investigation methods. The CLD modulators were used to study the poling process by varying parameters such as poling time, poling temperature, and poling voltage. The effects of these changes on the poling efficiency were evaluated by measuring V_{π}. The results of these experiments were in good agreement with the theoretical findings.

A review of past research and a definition of the scope of this research effort are defined in Chapter 1. The basic theory for the design of an EO polymer modulator can be divided into 2 parts: modulation theory and electrical poling theory. Modulation theory is reviewed in Chapter 2. In this chapter waveguide theory, electro-optical modulation theory and new developments for the waveguide electrical transfer function are presented. Electrical poling theory is addressed in Chapter 3. Molecular orientation of molecules, various poling methods, basic charge transport theory for single layers, new developments in poling charge transport for a 3 layer waveguide, new developments relating macroscopic charge densities to the molecular orientation in the poling field, and waveguide electrostriction are discussed in detail. In Chapter 4 the statistical Design of Experiment used to study the effects of some poling parameters and the equipment used for all poling experiments and measurements are presented. Experimental results and explanations are provided in Chapter 5. Summary and conclusions of this work are presented in Chapter 6. Several appendixes are included for reference. Appendix A contains a detailed review of the material systems studied over the last 15 years in poling experiments. Appendix B contains additional data plots and tables from the experimental evaluations. Appendix C contains the Matlab programs written in support of the theoretical developments.

CHAPTER 2

Modulator Theory

Modulator theory is composed of the waveguiding mechanisms required to confine a propagating optical mode and the modulation necessary to produce a modulation in the intensity of the optical mode. Fabrication of a modulator starts with a thin film polymer stack consisting of a lower cladding spun on a substrate, a core material, and an upper cladding. Lower electrodes are deposited on the substrate before the lower cladding. A channel waveguide is fabricated in the core material during processing to produce the modulator input, output, and arm channels. Y-branch couplers are fabricated to connect the arms to the input and output channels. Upper electrodes are deposited over the lower cladding to complete the Mach-Zehnder modulator. The device is then electrically poled using the modulator electrodes to induce molecular symmetry of the electro-optic chromophores, completing the modulator. Material properties and layer geometries play a large role in the waveguiding and modulating properties of the device. Waveguiding properties are dependant on the index of refraction of the materials, thickness of the layers, and width of the channel. Poling efficiency is dependant on the material electrical transfer function. Optical modes traveling in a channel waveguide are modulated using the electro-optic effect in the modulator. The strength of the voltage required to modulate the optical signal is determined by the electrical poling mechanisms of the device.

2.1 Waveguide Theory

A channel waveguide is used to confine the propagating light in an integrated optical device such as an optical communication transceiver or a fiber optic gyroscope. The index of refraction and geometry of the channel defines the optical mode of the propagating light beam. The propagating optical mode is found by solving Maxwell's equations in each region indicated by Figure 2.1 and matching solutions at the boundaries. For a channel waveguide, Marcatili's Method can be used to define the general equations for the optical mode. [36] Using the structure illustrated in Figure 2.1, Marcatili assumed that the fields in the corner regions were negligible and could be ignored. He, therefore, solved the fields in the remaining 5 regions and matched the solutions at the region boundaries. The basic equations are the cross products relating the electric and magnetic fields:

$$\vec{\nabla} x \vec{E} = -\mu_0 \frac{\partial}{\partial t} \vec{H} \tag{2.1}$$

$$\vec{\nabla} x \vec{H} = \varepsilon_0 n^2 \frac{\partial}{\partial t} \vec{E} \tag{2.2}$$

Assuming the fields have the form:

$$\vec{A}(x,y,z) = (A_x + A_y + A_z) e^{-j(\omega t - \beta z)} \quad , \tag{2.3}$$

(where A represents E or H) then the cross products can be taken to find equations relating each field component as:

$$\frac{\partial}{\partial y} E_z + j\beta E_y = -j\omega\mu_0 H_x \tag{2.4}$$

$$-\frac{\partial}{\partial x} E_z - j\beta E_x = -j\omega\mu_0 H_y \tag{2.5}$$

$$\frac{\partial}{\partial x}E_y - \frac{\partial}{\partial y}E_x = -j\omega\mu_0 H_z \tag{2.6}$$

$$\frac{\partial}{\partial y}H_z + j\beta H_y = j\omega\varepsilon_0 n^2 E_x \tag{2.7}$$

$$-\frac{\partial}{\partial x}E_z - j\beta E_x = j\omega\varepsilon_0 n^2 E_y \tag{2.8}$$

$$\frac{\partial}{\partial x}H_y - \frac{\partial}{\partial y}H_x = j\omega\varepsilon_0 n^2 E_z \quad . \tag{2.9}$$

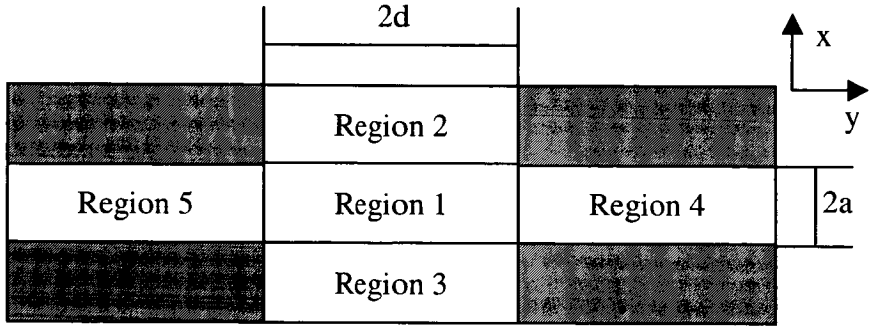

Figure 2.1: Channel Waveguide Structure

For a 3-dimensional waveguide structure, the light is confined in both the x and y directions. Thus, there are not true Transverse Electric (TE) or Transverse Magnetic (TM) modes. Instead the modes are Transverse Electric Magnetic (TEM) modes. Therefore, Marcatili assumed that a TE mode could be defined as a mode where E_y and H_x where the predominate fields and that H_y was approximately zero. Similarly the TM mode was defined as a mode where E_x and H_y are the predominate fields and H_x was approximately zero. Using the assumptions that H_y (TE) or H_x (TM) are zero, Equations (2.4) to (2.9) may be used to write field expressions in terms of either H_y or H_x.

TM mode:

$$\frac{\partial^2}{\partial x^2}H_y + \frac{\partial^2}{\partial y^2}H_y + (k_0^2 n^2 - \beta^2)H_y = 0 \tag{2.10}$$

$$E_x = \frac{\omega\mu_0}{\beta}H_y + \frac{1}{\omega\varepsilon_0 n^2 \beta}\frac{\partial^2}{\partial x^2}H_y \tag{2.11}$$

$$E_y = \frac{1}{\omega\varepsilon_0 n^2 \beta}\frac{\partial^2}{\partial x \partial y}H_y \tag{2.12}$$

$$E_z = \frac{-j}{\omega\varepsilon_0 n^2}\frac{\partial}{\partial x}H_y \tag{2.13}$$

$$H_z = \frac{-j}{\beta}\frac{\partial}{\partial y}H_y \tag{2.14}$$

TE mode:

$$\frac{\partial^2}{\partial x^2}H_x + \frac{\partial^2}{\partial y^2}H_x + (k_0^2 n^2 - \beta^2)H_x = 0 \tag{2.15}$$

$$E_x = -\frac{1}{\omega\varepsilon_0 n^2 \beta}\frac{\partial^2}{\partial x \partial y}H_x \tag{2.16}$$

$$E_y = -\frac{\omega\mu_0}{\beta}H_x - \frac{1}{\omega\varepsilon_0 n^2 \beta}\frac{\partial^2}{\partial y^2}H_x \tag{2.17}$$

$$E_z = \frac{j}{\omega\varepsilon_0 n^2}\frac{\partial}{\partial y}H_x \tag{2.18}$$

$$H_z = \frac{-j}{\beta}\frac{\partial}{\partial x}H_x \tag{2.19}$$

Equations (2.10) and (2.15) represent 2nd order partial differential equations (PDE). These PDE's may be solved using the separation of variable technique, where H = F(x)G(y). This leads to 2 ordinary differential equations (ODE):

$$F_{xx} - K^2 F = 0 \tag{2.20}$$

$$G_{yy} - (A+K^2)G = 0 \tag{2.21}$$

where $A = k_0^2 n^2 - \beta^2$.

The solutions of these ODE's depend on the value of the coefficients, K^2 or $A+K^2$. These solution regimes are:

$K^2 = 0$ or $A+K^2 = 0$

$F = Ax + B$ or $G = Ax + B$

However, for a physical electric or magnetic field, the field must go to zero at infinity. Thus, A and B are both zero for this boundary condition and the solution is trivial.

$K^2 < 0$

Assume $F = e^{mx}$, and $\alpha^2 = -K^2$ then

$m^2 e^{mx} + \alpha^2 e^{mx} = 0$

$m^2 = -\alpha^2$

$m = \pm j\alpha$

$F(x) = C e^{j\alpha x} + De^{-j\alpha x} = C\cos(\alpha x) + jC\sin(\alpha x) + D\cos(\alpha x) - jD\sin(\alpha x)$

$F(x) = (C+D)\cos(\alpha x) = H\cos(\alpha x)$

Where $H = C+ D$. The value of α can be found by noting that $\cos(2\pi) = 0$ or $\alpha x = 2\pi$. Since, we are dealing with electromagnetic waves, the phase of the light will depend on its wavelength such that $x = \lambda$ and so $\alpha = 2\pi/\lambda = k_x$. Since the phase of the solution is unknown, an arbitrary phase constant is added:

$$F(x) = H\cos(k_x x + \phi_x) \qquad (2.22)$$

$K^2 > 0$

Assume $F = e^{mx}$, then

$m^2 e^{mx} - K^2 e^{mx} = 0$

$m^2 = K^2$

$m = \pm K$

$F(x) = C e^{Kx} + De^{-Kx}$

Now, at infinity, F must be zero for a physical field. Therefore C = 0 and defining D = H and $\gamma_x = K$.

$F(x) = He^{-\gamma_x x}$ (2.23)

$A+K^2 < 0$

Assume $G = e^{my}$, and $\alpha^2 = -A-K^2$ then

$m^2 e^{my} + \alpha^2 e^{my} = 0$

$m^2 = -\alpha^2$

$m = \pm j\alpha$

$G(y) = C e^{j\alpha y} + De^{-j\alpha y} = C\cos(\alpha y) + jC\sin(\alpha y) + D\cos(\alpha y) - jD\sin(\alpha y)$

$G(y) = (C+D)\cos(\alpha y) = H\cos(\alpha y)$

Where H = C+ D.

Since the phase of the solution is unknown, an arbitrary phase constant is added and denote α as k_y similar to the derivation of Equation (2.22).

$G(y) = H\cos(k_y y + \phi_y)$ (2.24)

$A+K^2 > 0$

Assume $G = e^{my}$, then

$m^2 e^{my} - (A+K^2)e^{my} = 0$

$m^2 = A+K^2$

$$m = \pm\sqrt{A + K^2}$$

$$G(y) = Ce^{\sqrt{A+K^2}y} + De^{-\sqrt{A+K^2}y}$$

Now, at infinity, G must be zero for a physical field. Therefore C = 0 and defining D = H and $\gamma_y = \sqrt{A + K^2}$.

$$G(y) = He^{-\gamma_y y} \tag{2.25}$$

Using Equations (2.22) to (2.25), relationships between k_x, k_y, γ_x, and γ_y can be found. Noting from the derivation of 2.22 that $k_x^2 = \alpha^2 = -K^2$ and from the derivation of Equation (2.23) $k_y = -\sqrt{A + K^2}$ then:

$$k_y^2 = k_0^2 n^2 - \beta^2 - k_x^2 \text{ or,}$$

$$-k_y^2 - k_x^2 + k_0^2 n^2 - \beta^2 = 0 \tag{2.26}$$

This relationship can then be used to define the relationships with γ_x and γ_y. From the derivation of Equations (2.22) and (2.25), $\gamma_x = -k_x$ and $\gamma_y = -k_y$. Squaring and using the relationship defined in Equation (2.26) yields:

$$\gamma_x^2 - k_y^2 + k_0^2 n^2 - \beta^2 = 0 \tag{2.27}$$

$$\gamma_y^2 - k_x^2 + k_0^2 n^2 - \beta^2 = 0 \tag{2.28}$$

The phase constants may also be defined by noting that the solutions in the core Region 1of Figure 2.1 will be either symmetric or antisymmetric. Symmetric solutions have $\cos(k_x x + \phi_x) = 1$ and antisymmetric solutions have $\cos(k_x x + \phi_x) = 0$ at x = 0, respectively. Thus, $\phi_x = \pi$ or $\pi/2$ which can be written in terms of the periodic mode number, p, as:

$$\phi_x = (\pi/2)(p-1), \qquad p = 1,2,3,\ldots \tag{2.29}$$

Following a similar course for ϕ_y using q as the mode number yields:

$$\phi_y = (\pi/2)(q-1), \qquad q = 1,2,3,.... \tag{2.30}$$

Now, at the boundaries of each region, the solutions must match so that the wave is continuous across the boundary. In Region 1, the solution has the basic form:

$$H(x,y) = H_1\cos(k_x x + \phi_x)\cos(k_y y + \phi_y). \tag{2.31}$$

In Region 2, the solution has the basic form $H_2 \cos(k_y y + \phi_y)\exp\{\gamma_x x\}$. Equating the solutions for Regions 1 and 2 and solving for H_2 at x = a yields $H_2 = H_1\cos(k_x a + \phi_x)$ where the exponential is set equal to one at the boundary by shifting the argument to a. Thus the solution in Region 2 is:

$$H(x,y) = H_1\cos(k_x a + \phi_x)\exp\{\gamma_x(x-a)\}\cos(k_y y + \phi_y). \tag{2.32}$$

The solution in Region 3 can be found in a similar noting the boundary is at x = -a:

$$H(x,y) = H_1\cos(k_x a - \phi_x)\exp\{\gamma_x(x+a)\}\cos(k_y y + \phi_y). \tag{2.33}$$

The solutions in Regions 4 and 5 can also be found similarly, noting that the boundary is now at y = d and y = -d:

$$H(x,y) = H_1\cos(k_x x + \phi_x)\exp\{\gamma_y(y-d)\}\cos(k_y d + \phi_y). \tag{2.34}$$

$$H(x,y) = H_1\cos(k_x x - \phi_x)\exp\{\gamma_y(y+d)\}\cos(k_y d - \phi_y). \tag{2.35}$$

Equations (2.31) to (2.35) apply to both TE and TM mode solutions. In the case of TE mode, $H(x,y) = H_y$ and for TM mode, $H(x,y) = H_x$. As noted above, these are not true TE or TM modes since the electric field has components in both the E_x and E_y direction for both solutions. A more correct way to designate the modes is by using the mode number defined in Equations (2.29) and (2.30). The TE mode then corresponds to the E_{pq}^{y} mode (signifying the predominant field is in the y direction) and the TM mode to

the E_{pq}^{x} mode (signifying the predominant field is in the x direction). The dispersion relationships can then be found for the TE and TM modes by using the solutions defined in Equations (2.31) to (2.35) in Equations (2.15) to (2.19) and in Equations (2.10) to (2.14). This is done, by noting, that the tangential components (E_z, H_z) of the field are continuous at the boundary. Thus for the TE mode, Equations (2.31) to (2.35) are substituted for H_x in Equations (2.18) and (2.19) at the appropriate boundaries. Thus, at the boundary for x = a,

$$\frac{-j}{\beta}\frac{\partial}{\partial x}H_1\cos(k_x a+\phi_x)e^{-\gamma_x(x-a)}\cos(k_y y+\phi_y)=\frac{-j}{\beta}\frac{\partial}{\partial x}H_1\cos(k_x x+\phi_x)\cos(k_y y+\phi_y)$$

Taking the partial derivatives and setting x = a in the result yields:

$$k_x a=\tfrac{\pi}{2}(p-1)+\tan^{-1}(\tfrac{\gamma_x}{k_x});\quad \text{TE} \tag{2.36}$$

Similarly, at the boundary for y = d,

$$\frac{j}{\omega\varepsilon_0 n_c^{\,2}}\frac{\partial}{\partial y}H_1\cos(k_x x+\phi_x)e^{-\gamma_y(y-d)}\cos(k_y y+\phi_y)=\frac{j}{\omega\varepsilon_0 n_g^{\,2}}\frac{\partial}{\partial y}H_1\cos(k_x x+\phi_x)\cos(k_y y+\phi_y)$$

Taking the partial derivatives and setting y = d in the result yields:

$$k_y d=\tfrac{\pi}{2}(q-1)+\tan^{-1}(\tfrac{n_g^{\,2}}{n_c^{\,2}}\tfrac{\gamma_y}{k_k});\ \text{TE} \tag{2.37}$$

A similar process leads to the TM equations.

$$k_x a=\tfrac{\pi}{2}(p-1)+\tan^{-1}(\tfrac{n_g^{\,2}}{n_c^{\,2}}\tfrac{\gamma_x}{k_x});\ \text{TM} \tag{2.38}$$

$$k_y d=\tfrac{\pi}{2}(q-1)+\tan^{-1}(\tfrac{\gamma_y}{k_k});\ \text{TM} \tag{2.39}$$

There are 3 basic methods to fabricate channel waveguides: Rib, trench, and photo-bleached. To fabricate a rib, a thick core layer is spun over the lower cladding. The rib is then patterned on the core, and Reactive Ion Etching (RIE) is performed to etch

back the core region outside of the waveguide region. This produces the structure illustrated in Figure 2.2. As the core layer is etched, the sides of the rib waveguide become exposed to the RIE plasma. This can be destructive to the core material, in particular the NLO chromophore as discussed in Section 3.0. Etching of the rib can also create rough sidewalls leading to optical losses as well. Therefore, only a portion of the core layer is etched back, producing the small ridge over the planar core layer. This ridge is sufficient to confine the light in the y direction, producing a channel waveguide.

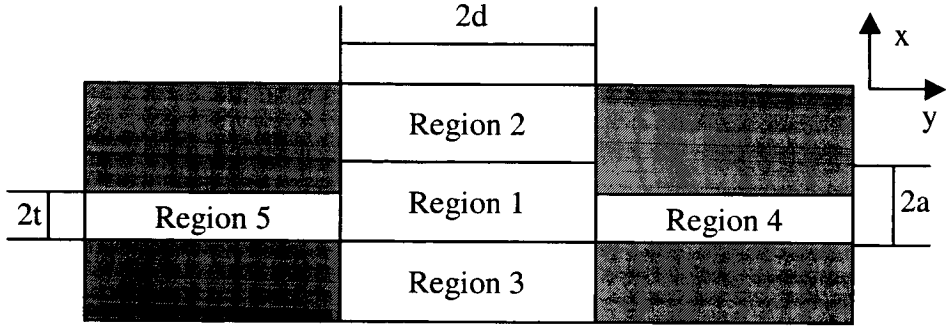

Figure 2.2: Rib Waveguide Structure

Note, as illustrated in Figure 2.2, this further complicates the equations for the waveguide solutions, since there is an additional region that must be considered by the equations. Marcatili's method assumes the corner regions have small field contributions that are negligible in calculating the solutions. However, for these rib waveguides the corner regions are extended. One possible method is to assume that Marcatili's assumptions hold, even under this extended corner region. However, this assumes t is approximately equal to a and that $n_c = n_g$. These assumptions form a planar waveguide stack with no confinement in the y direction. So, Marcatili's method does not hold for this complicated geometry. Koumar's method extends Marcatili's work to account for field components in the corner regions. The effective index method provides for a more

accurate model that can approximate the more complicated geometry of the rib waveguide. The most accurate solution method, however, is the numerical solutions produced by finite element analysis. [36]

Finite element analysis breaks the waveguide structure into a mesh of small cells and then solves for the electromagnetic fields at the boundary of each cell. Very complicated geometries can be accommodated by adjusting the dimensions of the cells in the mesh. For this work, Apollo Photonics Optical Waveguide Mode Solver (OWMS) software will be used to generate the waveguide solutions. OWMS finds supported modes by solving the following matrix equations assuming weak polarization coupling:

$$P_{xx}E_x = \beta_x^2 E_x \tag{2.40}$$

$$P_{yy}E_y = \beta_y^2 E_y \tag{2.41}$$

$$Q_{xx}H_x = \beta_x^2 H_x \tag{2.42}$$

$$Q_{yy}H_y = \beta_y^2 H_y \tag{2.43}$$

where,

$$P_{xx}E_x = n_{xx}^2 k^2 E_x + \frac{\partial}{\partial x}\left[\frac{1}{n_{zz}^2}\frac{\partial}{\partial x}\left(n_{xx}^2 E_x\right)\right] + \frac{\partial^2 E_x}{\partial y^2} \tag{2.44}$$

$$P_{yy}E_y = n_{yy}^2 k^2 E_y + \frac{\partial}{\partial y}\left[\frac{1}{n_{zz}^2}\frac{\partial}{\partial y}\left(n_{yy}^2 E_y\right)\right] + \frac{\partial^2 E_y}{\partial x^2} \tag{2.45}$$

$$Q_{xx}H_x = n_{yy}^2 k^2 H_x + \frac{\partial^2 H_x}{\partial x^2} + n_{yy}^2 \frac{\partial}{\partial y}\left[\frac{1}{n_{zz}^2}\frac{\partial H_x}{\partial x}\right] \tag{2.46}$$

$$Q_{yy}H_y = n_{xx}^2 k^2 H_y + \frac{\partial^2 H_y}{\partial y^2} + n_{xx}^2 \frac{\partial}{\partial x}\left[\frac{1}{n_{zz}^2}\frac{\partial H_y}{\partial y}\right] \tag{2.47}$$

These equations are similar to Equations (2.10) and (2.15), but account for spatial variation of the index of refraction and allow for all TEM modes. This is done by solving Equations (2.4) to (2.9) in terms of each of the major field components by assuming the orthogonal field component is zero. OWMS solves these equations as a set of linear equations in matrix form:

$$AE = \beta^2 E \tag{2.48}$$

The power method is used to solve for the eigenvalues (β^2) and eigenvectors (E). [37]

2.2 Waveguide Modeling

To illustrate the application of the theory developed in Section 2.1, models of the different waveguide designs have been generated using OWMS to illustrate their optical mode profiles. These models are based on a CLDZ/APC (Amorphous Polycarbonate) core with Norland Optical Adhesive (NOA) 71 upper and lower claddings. Figure 2.3 portrays the optical mode calculated by OWMS. The optical mode profile was generated for the design case discussed in Section 5.1.

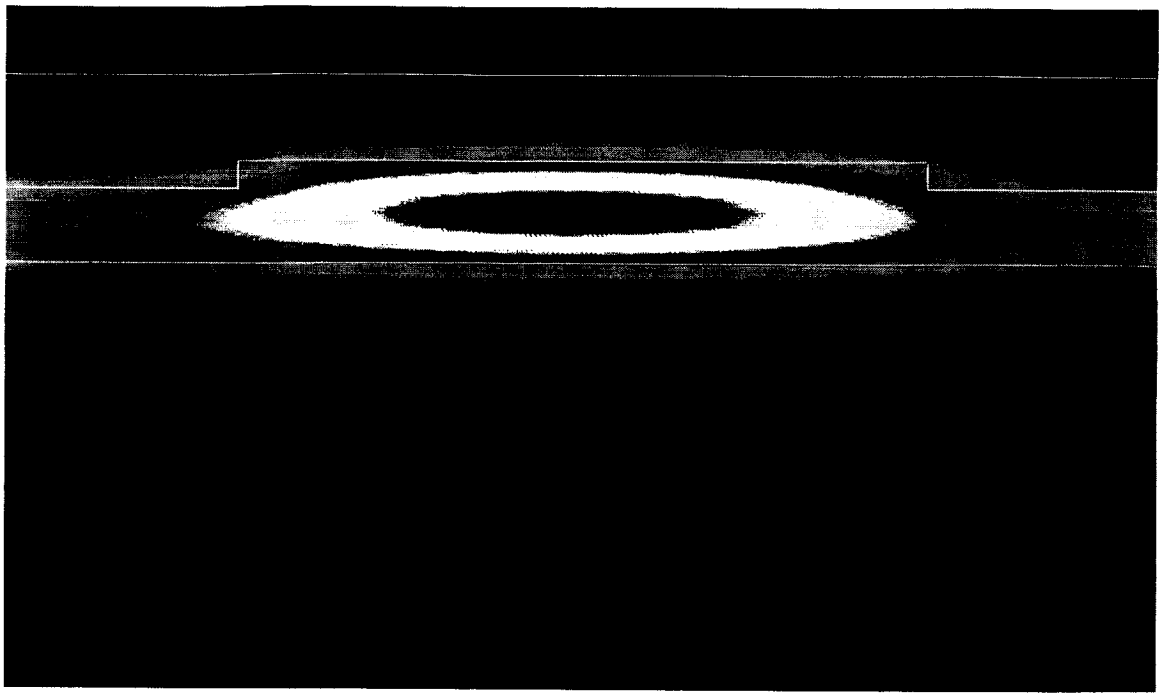

Figure 2.3: Optical Mode Profile (1.55 μm) for a Rib Waveguide 6.5 μm wide by 3.0 μm high

A trench waveguide is simply an inverted rib where a trench is fabricated in the lower cladding and the core layer is then deposited over (and into) the trench as illustrated in Figure 2.4. This eliminates concerns for exposing the core to the RIE plasma, but sidewall roughness is still a possibility. Thus, only a small portion of the trench is etched into the lower cladding. Figure 2.5 illustrated the mode profile. The optical mode profile was generated for the design case (in this case an inverted rib structure) discussed in Section 5.1. Upper and Lower claddings are both NOA 71 and the core is CLDZ/APC.

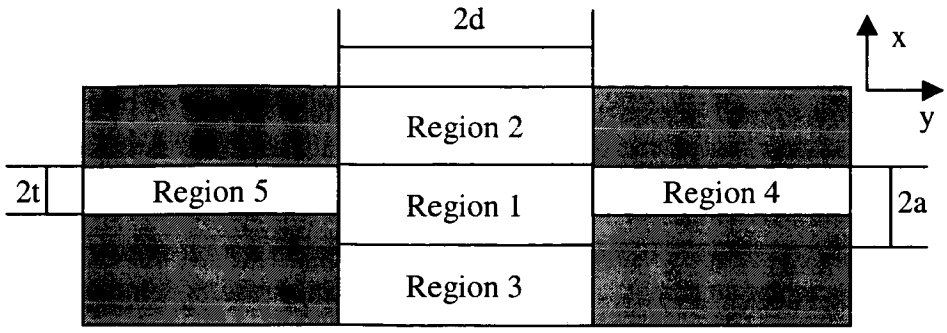

Figure 2.4: Trench Waveguide Structure

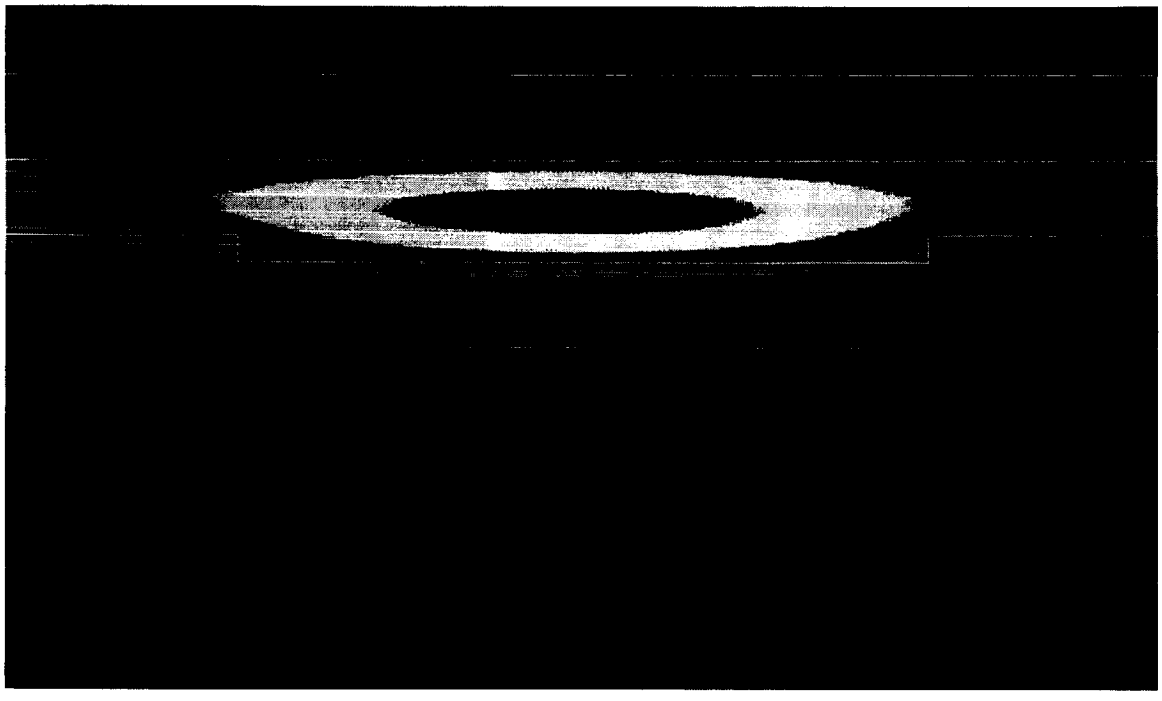

Figure 2.5: Optical Mode Profile (1.55 μm) for a Trench Waveguide 6.5 μm wide by 3.0 μm high

Photo-bleached waveguides are produced by depositing and patterning a thick core layer on a lower cladding, similar to rib waveguide fabrication. UV light exposure is then used to "bleach" the field destroying the NLO chromophore and lowering the index of refraction in the exposed area to that of the host or main chain polymer. This produces a structure as illustrated in Figure 2.1 with an optical mode profile as illustrated in Figure

2.6. The optical mode profile was generated for the design case discussed in Section 5.1. Upper and Lower claddings are both NOA 71 and the core is CLDZ/APC. The bleached core area index of refraction is 1.541 (the index of refraction of APC with no chromophore) In this case, there is no RIE to possibly damage the core layer or to create rough sidewalls. The solutions for the photobleached waveguide follow the Marcatili method very well since there is no ridge area and mode solutions follow Equations (2.31) to (2.35).

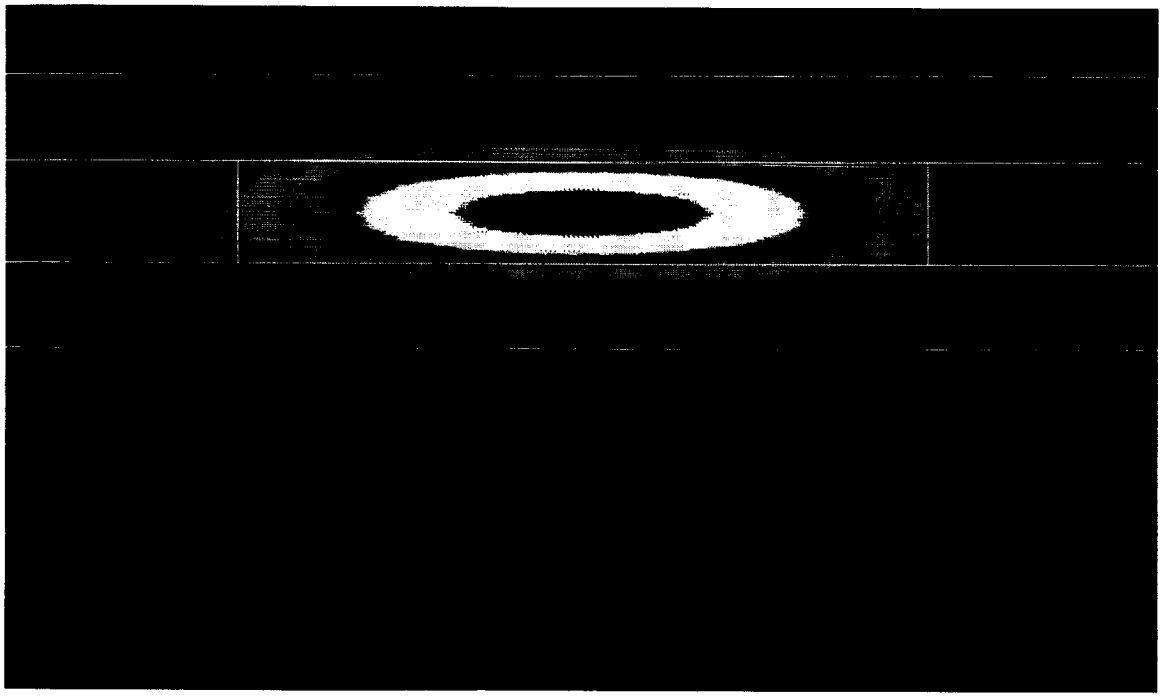

Figure 2.6: Optical Mode Profile (1.55 μm) for a Photobleached Waveguide

2.3 Modulation Theory

Figure 2.7 illustrates a Mach-Zehnder modulator. Modulation of an optical mode confined in a waveguide channel in a Mach-Zehnder (MZ) configuration is accomplished by creating a time varying phase difference in the light propagating in each arm of the

modulator. By taking advantage of the linear electro-optic effect in a material, a time varying electrical signal can be used to create an optical modulation. Light is input via a channel waveguide. The light is then split by a symmetric (i.e. couples 50% into each arm) Y-branch coupler into the 2 modulator arms. A time varying voltage is then applied to electrodes over the modulator arms producing an index of refraction change in one arm relative to the other arm. This produces a phase difference in the 2 arms of the modulators. A symmetric y-branch channel then couples the modes in each arm of the modulator. Since the 2 modes now have a varying phase, the output coupler produces an interference signal varying directly with the modulation signal.

The phase of a light signal propagating in a medium is defined by the optical path length as:

$$\phi = knd \tag{2.49}$$

where,

$k = 2\pi/\lambda$
n = index of refraction
d = propagation distance in the medium

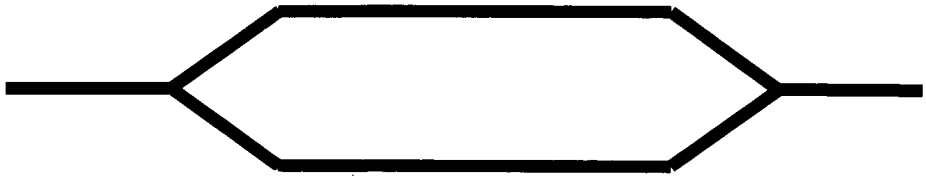

Figure 2.7: Mach-Zehnder Modulator Geometry

The propagation distance, d, and the wavelength, λ, are fixed, but the index of refraction varies with an applied electrical field as defined by equation of the index ellipsoid:

$$\left(\frac{1}{n_x^2} + r_{1k}E_k\right)x^2 + \left(\frac{1}{n_y^2} + r_{2k}E_k\right)y^2 + \left(\frac{1}{n_z^2} + r_{3k}E_k\right)z^2 + 2yzr_{4k}E_k + 2zxr_{5k}E_k + 2xyr_{6k}E_k = 1 \tag{2.50}$$

where,

k = x,y,z and

r is the linear electro-optic coefficient defined by the expansion of the material impermeability tensor, h, as:

$$\eta_{ij} = \eta_o + r_{ijk}E_k + s_{ijkl}E_kE_l + \ldots \quad (2.51)$$

and

$$\eta_{ij} = \varepsilon_0(\varepsilon^{-1})_{ij} = \varepsilon_0(1/n^2)_{ij} \quad (2.52)$$

Thus, r represents the first order variation of the index with an electric field.

The possible values of r are dependent on the crystalline symmetry of the material. As discussed in Section 3.1, poling of the electro-optic polymer produces symmetry along the poling direction (the z crystalline axis). Thus, r_{333}, r_{223}, and r_{113} are the typical coefficients seen by the optical wave propagating through the medium. Using the symmetry relations discussed in Section 3.1 allows the subscripts to be contracted as[38]:

$$\begin{aligned} &1 = (11),\\ &2 = (22),\\ &3 = (33),\\ &4 = (23) = (32),\\ &5 = (13) = (31),\\ &6 = (12) = (21). \end{aligned} \quad (2.53)$$

So that,

$$\begin{aligned} r_{333} &= r_{33},\\ r_{223} &= r_{23},\\ r_{113} &= r_{13}. \end{aligned}$$

The symmetry relations also result in the following relationships:

$$r_{43} = r_{53} = r_{63} = 0, \quad (2.54)$$

$$r_{23} = r_{13}. \quad (2.55)$$

When an electric field is applied along the crystalline z axis, the cross terms in Equation (2.50) are zero and the index ellipsoid can be written as:

$$\left(\frac{1}{n_o^2}+r_{13}E_z\right)x^2+\left(\frac{1}{n_o^2}+r_{13}E_z\right)y^2+\left(\frac{1}{n_e^2}+r_{33}E_z\right)z^2=1 \tag{2.56}$$

where $n_x = n_y = n_o$ is the ordinary index of the crystal and $n_z = n_e$ is the extraordinary index of the crystal.

Equation (2.56) defines the new crystalline axis in the prescience of an electric field. Thus, the orientation of the crystalline axis remain unchanged, but the index of refraction seem by the propagating wave is modified. The new index of refraction can be determined by comparing Equation (2.56) to the normalized equation of the index ellipsoid:

$$\frac{x'^2}{n_{x'}^2}+\frac{y'^2}{n_{y'}^2}+\frac{z'^2}{n_{z'}^2}=1 \tag{2.57}$$

Comparing similar terms yields:

$$\frac{1}{n_{x'}^2}=\frac{1}{n_o^2}+r_{13}E \tag{2.58}$$

$$\frac{1}{n_{y'}^2}=\frac{1}{n_o^2}+r_{13}E \tag{2.59}$$

$$\frac{1}{n_{z'}^2}=\frac{1}{n_e^2}+r_{33}E \tag{2.60}$$

Assuming that $r_{13}E << n_o^{-2}$ and $r_{33}E << n_e^{-2}$ then $r_{13}E$ and $r_{33}E$ can be taken as small differential changes in n_o and n_e producing the new indexes of refraction $n_o' = n_x' = n_y'$ and $n_e' = n_z'$. Taking the derivative of n_o^{-2} and n_e^{-2} gives:

$d(n_o^{-2})/dn_o = -2n_o^{-3}$, or $dn_o = -0.5n_o^3 d(n_o^{-2})$

$d(n_e^{-2})/dn_e = -2n_e^{-3}$, or $dn_e = -0.5n_e^3 d(n_e^{-2})$.

Using these assumptions and relationships to write of n_o' and n_e' as a differential change to n_o and n_e gives:

$$n_o' = n_o + dn_o = n_o - 0.5n_o^3 r_{13}E, \text{ and} \tag{2.61}$$

$$n_e' = n_e + dn_e = n_e - 0.5n_e^3 r_{33} E. \quad (2.62)$$

Having defined the polymer index of refraction in the prescience of an electric field, the phase difference seen by the 2 orthogonal modes in a light beam incident at 45 degrees to the crystalline axis is expressed as:

$$\Gamma = kd(n_e' - n_o') = kd[n_e - n_o - 0.5(n_e^3 r_{33} - n_o^3 r_{13})E]. \quad (2.63)$$

For a waveguide modulator, the light propagates transversely to the electrodes. The electric field in this case is distributed across the waveguide core scaling the field as:

$$E = V_{applied}/t, \quad (2.64)$$

where V is the applied voltage

t is the waveguide core thickness.

The voltage is further reduced by the electrical transfer function of the waveguide stack. The applied voltage is reduced by the waveguide electrical transfer function resulting in an effective core voltage of:

$$V_{core} = H_{wg}(j\omega)V_{applied} \quad (2.65)$$

Thus, the phase change, Γ, can be written as:

$$\Gamma = kd[n_e - n_o - 0.5(n_e^3 r_{33} - n_o^3 r_{13})\,(1/t)(H_{wg}(j\omega)V_{applied})]. \quad (2.66)$$

If the light propagating in the waveguide is a TM or TE mode, then only n_e or n_o index is seen. Thus, the phase change in each case would be:

$$\Gamma_{TM} = kd[n_e - 0.5n_e^3 r_{33}\,(1/t)V_{core}], \text{ and} \quad (2.67)$$

$$\Gamma_{TE} = kd[n_o - 0.5n_o^3 r_{13}\,(1/t)V_{core}]. \quad (2.68)$$

Now, for a Mach-Zehnder (MZ) modulator, a phase difference can be generated by changing the index of refraction in one arm of the modulator with respect to the other arm. Thus, if $V_{applied2} = 0$ and $V_{applied1} = V$, then:

$$\Delta\Gamma_{TM} = kd[n_e] - kd[n_e - 0.5n_e^3 r_{33}\,(1/t)V_{core}] = kd[0.5n_e^3 r_{33}\,(1/t)V_{core}] \quad (2.69)$$

$$\Delta\Gamma_{TE} = kd[n_o] - kd[n_o - 0.5n_o^3 r_{13}\,(1/t)V_{core}] = kd[0.5n_o^3 r_{13}\,(1/t)V_{core}] \quad (2.70)$$

The voltage required to produce a phase change of π can be solved for TM and TE modes using Equations (2.69) and (2.70). Setting $\Delta\Gamma = \pi$, setting d = L, the waveguide interaction length, and solving for V_{core} yields:

$$V_{\pi core} = \frac{t\lambda}{Ln_e^3 r_{33}} \qquad \text{TM} \quad (2.71)$$

$$V_{\pi core} = \frac{t\lambda}{Ln_o^3 r_{13}} \qquad \text{TE} \quad (2.72)$$

Adjusting for cladding layer resistances, then yields V_π as:

$$V_\pi = \frac{1}{H_{wg}(j\omega)} \frac{t\lambda}{Ln_e^3 r_{33}} \qquad \text{TM} \quad (2.73)$$

$$V_\pi = \frac{1}{H_{wg}(j\omega)} \frac{t\lambda}{Ln_o^3 r_{13}} \qquad \text{TE} \quad (2.74)$$

Considering Equations (2.73) and (2.74), V_π is noted to be proportional to t, λ, and the electrical transfer function of the stack. V_π is inversely proportional to the length, L, n_o or n_e, and r_{33} or r_{13}. For a give wavelength, V_π can be made small by minimizing the waveguide thickness, t, maximizing the electrical transfer function, and maximizing the length of interaction, L.

The modulator may also be operated in a push-pull mode where the applied voltage is + in one arm and - in the other arm. In this case, $V_{applied2} = -V$ and $V_{applied1} = +V$, and:

$$\Delta\Gamma_{TM} = kd[n_e + 0.5n_e^3 r_{33}\,(1/t)V_{core}] - kd[n_e - 0.5n_e^3 r_{33}\,(1/t)V_{core}]$$

$$= kd[n_e^3 r_{33}\,(1/t)V_{core}], \qquad \text{push-pull} \quad (2.75)$$

$$\Delta\Gamma_{TE} = kd[n_o + 0.5n_o^3 r_{13} (1/t)V_{core}] - kd[n_o - 0.5n_o^3 r_{13} (1/t)V_{core}]$$

$$= kd[n_o^3 r_{13} (1/t)V_{core}], \qquad \text{push-pull.} \tag{2.76}$$

Comparing Equations (2.75) and (2.76) with Equations (2.69) and (2.70) a factor of 2 increase in phase difference between the arms of the modulator is noted for the push-pull configuration.

The light intensity is a function of the phase retardation as given by:

$$I = EE^* = 0.5\cos^2(\Delta\Gamma/2) \tag{2.77}$$

Thus, a modulation of the index yields a direct modulation of the output intensity. If a time varying voltage signal is applied to the modulator, then

$$V_{applied} = V_m \sin(\omega_m t), \tag{2.78}$$

where V_m is the modulation voltage magnitude,

ω_m is the modulation frequency, and

t is time.

Thus, substituting Equation (2.78) into Equations (2.65) to (2.76) shows the phase difference for the TM and TE modes will vary directly with the modulating frequency as will the intensity of the modulator output given in Equation (2.78).

2.4 Electrical Transfer Function

Waveguide stacks have been generally described as a series of 3 large resistors [10] as illustrated in Figure 2.8. This model is based on the high resistance values of the dielectrics but does not incorporate the capacitance of each layer.

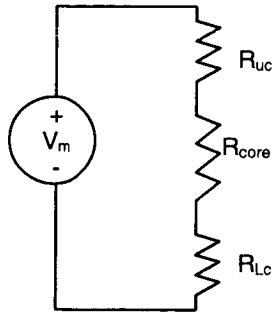

Figure 2.8: Resistive Waveguide Electrical Model

Including the bulk capacitance of each layer leads to 3 parallel RC circuits connected in series as shown in Figure 2.9. This particular circuit provides an improved model of the waveguide stack. The bulk properties of the circuit correspond to the space charge contained within the dielectric layers including the dipoles. This gives rise to the bulk capacitance. The bulk capacitors are charged and discharged during modulation. The resistance of polar layers has two conduction paths: host backbone and chromophore. These components are dispersed within the layer and so are parallel to each other. Thus, the core layer resistance (R_{core}) is the parallel combination of the host (R_{host}) and chromophore (R_{chr}) resistances written as:

$$R_{core} = \frac{R_{host} R_{chr}}{R_{host} + R_{chr}}. \tag{2.79}$$

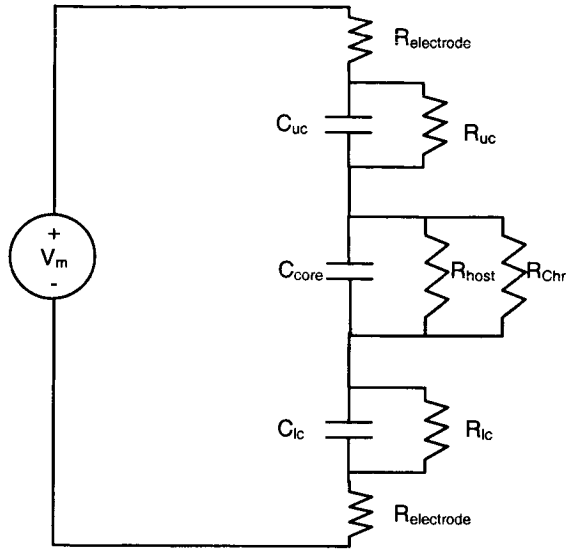

Figure 2.9: Bulk RC Waveguide Electrical Model

The frequency response of a series of parallel RC circuits has an infinite pass band. However, the frequency response is limited when the interface resistance is included in the total stack impedance. Assuming sputtered gold electrodes, there is not a separation between the electrode and the upper cladding layer. Similarly, adhesion of the spun lower cladding on the lower gold electrode is very good. Therefore, the interface impedance can be represented by a resistance at each of the electrode cladding interfaces. As this resistance increases, the pass band is reduced. High frequency cut-offs have been demonstrated to 100 GHz in the literature. [32, 33, 34, 35] This corresponds to an interface resistance on the order of 0.1 Ω. So,

$$R_{electrode} = 0.1\ \Omega. \tag{2.80}$$

This model provides a good high frequency response model, but assumes that the interface between the layers is perfect (i.e. a straight, no resistance wire). However, this model does not support the transient response seen for square wave inputs in some material systems at frequencies below the microwave range. These responses can be explained by incorporating the capacitance and resistance of the interface layer as

illustrated in Figure 2.10. The interface resistance represents the chemical interconnection between the layers. Similarly, the interface capacitance represents the separation of the layers at the interface. The value of the capacitance is strongly influenced by the boundary charge density formed at the layer boundaries as discussed in Section 3.4. Both of these effects are physically related to the layer adhesion. As the layers adhere better, the capacitance increases due to the reduce charge separation and the resistance decreases due to the increased bonds available for charge transfer. Conversely, as the adhesion worsens, the layers separate lowering the interface capacitance and increasing the resistance as bonds between the layers are broken. These additional RC components have a large effect on the electrical transfer function.

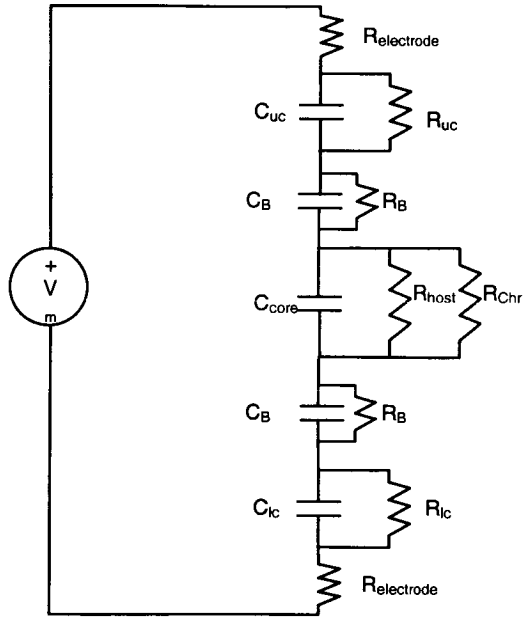

Figure 2.10: 3 Layer Waveguide Electrical Model

The electrical transfer function is defined by a series connection of parallel RC circuits. For a parallel RC circuit the impedance can be written as:

$$Z = \frac{R - j\omega R^2 C}{1 + \omega^2 R^2 C^2} \tag{2.81}$$

Thus, the impedance of the upper cladding (Z_{uc}), core (Z_{core}), lower cladding (Z_{lc}) and the boundary interface (Z_B) is given by:

$$Z_{uc} = \frac{R_{uc} - j\omega {R_{uc}}^2 C_{uc}}{1 + \omega^2 {R_{uc}}^2 {C_{uc}}^2} \tag{2.82}$$

$$Z_{core} = \frac{R_{core} - j\omega {R_{core}}^2 C_{core}}{1 + \omega^2 {R_{core}}^2 {C_{core}}^2} \tag{2.83}$$

$$Z_{lc} = \frac{R_{lc} - j\omega {R_{lc}}^2 C_{lc}}{1 + \omega^2 {R_{lc}}^2 {C_{lc}}^2} \tag{2.84}$$

$$Z_B = \frac{R_B - j\omega {R_B}^2 C_B}{1 + \omega^2 {R_B}^2 {C_B}^2} \tag{2.84}$$

These impedances are then added to produce the total stack impedance (Z_{stack}) as,

$$Z_{stack} = Z_{uc} + Z_{core} + Z_{lc} + 2Z_B + 2R_{electrode} \tag{2.85}$$

The transfer function of interest is the relationship of the core voltage to the applied modulation voltage. This can be solved as:

$$H_{wg}(j\omega) = \frac{Z_{core}}{Z_{stack}} \tag{2.86}$$

This transfer function can then be substituted into Equations (2.67) to (2.70), (2.75), and (2.76) to give the optical response in terms of applied modulation voltage.

Interface capacitance and resistance have a clear effect on the sub-microwave frequency performance of 3 layer waveguide stacks. These effects have been incorporated into the stack electrical transfer function defined by Equation(2.86). As seen with Equations (2.67) to (2.70), (2.75), and (2.76), the boundary capacitance and

resistance have a direct effect on the measured V_π of the waveguide. The low frequency performance of the waveguide stack shows the stack is a capacitive voltage divider for all practical applications. Voltages must be stable across the core for 1000 hours or more for the core voltage to stabilize and the circuit relax to a simple resistive voltage divider. Thus, the dielectric properties, critical to the waveguide performance also have a significant effect on the stack frequency response indicating that material selection must consider both electrical frequency response and optical waveguide performance. These effects are also significant when determining r_{33} from measured modulator performance. The core voltage must be calculated using the transfer function incorporating the low frequency capacitive effects and including the boundary capacitance and resistance.

Having addressed the modulation performance, Chapter 3 considers the effects of the poling parameters on the waveguide stack and the source of the boundary charge densities which determine the boundary capacitance values.

CHAPTER 3

Poling Theory

Poling establishes the modulation properties of an electro optic modulator. An understanding of the poling mechanisms is key to defining optimal poling processes. These mechanisms are defined by the poling electric field, the corresponding induced charge transport, and the induced dipole alignments. The poling field is an external macroscopic parameter which effects the molecular environment of the polymer material. An understanding of these processes requires a relationship of the molecular effects to the macroscopic effects be defined. In addition to modulation voltage, poling fields also induce electrostriction which effect the optical losses of the waveguide channels.

When a polymer core material is first spun on a wafer, the chromophore molecules are randomly oriented such that there is centrosymmetry in the molecular structure. Thus, no electro-optic effect is present. By applying an electric field to the material, the chromophore dipoles will orient themselves along the field lines, producing the necessary noncentrosymmetric structure to produce an electro-optic effect. Thus, "poling" of a material is the process of orienting the dipoles using an electro-magnetic field.

The main polymer chain may also be aligned by the electric field in some polymer materials. The effect of this alignment is generally much smaller than the effects of the chromophore alignment and is not a factor with the APC and APEC hosts used in this research.

In order for poling to be effective, the chromophore molecules must be free to orient themselves along the electric field. At room temperature, polymers are in a glassy state (i.e. a highly viscous fluid state). The polymer chains have found a thermal equilibrium state with neighboring polymer chains and chromophores. Thus, there is a high energy level necessary to reorient the chromophore and polymer chains from their equilibrium spacing. By adding heat to the mixture, the energy level of the system can be raised, allowing the chromophore molecules to freely orient. Raising the temperature to the material system glass transition temperature (T_g), the molecules of the polymer host and chromophore become fluid. Physically, the thermal energy has raised the energy of the system above the equilibrium wells and the molecules are now free to reorient. This new energy level results in an increase in the spacing of the polymer system molecules.

Without the presence of an electric field, the molecules would achieve a new random orientation as they are cooled. However, by applying an electric field to the system, the chromophore at T_g freely aligns to the direction of the field. In addition, some orientation of the polymer chains is also possible in the electric field at T_g. As the system is cooled under the applied electric field, the orientation of the chromophore is maintained as the system obtains a new room temperature equilibrium position. This equilibrium is maintained upon the removal of the electric field at room temperature.

The poled state represents an induced molecular alignment that is not close to the thermodynamic equilibrium state of the material. If free space between the polymer chains exist in the poled sample at room temperature, then the chromophores may re-orient toward a more thermodynamically stable position. Under the presence of local effects such as local fields produced by the polymer chains and space charge, some relaxation is possible at room temperature. Thus, free space left between polymer chains

can greatly degrade thermal stability of a poled polymer. These relaxation processes determine the thermal stability of the poled polymer system. [39]

3.1 Poling Theory

Polarizability is created at the molecular level, but measured macroscopically in nonlinear optical (NLO) polymer films. Thus, polarization must be understood at the molecular level and translated to measurable macroscopic parameters.

The chromophore is responsible for the molecular electro-optic effect in a polymer film. NLO chromophores have a dipole structure formed by π-electrons. π-electrons are loosely associated electrons attached to a molecular chain. These electrons are readily oriented by an external electric field. The local field polarizability of these molecules is given by the polarization tensor:

$$p = \mu + \alpha\xi(\omega) + \beta(-\omega; \omega_1, \omega_2)\, \xi(\omega_1)\xi(\omega_2) + \ldots \qquad (3.1)$$

where ,

μ = permanent dipole moment,
α = linear polarizability tensor,
β = first hyperpolarizability tensor.

The first hyperpolarizibility, β, describes the 2nd order nonlinear optical effect at the molecular level. The notation $\beta(-\omega; \omega_1, \omega_2)$ indicates the frequencies ω_1 and ω_2 interact with the molecule causing an emission of ω. This may be written as $\omega_2 - \omega_1 = -\omega$.

Polarization properties, being based on the fundamental properties of the material system follow the same symmetry properties as the material. If a material has inversion symmetry (i.e. centrosymmetric), then the polarization properties must hold inversion symmetry. So, taking a parameter, β, through an inversion operation, P_i, from a point R on the crystal to a point –R:

$$P_ib = \beta' = -\beta \tag{3.2}$$

But, if inversion symmetry exists, then $\beta = -\beta$ which is true only for $\beta = 0$. Thus, in a centrosymmetric material, no 2nd order NLO effect is present. But, for a noncentrosymmetric material, inversion symmetry does not hold and 2nd order NLO effects are present.[38]

To derive the relationship between the molecular hyperpolarizability and the macroscopic polarization constants for organic polymers, the dipole approximation is employed. The dipole approximation assumes that anharmonic vibrations produce dipoles in response to an external field, $E(\omega)$. Spatial dispersion effects are ignored and the wavelength of the external disturbance field is assumed to be large compared to the polarizable chromophores. For organic polymers, anharmonic vibrations are the result of nuclear vibrations and rotations at Infrared (IR) wavelengths and electronic vibrations at Ultra-Violet (UV) wavelengths. Macroscopically, the polarization vector is related to the electric field vector through the electric susceptibility tensor, χ, by [38]:

$$P = \varepsilon_0 \chi E. \tag{3.3}$$

where,

$$\chi_{ij} = \frac{\varepsilon_{ij} - \varepsilon_0}{\varepsilon_0} \tag{3.4}$$

The macroscopic polarization, P, can be expanded as was done for the microscopic polarization, p. This produces the relationship:

$$P(\omega) = \chi^{(1)}E(\omega) + \chi^{(2)}E(\omega_1)E(\omega_2) + \cdots \tag{3.5}$$

But, the macroscopic polarization can also be written as the summation of the microscopic polarizabilities in the polymer crystal. If the crystal has N chromophores per unit volume (the number density of chromophores), then the macroscopic polarization is:

$$P(\omega) = Np(\omega) = N[\mu + \alpha\xi(\omega) + \beta(-\omega; \omega_1, \omega_2)\, \xi(\omega_1)\xi(\omega_2) + \ldots] \quad (3.6)$$

Now, E_j and E_k represent the local fields of the individual chromophores. These fields can be related to the macroscopic fields by correcting the macroscopic field for local field effects. Representing the local field by ξ and the macroscopic field as E yields:

$$\xi(\omega) = f(\omega) \cdot E(\omega) \quad (3.7)$$

Where $f(\omega)$ are the local field correction factors,

$$f(\omega) = 1 + (\varepsilon_\omega - 1)/L. \quad (3.8)$$

L is the demagnetization factor and describes the shape of the local field. This parameter was first derived for magnetic dipoles, but generally describes the shape of dipoles whether magnetic or electric. The local field is assumed to be elliptical in general with major axis lengths of a_1, a_2, a_3. L then has 3 components given by:

$$L_I = \frac{a_1 a_2 a_3}{2} \int_0^\infty \frac{ds}{(s + a_I^2)\sqrt{(s + a_1^2)(s + a_2^2)(s + a_3^2)}}, \quad (3.9)$$

and are related by:

$$L_1 + L_2 + L_3 = 1. \quad (3.10)$$

Since β is represents the interaction of 3 frequencies: ω_1, ω_2, $-\omega$, then 3 field correction factors are required. Substituting Equation (3.7) into (3.6) and comparing the second order terms with the 2nd order terms in Equation (3.5) yields:

$$\chi^{(2)} = f(-\omega)f(\omega_1)f(\omega_2)N\beta(-\omega;\omega_1,\omega_2) \quad (3.11)$$

This represents relationship between the microscopic and macroscopic polarization constants. [12]

Now, the macroscopic polarization induced by a static electric field can be considered as a measure of the dipole orientation. When the poling field in applied, the

chromophore dipoles align with the polar axis parallel to the field creating a noncentrosymmetric crystalline symmetry. The structure is Uniaxial, with the extraordinary index formed in the direction of the poling field and the ordinary index lying in the waveguide plane.

During poling, the system is raised to the glass transition temperature, T_g, and thus becomes fluid. The energy of a molecule in the prescience of an electric field can be given by:

$$W = -\mu \cdot E_p = \mu E_p \cos\theta \,, \tag{3.12}$$

where μ is the permanent molecular dipole moment, E_p is the poling field, and $\cos\theta$ is the orientation of the molecule with respect to the poling field direction. Assuming that all molecular orientations are equally probably in the absence of the poling field, the average orientation of the molecules when the poling field is applied can be calculated using Boltzman's Law:

$$\overline{\cos\theta} = \frac{\int_0^{\pi} \cos\theta e^{(\mu E_p \cos\theta / k_B T)} \frac{1}{2} \sin\theta d\theta}{\int_0^{\pi} e^{(\mu E_p \cos\theta / k_B T)} \frac{1}{2} \sin\theta d\theta} \tag{3.13}$$

where the denominator is a proportionality constant to maintain the total probability equal to 1:

$$\int_0^{\pi} p(\theta) d\theta = 1 \tag{3.14}$$

$$\text{for } p(\theta) = \frac{e^{(\mu E_p \cos\theta / k_B T)} \frac{1}{2} \sin\theta d\theta}{\int_0^{\pi} e^{(\mu E_p \cos\theta / k_B T)} \frac{1}{2} \sin\theta d\theta} \tag{3.15}$$

Evaluating Equation (3.13), the average molecule orientation in the presence of an electric field may be represented by the Langevin function:

$$L(a) = \coth a - 1/a = (1/3)a - (1/45)a^3 + (2/945)a^5 - (2/9450)a^7 + \ldots \quad (3.16)$$

where $a = (\mu E_p)/(k_B T)$.

For the assumption that $(\mu E_p)/(k_B T) < 1$, only the first term of the Langevin expansion is significant and the average orientation of molecules in a fluid can be approximated as:

$$\overline{\cos\theta} = \frac{\mu \cdot E_P}{3k_B T_P} \quad (3.17)$$

where θ is the angle describing the alignment
E_p is the poling field
T_p is the poling temperature
μ is the permanent dipole moment
k_B is Boltzman's constant. [40]

The average value of the hyperpolarizability can then be written as

$$\langle\beta\rangle = \beta\overline{\cos\theta} = \frac{\mu \cdot E_P}{5k_B T_P}\beta \quad (3.18)$$

where a scaling factor of 3/5 has been used to reflect a uniaxial symmetry with β in the direction of the poling field [12] so that the relation between χ and β is given by [1]:

$$\chi_{33}^{(2)} = N\beta_{33}\frac{\mu E_z}{5kT} \quad (3.19)$$

$$\chi_{13}^{(2)} = N\beta_{33}\frac{\mu E_z}{15kT} \quad (3.20)$$

From these 2 relationships it can be seen that the magnitude of the 2nd order effects is dependent on the product $\mu\beta_{33}$. Thus, polymers with good nonlinear optical properties are often described as high $\mu\beta$ materials. Also note that χ_{33} is 3 times larger

than χ_{13}. Also, note that the measure of χ gives an indication of the average orientation of the chromophores in the material. Thus, Equations (3.16) through (3.18) may be used to determine the average dipole orientation.

Now, as noted in Section 2.3, electro-optic modulation is related to the linear electro-optic coefficient, r_{ijk}. r_{ijk} is formed from a power series expansion of the material system impermeability matrix, η_{ij}, where[41],

$$\eta_{ij} = \varepsilon_{ij}^{-1} = \eta_{ij}^{(0)} + \sum_{k} r_{ijk} E_k + \cdots \tag{3.21}$$

r_{ijk} can then be related to χ_{ijk} as:

$$r_{ijk} = -2n_i^2 n_j^2 \chi_{ijk}. \tag{3.22}$$

where n_i^2 and n_j^2 are 2 principle indexes of the material system.[12] rijk is a function of the polarization field, E_k, only. This is known as the linear electro-optic effect. However, β is a second order effect depending on both $E(\omega_1)$ and $E(\omega_2)$. This is reconciled by noting that the linear electro-optic effect occurs when $E(\omega_1) >> E(\omega 2) \approx 0$. Thus the linear electro-optic effect is a special case of second order polarization properties. Since χ_{33} is 3 times larger than χ_{13}, as noted from Equations (3.19) and (3.20), then:

$$r_{33} = 3r_{13}\,. \tag{3.23}$$

Another parameter often seen in the literature is the nonlinear optical coefficient, $d^{(2)}$. $d^{(2)}$ is related to χ as $d^{(2)} = 0.5\chi$ and therefore, the electro-optic coefficient, r as [42]:

$$r_{ij} = 4n_i^2 n_j^2 d_{ji}^{(2)}\,. \tag{3.24}$$

3.2 Poling Methods

There are various poling methods reported in the literature for application of an electric field including corona, electrode, electron beam, and optical poling. Optical poling is performed using an optical beam to create high electro-magnetic field within the beam diameter. This method is good for narrow poling geometries required for gratings, etc. There are various forms of optical poling reported, [43] but since they are good for only small features, they will not be considered for this research.

Electron beam poling is performed by irradiating the top surface of a sample with an electron beam. The beam forms a negative charge layer on the top surface of the sample inducing a positive charge on the ground electrode. This creates a field under which the dipoles can align. Thermal stability has been an issue for this type of poling due to fast cooling rates and short poling times. Beam energies reported for this technique are 2 – 20 keV generating a current density of .5 mA/m^2 through the sample. [44]

Corona poling is another method used for poling of polymer films. Coronas are produced using a high voltage (1 KV to 10 KV) applied to either a needle or wire. A voltage grid (50 μm wire in a 500 μm grid mesh) is used to maintain a constant current through the sample. Figure 3.1 illustrates the basic corona triode configuration for needle poling. The needle produces a circular poling distribution on the sample surface. The current controlled voltage source controls the grid voltage to maintain a constant current through the sample. The other voltage sources are referenced to the grid voltage and operated for constant current. This provides a configuration where the grid voltage is used to maintain the current constant through the sample and also gives a measure of the surface charge. As the surface charge changes, the voltage across the air gap between the

grid and the sample surface change inversely. This causes a change in current that leads to an adjustment of the grid voltage to counter the change in surface charge and maintain constant current. Thus, the triode configuration provides the ability to monitor surface charge and adjust for changes preventing sample damage due to excessive current flow while poling. [45]

Wire poling is similar to needle poling, except a wire is used to apply the high voltage electric field. This results in a cylindrical electric field distribution that projects a rectangular poling field on the sample surface. Corona poling is excellent for planar fields and provides good uniformity over a circular (needle poling) or rectangular (wire) poling area. However, upper electrodes cannot be placed over the film until after the poling is completed. Deposition of the electrodes after poling exposes the sample to heating during photoresist curing and metal deposition processes. This can adversely effect the dipole orientation, and can cause complete dipole relaxation depending on temperatures used and the material thermal stability. Thus, corona poling is not optimal for modulator fabrication.

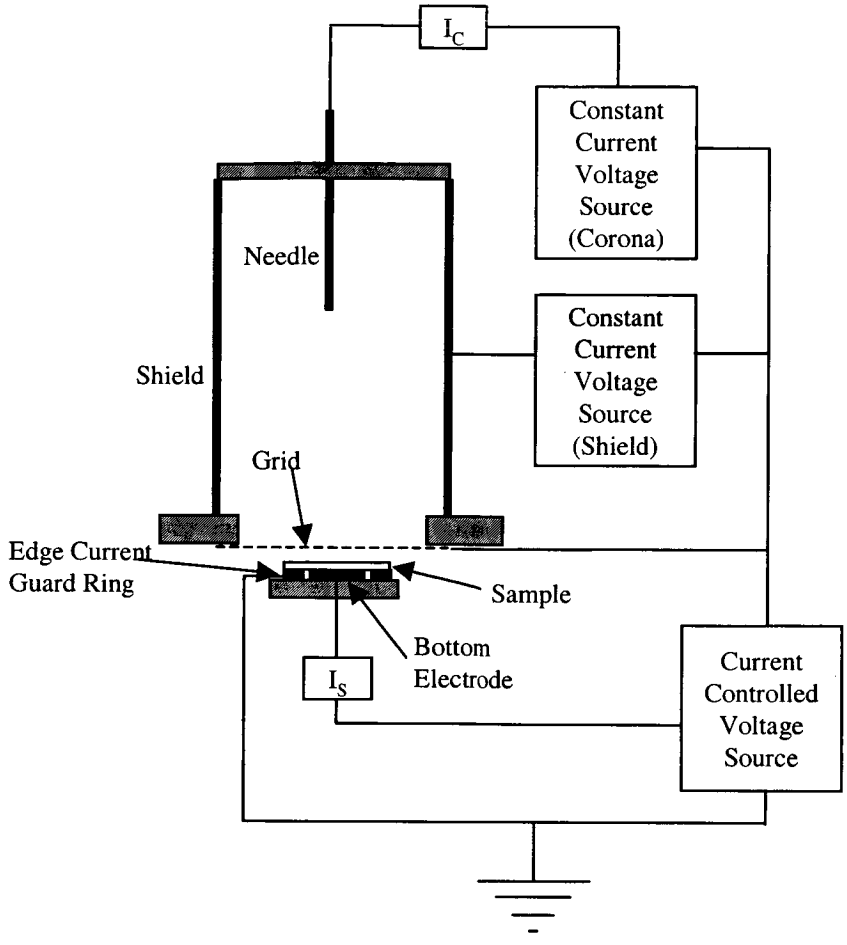

Figure 3.1: Corona Triode Poling Configuration

For devices such as modulators, which require upper electrodes, the device electrodes can be used for poling as well as modulation. The poling geometry conforms to the electrode geometry, so that there is good flexibility in poling geometry. Electrodes also offer the ability to pole the material for either TE or TM mode polarization. Figures 2.2 and 2.3 illustrate electrode geometries for TE and TM polarization orientations. Since the modulation electrodes are used for poling, no further fabrication processing is required after device poling.

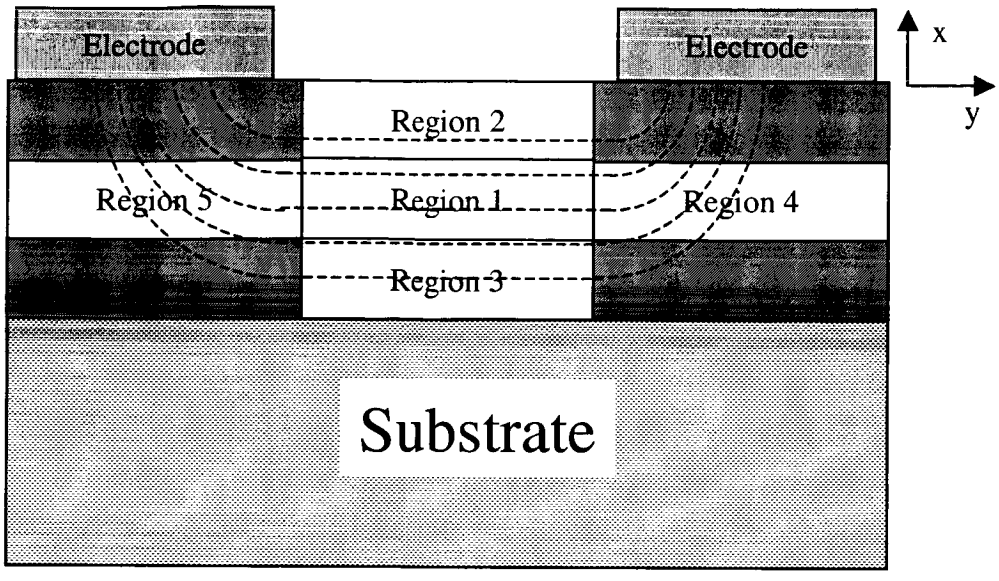

Figure 3.2: TE Mode Electrode Poling

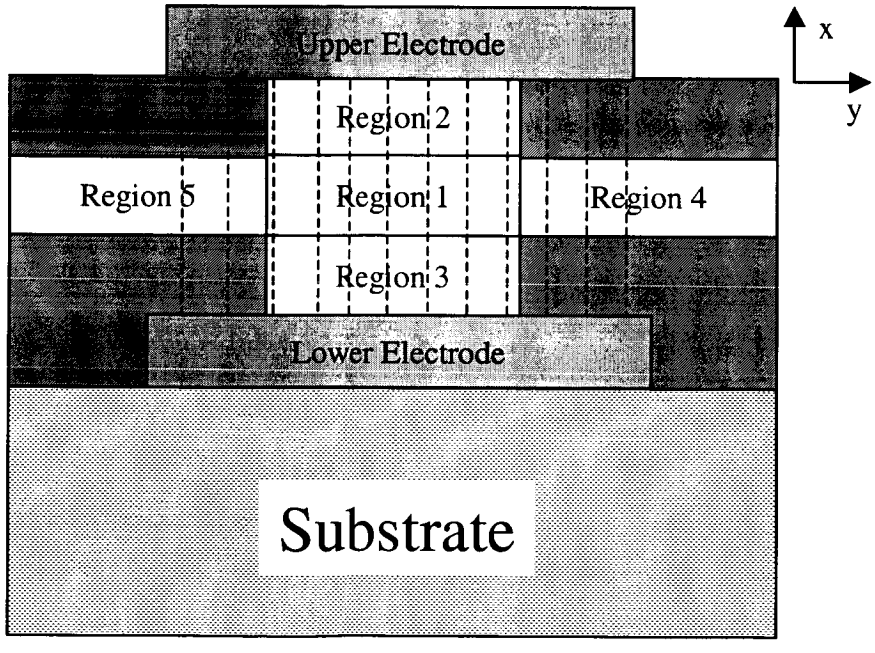

Figure 3.3: TM Mode Electrode Poling

Poling of modulators involve application of the electric field across a material stack consisting of the upper cladding, core, and lower cladding as illustrated in Figures

3.2 and 3.3. An electro-magnetic field is applied in the core producing an alignment of the electro-optic chromophore in the direction of the electrical field. The field strength in the core is related to the poling field through the waveguide electrical transfer function, $H_{wg}(j\omega)$ as given by Equation (2.86). Thus, resistance and capacitance of the cladding layers at the poling temperature is an important consideration for effective poling. Poling effectiveness can be obtained by determining the r_{33} coefficient through the measurement of V_π as indicated in Equation (2.73). The lower the V_π, the higher the r_{33} coefficient and the better the alignment of the chromophores in the polymer system.

3.3 Single Layer Charge Measurements and Effects

Dipole alignment processes can be monitor externally by measuring thermally stimulated currents during poling and depoling processes. These currents known as Thermally Stimulated Poling (TSP) and Thermally Stimulated Depoling (TSD) currents are the result of the movement of various charges in the polymer films. The main sources of these charges are dipole alignment, surface charge build-up, and space charge effects. Space charges in polymer films result from isolated free radicals, catalyzers, and plasticizers trapped in the film during fabrication. [46] Surface charges are a result of the poling process used. Electron beam poling works by inducing a large surface charge potential. Similarly, corona poling can induce a surface charge. Surface charge induced by these methods decays slowly as there is no conduction path to bleed off the charge. This affects poling stability since a short term decrease in poling effects are typically seen over the first several hours after poling as the surface charge slowly dissipates. [39] Electrode poling, on the other hand, does not produce any surface charge since the charge is free to migrate through the electrodes and is quickly dissipated. Dipole alignment is

responsible for the NLO effects of the polymer, but is influenced by the fields created in the sample due to surface and space charges.

A simple model [46] has been developed to represent charge carriers within a polymer film. Charge carriers are either trapped in deep traps or are trapped in shallow traps below the conduction band of the material. Deeply trapped charge carriers are not generally available during poling, but the thermal energy available in a system near T_g, provides sufficient thermal energy to promote charge carriers in shallow traps up to the conduction band. The energy required to free a trapped charge carrier is the activation energy, E_A. Using this simple model, charge carriers in states whose activation energy is larger than kT_p are considered trapped charge carriers. Charge carriers whose activation energy is less that kT_p become free at the poling temperature. Note the charge carriers occupy many states but in this model are classified as either being trapped ($E_A < kT_p$) or free ($E_A > kT_p$). The total density of charge carriers is the sum of the trapped and free charge carriers and can be written as:

$$\rho = \rho_{Trapped} + \rho_{free}. \tag{3.25}$$

Considering depolarization currents, which are similar to the poling case except for the absence of an external electric field, the space charge current density can be defined by assuming the density of free and trapped charge carriers to be uniform within the film. Then a differential charge element can be written as:

$$dQ = \rho dx \tag{3.26}$$

This differential charge then contributes to the thermally stimulated current density as:

$$dj = VdQ/t = I(x)dx/t, \tag{3.27}$$

where, t is the thickness of the layer,

V is the velocity of the charge layer,

I(x) is the local current due to motion of the charge carriers in the space charge field.

The current, I(x) can be expressed using Ohm's Law as:

$$I(x) = Q\mu E(x), \tag{3.28}$$

where μ is the charge mobility, and E(x) is the local field at x.

Using Poisson's Equation,

$$dE/dx = Q_T/\varepsilon_o\varepsilon_r, \tag{3.29}$$

where Q_T is the total free and trapped charge.

Now, assuming $Q_T = e$ (the electronic charge) and integrating Equation (3.29) to solve for E(x) and substituting this result into Equation (3.28) and then substituting the resulting value of I(x) in Equation (3.27) and integrating yields a general equation for the free space current density as:

$$j = \frac{\mu e^2 \delta^2}{2\varepsilon_0 \varepsilon_r t} n_f (n_f + n_t), \tag{3.30}$$

where n_f is the free carrier density,

n_t is the trapped carrier density,

d is the depth of penetration.

The thermal dependency of the free carrier density has been defined for a system that is raised from a temperature, T_0, to a temperature, T, as:

$$j_{sp}(T) = \frac{\mu e^2 \delta^2 n_{to}^2 \tau}{2\varepsilon_0 \varepsilon_r s \tau_0} e\left\{-\frac{E_a}{kT} - \frac{2}{\beta\tau_0}\int_{T_0}^{T} e^{-\frac{E_A}{kT}} dT\right\}, \tag{3.31}$$

where n_{to} is the initial trapped charge density,

$1/\tau_0$ is the trap escape frequency,

k is Boltzmann's constant,

β is the heating rate, and

$\tau = \tau_0 e^{-\frac{E_A}{kT}}$ is the lifetime of a charge in traps. (3.32)

Taking the natural logarithm of Equation (3.32) provides a relationship between the charge lifetime in traps (i.e. the space charge relaxation time) and Temperature, T as

$$\ln[\tau(T)] = -\ln(\tau_0) + \frac{E_A}{kT} \tag{3.33}$$

This provides a model for evaluation of TSD current densities and activation energy as a function of the temperature change. A plot of Equation (3.33) yields a straight line with slope = E_A. [47]

A similar derivation [48] has been made for TSD currents due to dipole relaxation as:

$$j_D(T) = \frac{N\mu^2 E}{3kT\tau_r} e\left\{-\frac{E_A}{kT} - \frac{2}{\beta\tau_0}\int_{T_0}^{T} e^{-\frac{E_A}{kT}} dT\right\}, \tag{3.34}$$

where, E is the poling electric field,

N is the dipole concentration,

τ_r is the dipole relaxation time.

Taking the natural logarithm of this equation yields:

$$\ln[j_D(T)] = C - \frac{E_A}{kT} \tag{3.35}$$

where,

$$C = \ln\left[\frac{N\mu^2 E}{3kT\tau_r}\right] - \frac{2}{\beta\tau_0}\int_{T_0}^{T} e^{-\frac{E_A}{kT}} dT \,. \tag{3.36}$$

As with Equation (3.33), Equation (3.35) may be plotted yielding a straight line whose slope is the activation energy, E_A.

TSP current densities provides more detailed information on charge flow processes in polymer films. Debye theory gives saturation polarization as:

$$P_s = \frac{N\mu^2 E_P}{3kT}, \tag{3.37}$$

where the poling temperature can be related to the initial temperature through the heating rate:

$$T = T_0 + \beta t \tag{3.38}$$

where, t is the heating time.

However, the total polarization can also be defined by integrating the current density and dividing by the heating rate yielding:

$$P_s(T) = \frac{1}{\beta}\int_{T_0}^{T} j_P(T)dT \tag{3.39}$$

Equations (3.37) to (3.39) can be combined and differentiated to solve for the poling current as:

$$j_P(T) = -\frac{N\mu^2 E_P}{3k(T_0 + \beta t)^2} \tag{3.40}$$

$\tau(T)$ may be defined as:

$$\tau(T) = \frac{\int_{T_0}^{T} \frac{1}{\beta} j_P(T)dT}{j_P(T)}. \tag{3.41}$$

Having defined the current densities of polarization and depolarization currents, a useful tool has been developed to study poling effects on polymer materials. These effects are a direct consequence of the local and external electric fields in the polymer. A general derivation has been made defining the local electric field as a result of space charge density, dipole densities, and the external electric field. [49]

Using the propagation coordinate system, the poling field is applied along the x axis. The space charge is assumed to be homogeneously distributed in the polymer with the E_x causing a displacement of the charge during poling. The space charge volume density is represented as ρ_{sp} and the polarization charge density is defined as:

$$\rho_p(x,t) = -\frac{dP(x,t)}{dx} \tag{3.42}$$

Using Equation (3.25) with the total charge, $Q_T = \rho_{sp} + \rho_p$ yields:

$$\varepsilon_o\varepsilon_r \, dE(x,t)/dx = \rho_{sp} + \rho_p, \tag{3.43}$$

Integrating this relationship from x = 0 (positive electrode) to x,

$$\varepsilon_0\varepsilon_r[E_P(x,t) - E_P(0,t)] = \int_0^x \rho_{sp}(x,t)dx + \int_0^x \rho_p(x,t)dx$$

(3.44)

Integrating again for x = t (bottom electrode) to find a relationship for E(0,t):

$$E_P(0,t) = \frac{V(t)}{d} - Q_{sp}(x,t)\frac{1/2 - c(t)/d}{\varepsilon_0\varepsilon_r A} - Q_p(x,t)\frac{1/2 - c'(t)/d}{\varepsilon_0\varepsilon_r A} \tag{3.45}$$

where, V(t) is the applied voltage derived from the line integral condition

$$V(t) = \int_0^d E_P(x,t)dx, \tag{3.46}$$

c(t) is the location of the space charge centroid,

c'(t) is the location of the polarization charge centroid,

A is the area of the electrodes,

$$Q_{sp} = \int_0^d \rho_{sp}(x,t)dx \text{ , and} \tag{3.47}$$

$$Q_p = \int_0^d \rho_p(x,t)dx \text{ .} \tag{3.48}$$

Note, that $\int_0^x \rho(x,t)dx = \frac{d/2 - c(t)}{A}\rho(x,t)$ so that the charge centroid is referenced to the center of the film (d/2) and the charge is distributed uniformly under the electrode area (A). Equation (3.45) provides a value of E(0,t) that may be substituted back into Equation (3.44) resulting in:

$$\begin{aligned} E_P(x,t) = {} & \frac{V(t)}{d} - Q_{sp}(x,t)\frac{1/2 - c(t)/d}{\varepsilon_0 \varepsilon_r A} + \frac{1}{\varepsilon_0 \varepsilon_r}\int_0^x \rho_{sp}(x,t)dx \\ & - \frac{\langle P(x,t)\rangle_x}{\varepsilon_0 \varepsilon_r} + \frac{d}{\varepsilon_0 \varepsilon_r}\left\langle \frac{dP(x,t)}{dx}\right\rangle_x \left(\frac{1}{2} - \frac{c_P}{d}\right) - \frac{1}{\varepsilon_0 \varepsilon_r}[P(x,t) - P(0,t)] \end{aligned} \tag{3.49}$$

Sources of electric field can be identified as follows:

V(t)/d is the field due to the externally applied voltage,

the Q_{sp} term is the induced electrode field due to the space charge,

the integral of ρ_{sp} is the space charge distribution,

$\langle P(x,t)\rangle_x$ represents the spatial distribution of the polarization field

$\langle dP(x,t)/dx\rangle_x$ represents the spatial variation in the polarization field

[P(x,t) – P(0,t)] represents the polarization difference from x = 0 to x.

Note, that for c(t) = 0.5d then the term with Q_{sp} is zero. Similarly, if c_p = .5d, then the field due to the spatial variation of the polarization is zero. If there is no space charge, then $\rho_{sp} = 0$, so that the polarization becomes homogeneous in x and dP(x,t)/dx = 0, <P(x,t)>x = P(t), and P(x,t) – P(0,t) = 0, and

$$E_P(t) = V(t)/d - P(t)/\varepsilon. \tag{3.50}$$

In the case of a constant poling field, the time dependency of E is removed and

$$P = \varepsilon V/d. \tag{3.51}$$

The term $\langle P(x,t)\rangle_x$ can be related to the Voltage, V(t), starting with the basic relationship between P and E,

$$P(x,t) = \varepsilon E_P(x,t) \tag{3.52}$$

Integrating both sides from x = 0 to d and applying the line integral condition from Equation (3.46) yields:

$$\langle P(x,t)\rangle_x = \frac{\varepsilon_0 \varepsilon_r V(t)}{d} \tag{3.53}$$

Thus, if $\langle P(x,t)\rangle_x$ changes independently from V(t), then P(x,t) is not in equilibrium with $E_P(x,t)$. As seen in Equation (3.49), this is a result of space charge distribution in the material. Since at t = 0, $\langle P(x,0)\rangle_x \neq \frac{\varepsilon_0 \varepsilon_r V(0)}{d}$, the time for the spatial distribution of P(x,t) to equal this value the dipole response time, τ. P(x,t) can continue to change after this point, reaching a constant value when ρ_{sp} reaches a steady state value (no longer changing with time). Equation (3.52) can e modified to reflect the dipole response time as:

$$P(x,t) = \left[1 - e^{-t/\tau}\right] \varepsilon E_P(x,t) \tag{3.54}$$

3.4 Three Layer Waveguide Stack Charge Distribution

Poling of a material stack can be described in terms of the charge densities and current densities produced through the poling process. [50] Charge distributions within the dielectric layers lead to a boundary charge density along the boundaries between layers with differing dielectric constants. These represent Maxwell-Wagner

boundaries In addition, polarization charge densities exist within polar layers. The motion of these charge densities leads to the material current densities and are directed by the poling field which also provides a conduction current density within the layers. These charge densities and current densities are determined by the layer material properties. Boundary charge densities are determined by the differences in layer conductivities and dielectric constants. Polarization charge densities are related to the alignment of dipoles. These alignments are related to the dipole activation energy (E_A) and relaxation frequency (α_r). Activation energy is the energy required to orient a molecule. The E_A is strongly dependent on the molecular environment surrounding the dipole. Natural frequency is a function of molecular shape and size.[13] For guest/host polymer systems, the chromophores are all of similar shape and size, so the natural frequency should be a constant. However, the local molecular environment can vary greatly, depending on where the chromophore molecule is located with relationship to host molecule segments, the compactness of the host molecules, and the chromophore loading density. Thus, for guest/host polymer systems, distributions are expected in terms of the chromophore activation energy.

Figure 3.3 illustrates the typical photo bleached waveguide geometry. This geometry consists of 2 separate nonpolar polymer films sandwiching a polar guest/host polymer. Photo bleaching forms a narrow region in the core film providing lateral optical confinement. The photo bleaching destroys the chromophore molecules in the exposed region leaving only the waveguide core containing chromophore. Thus, photobleached waveguides can be modeled by noting that only the core region will have dipole orientations. The bleached core region can then be treated as a nonpolar material. Assuming diffusion is not a strong factor in TSD [13] the bleached regions will not

contribute significantly to the discharge current. These regions have a similar molecular structure to the core, missing only the guest molecule. When poled, the dipoles in the bleached region are aligned parallel to the electric field as shown in Figure 3.3. Both negative and positive charges exist along the bleaching boundary and the surface retains a neutral charge. Thus, the bleaching boundary does not form a Maxwell Wagner boundary.

Between the 3 film layers, Maxwell Wagner boundaries do exist. For optical waveguides the poling region and therefore the electrodes are typically confined to the waveguide region. Thus, no significant poling field exists outside the waveguide core and a rectangular geometry can be assumed for the model as shown in Figure 3.3. Based on this assumption, no conduction charge is expected to be created in the bleached (nonpolar) core region. Thus, a 3 layer model can be employed with Maxwell Wagner charge boundaries between the upper cladding and core and between the core and lower cladding.

Rib waveguides, as illustrated in Figure 2.2, have a more challenging structure but the same assumptions apply. During poling, only the waveguide core region is poled. Thus, there is a boundary between poled and unpoled core regions. Again, however, this boundary does not produce a charge surface, but merely represents a transition from vertically oriented dipoles to randomly oriented dipoles. Because the poling field is confined to the waveguide core region, and no conduction charge is generated outside the poling field. Thus rib waveguides, as well as trench waveguides which can be viewed as inverted ribs, can be represented by a 3 layer model with Maxwell Wagner charge boundaries between the upper cladding and core and between the core and lower cladding.

The initial model will be developed following the original approach employed by J. Turnhout for a 2 layer nonpolar planar structure and a polar layer separated by an air gap from the upper electrode. [13] The most general waveguide case is the asymmetric waveguide: a polar layer sandwiched by 2 different nonpolar layers. Equations for the charge density and polarization can be derived beginning with the current density for a 3 layer stack. The single relaxation Debye Equation can then be employed to form a set of coupled differential equations.

Figure 2.10 illustrates the electrical model for a 3 layer stack. No space charge is assumed to be stored prior to poling. The current density through each layer must be equal following Kirchoff's Laws. The poling field directs all current flows and dipole alignments in the same direction. So, the current density relationship can be written employing Gauss Law ($\sigma_L/A^2 = \varepsilon_0\varepsilon_L E_L$) as:

$$J(t) = \varepsilon_o\varepsilon_c \frac{dE_c(t)}{dt} + \gamma_c(T)E_c(t) = \varepsilon_o\varepsilon_g \frac{dE_g(t)}{dt} + \gamma_g(T)E_g(t) + \frac{dP_s(t)}{dt} = \varepsilon_o\varepsilon_s \frac{dE_s(t)}{dt} + \gamma_s(T)E_s(t) \quad , \tag{3.55}$$

where,

ε_0 is the permittivity of free space,

ε_c, ε_g, ε_s are the dielectric constants for the upper cladding, waveguide core (guiding region), and lower cladding respectively,

γ_c, γ_g, γ_s are the material conductivity of the upper cladding, waveguide core (guiding region), and lower cladding respectively,

$E_c(t)$, $E_g(t)$, $E_s(t)$ are the electric fields in the upper cladding, waveguide core (guiding region), and lower cladding respectively,

$P_s(t)$ is the persistent polarization of the dipoles.

Similarly, the voltage relationship is:

$$V_P = E_c(t)h_c + E_g(t)h_g + E_s(t)h_s = V_c(t) + V_g(t) + V_s(t), \tag{3.56}$$

where,

$V(t) = E(t)h$

V_P is the poling voltage

and h_c, h_g, h_s are the thicknesses of the upper cladding, waveguide core (guiding region), and lower cladding respectively.

Now, from Ohm's Law, $V(t) = i(t)/\gamma(T)$ and assuming that the upper and lower claddings differ only in their resistivity so that the currents in these layers are equal:

$$V_s(t) = V_c(t)\frac{\gamma_c(T)}{\gamma_s(T)} \tag{3.57}$$

and

$$V_P = V_g(t) + V_c(t)\left(\frac{1}{1+\frac{\gamma_c(T)}{\gamma_s(T)}}\right) = V_g(t) + V_c(t)\Gamma_{cs}(T), \tag{3.58}$$

$$\text{where,}\quad \Gamma_{cs}(T) = \left(\frac{1}{1+\frac{\gamma_c(T)}{\gamma_s(T)}}\right). \tag{3.59}$$

The surface charge along the Maxwell Wagner boundaries between the upper cladding and core and between the core and lower cladding can be written using Gauss Law as:

$$\sigma_{cg}(t) = \varepsilon_0 \varepsilon_g E_g(t) + P_s(t) - \varepsilon_0 \varepsilon_c E_c(t) \tag{3.60}$$

and

$$\sigma_{gs}(t) = \varepsilon_0 \varepsilon_s E_s(t) - \varepsilon_0 \varepsilon_g E_g(t) - P_s(t) \tag{3.61}$$

Using Equations (3.60) and (3.58), $V_g(t)$ can be written in terms of $\sigma_{cg}(t)$, $P_s(t)$ and V_p as:

$$V_g(t) = \frac{\sigma_{cg}(t) - P_s(t) + \frac{\varepsilon_0 \varepsilon_c}{h_c} V_P}{\left(\frac{\varepsilon_0 \varepsilon_g}{h_g} + \frac{\varepsilon_c}{h_c \varepsilon_g} \Gamma_{cs}(T) \right)} \tag{3.62}$$

Using the first 2 equalities from Equation (3.55) and substituting E(t) = V(t)/h:

$$J(t) = \frac{\varepsilon_o \varepsilon_c}{h_c} \frac{dV_c(t)}{dt} + \frac{\gamma_c(T)}{h_c} V_c(t) = \frac{\varepsilon_o \varepsilon_g}{h_g} \frac{dV_g(t)}{dt} + \frac{\gamma_g(T)}{h_g} V_g(t) + \frac{dP_s(t)}{dt} . \tag{3.63}$$

Using Equation (3.58) to rewrite $V_c(t)$ in terms of V_P and $V_g(t)$ and substituting into Equation (3.63):

$$\begin{aligned} &\frac{dV_g(t)}{dt} + \left(\frac{\frac{h_c \gamma_g(T)}{h_g \varepsilon_0 \varepsilon_c \Gamma_{cs}(T)} + \frac{\gamma_c(T)}{\varepsilon_0 \varepsilon_c \Gamma_{cs}(T)}}{1 + \frac{\varepsilon_g h_c}{\varepsilon_c h_g \Gamma_{cs}(T)}} \right) V_g(t) + \left(\frac{\frac{h_c}{\varepsilon_0 \varepsilon_c \Gamma_{cs}(T)}}{1 + \frac{\varepsilon_g h_c}{\varepsilon_c h_g \Gamma_{cs}(T)}} \right) \frac{dP_s(t)}{dt} \\ &= \left(\frac{\frac{\gamma_c(T)}{\varepsilon_0 \varepsilon_c}}{1 + \frac{\varepsilon_g h_c}{\varepsilon_c h_g \Gamma_{cs}(T)}} \right) V_P \end{aligned} . \tag{3.64}$$

Equation (3.62) may also be substituted into the 2nd equality given in Equation (3.63) to write the charging current density as:

$$J(t)=\left(\frac{\frac{\gamma_g(T)}{h_g}\left(\sigma_{cg}(t)-P_s(t)+\frac{\varepsilon_0\varepsilon_c}{h_c}\Gamma_{cs}(T)V_P\right)}{\left(\frac{\varepsilon_0\varepsilon_g}{h_g}+\frac{\varepsilon_0\varepsilon_c}{h_c}\Gamma_{cs}(T)\right)}+\frac{\frac{\varepsilon_0\varepsilon_g}{h_g}\frac{d\sigma_{cg}(t)}{dt}+\frac{\varepsilon_0\varepsilon_c}{h_c}\Gamma_{cs}(T)\frac{dP_s(t)}{dt}}{\left(\frac{\varepsilon_0\varepsilon_g}{h_g}+\frac{\varepsilon_0\varepsilon_c}{h_c}\Gamma_{cs}(T)\right)}\right). \quad (3.65)$$

Now let,

$$\beta_w(T)=\left(\frac{\gamma_c(T)}{h_c\left(\frac{\varepsilon_0\varepsilon_c}{h_c}\Gamma_{cs}(T)+\frac{\varepsilon_0\varepsilon_g}{h_g}\right)}\right). \quad (3.66)$$

Substituting Equation (3.66) into Equation (3.64) and then using Equation (3.62) then gives a differential equation for $\sigma_{cg}(t)$ as:

$$\frac{d\sigma_{cg}(t)}{dt}+\Gamma_{gc}(T)\beta_w(T)\sigma_{cg}(t)$$
$$=\Gamma_{gc}(T)\beta_w(T)P_s(t)+\beta_w(T)\Gamma_{cs}(T)\left(\frac{\varepsilon_0\varepsilon_g}{h_g}+\frac{\varepsilon_0\varepsilon_c}{h_c}\left(\Gamma_{cs}(T)-\Gamma_{gc}(T)\right)\right)V_P \quad ,(3.67)$$

where,

$$\Gamma_{gc}(T)=\left(1+\frac{h_c\gamma_g(T)}{h_g\gamma_c(T)}\right). \quad (3.68)$$

Now this gives an equation in 2 unknowns, $\sigma_{cg}(t)$ and $P_s(t)$. A second equation can be found for $P_s(t)$ by using Equation (3.62) in the Debye Equation given by Turnhout. [13] The single relaxation frequency Debye equation is given by:

$$\frac{dP_s(t)}{dt}+\alpha(T)P_s(t)=\varepsilon_0(\varepsilon_{slow}-\varepsilon_g)\alpha(T)E_g(t). \quad (3.69)$$

Substituting $E_g(t) = V_g(t)/h_g$ and using Equation (3.62) for $V_g(t)$ yields:

$$\left(\frac{h_c\varepsilon_g}{\varepsilon_c}+h_g\Gamma_{cs}(T)\right)\frac{dP_s(t)}{dt}+\alpha(T)\left(h_g\Gamma_{cs}(T)+\frac{h_c\varepsilon_{slow}}{\varepsilon_c}\right)P_s(t)$$
$$=(\varepsilon_{slow}-\varepsilon_g)\alpha(T)\left(\varepsilon_0 V_P+\frac{h_c}{\varepsilon_c}\sigma_{cg}(t)\right) \quad (3.70)$$

where ε_{slow} is the low frequency dielectric response of the core material and $\alpha(T)$ is the dipole relaxation frequency.

Equations (3.67) and (3.70) form a coupled set of differential equations which can be solved to give the boundary charge density, $\sigma_{cg}(t)$, and the polarization, $P_s(t)$. These equations apply to both the poling phase and the cool down phase while the voltage is still applied to the waveguide stack.

The ultimate value of these equations can be derived assuming that the polarization and boundary charge densities cannot grow infinitely, but reach some maximum value during charging. This corresponds to saturation of charge sites able to be occupied by the boundary charge and orientation of all dipoles in the core layer. For these conditions, the charge densities are constant and the time derivative terms in Equations (3.67) and (3.70) are zero. Thus, there are now 2 equations with 2 unknowns ($\sigma_{cg}(\infty)$ and $Ps(\infty)$) which can be solved to yield:

$$\sigma_{cg}(\infty)=\left[\frac{\frac{\Gamma_{cs}(\infty)}{\Gamma_{gc}(\infty)}\left(\frac{\varepsilon_0\varepsilon_g}{h_g}+\frac{\varepsilon_0\varepsilon_c}{h_c}\left(\Gamma_{cs}(\infty)-\Gamma_{gc}(\infty)\right)\right)}{\frac{h_c\varepsilon_g}{\varepsilon_c}+h_g\Gamma_{cs}(\infty)}\left(h_g\Gamma_{cs}(\infty)+\frac{h_c\varepsilon_{slow}}{\varepsilon_c}\right)+\frac{\varepsilon_0(\varepsilon_{slow}-\varepsilon_g)}{\frac{h_c\varepsilon_g}{\varepsilon_c}+h_g\Gamma_{cs}(\infty)}\right]V_P \quad (3.71)$$

$$P_s(\infty)=\varepsilon_0(\varepsilon_{slow}-\varepsilon_g)\left[\frac{1}{\frac{h_c\varepsilon_g}{\varepsilon_c}+h_g\Gamma_{cs}(\infty)}+\frac{\Gamma_{cs}(\infty)}{\Gamma_{gc}(\infty)}\frac{\left(\frac{\varepsilon_g h_c}{\varepsilon_c h_g}+\Gamma_{cs}(\infty)-\Gamma_{gc}(\infty)\right)}{\frac{h_c\varepsilon_g}{\varepsilon_c}+h_g\Gamma_{cs}(\infty)}\right]V_P \quad (3.72)$$

$$\sigma_{cg}(\infty) - P_s(\infty) = \left[\frac{\Gamma_{cs}(\infty)}{\Gamma_{gc}(\infty)} \left(\frac{\varepsilon_0 \varepsilon_g}{h_g} + \frac{\varepsilon_0 \varepsilon_c}{h_c} \left(\Gamma_{cs}(\infty) - \Gamma_{gc}(\infty) \right) \right) \right] V_P . \qquad (3.73)$$

These Equations show that both charge densities are linearly proportional to the poling voltage and also depend on the material properties (dielectric constants and conductivities) and waveguide geometry (thickness). Thus, dipole orientation efficiency is linearly proportional to the poling field. Equation (3.73) shows the difference between the maximum values is a constant as well. Note, that the polarization charge density can be seen as driven by the boundary charge density as will be clear from the experimental section below. Also, if the material conductivities for each layer vary similarly with temperature, then Γ_{cs} and Γ_{gc} will be constants across all temperatures.

Now, for a distribution in Activation Energy, E_A, the dipole relaxation frequency takes the form of an Arrhenius Equation with constant natural frequency (relaxation time for infinite frequency), α_r, as:

$$\alpha(T) = \alpha_r g(E_A) e^{-E_A / k_B T}, \qquad (3.74)$$

where,

k_B is boltzmann's constant, and

$g(E_A)$ is the activation energy distribution shape function defined as

$$\int_0^\infty g(E_A) dE_A = 1 .$$

Equation (3.70) involves a single relaxation frequency. By solving this equation for each possible activation energy and then summing all of the solutions, a final equation is obtained for the distribution. The summation can be treated as an integral in general,

since many activation energies are assumed for the chromophore molecules dependent on their local molecular environment. Since Equation (3.70) is a time dependent differential equation and Equation (3.74) is time independent, Equation (3.74) may be substituted into Equation (3.70) and integrated yielding:

$$\left(\frac{h_c\varepsilon_g}{\varepsilon_c}+h_g\Gamma_{cs}(T)\right)\frac{dP_s(t)}{dt}+\alpha_r\left(\int_0^\infty g(E_A)e^{-E_A/k_BT}dE_A\right)\left(h_g\Gamma_{cs}(T)+\frac{h_c\varepsilon_{slow}}{\varepsilon_c}\right)P_s(t) \qquad (3.75)$$
$$=(\varepsilon_{slow}-\varepsilon_g)\alpha_r\left(\int_0^\infty g(E_A)e^{-E_A/k_BT}dE_A\right)\left(\varepsilon_0V_P+\frac{h_c}{\varepsilon_c}\sigma_{cg}(t)\right)$$

Equations (3.67) and (3.75) may then be solved numerically to find solutions for $\sigma_{cg}(t)$ and $P_s(t)$ for a distribution in Activation Energies.

During Thermally Stimulated Discharge (TSD), the waveguide electrodes are grounded so that Vp = 0. Solving Equations (3.65), (3.67), and (3.70) for this condition provides the charge densities, and released current densities during the TSD phase. Following the same approach as for the charging phase yields the following equations for $P_s(t)$, $\sigma_{gc}(t)$, and $J_r(t)$.

$$\beta_{TSD}(T)=\left(\frac{\frac{\gamma_g(T)}{h_g}+\frac{\gamma_c(T)}{h_c}\Gamma_{cs}(T)}{\frac{\varepsilon_0\varepsilon_g}{h_g}+\frac{\varepsilon_0\varepsilon_c}{h_c}\Gamma_{cs}(T)}\right) \qquad (3.76)$$

$$\frac{d\sigma_{cg}(t)}{dt}=\beta_{TSD}(T)\left(P_s(t)-\sigma_{cg}(t)\right) \qquad (3.77)$$

$$\frac{dP_s(t)}{dt}=\alpha(T)\left(\frac{\frac{\varepsilon_0}{h_g}(\varepsilon_{slow}-\varepsilon_g)\sigma_{cg}(t)}{\frac{\varepsilon_0\varepsilon_g}{h_g}+\frac{\varepsilon_0\varepsilon_c}{h_c}\Gamma_{cs}(T)}-\frac{\left(\frac{\varepsilon_0}{h_g}(\varepsilon_{slow}-\varepsilon_g)+\frac{\varepsilon_0\varepsilon_g}{h_g}+\frac{\varepsilon_0\varepsilon_c}{h_c}\Gamma_{cs}(T)\right)P_s(t)}{\frac{\varepsilon_0\varepsilon_g}{h_g}+\frac{\varepsilon_0\varepsilon_c}{h_c}\Gamma_{cs}(T)}\right) \qquad (3.78)$$

$$\Gamma_{TSD}(T) = \frac{1}{\frac{\varepsilon_0 \varepsilon_g}{h_g} + \frac{\varepsilon_0 \varepsilon_c}{h_c}\Gamma_{cs}(T)} \tag{3.79}$$

$$J_r(t) = \frac{\varepsilon_0 \varepsilon_g}{h_g}\Gamma_{TSD}(T)\frac{d\sigma_{cg}(t)}{dt} + \left(1 - \frac{\varepsilon_0 \varepsilon_g}{h_g}\Gamma_{TSD}(T)\right)\frac{dP_s(t)}{dt} + \frac{\gamma_g}{h_g}\Gamma_{TSD}(T)\left(\sigma_{cg}(t) - P_s(t)\right). \tag{3.80}$$

For an asymmetric waveguide, Equations (3.56) to (3.59), and (3.61) can be used to find the solution for $\sigma_{gs}(t)$ based on the solution to Equation (3.67) for $\sigma_{cg}(t)$. For a symmetric waveguide, the upper and lower claddings are the same. Thus, $\gamma_c = \gamma_s$, $\varepsilon_c = \varepsilon_s$. Combining these equalities with $i_c(t) = i_s(t)$ by Ohm's Law yields $V_c(t) = V_s(t)$. Assuming, equal upper and lower cladding thickness, $h_c = h_s$, then gives $E_c(t) = E_s(t)$. Using these equalities with Equations (3.60) and (3.61) then yields:

$$\sigma_{cg}(t) = -\sigma_{gs}(t). \tag{3.81}$$

Thus, as expected for a symmetric waveguide the model shows the two charge layers have equal and opposite charge.

In most optical waveguide applications, the electrodes extend well outside the waveguide channel as illustrated in Figure 3.3. For a photo bleached waveguide, no chromophore exists outside the waveguide channel. Therefore the poling field outside the channel induces a conduction current, but does not affect the dipole orientation TSD current peak. No charge boundaries are formed either between the bleached and unbleached regions as discussed previously. In addition, no Maxwell Wagner charge boundary is assumed to form at the edge of the poling field in the bleached region. Since the bleached region is nonpolar, no charge sources are assumed to produce a charge surface.

For a rib waveguide, the extended electrode configuration is more difficult. A Maxwell Wagner charge boundary does exist along the side of the waveguide channel between the core and cladding layers as illustrated in Figure 3.4. The vertical portion of this boundary can effect dipole orientation, particularly if the waveguide channel is trapezoidal in shape. The charge along this boundary produces a local field which counters full alignment of the dipole along the electric field. Instead, the dipoles are influenced to align perpendicular to the boundary charge creating a misalignment with respect to the poling field. Since the chromophore now has an alignment vector component in the horizontal direction, the optical wave propagating through the waveguide sees a poling induced index change along the trapezoidal boundary which acts to constrict the waveguide channel. Thus, V_π will be reduced by this misalignment and optical losses can be increased during poling. The planar portion of the waveguide core material creates an extended Maxwell Wagner charge boundary and also contributes additional dipole alignment current during TSD current measurements. This dipole current will be reduced by the reduced thickness of the planar core layer but must be included in the equations as an additional dipole current source. Thus the planar area in the poling field contributes to both the conduction and the dipole currents. Conversely, the trapezoidal portion of the charge boundary, creates some dipole misalignment in the waveguide channel. Although the dipole relaxation along the trapezoidal boundaries still releases charge, the molecular environment is modified leading a further distribution in activation energy, E_A.

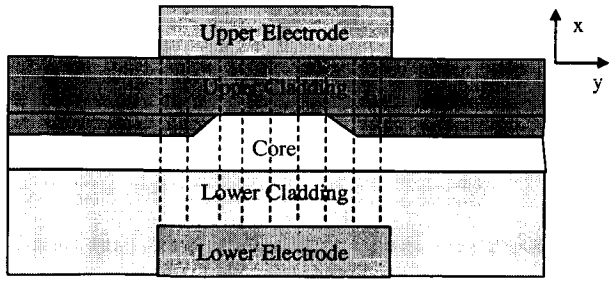

Figure 3.4: Rib Waveguide Extended Electrode Geometry

3.5 Macroscopic Field Effects on Molecular Polarization

In Equations (3.70) and (3.75) we have the term ($\varepsilon_{slow} - \varepsilon_g$). This term also appears in the Onsager Equation (for a spherical dipole) [40]:

$$\mu^2 = \frac{9k_BT}{4\pi N}\frac{\varepsilon_0(\varepsilon_{slow} - \varepsilon_g)(2\varepsilon_{slow} + \varepsilon_g)}{\varepsilon_{slow}(\varepsilon_g + 2)^2}, \tag{3.82}$$

where N = #dipoles/cm^3.

Writing the Onsager Equation in terms of ($\varepsilon_{slow} - \varepsilon_g$) yields,

$$\varepsilon_0(\varepsilon_{slow} - \varepsilon_g) = \frac{4\pi}{3}\frac{N\mu^2}{3k_BT}\frac{\varepsilon_{slow}(\varepsilon_g + 2)^2}{(2\varepsilon_{slow} + \varepsilon_g)}. \tag{3.83}$$

Now, Bottcher [40], defines the dipole polarization (due to rotations, but not translations) as:

$$P_\mu = \frac{N\mu^2}{3k_BT}E_D \tag{3.84}$$

where E_D is the directing field.

Examining Equations (3.70) or (3.75) shows that the directing field is represented as:

$$E_D = \left(\frac{V_P}{h_c} + \frac{\sigma_{cg}(t)}{\varepsilon_0\varepsilon_c}\right). \tag{3.85}$$

This shows that both the poling field and the boundary charge play a role in dipole orientation.

So, multiplying Equation (3.83) by E_D and substituting with Equation (3.84) yields:

$$\varepsilon_0(\varepsilon_{slow}-\varepsilon_g)E_D=\frac{4\pi}{3}\frac{\varepsilon_{slow}(\varepsilon_g+2)^2}{(2\varepsilon_{slow}+\varepsilon_g)}P_\mu \tag{3.86}$$

so that the difference in the slow and fast dielectric response in the presence of the directing field represents the dipole polarization, P_μ. Corrections to the Onsager Equation such as for elliptical dipoles, can be readily incorporated into Equation (3.86) showing that TSD currents clearly indicate the polarization of the chromophore dipoles.

Substituting Equation (3.86) into Equation (3.70) yields Equation (3.87) showing a relationship between P_s and P_μ. P_s is the macropolarization, while P_μ is the molecular polarization. Thus, a relationship is achieved showing the relationship between the polarization charge density and the molecular polarization.

$$\left(\frac{h_c\varepsilon_g}{\varepsilon_c}+h_g\Gamma_{cs}(T)\right)\frac{dP_s(t)}{dt}+\alpha(T)\left(h_g\Gamma_{cs}(T)+\frac{h_c\varepsilon_{slow}}{\varepsilon_c}\right)P_s(t)$$
$$=\alpha(T)h_c\left(\frac{4\pi}{3}\frac{\varepsilon_{slow}(\varepsilon_g+2)^2}{(2\varepsilon_{slow}+\varepsilon_g)}\right)P_\mu \tag{3.87}$$

3.6 Electrostriction

Electric fields produce an electric force on the polymer layers which can lead to translation of the chromophore and/or host molecules. As the molecules translate, the density of the molecules increase. A relationship for the increase in density can be

defined following Brottcher [40]. Starting with Boltzmann's Distribution Law, the #moles/cm^3 of a molecular gas in an electric field, E_D, can be written as:

$$n = n_0 e^{-\frac{W}{k_B T}} \tag{3.88}$$

where W is the average work to bring a molecule into the field and n_0 is the #moles/cm^3 for zero electric field strength.

Now,

$$W = W_D + W_{chr} . \tag{3.89}$$

Where W_D is the work to move the molecule into a constant field and W_{chr} is the work to move a randomly oriented molecule into the field.

The total work to move a molecule into a uniform field, W_D, can be written as:

$$W = \frac{1}{8\pi} \iiint_{\infty} E \cdot D dv \tag{3.90}$$

The difference in work to move a molecule in the presence of field, E_D, in a region of free spae (W_0) and in a dielectric (W_D) is:

$$\Delta W = W_D - W_0 \tag{3.91}$$

Now, the charge distribution, ρ, for these 2 cases is assumed to be the same so that,

$$\text{div } D = \text{div } E_0 = 4\pi\rho \tag{3.92}$$

or

$$\text{div}(D - E_0) = 0 \ . \tag{3.93}$$

Applying integral identities then leads to:

$$\Delta W = -\frac{1}{8\pi} \iiint_{\infty} (D - E) \cdot E_0 dv = -\frac{1}{2} \iiint_{v} P \cdot E_0 dv \tag{3.94}$$

where $4\pi P = (D - E)$ is the polarization field and the charge distribution is assumed to be zero outside of volume v so that the region of integration can be taken over v only.

Now, the dipole momentum is defined as:

$$m = \alpha E_0 = \iiint_v P dv \tag{3.95}$$

where α is the first order hyperpolarizibility.

So,

$$\Delta W = -\frac{1}{2}\alpha E_0^2 . \tag{3.96}$$

This defines the work to move a dipole in a uniform field. Now, the amount of work to move a randomly oriented dipole into a field, W_{chr}, is dependent on the orientation of the molecule to the field normal. This is defined by Equation (3.12). Now a differential change in orientation results in a differential change in work so:

$$dW_{chr} = -\mu E_D d(\overline{\cos\theta}) . \tag{3.97}$$

This can be rewritten using Equation (3.17) as:

$$dW_{chr} = -\frac{\mu^2}{3k_B T} E_D dE_D . \tag{3.98}$$

Integrating both side of Equation (3.98) yields

$$W_{chr} = -\frac{\mu^2}{6k_B T} E_D^2 , \tag{3.99}$$

and, combining Equation (3.96) (which is the work to move a dipole in a uniform field) and (3.99) (the work to move a randomly oriented chromophore in a field):

$$W = -\frac{1}{2}\left(\alpha + \frac{\mu^2}{3k_BT}\right)E_D^2 . \tag{3.100}$$

Substituting Equation (3.100) into (3.88) yields:

$$n = n_0 e^{\frac{1}{2}\left(\alpha + \frac{\mu^2}{3k_BT}\right)\frac{E^2}{k_BT}} . \tag{3.101}$$

Now, the change in density of the chromophore can be written as the change in n as:

$$\Delta d = M(n - n_0), \tag{3.102}$$

where M is the Molecular Weight of the chromophore.

Substituting Equation (3.101) in Equation (3.102) yields,

$$\Delta d_{chr} = \frac{E_D^2 M n_0}{2k_BT}\left(\alpha + \frac{\mu^2}{3k_BT}\right) = \frac{E_D^2 A_v d_0}{2RT}\left(\alpha + \frac{\mu^2}{3k_BT}\right) \tag{3.103}$$

where A_v is Avogadro's Number and R is the gas constant.

Thus, in an electric field the chromophore is translated proportional to the field strength increasing the density of the chromophore. As this density increases, three effects occur: increase in dielectric constant, compacting of guiding layer volume, and increased interference of chromophore alignment. As the density increases, the dielectric constant will also increase. However, the volume of the guiding region decreases as the chromophore is compacted. In addition, as the density increases, the chromophore eventually begin to interfere with each other's alignment and commensurate increase in V_π will occur.

The interference of the chromophore is related to their configurations in the unpoled state. Two primary configurations have been postulated to be predominant: H-

type and J-type. [51] These configurations are illustrated in Figure 3.5. Both type of configurations are a result of acceptor-donor attraction between two adjacent chromophore molecules. H-type configurations occur when the acceptor-donor of two chromophores are 180 out of alignment. This type of configuration would tend to not align if the poling field is limited to rotational orientations only. However, for electrostriction, the 2 chromophores will translate in opposite directions and can be separated during poling. J-type configurations occur when the acceptor-donors of two chromophore are aligned end-to-end. Poling will lead to rotation of one or both molecules and each molecule will translate in the same direction.

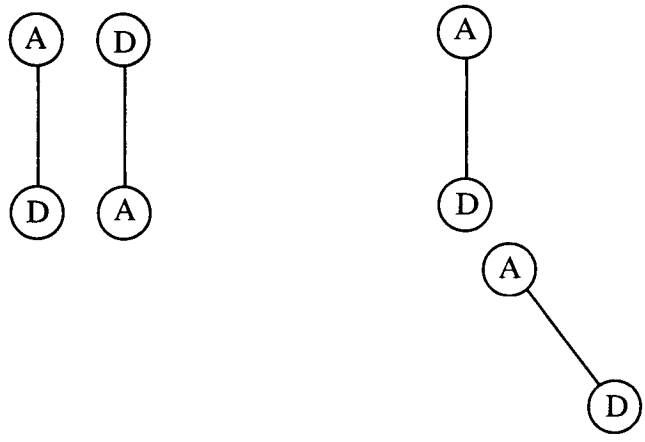

Figure 3.5 Chromophore Molecular Alignment Configurations

The increase in dielectric constant can be written as:

$$\left(\frac{\partial \varepsilon}{\partial d}\right)_T = \frac{4\pi A_v}{M}\left(\alpha + \frac{\mu^2}{3k_B T}\right) \tag{3.104}$$

and ,

$$\Delta d = \frac{E_D^2}{8T} C d_0^2 \left(\frac{\partial \varepsilon}{\partial d} \right)_T = \frac{E_D^2 A_v \pi}{2TM} C d_0^2 \left(\alpha + \frac{\mu^2}{3k_B T} \right), \tag{3.105}$$

where C is the compressibility of the chromophore molecules.

The volume of the waveguide is the product of the thickness, h_g, width, w, and modulator length, L. Assuming the electric field is normal to the waveguide thickness, then the compressibility is simply a change in the thickness. This relationship can be written as:

$$\Delta d = \frac{A_v}{MwL} \left(\frac{1}{h_{comp}} - \frac{1}{h_g} \right) = \frac{A_v \Delta h_g}{MwLh_g h_{comp}}, \tag{3.106}$$

or,

$$\Delta h_g = \frac{MwLh_g h_{comp}}{A_v \Delta d}. \tag{3.107}$$

Electrostriction is a direct result of the poling process. For polymers with high chromophore densities, the density increase induced by poling can cause chromophore misalignment on the molecular level, resulting in lower V_π performance. Electrostriction is generated not only by the poling field but also by the induced boundary charge density. This charge density is a direct result of the Maxwell-Wagner boundary of any stack with dissimilar material layers. The boundary charge density also plays a role in the aligning of the chromophore dipoles which is reflected by the coupling between the polarization charge density and the boundary charge density. The charge densities are limited by the poling voltage applied, the material dielectric constants, and material conductivities. The charge densities are both time and temperature dependent. Thus, the poling process is a function of poling voltage, temperature, and time. The significance of these parameters

and verification of these theoretical properties can be determined through experiments. The design of experiments and experimental equipment is defined in Chapter 4. This is followed by the results of experiments in Chapter 5 to explore the poling process and electrical transfer function properties that have been developed in Chapters 2 and 3.

CHAPTER 4

Experiment Design and Equipment

Experiments were defined to explore the range of poling time, temperature, and voltage effects. Because materials for these experiments are expensive and not available in large quantities, experiments were defined to minimize the number of wafers required to study the full parameter range. To understand the various factors that influence experimental measurements, a Design of Experiment (DOE) approach was used to analyze the fabrication, material, and treatment effects and ensure they are properly accounted in the experiments. The DOE analysis and approach is described in Section 4.1. The equipment used to conduct these poling experiments and the experimental measurements is described in Section 4.2.

4.1 Design of Experiment

A DOE approach provides for identification of statistically relevant measurements in the presence of fabrication and material variations. The DOE process involves identifying the variations to be statistically eliminated and the treatments to be statistically measured. A blocking scheme is defined to accommodate the statistical measurements. Finally, blocking methods available and the experiment design are described.

4.1.1 Device Fabrication

Modulators are fabricated on 4" wafers with 3 modulators and 9 straight channel waveguides on a die and 3 dies on a wafer. Each wafer has a specific material batch for

the core material. The batches can have chemical variations, but these are generally known. A separate batch is generally mixed for each wafer, although 2 wafers can sometimes be produced from one batch mixture. The %wt of chromophore is determined prior to mixing for guest/host materials. The mixture then distributes the chromophore within the host material. The cladding layers are Norland Optical Adhesive (NOA) 71. NOA is a commercial product and several wafers can be produced from the same bottle of material. Some uniformity variations have been noted between bottles in terms of pin hole defects. The modulators are fabricated by spin coating the layers. Adhesion promoter is used between the substrate and lower cladding and between the lower cladding and the core. No adhesion promoter is used between the core and upper cladding due to solvent compatibility. The waveguide structures are fabricated either by photobleaching or Reactive Ion Etching (RIE). Rib waveguides are produced by the RIE process and there are several additional steps to this fabrication method. These steps involve the use of NOA71 as a hard mask for the etching process.

4.1.2 Device and Wafer Variations

From a poling standpoint, only variations in dielectric constant (ε), resistivity (ρ), layer thickness (h), adhesion (A), and chromophore density (M_{CD}) effect the poling response as indicated by the measured V_{π}. These variations can be combined into 3 types of effects: Chemistry variations (C), mixture uniformity (M), and fabrication variance (F). Chemistry variations consist of dielectric constant (ε), resistivity (ρ), and adhesion (A) variations. Chemistry variations affect the bonding interfaces of the materials. Fabrication process can also affect adhesion, but assuming the same process steps are used for each wafer, adhesion effects can be attributed to chemistry variations.

Mixture uniformity is primarily the chromophore density. Fabrication variances affect the thickness of the layer. It is assumed that treatments of rib waveguide modulators are statistically compared separately from photobleached waveguides. Thus, the fabrication process variances do not play a role in the experimental analysis. In the special case where the results of rib and photobleached waveguides are made, then an additional fabrication process variation (F_P) will have to be statistically included in the model. Other effects such as pin holes in the layers affect optical loss properties, but not the poling properties. These pin holes can lead to shorting during poling, but this is a catastrophic effect which is detectable during the poling run. Assuming an additive model for these variation effects the main variations can be written as:

$$C = \Delta\varepsilon + \Delta\rho + A\,, \tag{4.1}$$

$$M = M_{CD}\,, \tag{4.2}$$

$$F = \Delta h + F_P\,, \tag{4.3}$$

and, in general,

$$\beta = C + M + F\,. \tag{4.4}$$

Now, there are three cases in which to consider these variations: between devices on a single die, between die on a single wafer, and between die on separate wafers. For die from the same wafer, variations in chemistry (C) are assumed to be distributed evenly through out the wafer and thus can be ignored. Variations in mixture (M) are present and can affect the poling results between devices. Variations in fabrication (F) can also be ignored. The layer thickness (h) can be accurately measured in the lab and assuming the spinning process yields reasonably uniform film thickness then the affects of Δh can be

ignored. Thc fabrication process is considered to be uniform across the wafer as well and so F can be ignored. Thus, between die from the same wafer,

$$\beta_d = M \tag{4.5}$$

Between wafers both chemistry (C)and mixture (M) variations can exist. Variations in thickness can be ignored as discussed above and the effects of F_P can be ignored when comparisons are made only between similarly processed wafers. So, F can be excluded as a variation between wafers. Thus,

$$\beta_w = C + M \tag{4.6}$$

Devices on the same die see the same treatments and have the same variations as for the die level. Thus, device level variations are not a measure of treatment, but of the mixture variations, M, across the die as defined by Equation (4.5). This measure, however, provides for the mixture variations across the die only. Therefore, statistically, die level comparisons provide the proper evaluation of treatment affects. The measurements of devices on a single die are averaged. This average is then compared between die to determine the statistical effects of the treatment applied to the die.

4.1.3 Treatments

Treatments can be applied singly to an individual device or in combinations to a single device. Treatments to be studied are poling time (t_p), poling temperature (T_p), poling voltage (V_p), heating temperature ramp (r_h), and cooling temperature ramp (r_c). For single treatments applied to devices from different wafers and assuming an additive model individual measurements can be written as:

$$y_{ti} = G + \beta_{wi} + \tau_t + e_{ti} \tag{4.7}$$

where G is the grand average of all measurements,

τ is the treatment effect, and

e is the residual error.

For combinations of treatments, the interaction effects cannot be measured separately. So, the model becomes

$$y_{ti} = G + \beta_{wi} + T_t + e_{ti} \tag{4.8}$$

where T is the combined treatment effect.

Essentially, the combined treatment is considered as a new single treatment. The interaction effect can be estimated by comparing T_t with the sum of the individual τ_t's and attributing the differences as the interaction term, I_t. Thus,

$$T_t = \Sigma\tau_t + I_t . \tag{4.9}$$

Note, that the quantitative value of I_t can be determined from experimental data and may be + or -. However, the actual functional form of I_t may not be determinable in this manner and is expected to be a complex function of the included treatment effects.

4.1.4 Blocking

The experiments may be blocked by wafer. Thus, the block size = 3. Again, the blocks are based on the number of die per wafer as discussed previously. If a single mixture is used to fabricate 2 wafers, then this may be extended to 6. If the number of treatment variations (e.g. number of different poling voltages) is 3, then a 3x3 Latin square design may be used. If other than 3 wafers (i.e. 2 or > 3) are used or more than 3 treatment variations are studied, then a balanced incomplete block design is used. Since the treatments may also be blocked by die, the incomplete block design reduces to a Youden Square design.

The treatments are randomly applied to the devices on each wafer for any of these designs to reduce the impact of the wafer variations. A baseline treatment is always applied to one die (randomly selected) on each wafer. Thus, each wafer has an identically treated die. This allows for a direct measure of variations between wafers enhancing the statistical detection of wafer variations effects (β_w).

4.1.5 Latin Square Design

For an experiment with 3 treatments over 3 wafers, a Latin Square design may be employed as illustrated in Table 4.1. The treatments are randomly applied to the dies on each wafer. The assignments in Table 1 were determined by using Matlab to generate a random order of 1, 2, 3 and inserting these in Table 4.1. Table 4.2 shows the analysis of variance table for the 3x3 Latin Square. [52]

Table 4.1: 3x3 Latin Square Design

	Die 1	Die 2	Die 3
Wafer 1	Treatment 2	Treatment 3	Treatment 1
Wafer 2	Treatment 1	Treatment 2	Treatment 3
Wafer 3	Treatment 2	Treatment 1	Treatment 3

Table 4.2: 3x3 Latin Squares Analysis of Variance Table

Source of Variation	Sum of Squares	Degrees of Freedom	Mean Square	Expected Value Mean Square	Ratio of Mean Squares
Grand Average (G)	S_G	ν_G	s_G^2	-	-
Wafers (β_w)	S_w	ν_w	s_w^2	$\overline{E_w}^2$	s_w^2 / s_R^2
Die (β_d)	S_d	ν_d	s_d^2	$\overline{E_d}^2$	s_d^2 / s_R^2
Treatments (τ_t)	S_t	ν_t	s_t^2	$\overline{E_t}^2$	s_t^2 / s_R^2

Residuals (R)	S_R	ν_R	s_R^2	$\overline{E_R}^2$	-
Total	S	ν			

Following [52] there are several quantities calculated in Table 4.2 to analyze the variances within the data to determine statistical significance for the differences in the treatment values. The Sum of Squares (S) is the sum of the square of averages or average deviations for each row category in the table. The grand average, G, is simply the average value of all observations, y_{ti}. Thus,

$$G = \bar{y} = \sum_i \sum_j \frac{y}{ij} \tag{4.10}$$

Thus, the sum of squares of G can be written as:

$$S_G = ij\bar{y}^2 \tag{4.11}$$

All other effects and treatments can then be determined from their variance from the grand average, G. So,

$$\beta_{wi} = \bar{y}_i - \bar{y}, \tag{4.12}$$

$$\beta_{dj} = \bar{y}_j - \bar{y}, \tag{4.13}$$

$$\tau_t = \bar{y}_t - \bar{y}, \quad \text{and} \tag{4.14}$$

$$R = e_{tij} = y_{tij} - \bar{y}_t - \bar{y}_i - \bar{y}_j + \bar{y}. \tag{4.15}$$

R is the residual error that occurs within treatments due mixture variations, rounding, and estimation errors not accounted in the other terms. The sum of squares for each of these terms is then,

$$S_w = i\sum_t \sum_j \beta_{w_{tj}}^2 \tag{4.16}$$

$$S_d = j\sum_t\sum_i \beta_{d_{ti}}{}^2 \tag{4.17}$$

$$S_t = t\sum_i\sum_j \tau_{t_{ij}}{}^2 \tag{4.18}$$

$$S_R = \sum_t\sum_i\sum_j R_{tij}{}^2 . \tag{4.19}$$

Thus the total sum of squares, S, may be written as:

$$S = S_G + S_w + S_d + S_t + S_R . \tag{4.20}$$

The degrees of freedom, ν, for each measure are used to determine the variance as they define the number of ways in which a particular quantity may vary. In general, ν is defined as:

$$\nu = (n-1). \tag{4.21}$$

Therefore,

$$\nu_w = (i - 1), \tag{4.22}$$

$$\nu_d = (j - 1), \quad \text{and} \tag{4.23}$$

$$\nu_t = (t - 1). \tag{4.24}$$

The residual degrees of freedom, ν_R, for a k x k Latin Square design are:

$$\nu_R = (k-1)(k-2). \tag{4.25}$$

For the Grand Average, only 1 value is free to vary, as the average is determined from all of the data measurements. Hence,

$$\nu_G = 1. \tag{4.26}$$

So,

$$\nu = \nu_G + \nu_w + \nu_d + \nu_t + \nu_R. \tag{4.27}$$

The mean square, is simply the sum of squares divided by the total degrees of freedom. So,

$$s_G^2 = S_G/\nu_G, \tag{4.28}$$

$$s_w^2 = S_w/\nu_w, \tag{4.29}$$

$$s_d^2 = S_d/\nu_d, \tag{4.30}$$

$$s_t^2 = S_t/\nu_t, \quad \text{and,} \tag{4.31}$$

$$s_R^2 = S_R/\nu_R\,. \tag{4.32}$$

The expected value of the mean square is the variance. As such there is not variance for the Grand Average as all values are identical. For the residuals, the variance can be used directly. For the consideration of variance for the wafer, die, and treatment effects the overall variance is inflated by the averaging of the values over the partial data set. Thus the variance is corrected by the average of the square of these effects. So,

$$\overline{E_w}^2 = \sigma^2 + i\sum_{n=1}^{i}\frac{\beta_{wn}^{\,2}}{(i-1)}, \tag{4.33}$$

$$\overline{E_d}^2 = \sigma^2 + j\sum_{n=1}^{j}\frac{\beta_{dn}^{\,2}}{(j-1)}, \tag{4.34}$$

$$\overline{E_t}^2 = \sigma^2 + t\sum_{n=1}^{t}\frac{\tau_n^{\,2}}{(t-1)}, \text{ and} \tag{4.35}$$

$$\overline{E_R}^2 = \sigma^2, \tag{4.36}$$

Finally, the ratio of mean squares shown in Table 4.2 is the comparison of the wafer, die, and treatment mean squares with the residual mean square. This comparison indicates any non-additive relationships. Should the data show these types of relationships, additional data conditioning can be applied to adjust the additive model

with correction factors. These correction factors then serve of as an indication of the functional relationship between these variables.

4.1.6 Youden Square Design

The Youden Square is a form of the Balanced Incomplete Block Design. Equations for the Youden Square can be found following [52]. For a Balanced Incomplete Block Design, the number of treatments is greater than the block size. Since the block size is always k = 3, treatments, t, greater than 3 (t > 3) require the following number of blocks, b, replicates of treatments, r, and yields the total number observations, N, as:

$$b = t(t-1)(t-2)/6 \tag{4.37}$$

$$r = (t-1)(t-2)/2 \tag{4.38}$$

$$N = bk = rt = t(t-1)(t-2)/2 \tag{4.39}$$

$$\lambda = r(k-1)/(t-1) \tag{4.40}$$

The quantity, λ, [53] defines the number of times a pair of treatments appears together in the same block. These relationships will always yield Balanced Incomplete Block Designs, but sometimes reduced numbers of blocks and replicates can be used. N represents the total number of die required for a statistical analysis. The treatments are randomly distributed across the 3 die on each wafer. r is the number of times each treatment is replicated. [52] lists the reduced combinations and gives the combinations of blocks to meet the replicate requirements (which can be complicated). The combinations for k = 3 are listed in Table 4.3 [52].

Table 4.3: Balanced Incomplete Block Designs for k = 3

t	b	r	N	Combinations
4	4	3	12	Combinatoric: all t!/(k!k!) combinations
5	10	6	30	Combinatoric: all t!/(k!k!) combinations
6	10	5	30	(1,2,5);(1,2,6);(1,3,4);(1,3,6);(1,4,5) (2,3,4);(2,3,5);(2,4,6);(3,5,6);(4,5,6)
7	7	3	21	(1,2,5);(3,4,5);(1,3,6);(2,4,6);((1,4,7);(2,3,7);(5,6,7)

The formulae for the 3x3 Latin Square must be adjusted for the Youden Square Design as defined by [52]. The first adjustment is to find the sum of treatment effects for each treatment, T_u, for each wafer, T_m, and each die position, T_n, as:

$$T_u = \sum_{i=1}^{r} \tau_i \,, \quad \text{where u} = 1,\ldots, \text{t} \tag{4.41}$$

$$T_m = \sum_{i=1}^{k} \tau_{mi} \,, \quad \text{where m} = 1,\ldots,\text{b} \qquad \text{(wafer)} \tag{4.42}$$

$$T_n = \sum_{i=1}^{b} \tau_{ni} \,, \quad \text{where n} = 1,\ldots,\text{k} \qquad \text{(die)} \tag{4.43}$$

Now, since all treatments are not contained in all blocks, a total is required of all blocks containing treatment, u. So,

$$B_u = \sum_{s} \text{v}_\text{s} \,, \tag{4.44}$$

where s is the total number of values in all blocks containing treatment u. This may then be used to adjust the treatment totals as:

$$Q_u = kT_u - B_u \tag{4.45}$$

This value is then used to adjust the treatment effects for the incomplete distribution across the blocks as:

$$\hat{\tau}_u = \frac{Q_u}{t\lambda}, \tag{4.46}$$

where,

$$\sum_{u=1}^{t} \hat{\tau}_u = 0, \tag{4.47}$$

The sample average can then be adjusted by this factor:

$$\bar{y}_{u(adjusted)} = \bar{y} + \hat{\tau}_u . \tag{4.48}$$

This then leads to an adjusted variance for the treatment average:

$$V(\bar{y}_{u(adjusted)}) = s^2_{adjusted} = \frac{k\sigma^2}{t\lambda}. \tag{4.49}$$

$s_{adjusted}^2$ is used to determine the proper t or F distribution for a given data set.

The grand average is defined the same as for the Latin Square in Equation (4.11). The corresponding sum of squares for the wafers, dies, and treatments then can be written as:

$$S_w = \left(\sum_{m=1}^{b} \frac{T_m^2}{b} \right) - S_G, \tag{4.50}$$

$$S_d = \left(\sum_{n=1}^{k} \frac{T_j^2}{k} \right) - S_G, \tag{4.51}$$

$$S_t = \left(\sum_{u} \frac{Q_u^2}{\lambda kt} \right), \tag{4.52}$$

The residual sum of squares can then be written as:

$$S_R = \left(\sum_{m} \sum_{n} y_{mn}^2 \right) - S_G - S_w - S_d - S_t . \tag{4.53}$$

The degrees of freedom for the grand average, ν_G, wafers, ν_w, die, ν_d, and treatments, ν_t, are the same as the Latin Square design and are defined by Equations (4.22) to (4.24), and (4.26). The degrees of freedom for the residuals are updated by the adjusted values and can be written as:

$$\nu_R = bk - \nu_G - \nu_w - \nu_d - \nu_t = bk - t - b + 1 . \quad (4.54)$$

The mean square are then calculated as defined by Equations (4.28) to (4.32) with the updated values for ν and S as defined in Equations (4.50) to (4.54). Table 4.4 shows the Youden Squares Analysis of Variance Table [52].

Table 4.4: Youden Square Analysis of Variance Table

Source of Variation	Sum of Squares	Degrees of Freedom	Mean Square	Ratio of Mean Squares
Grand Average (G)	S_G	ν_G	s_G^2	-
Wafers (β_w)	S_w	ν_w	s_w^2	s_w^2 / s_R^2
Die (β_d)	S_d	ν_d	s_d^2	s_d^2 / s_R^2
Treatments (τ_t)	S_t	ν_t	s_t^2	s_t^2 / s_R^2
Residuals (R)	S_R	ν_R	s_R^2	-
Total	S	ν		

4.1.7 Experiment Design

Considering the number of blocks (i.e. wafers) indicated as necessary in Table 4.3, treatments variations should be either 3, 4, or 7. Three or 4 treatments are desirable to limit the number of wafers to < 5. This can be accomplished through an exploratory experimental approach. The domain of interest can be explored to determine where significant changes are likely to occur in the treatment variables (e.g. maximums,

minimums, no changes). These measurements can provide verification of the theoretical developments of this dissertation. In the case were small changes are measured, a 3x3 Latin Square can be employed to statistically examine the experimental results.

Variations for the treatments being studied, t_p, T_p, and V_p, can be defined as shown in Table 4.5. 3 variations of each treatment have been identified. The studies will be carried out on photobleached waveguide modulators. The separate treatment results will then be analyzed to verify theoretical predictions.

Table 4.5: Treatment Variations for 3x3 Latin Square Study

	Treatment 1	Treatment 2	Treatment 3
Poling Time (t_p)	10 minutes	30 minutes	50 minutes
Poling Temperature (T_p)	145 C	150 C	155 C
Poling Voltage (V_p)	500 V	750 V	1000 V

Poling times (t_p) were selected as 2, 10, 20, 30, 50, and 60 minutes. Poling temperature (t_p) is limited by the chromophore temperature sensitivity to a maximum of 160 C. As the temperature increases, then the activation energies increase so that reducing temperatures limits the dipole response. Therefore, the temperature range of study is 145 – 155 C. The poling voltage (V_p) has a linear relationship with the charge densities induced and the infinite time response of the system increases with increasing poling voltage. The maximum poling voltage is limited by dipole availability and dielectric breakdown. Therefore 1000 V is the maximum voltage which may be studied. Dwell time has a large effect on poling efficiency. This is primarily captured by poling time. Thus, there is little to indicate that the heating (r_h) or cooling (r_c) ramps will significantly effect poling and these factors are not directly studied.

These tests will provide a significant evaluation of the poling parameters of interest in modulator V_π performance. The tests will provide an indication of how the individually controllable parameters affect the performance. This provides a strong scientific basis for establishing efficient poling methods.

4.2 Poling and Measurement Equipment

Various poling and measurement equipment were configured to support this dissertation research. The poling station is described in Section 4.2.1. Optical loss measurement equipment is described in Section 4.2.2. V_π measurement equipment is described in Section 4.2.3.

4.2.1 Poling Station

The Electrode poling station consists of a heating source to heat the sample to the poling temperature (near the T_g), a high voltage DC power supply to generate the poling field, and current monitoring circuitry to ensure breakdown of the material is not occurring. A FairweatherTPSR5CC-V3XW hot plate with programmable controller is used as the heating source. The controller is remote controllable via a General Purpose Interface Base (GPIB) port. The hot plate provides a vacuum chuck surface and supports water circulation for cooling. The temperature range supported is room temperature (20 – 25 C) to 250 C and a K-type thermal couple is located on the bottom surface of the hot plate for active temperature monitoring.

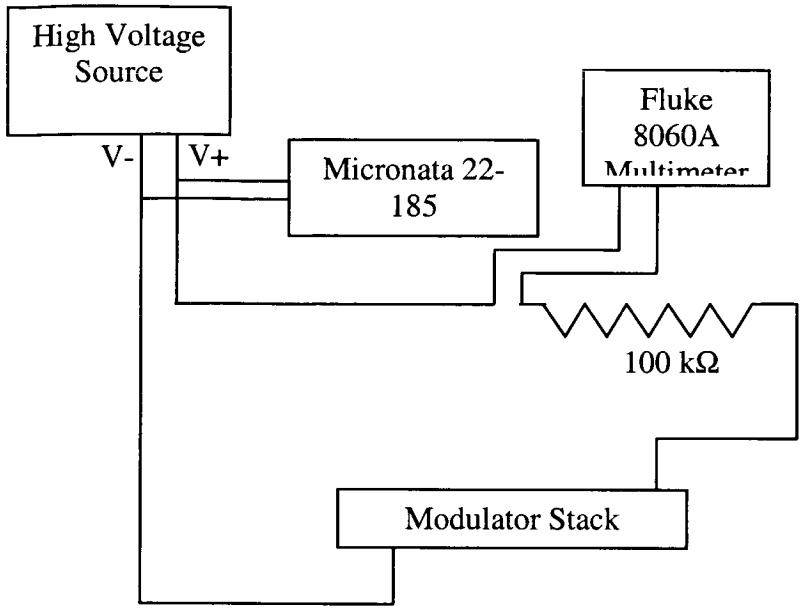

Figure 4.1: Poling Station Electrical Connections

Figure 4.1 illustrates the electrical connections for the poling station. A HP 6516A DC Power Supply provides the DC voltage. The source is capable of + 10 kV, but is not programmable nor remote controllable. Whisker probes (Signatone 5-725-SRM probe stations with Signatone SE-TD probe tips) connected via coaxial cable adapters are used to contact the pads on the modulator chips during poling. The ground is applied to the bottom surface of the Si chip via a gold contact pad. Gold contact pads are also supplied on the top surface of the chip with all channels connected together to support poling. A Fluke 8060A digital multimeter is connected through the circuitry as shown in Figure 4.1 to monitor current. A Micronata 22-185A multimeter is used to monitor the poling voltage applied across the modulator stack. Once poling is completed, the electrodes over the modulators are separated from the shorting lines using wet etch lithography.

Data is taken manually with the current poling instrumentation. Data points are taken every 5 – 10 degrees C by recording the current (I_p) and temperature (T). Manual

control of the high voltage source and manual changing of the temperature set-points are also performed. Thermally Stimulated Polarization (TSP) currents are measured using the current meter as discussed above for the poling station. Current values are read every 5 – 10 C.

4.2.2 Optical Loss Measurement

Optical losses are measured by inserting the modulator into the configuration illustrated in Figure 4.2. Two laser diode sources are used for optical loss measurements: 1.3 μm and 1.55 μm. The 1.3 μm source is fixed on the optical axis, and the 1.55 μm source is manually moved in and out of the beam line as needed. Modulator die are placed between the input and output focusing objectives and held firmly via a vacuum chuck on a 3 Degree of Freedom (DOF) optical stage. Similarly, planar waveguide films may be measured by placing the film between the objectives, using microscope slides as a support base instead of the vacuum chuck. The vacuum chuck requires die to be wider than 2 cm in order for the edges to be focused correctly by the objectives. Typical planar die are $\leq$ 1.3 cm and so microscope slides are used instead. The measurement techniques for channel and planar waveguides are different as discussed in the following sections.

4.2.2.1 Channel Waveguide Losses

Channel waveguide optical losses are determined by measuring the reference optical throughput without the die in place. A modulator is then put in place and the power output through a waveguide channel is measured. The optical loss is then calculated as:

$$L = [10\log(P_{meas}/P_{ref}) - L_{coupling}]/\text{length dB/cm} \quad (4.55)$$

where, P_{meas} = measured output power,

P_{ref} = referenced power,

Length = waveguide channel length, $L_{coupling}$ = input coupling losses.

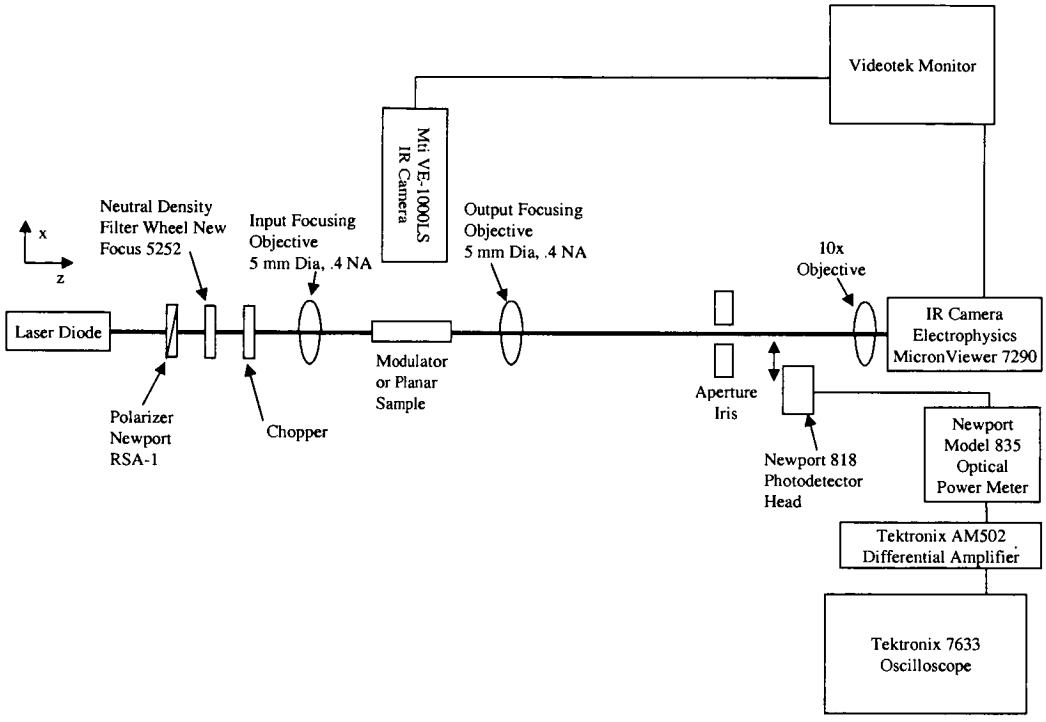

Figure 4.2: Optical Loss Measurement Configuration

Using this technique, losses from the various system components are already present in the reference power measurement. Therefore, only the losses due to coupling and propagation through the die are represented in the power ratio (the other losses are divided out). The coupling loss was previously determined to be -3 dB for waveguides of the geometry discussed in Section 5.1 using the cutback method [54] where,

$$L_{coupling} = |10\log(P_1/P_2)[length_1 - length_2]| \text{ dB/cm} \quad (4.56)$$

where, P_1 = measured output power at length 1,

P_2 = measured output power at length 2,

$length_1$, $length_2$ are the lengths of the die for each measurement.

The reference power for the 1.3 μm source is 390 ± 3 μW. The reference power for the 1.55 μm source is measured each time, since this source is move in and out of the system when needed. The reference power varies from 1.35 mW to 1.55 mW.

4.2.2.2 Planar Waveguide Losses

Initial evaluations of new material stacks are often done with planar waveguide stacks. Planar waveguide losses are measured in a fashion similar to channel waveguide, but the data must be interpreted slightly differently. Channel waveguides confine the propagation light in both the x and y directions. Planar waveguides, however, confine the propagating light in only the x direction. The light beam then spreads as a gaussian beam in the y direction. The gaussian beam from the laser diode is incident on the input focusing objective (f = 6.25 mm) with a beam waist, ω_0 = 2 mm. Then the beam waist focused on the planar waveguide face is:

$$\omega_1 = \frac{f\lambda}{\pi\omega_0} \tag{4.57}$$

Using q-parameter calculations and a slab transmission matrix,

$$T = \begin{bmatrix} 1 & \frac{n_g d}{n_c} \\ 0 & 1 \end{bmatrix} \tag{4.58}$$

then, the output beam waist can be calculated as:

$$\omega_2 = \sqrt{\frac{\pi}{\lambda}\left(\frac{n_g^2 d^2}{n_c^2 z_0} + z_0\right)} \tag{4.59}$$

Now, the output power from the planar waveguide can be calculated as:

$$P = \frac{1}{2}\int_0^T\int_{-S}^{S}\frac{EE^*}{\eta}dxdy \tag{4.60}$$

where,

$$E_0 = \sqrt{\frac{4P_0\eta}{\pi\omega_1^2}}, \tag{4.61}$$

$$\eta = \sqrt{\frac{\mu_0}{\varepsilon_0 n}}, \text{ and} \tag{4.62}$$

$$E = E_0 \frac{\omega_1}{\omega_2} e^{-\frac{x^2+y^2}{\omega_2^2}}. \tag{4.63}$$

Now, for a planar waveguide, all light is contained in the x direction. Therefore, $T = \infty$, and the integral reduces to:

$$P_{output} = \frac{\sqrt{\pi}E_0^2\omega_1^2}{2\eta}\int_0^S e^{-\frac{y^2}{\omega_2^2}}dy \tag{4.64}$$

The integral can be evaluated using the error function (erf) over a finite interval that is defined as:

$$\int_0^b e^{-ay^2}dy = \tfrac{1}{2}\sqrt{\tfrac{\pi}{a}}\,\mathrm{erf}\left(b\sqrt{a}\right), \text{ for } a > 0. \tag{4.65}$$

So, the output power is then,

$$P_{output} = \frac{\pi E_0^2\omega_1^2}{4\eta}\mathrm{erf}\left(\frac{\sqrt{2}S}{\omega_2}\right) = P_0\mathrm{erf}\left(\frac{\sqrt{2}S}{\omega_2}\right), \tag{4.66}$$

where,

$$P_0 = \frac{\pi E_0^2\omega_1^2}{4\eta}. \tag{4.67}$$

P_0 can be experimentally found as discussed in Section 4.2.2.1 above. This experimental value includes fresnel losses from the output focusing objective and camera lens that can be accounted for using the fresnel equations. The value of S depends on the

viewable distance that is controlled by the output aperture stop and camera lens magnification. Experimentally, 10 μm viewed is magnified to 24 mm on the monitor. Thus, the viewed area, V, can be measured on the monitor screen and correlated to the viewing size as:

$$S = \frac{1}{2}\frac{10x10^{-6}}{24x10^{-3}}V . \tag{4.68}$$

Thus, Equations (4.68), (4.66), and (4.59) can be used to determine the actual power output by the planar waveguide. This must be correlated then to the optical propagation loss in dB/cm. Optical losses can be calculated by comparing the measured output power with the output power calculated using Equation (4.66) as:

$$\text{Loss} = [10\log(P_{meas}/P_{output}) - 3\ \text{dB}]/d. \tag{4.69}$$

where, 3 dB is assumed to be the coupling input loss based measurement previously done with channel waveguides as discussed in Section 4.2.2.1 and d is the length of the planar waveguide sample.

4.2.3 V_π Measurement

V_π is measured using the optical loss bench illustrated in Figure 4.2. Prior to measuring the modulation, the electrodes for each modulator arm are separated from the poling electrodes so that each arm may be driven separately. Once the modulator is placed on the bench, a modulator waveguide channel is aligned on the optical axis and an optical loss measurement is made. Following this measurement, whisker tip probes (Signatone 5-725-SRM probe stations with Signatone SE-TD probe tips) are used to connect the modulator to a periodic high voltage signal as illustrated in Figure 4.3. A saw tooth waveform is applied to the modulator varying from 0 V to – 330 V with a period of about 30 seconds. The saw tooth waveform is generated via a Tektronics FG502 function

generator. 2 Volt Ohm Meters (VOM), Micronata 22-185 Multimeters, provide monitoring of the voltage applied across the modulator. The outputs of the high voltage source (through a 1% voltage division resistor bridge) and the optical power meter (through a differential amplifier) are connected to the oscilloscope. Operating in dual trace mode, the oscilloscope sweeps through all most 2 full periods of the modulation voltage, allowing the output optical modulation to be detected. A Polaroid picture is made of the oscilloscope screen to capture the traces over one full sweep. The picture clearly shows the optical modulation. Using the picture the V_π can be calculated as:

$$V_\pi = \frac{\text{voltage drop}}{\#\,\text{modulation half periods}} \tag{4.70}$$

The modulation depth can also be calculated by determining the maximum and minimum optical power detected in the modulation waveform. This is typically done manually by varying the voltage and noting the maximum and minimum power readings on the optical power meter. A background optical power measurement may also be taken by blocking the laser beam input to the optical power meter detector and reading the detected optical power level. The modulation depth can then be calculated as:

$$M_D = 10\log\left(\frac{P_{min} - P_{bg}}{P_{max}}\right)\ \text{dB}. \tag{4.71}$$

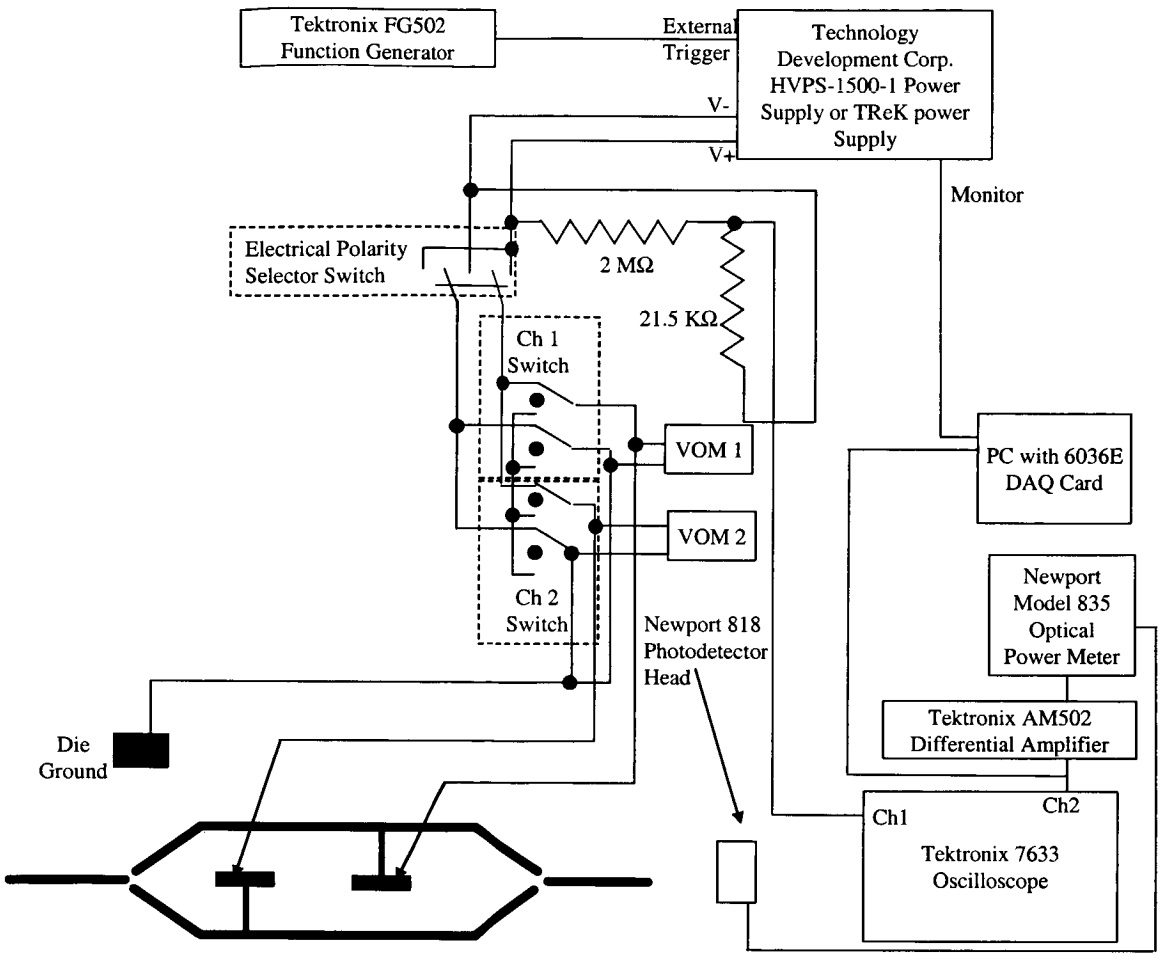

Figure 4.3: Modulator Electrical Circuits

A National Instrument PCI-6036E digital/analog card was inserted into this configuration to record waveforms. A Labview program was updated to provide recording and display of the modulation waveform. The PC executing the Labview program and DAQ card, was operated in parallel to the Tektronix oscilloscope. This system worked well to store the data, but had noise problems associated with ground loops through that generated noise on the modulation voltage data. This limited the use of the modulation data to long period measurements where the noise (±5 V) was not a significant level. A TREK high voltage power supply was added in place of the HVPS power supply for the square wave forms used to study transient responses. The HVPS

set-up, however, was used for the modulation voltage studies as the clipped saw tooth could not be generated with the TREK system.

This experimental equipment and techniques defined in this chapter were used in the experimental studies conducted to verify the theoretical developments of this dissertation. Chapter 5 presents the results of these studies.

CHAPTER 5

Experimental Results

Mach Zehnder modulators were used to measure V_π and therefore the poling effects on CLD material systems. CLDZ/APEC and CLDX/APC material systems and device fabrication used for this research are discussed in Section 5.1. Experiments investigating poling time are discussed in Section 5.2. Experiments investigating poling temperature are discussed in Section 5.3. Experiments investigating poling voltage are discussed in Section 5.4. Finally, experiments investigating the electrical transfer function are discussed in Section 5.5.

5.1 Experimental Device Fabrication

Guest/host systems involve the mixing of a guest chromophore in a host polymer matrix. As the %wt. of the guest increases, the spacing between host chains increases and the material T_g decreases below that of the host material with no guest molecules. Thus, guest/host systems tend to have lower T_g and therefore thermal stability temperatures are lower.

CLD is the most promising chromophore currently being investigated. CLD1, most recently referred to as CPW1 in some articles, has generated the best results to date. CLD1 has a melting temperature of 252 C, but the molecules begin to disassociate at much lower temperatures. A $\mu\beta$ product of 14,065 x 10^{-48} esu was measured at 1.907 μm. [9] CLDZ is a version of CLD that has been optimized for better solubility than

CLD1 making the films easier to reliably fabricate. For CLDZ the chromophore is thermally stable to 160 °C.

Amorphous polycarbonate (APC) has been shown to be one of the best host materials evaluated to date. APC has a high T_g of 205 °C. CLDZ/APC is mixed at 25 %wt. to 35 %wt as indicated for each wafer below. The mixed ratio reduces the guest/host system. The material is amorphous so the T_g has not been directly measurable. The T_g has been estimated to be approximately 145 °C.

The cladding material is the commercially available Norland Optical Adhesive (NOA) 71. The NOA71 is a low resistance cladding material with good adhesion properties to the core materials and no birefringence. Table 5.1 gives the typical index of refraction value for the core and cladding materials. Note, these are typical values; actual values vary from batch to batch of material.

Table 5.1: Optical Properties of Modulator Materials

Material	$n_{TE}, \lambda = 1.3\mu m$	$n_{TM}, \lambda = 1.3\mu m$	$n_{TE}, \lambda = 1.55\mu m$	$n_{TM}, \lambda = 1.55\mu m$
CLDZ/APC	1.650	1.648	1.639	1.636
NOA71	1.548	1.547	1.547	1.546

Two primary waveguide fabrication methods were used for modulators: rib waveguide and photobleached waveguides. The waveguide geometries for each of these methods are illustrated in Figures 5.1 and 5.2. This design produces a single mode at 1.55 μm and double modes at 1.3 μm. The optical mode profile for this case is illustrated in Figures 2.3 and 2.6. For these devices, the upper and lower claddings are both NOA 71 and the core is CLDZ/APC. The electrode length, L, for all of these devices was 1.36 cm.

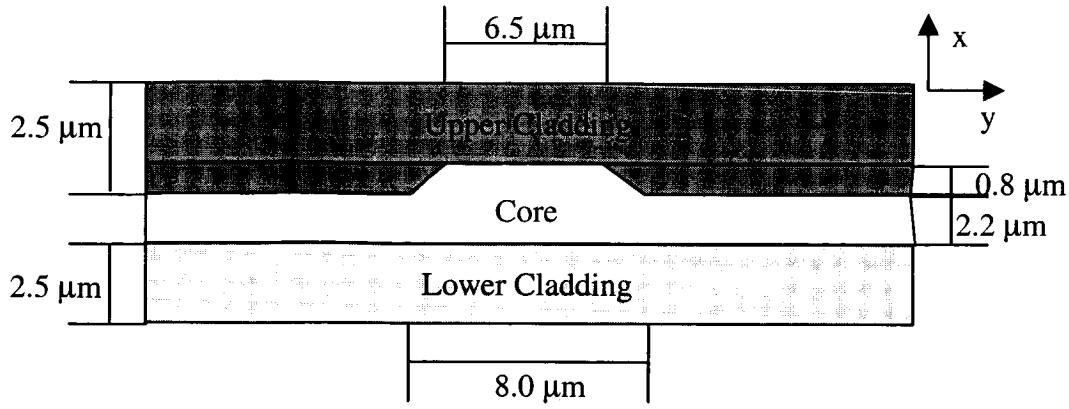

Figure 5.1: Rib Waveguide Geometry

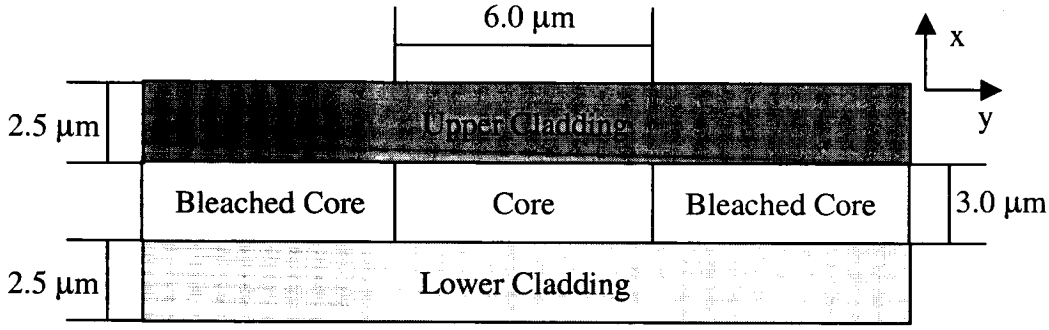

Figure 5.2: Photobleached Waveguide Geometry

To determine the factors and ranges of interests experiments were performed to evaluate the performance of various modulators. The modulator construction is defined below. All modulator die were measured at 1.55 μm. To provide a basis for comparison between modulators a baseline poling process was defined. The process steps were:

1) GN_2 purge for 15 mintues
2) Ramp temperature to 120 °C in GN_2
3) Dwell 30 minutes in GN_2 to release trapped oxygen
4) Apply 500 V (poling voltage)
5) Ramp temperature to 145 °C (poling temperature) in GN_2
6) Dwell at poling temperature for 2 minutes (poling time) in GN_2

7) Ramp temperature to 30 °C using cooling water in GN_2

8) Voltage off, stop GN_2 purge

Poling efficiency can be defined as the percent of chromophore aligned. This is determined by the measurement of r_{33} which is an indication of the number of dipole aligned. If all dipoles are aligned, then looking at Equation (3.17), $\langle\cos\theta\rangle = 1$ so,

$$\overline{\cos\theta} = \frac{\mu \cdot E_P}{5k_B T_P} = 1 \tag{5.1}$$

where, μ is the permanent molecular dipole moment of the chromophore,

$V_{core} = E_{core}/h_g$ is the core layer voltage defined by Equation (2.65), and

k_B is the Boltzman constant (1.381×10^{-23}).

Using this value in Equation (3.19) yields,

$$\chi_{33}^{(2)} = \frac{5}{3} N_{chr} \beta_{33} \tag{5.2}$$

Using this relationship in Equation (3.22), the maximum value of r_{33} can be written in terms of the number density of chromophore molecules (N_{chr}) present in the core as:

$$r_{33_{max}} = -\frac{10}{3} N_{chr} \beta_{33} n_{ge}^{-2} n_{go}^{-2} \tag{5.3}$$

where,

β_{33} is the 2nd order polarizability of the chromophore,

n_{ge} and n_{go} are the extraordinary and ordinary indices of refraction,

N_{chr} in a guest/host solution can be found from the density and molecular weight of the chromophore/host mixture. This is written as [55]:

$$N_{chr} = \frac{A_v \%wt_{chr}}{M_{chr}\left(\frac{\%wt_{chr}}{D_{chr}} + \frac{\%wt_h}{D_h}\right)} \tag{5.4}$$

where, Av is Avogadro's Number (6.023×10^{23}),

$\%wt_{chr}$ is the percent weight of chromophore in the guest/host mixture,

$\%wt_h = 1 - \%wt_{chr}$ is the percent weight of host in the guest/host mixture,

M_{chr} is the molecular weight of the chromophore (mol/g),

D_{chr} is the density of the chromophore molecule (g/cm^3), and

D_h is the density of the host molecule (g/cm^3).

The $\mu\beta_{33}$ product is an indication of the total polarizability of the chromophore dipoles. For CLD1, this value is given as $\mu\beta_{33} = 14065 \times 10^{-48}$ esu (electrostatic units). Electrostatic units can be converted to MKS (Meter Kelvin Seconds) units by first noting that the esu of μ are statvolt·cm^2 and the units of β_{33} are cm^4/statvolt. These quantities can be converted to MKS units through the relationhips: 1 statvolt·cm^2 = 1 statCoulomb·cm = 3.3356×10^{-12} C·m and 1 cm^4/statvolt = 4.1888×10^{-10} m^4/V. [56] So, 1 esu = 13.972×10^{-22} C·m^5/V and for CLD1 converting m^5 to cm^5, $\mu\beta_{33} = 196.52 \times 10^{-57}$ C·cm^5/V.

Separate values of μ, β_{33}, and α (first order hyperpolarizability) have not been published for CLD chromophores. The value of μ, however, has been estimated to be 15 – 20 Debye (D). [57] Debye units can be converted to MKS units as: 1 D = 10^{-18} esu = 10^{-18} statvolt·cm^2 = 10^{-18} statCoulomb·cm = 3.3356×10^{-30} C·m. Thus, $\mu = 50 \times 10^{-30}$ C·m to 66.712×10^{-30} C·m. Using the published values for $\mu\beta_{33}$ yields an estimated value for $\beta_{33} = 5.89 \times 10^{-26}$ cm^4/V to 2.95×10^{-27} cm^4/V.

Since values of α are not available, experimental calculations of electrostriction cannot be made using Equations (3.103) to (3.107). Thus, while optical loss effects can be seen in the data as the charge densities increase, quantitative calculations of the electrostriction induced density increase and waveguide thickness compression cannot be made.

As seen in Equation (3.75) activation energy, E_A, and the dipole relaxation frequency, α_r, are important parameters to determine charge and current densities. As the energy required to free a molecule from local molecular constraints, E_A defines the glass transition temperature for a material. This relationship is defined [turnhout] as:

$$T_g = \frac{E_A(1.6\times10^{-19})}{k_B A} \tag{5.5}$$

where,

A is an experimentally defined parameter and T_g is in °K.

For these materials, a single E_A is assumed based on the good model fits to the experimental data. This value has been set based on the T_g of the CLD/APC guest/host system. This value is not specifically measurable, but has been estimated to be between 135 °C and 150 °C. Values of A = 56 and E_A = 2.0 eV, corresponds to a T_g = 140.78 °C. The values of A and E_A were selected by matching experimental data with calculated data. These values gave the best match. The value of A is also close to the value of 50 used by Turnhout [13] for amorphous polymer hosts in his original work. These values for A and E_A have been used for all theoretical plots.

The relaxation frequency must also be known. Relaxation frequencies have not been measured for CLD/APC or CLD/APEC. Therefore, the value is set by matching the

modeled curves to the experimental data. Table 5.2 summarizes the material data parameters for CLD/APC.

Table 5.2: CLD1 Material Parameters

Parameter	Value
M_{chr}	765.1 mol/g
D_{chr}	1.01 g/cm^3
D_h	1.15 g/cm^3
$\mu\beta_{33}$	196.52 x 10^{-57} C·cm^5/V
μ (estimate)	50 x 10^{-30} C·m to 66.712 x 10^{-30} C·m
β_{33} (estimate)	5.89 x 10^{-26} cm^4/V to 2.95 x 10^{-27} cm^4/V
A	56
E_A	2.0 eV
Tg	140.78 °C

Poling efficiency can then be written as:

$$\eta_P = \frac{r_{33}}{r_{33_{max}}} \tag{5.6}$$

Using typical values for CLDX/APC photobleached waveguides (h_g = 3.50 μm, n_{ge} = 1.636, n_{go} = 1.639) with an estimated β_{33} value of 1 x 10^{-27} produces r_{33max} = 1.67 x 10^5 pm/V. This is 3.5 orders of magnitude larger than the experimental values reported in Section 5.5. This indicates that the average orientation angle is typically 89.98 degrees off of normal. Thus, the orientation of the chromophore molecules is low due to the orientation induced during spin coating, indicating that the polymer host backbones provide significant interference in alignment of the molecules during poling and that additional factors related to molecule spacing must be included in a calculation of the maximum value of r_{33}. Because of the large differences between measured values and this theoretical maximum, Equation (5.6) is not a very sensitive measure of poling

efficiency. Due to this poor sensitivity, the uncertainty in the value of β_{33}, and the missing host interference factor Equation (5.6) will not be applied in the data analysis.

In evaluating the modulator results, V_π can be calculated using either the applied voltage, $V_{applied}$, or the core voltage, V_{core}. $V_{applied}$ is simply the total voltage applied to the wafer stack. Dividing this value by the number of modulation periods gives the wafer V_π. V_{core} is calculated from $V_{applied}$ using Equation (2.65). Dividing this value by the number of modulation periods gives the actual change in core voltage per modulation period producing the core V_π. Wafer V_π is the practical value of the modulation voltage required to drive the total stack. Core V_π, however, must be used to calculate the actual r_{33} coefficient obtained during poling.

5.2 Poling Time

Poling time was investigated using 14 die from 5 different wafers. The fabrication data for these wafers is given Table 5.3. A slightly modified version of CLDZ was used, CLDX, which sought to improve adhesion again. Wafer #775 was fabricated using the low ρ (p-doped silicon wafer for low resistivity) substrate pattern, but the substrate in this case was a standard silicon wafer. This raised the lower contact resistance to ground from 0.1 Ω to approximately 200 KΩ. This has a large effect on the frequency response of the die from this wafer, but is a small change in impedance of the wafer stack as can be seen from the electrical transfer function discussion in Section 2.4. Therefore poling performance is not measurably affected by this configuration. The other 3 wafers have the same electrode pattern, but are on low ρ substrates. Wafers 761 and 775 were fabricated with a $\%wt_{chr} = 34.64\%$. However, mixing problems resulted in a reduced chromophore loading By comparing index of refraction data the $\%wt_{chr}$ was

determined to actually be 29.0%. All of these wafers were poled following the standard poling process with V_p = 500 V and T_p = 145 °C. Table 5.4 provides the results of the testing and Figure 5.1 charts the change in measured V_π with poling time. Comparing the data between the wafers with 29.0% loading and 34.65% loading shows a 0.2 V average difference in the baseline V_π values at t_p = 2 minutes. The data in the Table also indicates that 30 minutes is the optimal poling time for this system.

Beyond 30 minutes, the optical losses begin to worsen. This is due to the increasing build up of the boundary charge which leads to an increase in the molecular directing field as seen by Equation (3.85). As this charge continues to build with poling time, the electrical force across the core increases leading to electrostriction described by Equation (3.103). Electrostriction is a compression of the chromophore by the poling field which leads to a compaction of the chromophore in the direction of the poling field as the directing field increases. Thus, the optical waveguide will eventually cut-off as the boundary charge density continues to increase. The compaction also increases the number density of the chromophore which leads to misalignment of dipoles as the density increases resulting in an increase in V_π.

Table 5.3: Wafer Fabrication Properties for Poling Time Experiments

Wafer #	Upper Cladding Thickness	Core Thickness	Lower Cladding Thickness	$\%wt_{chr}$
761	2.77	3.62	3.50	29.0
775	2.67	3.75	3.3	29.0
790	2.36	3.61	3.40	34.65
791	2.79	3.61	3.10	34.65
812	2.70	3.53	2.64	34.66

Table 5.4: Poling Time Results

Wafer-Die #	Post Poling Optical Loss (dB/cm)	Wafer V_π (V)	Poling Time (minutes)
761-2	3.6*	6.36	2
761-3	3.8*	7.1	30
775-1	4.1*	5.71	10
775-2	5.1*	5.0	20
775-3	3.1	6.36	2
790-1	5.2*	5.0	30
790-2	3.7*	6.0	2
790-3	4.6*	5.5	20
791-1	6.3*	6.3	2
791-2	8.5*	5.7	30
791-3	11.1	8.0	60
812-1	3.45*	6.5	10
812-2	5.38*	5.81	30
812-3	7.1*	6.67	50

*Ends not re-diced to remove end face damage from gold etchant

These results match well with the theory. Figures 5.3, 5.4, 5.5, and 5.6 show the modeled poling charge and current for wafer 791 assuming an unlimited temperature range. Figure 5.3 shows the poling charge density with the boundary charge density shown as a solid line and the polarization charge density shown as a dashed line. Figure 5.4 shows the poling current density with the total current density shown as a solid line, the boundary charge current density shown as a dotted line, the polarization charge density shown as a dashed line, and the conduction current density shown as a dot-dash line. Figure 5.5 shows the TSD charge density with the boundary charge density shown as a solid line and the polarization charge density shown as a dashed line. Figure 5.6 shows the TSD current density with the total current density shown as a solid line, the boundary charge current density shown as a dotted line, and the polarization charge density shown as a dashed line. Theoretical curves for the other wafers are in Appendix B. The model shows the peak poling current is found at 206.19 °C and complete charge

build up for this die is found at 233.31 °C. Since poling temperatures are limited to 160 °C by the thermal stability of the chromophore molecule, this poling curve is not achievable.

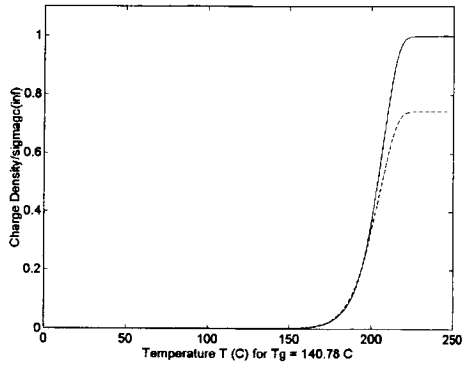

Figure 5.3 Wafer 791 Theoretical Poling Charge Densities

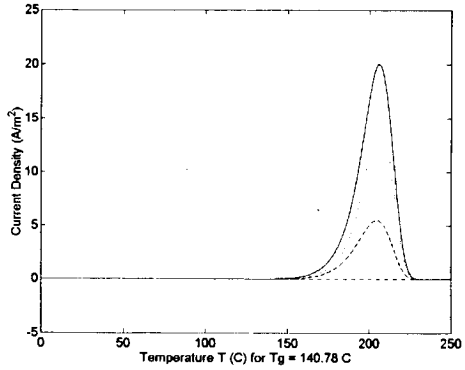

Figure 5.4: Wafer 791 Theoretical Poling Current Densities

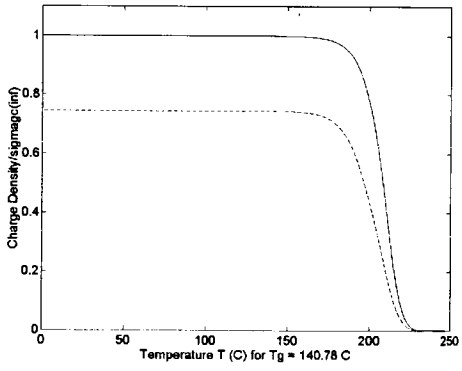

Figure 5.5 Wafer 791 Theoretical TSD Charge Densities

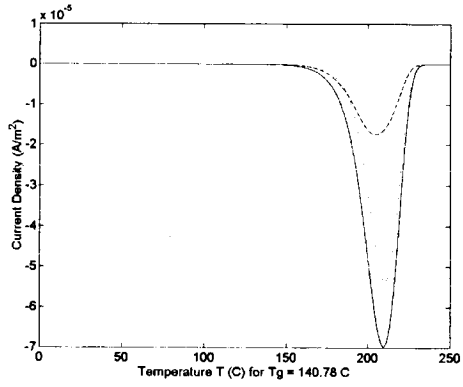

Figure 5.6 Wafer 791 Theoretical TSD Current Densities

Note, in comparing Figures 5.3 and 5.4 for Poling and Figures 5.5 and 5.6 for TSD, the poling currents provide the same amount of information as the TSD plots. There are some slight shifts in the charge curves with the peak TSD temperature at 209.64 °C and full charge depletion at 247.0 °C. These shifts are due to the absence of the poling field which reduces the energy seen by the molecules to reduce the alignment.

This results in a slight temperature increase for the depoling measured by TSD. Thus, studies of poling can be accomplished by examining the poling curves for the various die which provide the same information as TSD for electrode poled samples.

Since the poling temperature is limited, poling time is increased to allow the charge to build longer and improve the poling alignment. This is a result of the boundary charge forming part of the directing field for the molecular orientation as shown by Equation (3.85). This can be seen through the poling charge calculations for the various poling time experiments.

Die 791-1 was poled for the baseline 2 minutes, 500 V, 145 °C. Figures 5.7 and 5.8 show the poling charge and current densities for this die. Figure 5.7 shows the modeled charge densities for the Die 791-1 poling experiment with the boundary charge density shown by the + symbols and the polarization charge density shown by the dashed line. The charge densities are plotted as the ratios to the boundary charge infinite value. This wafer was poled for the minimum 2 minutes. Table 5.5 gives the calculated values of the poling boundary and polarization charge densities achieved for the poling experiment. The data in Table 5.5 is ordered by increasing poling times. Shaded rows are discussed in this section. The remaining row are duplicate poling times and plots for these die are presented in Appendix B. Equations (3.71) and (3.72) were used to calculate the infinite (or limiting) values of the charge densities in the table.

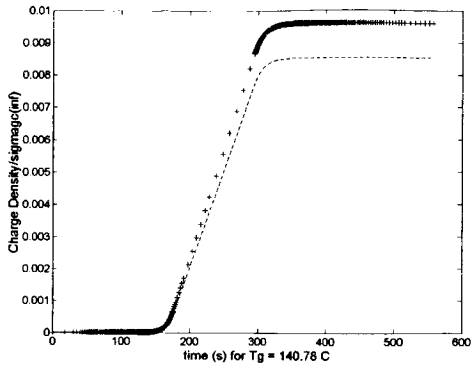

Figure 5.7 Die 791-1 Modeled Poling Charge Density

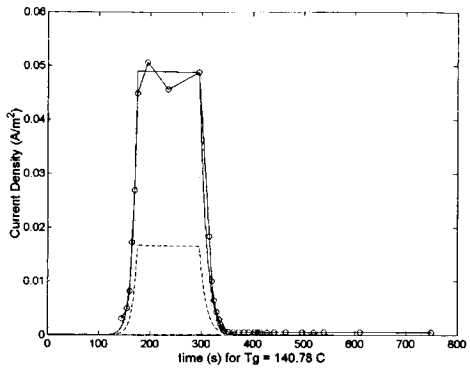

Figure 5.8 Die 791-1 Modeled and Measured Poling Current Density

Table 5.5 Calculated Charge Densities for Poling Time Experiments

Wafer-Die #	Poling Time (minutes)	α_r (10^{20} Hz)	σ_{gc}	$\sigma_{gc} / \sigma_{gc}(\infty)$	P_s	$P_s / P_s(\infty)$	$P_s / \sigma_{gc}(\infty)$
761-2	2	0.8	2.03×10^{-5}	0.0074	1.92×10^{-5}	0.0070	0.0092
775-3	2	0.1	0.73×10^{-5}	0.0028	0.25×10^{-5}	0.0009	0.0012
790-2	2	.55	1.53×10^{-5}	0.0058	1.42×10^{-5}	0.0054	0.0067
812-1	10	1.0	1.21×10^{-4}	.04.3	1.10×10^{-4}	0.052	0.039
790-3	20	1.25	2.80×10^{-4}	0.106	2.60×10^{-4}	0.098	0.122
761-3	30	0.9	2.76×10^{-4}	0.101	2.59×10^{-4}	0.094	0.124
790-1	30	1.1	3.58×10^{-4}	0.135	3.34×10^{-4}	0.126	0.157
812-2	30	1.0	3.34×10^{-4}	0.119	2.95×10^{-4}	0.140	0.105

Figure 5.8 shows the modeled and measured poling current density with the total modeled current density shown as a solid line, the modeled boundary charge current density shown as a dashed line, the modeled polarization charge current density shown as a dotted line, and the measured total current density shown as a solid line with circles marking the measured data points. The experiment and theory data match well in Figure 5.8. The differences are due to the accuracy in estimating the poling time for each run.

Experimental data was measured as current versus temperature. A baseline run was measured with temperature versus time. This temperature-time curve was then extrapolated for each experimental data run to produce the current versus time plots. The accuracy of this extrapolation is ± 3 seconds. The modeled data assumes that once the poling temperature is reached, the temperature remains constant until cool down. Experimentally, the temperature overshoots 1–3 °C and then settles to a minimum which is 0–1 °C below the T_p before settling at T_p. This can be clearly seen in the measured poling current density in Figure 5.8 as the measured current varies with the temperature.

The plots for other die (761-2, 775-3, and 790-2) poled for 2 minutes are presented in Appendix B.

Die 775-1 was poled for 10 minutes. Figures 5.9 and 5.10 show the poling charge and current densities for this wafer. The total measured current density in Figure 5.10 shows significant drift during the poling. This is attributed to the estimation of the α_r and E_A for the modeled current density and the thermal considerations discussed above. The plots fro die 812-1 are presented in Appendix B.

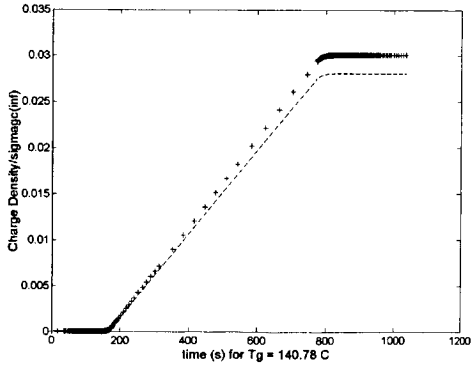

Figure 5.9 Die 775-1 Modeled Poling Charge Density

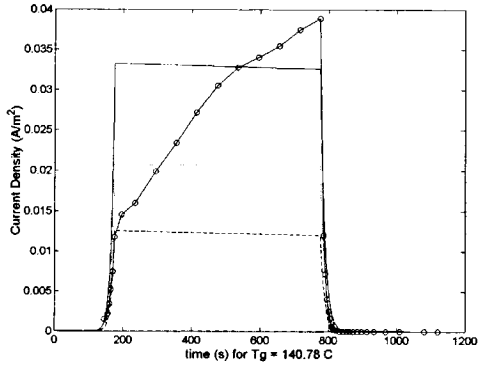

Figure 5.10 Die 791-1 Modeled and Measured Poling Current Density

Die 775-2 was poled for 20 minutes. Figures 5.11 and 5.12 show the poling charge and current densities for this wafer. The total measured current density in Figure 5.12 also shows significant drift during the poling which is attributed to the estimation of the α_r and E_A for the modeled current density and the thermal considerations discussed above. Die 790-3 was also poled for 20 minutes. Plots for this die are shown in Appendix B.

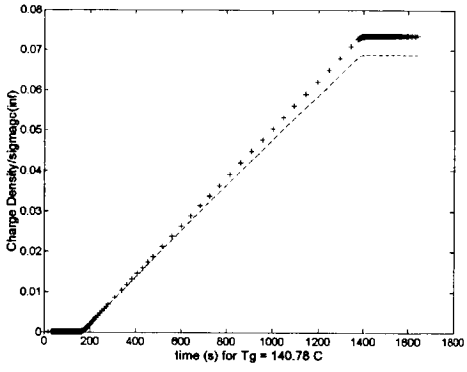

Figure 5.11 Die 775-2 Modeled Poling Charge Density

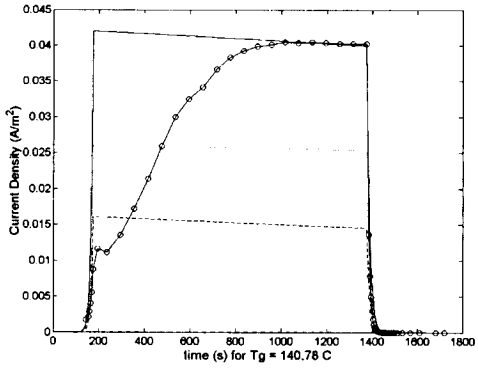

Figure 5.12 Die 775-2 Modeled and Measured Poling Current Density

Die 791-2 was poled for 30 minutes. Figures 5.13 and 5.14 show the poling charge and current densities for this wafer. The total measured current density in Figure 5.14 also shows significant drift during the poling which is attributed to the estimation of the α_r and E_A for the modeled current density and the thermal considerations discussed above. Die 761-3, 790-1, and 812-2 were also poled for 30 minutes. Plots for these Die are presented in Appendix B.

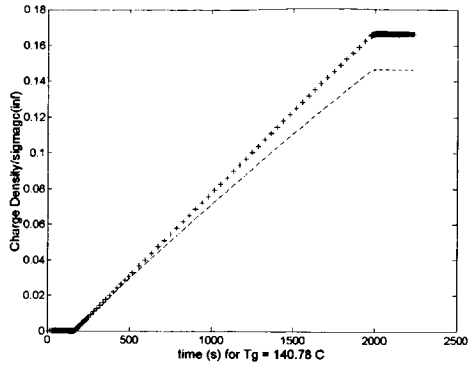

Figure 5.13 Die 791-2 Modeled Poling Charge Density

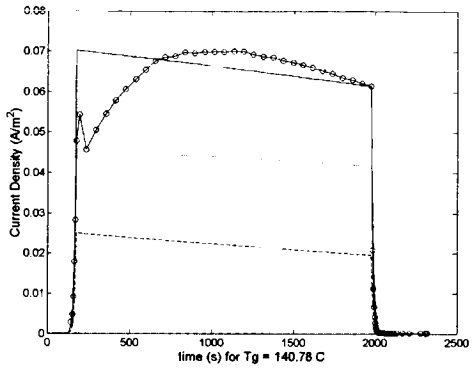

Figure 5.14 Die 791-2 Modeled and Measured Poling Current Density

Die 812-3 was poled for 50 minutes. Figures 5.15 and 5.16 show the poling charge and current densities for this wafer. The total measured current density in Figure 5.16 also shows significant drift during the poling which is attributed to the estimation of the α_r and E_A for the modeled current density and the thermal considerations discussed above.

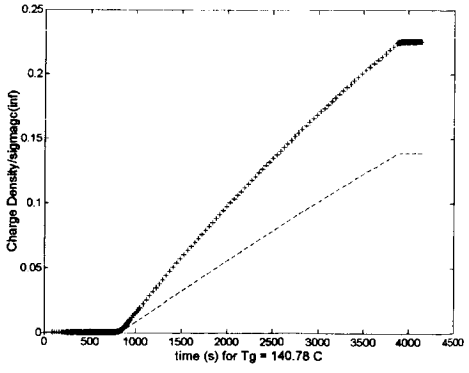

Figure 5.15 Die 812-3 Modeled Poling Charge Density

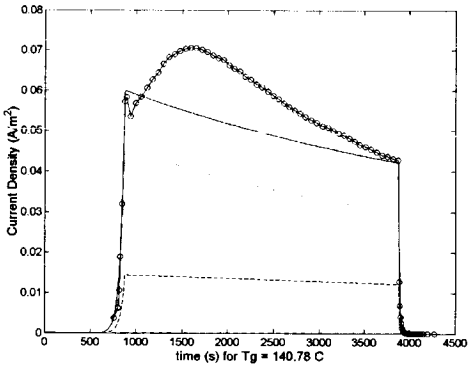

Figure 5.16 Die 812-3 Modeled and Measured Poling Current Density

Die 791-3 was poled for 60 minutes. Figures 5.17 and 5.18 show the poling charge and current densities for this wafer. The total measured current density in Figure

5.18 also shows significant drift during the poling which is attributed to the estimation of the α_T and E_A for the modeled current density and the thermal considerations discussed above.

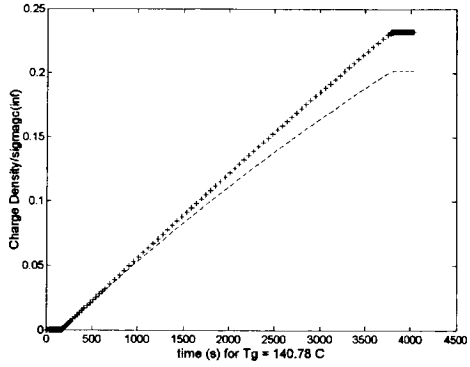

Figure 5.17 Die 791-3 Modeled Poling Charge Density

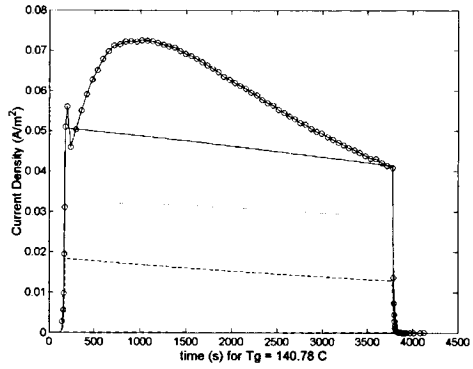

Figure 5.18 Die 791-3 Modeled and Measured Poling Current Density

The boundary charge and polarization charge densities are plotted versus poling time for these five die (the shaded rows in Table 5.5) in Figure 5.19. Note the significant increase in charge densities with increasing poling time showing that additional poling efficiency can be achieved through increased poling time.

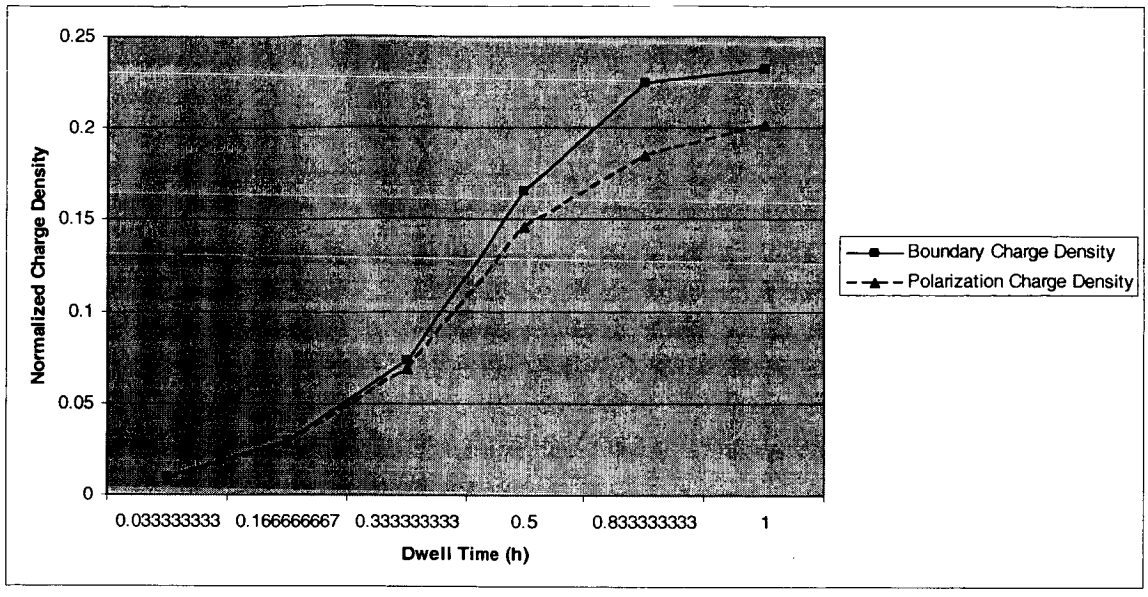

Figure 5.19 CLDX/APC Charge Density vs. Poling Time

To investigate the limits of the build up of boundary and polarization charge due to dwell time, Figure 5.20 plots the charge buildup with poling (or dwell) time. This plot shows that 91% of the boundary and polarization charge densities are reached after 4 hours and 99.9% of the full boundary and polarization charge is realized at a poling time of 11 hours. However, practical poling is limited by electrostriction which causes cutoff of the optical propagation mode.

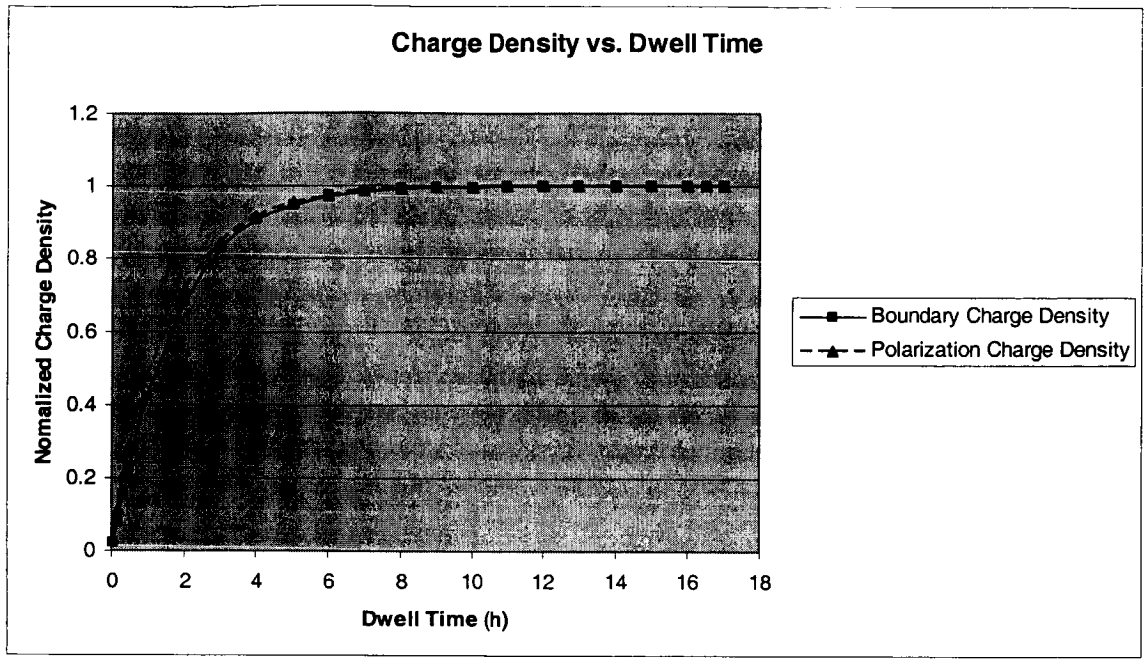

Figure 5.20: CLD1/APC Charge Density Change with Poling Dwell Time (t_p)

5.3 Poling Temperature

Poling Temperature was evaluated using 8 die from 3 wafers. Wafers 782 and 783 were fabricated with CLDX/APC while wafer 930 was fabricated with CLDZ/APEC. The fabrication data for these wafers is given Table 5.5. Wafer 782 had some adhesion problems resulting in the loss of die 2 and high initial losses in die 3. The optical losses in die 3 were greatly reduced by poling, indicating the thermal environment improved the adhesion of the layers. All of these wafers were poled following the standard poling process with V_p = 500 V and t_p = 2 minutes. Table 5.7 provides the results of the testing and Figure 5.8 charts the change in measured V_π with poling time. This data indicates that poling temperature does not affect poling efficiency for this system. The adhesion issues with wafer #782 create some uncertainty in the data given in Table 5.8. The

adhesion problems lead to increased layer separation, and reduced poling charge build-up. This can be seen by comparing the 2 surviving die from wafer #782. Die-1 has better adhesion as can be seen by the optical losses and also a lower V_π in spite of the lower poling temperature. Thus, the measured V_π is higher and more variable than for the #783.

Table 5.6: Wafer Fabrication Properties for Poling Temperature Experiments

Wafer #	Upper Cladding Thickness	Core Thickness	Lower Cladding Thickness	$\%wt_{chr}$
782	2.83	3.52	3.40	34.64
783	2.84	2.98	3.50	34.64
930	2.52	3.27	2.38	32.79

Table 5.7: Poling Temperature Results

Wafer-Die #	Post Poling Optical Loss (dB/cm)	Wafer V_π (V)	Poling Temperature (°C)
782-1	2.8*	5.85	145
782-3	5.1*	6.36	150
783-1	3.4*	5.0	155
783-2	3.4	5.0	155
783-3	3.0	5.0	145
930-1	4.70*	5.13	150
930-2	3.97*	5.13	145
930-3	3.85*	5.69	155

*Ends not re-diced to remove end face damage from gold etchant

Theoretical poling and TSD plots are presented in Appendix B for wafers 782, 783, and 930. For the experimental data, the maximum poling temperature is limited to 160 °C due to the chromophore thermal stability. Thus, poling temperature was only varied from 145 °C to 155 °C.

Die 783-3 was poled for the baseline 2 minutes, 500 V, 145 °C. Figures 5.21 and 5.22 show the poling charge and current densities for this die. Figure 5.21 shows the modeled charge densities for the Die 783-3 poling experiment with the boundary charge density shown by the + symbols and the polarization charge density shown by the dashed line. The charge densities are plotted as the ratios to the boundary charge infinite value. This wafer was poled for the minimum 2 minutes. Table 5.8 gives the calculated values of the poling boundary and polarization charge densities achieved for the poling experiment. The data in Table 5.8 is ordered by increasing poling temperatures. Since waver 782 had significant adhesion problems, which appear to have effected the poling results, only die 783-3, 783-2, and 930-1 are discussed here. Equations (3.71) and (3.72) were used to calculate the infinite (or limiting) values of the charge densities in the table.

Figure 5.21 shows the modeled and measured poling current density with the total modeled current density shown as a solid line, the modeled boundary charge current density shown as a dashed line, the modeled polarization charge current density shown as a dotted line, and the measured total current density shown as a solid line with circles marking the measured data points. The experiment and theory data match well in Figure 5.20. Variations in the modeled and experimental data are based on the estimation of the α_T and E_A for the modeled current density and experimental time estimation as discussed for Figure 5.8. Die 782-1, and 930-2 were also poled at 145 C. Plots for these Die are presented in Appendix B.

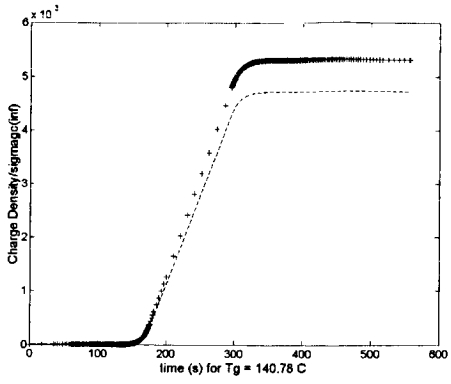

Figure 5.21 Die 783-3 Modeled Poling Charge Density

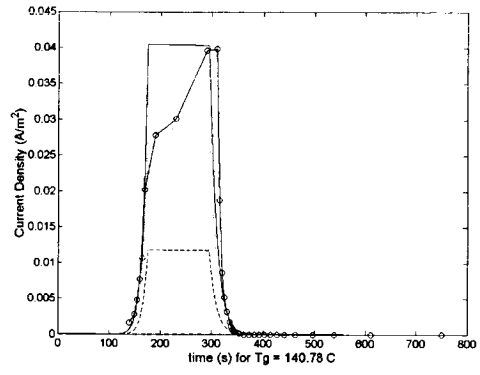

Figure 5.22 Die 783-3 Modeled and Measured Poling Current Density

Table 5.8 Calculated Charge Densities for Poling Temperature Experiments

Wafer-Die #	Poling Temperature (°C)	α_r (10^{20} Hz)	σ_{gc}	σ_{gc} / σ_{gc} (∞)	P_s	P_s / P_s (∞)	P_s /σ_{gc} (∞)
783-3	145	0.67	1.78×10^{-5}	0.0053	1.58×10^{-5}	0.0070	0.0047
782-1	145	0.7	1.71×10^{-5}	0.0061	1.57×10^{-5}	0.0079	0.0056
782-3	150	0.7	3.50×10^{-5}	0.0126	3.01×10^{-5}	0.0151	0.0108
783-2	155	0.7	8.47×10^{-5}	0.0252	5.99×10^{-5}	0.0266	0.0179
783-1	155	0.7	9.63×10^{-5}	0.0287	6.00×10^{-5}	0.0266	0.0179

Die 930-1 was poled at 150 °C. Figures 5.23 and 5.24 show the poling charge and current densities for this wafer. The total measured current density in Figure 5.24 also shows significant drift during the poling which is attributed to the estimation of the α_r and E_A for the modeled current density and the thermal considerations discussed above. Die 782-3 was also poled 150 °C. Plots for these Die are presented in Appendix B.

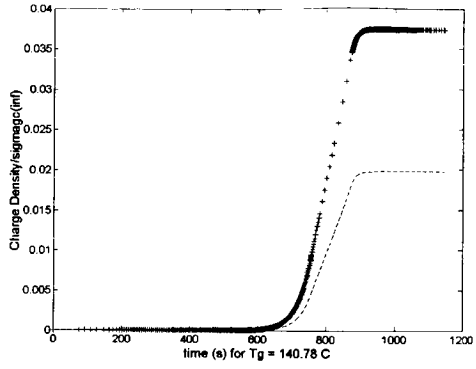

Figure 5.23 Die 930-1 Modeled Poling Charge Density

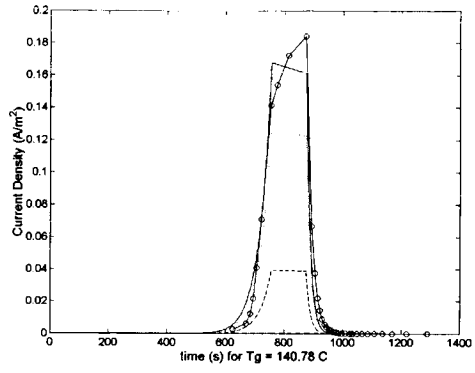

Figure 5.24 Die 930-1 Modeled and Measured Poling Current Density

Die 783-2 was poled at 155 °C. Figures 5.25 and 5.26 show the poling charge and current densities for this wafer. The total measured current density in Figure 5.26 also shows significant drift during the poling which is attributed to the estimation of the α_r and E_A for the modeled current density and the thermal considerations discussed above. Die 783-1 and 930-3 were also poled 155 °C. Plots for these Die are presented in Appendix B.

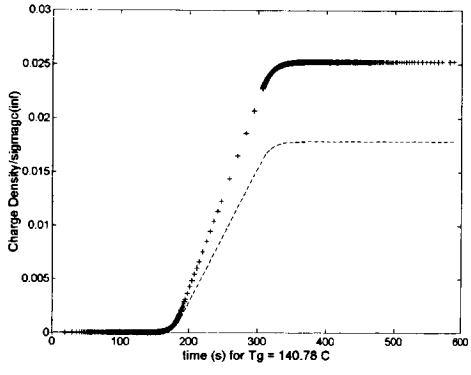

Figure 5.25 Die 783-2 Modeled Poling Charge Density

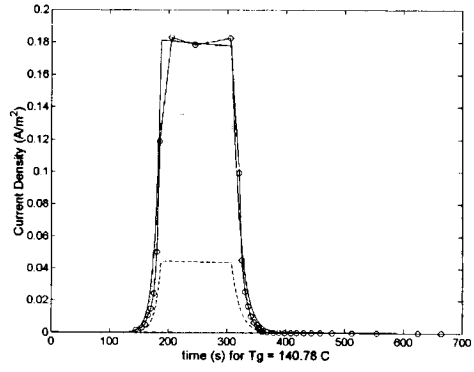

Figure 5.26 Die 783-2 Modeled and Measured Poling Current Density

As can be seen in Table 5.8, changing the temperature from 145 °C to 155 °C does not significantly increase the poling or boundary charge densities. Note that the

CLDX wafer (930) has a higher poling value than the CLDZ wafers (782 and 783). There is an increase in polarization charge for each 5 °C added to the poling temperature for either material as illustrated in Figure 5.27 for wafer 930, but these changes are small as compared to the poling time changes seen in Table 5.5. Comparing these two tables, increasing the poling temperature by 10 °C is about the same as increasing the poling time by 8 minutes (from 2 minutes to 10 minutes). Thus, poling time has more flexibility to increase the poling efficiency than does poling temperature due to the chromophore thermal stability limits.

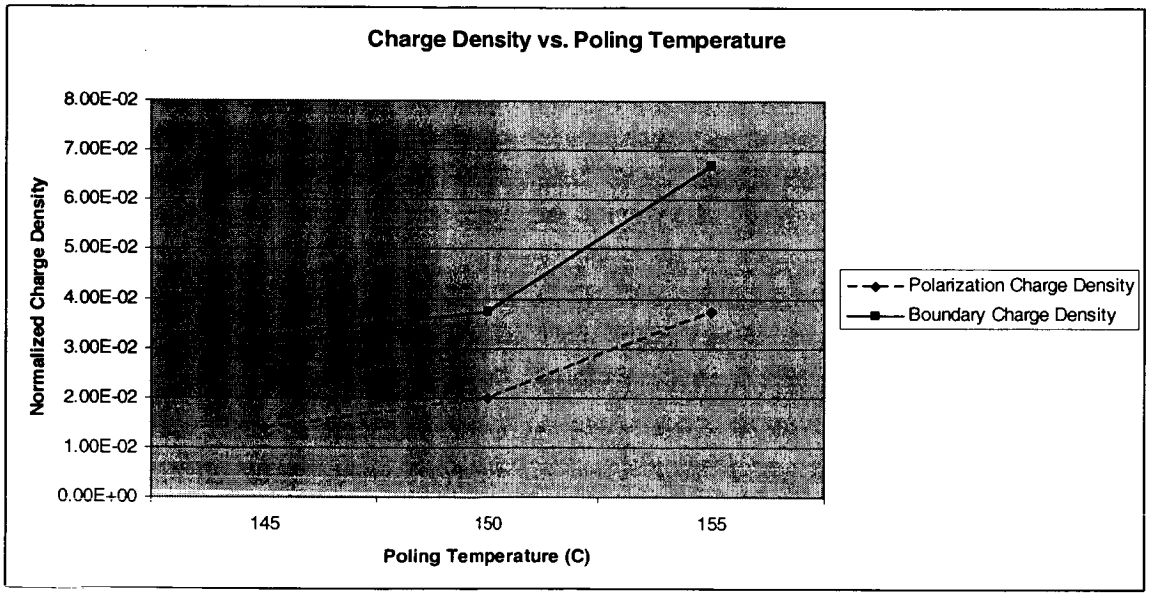

Figure 5.27 Wafer 930 Charge Density Change versus Poling Temperature

5.4 Poling Voltage

Poling voltage was evaluated for CLDZ/APEC in Phase 1 experiments using 9 die from 3 wafers. The fabrication properties for these wafers are shown in Table 5.9. These poling results for these systems is shown by Table 5.10. These results show a clear decrease in V_π as the poling voltage increases. This is

consistent with theoretical predictions that the poling alignment improves with increasing voltage. Note, that a wafer processing problem resulted in a partial removal of the upper gold electrode for die 929-3. This resulted in electrode lengths of 0.75 cm, 0.8 cm, and 1.0 cm instead of the standard 1.36 cm. Considering Equation (2.71), the measured wafer V_π values were adjusted for these electrode lengths using the relationship:

$$V_{\pi adjusted} = \frac{L}{1.36} V_\pi \,. \tag{5.7}$$

Table 5.9: Fabrication Properties for Poling Voltage Experiments

Wafer #	Upper Cladding Thickness	Core Thickness	Lower Cladding Thickness	$\%wt_{chr}$
929	2.61	3.33	2.50	32.79
931	2.52	3.25	2.50	32.79
932	2.57	3.53	2.64	32.79

Table 5.10 Poling Voltage Results

Wafer-Die #	Post Poling Optical Loss (dB/cm)	Wafer V_π (V)	Poling Voltage (V)
929-1	3.1*	5.5	750
929-2	3.75*	5.08	1000
929-3	3.49*	5.33	500
931-1	7.77*	5.0	1000
931-2	3.07*	6.45	500
931-3	2.90*	5.85	750
932-1	5.02*	7.41	500
932-2	3.92*	5.56	750
932-3	5.76	5.26	1000

*Ends not re-diced to remove end face damage from gold etchant

Table 5.11 gives the calculated charge densities for the different poling voltages.

Table 5.11: Calculated Charge Densities for Poling Voltage Experiments

Wafer-Die #	Poling Voltage (V)	α_r (10^{20} Hz)	σ_{gc}	σ_{gc} / σ_{gc} (∞)	P_s	P_s / P_s (∞)	P_s /σ_{gc} (∞)
932-1	500	0.4	1.57×10^{-5}	0.0051	1.28×10^{-5}	0.0057	0.0042
929-3	500	0.43	3.00×10^{-5}	0.0101	1.36×10^{-5}	0.0061	0.0046
931-2	500	0.7	2.56×10^{-5}	0.0084	2.27×10^{-5}	0.0100	0.0075
929-1	750	0.43	5.33×10^{-5}	0.0120	2.03×10^{-5}	0.0061	0.0046
931-3	750	0.7	7.77×10^{-5}	0.0170	3.41×10^{-5}	0.0100	0.0075
932-2	750	1.4	1.51×10^{-4}	0.0329	6.73×10^{-5}	0.0198	0.0147
929-2	1000	1.4	2.08×10^{-4}	0.0349	8.80×10^{-5}	0.0199	0.0148
932-3	1000	1.4	2.28×10^{-4}	0.0373	8.99×10^{-5}	0.0199	0.0147
931-1	1000	1.7	3.26×10^{-4}	0.0537	11.1×10^{-5}	0.0244	0.0182

Theoretical plots are for poling taken to a maximum temperature (520 K) with no dwell time. However, these plots vary in magnitude of response proportionally with poling voltage as predicated by theory and seen in Equations (3.71) and (3.72). Thus, theoretical plots are examined for the 3 experimental poling voltages: 500 V, 750 V, and 1000 V.

Figures 5.28 and 5.29 show the theoretical curves for wafer 931 poled at 500 V. Figures 5.30 and 5.31 show the corresponding TSD plots for wafer 931. Theoretical plots for wafers 929 and 932 poled at 500 V are presented in Appendix B.

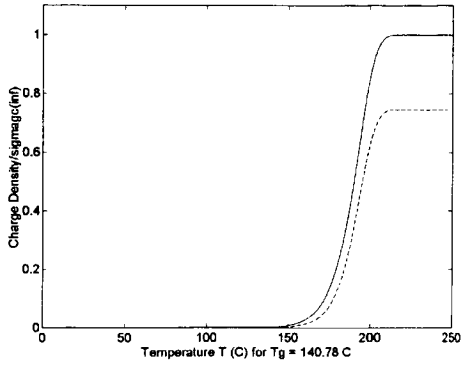

Figure 5.28 Wafer 931 Theoretical 500 V Poling Charge Densities

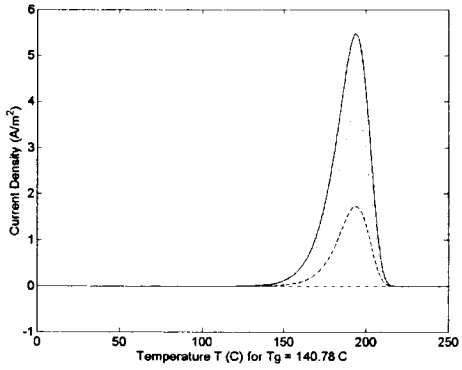

Figure 5.29 Wafer 931 Theoretical 500 V Poling Current Densities

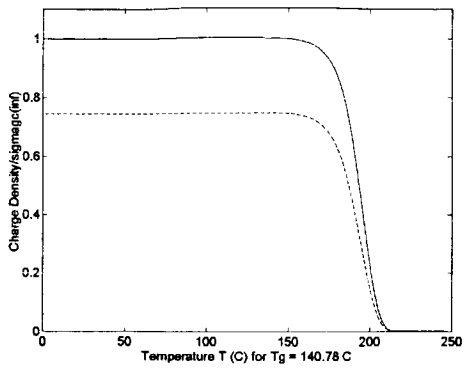

Figure 5.30 Wafer 931 Theoretical 500 V TSD Charge Densities

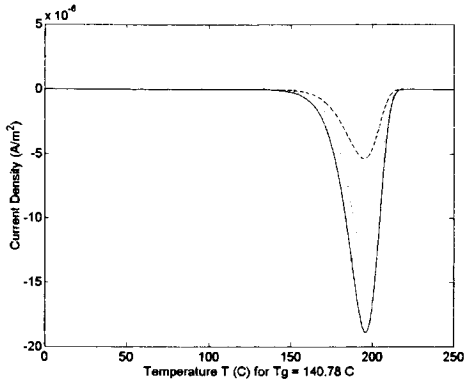

Figure 5.31 Wafer 931 Theoretical 500 V TSD Current Densities

Figures 5.32 and 5.33 show the theoretical curves for wafer 931 poled at 750 V. Figures 5.34 and 5.35 show the corresponding TSD plots for wafer 931. Theoretical plots for wafers 929 and 932 poled at 750 V are presented in Appendix B.

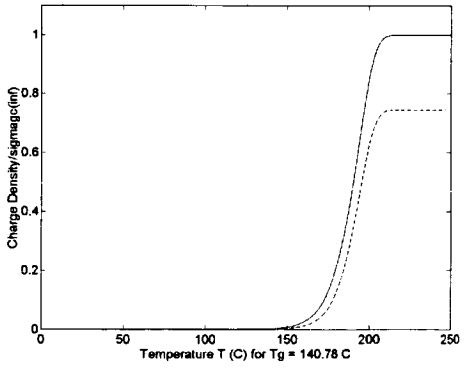

Figure 5.32 Wafer 931 Theoretical 750 V Poling Charge Densities

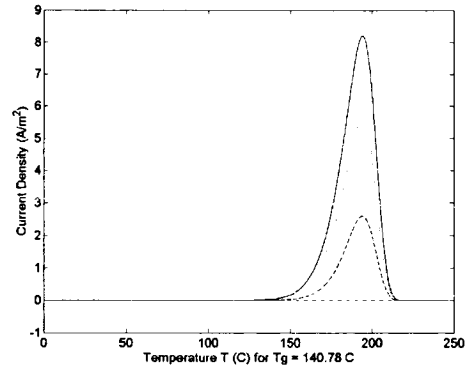

Figure 5.33 Wafer 931 Theoretical 750 V Poling Current Densities

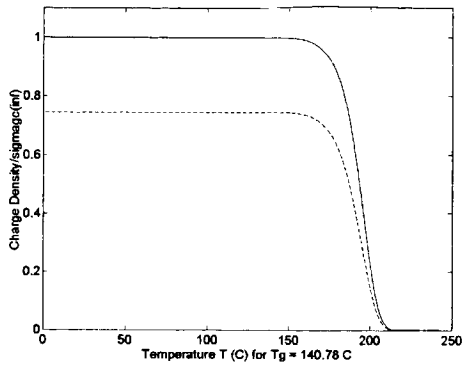

Figure 5.34 Wafer 931 Theoretical 750 V TSD Charge Densities

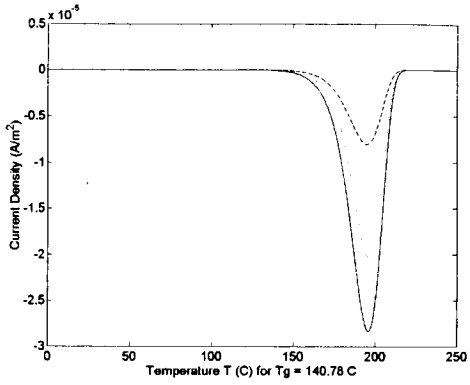

Figure 5.35 Wafer 931 Theoretical 750 V TSD Current Densities

Figures 5.36 and 5.37 show the theoretical curves for wafer 931 poled at 1000 V. Figures 5.38 and 5.39 show the corresponding TSD plots for wafer 931. Theoretical plots for wafers 929 and 932 poled at 1000 V are presented in Appendix B.

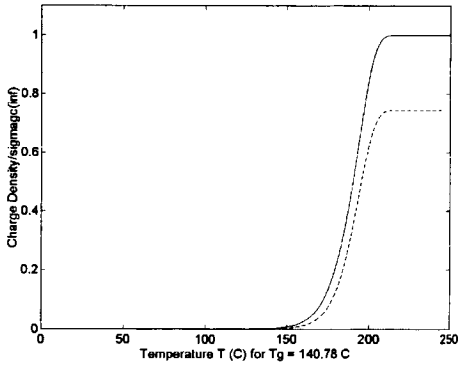

Figure 5.36 Wafer 931 Theoretical 1000 V Poling Charge Densities

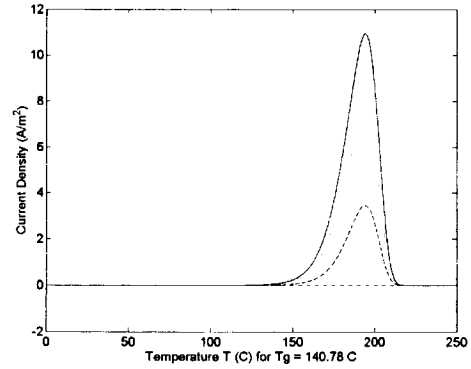

Figure 5.37 Wafer 931 Theoretical 1000 V Poling Current Densities

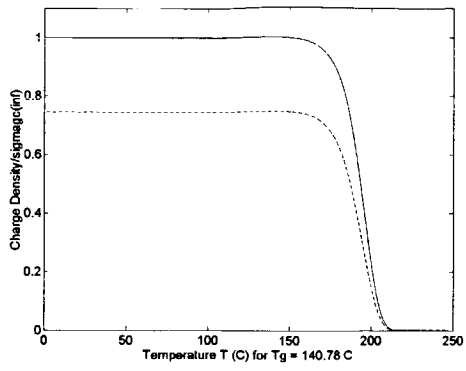

Figure 5.38 Wafer 931 Theoretical 1000 V TSD Charge Densities

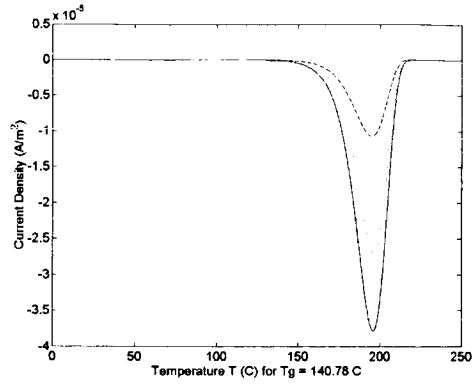

Figure 5.39 Wafer 931 Theoretical 1000 V TSD Current Densities

These plots show that the current density increases with poling voltage as also seen in the experimental measurements. While the theoretical charge plots show only small variation in charge densities, this is because the normalization factor, $\sigma_{gc}(\infty)$ increases proportional to V_p. Table 5.11, shows that the charge densities do in fact increase with poling voltage as expected from the theory.

Die 931-2 was poled at 500 V. Figures 5.40 and 5.41 show the poling charge and current densities for this wafer. The total measured current density in Figure 5.41 also shows significant drift during the poling which is attributed to the estimation of the α_r and E_A for the modeled current density and the thermal considerations discussed above. Die 929-3 and 932-1 were also poled at 500V. Plots for these Die are presented in Appendix B.

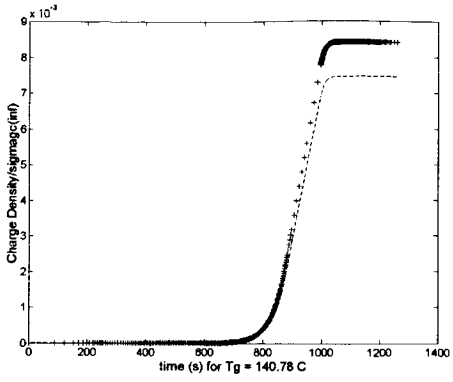

Figure 5.40 Die 931-2 Modeled Poling Charge Density

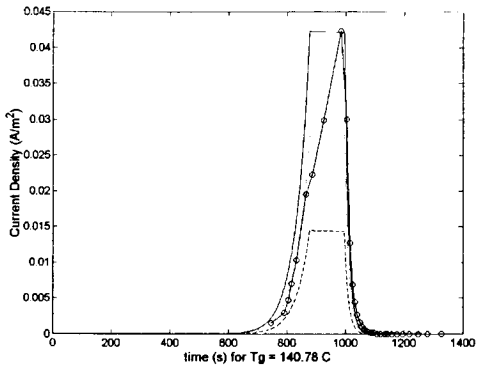

Figure 5.41 Die 931-2 Modeled and Measured Poling Current Density

Die 931-3 was poled at 750 V. Figures 5.42 and 5.43 show the poling charge and current densities for this wafer. The total measured current density in Figure 5.43 also shows significant drift during the poling which is attributed to the estimation of the α_r and E_A for the modeled current density and the thermal considerations discussed above. Die 929-1 and 932-2 were also poled at 750. Plots for these Die are presented in Appendix B.

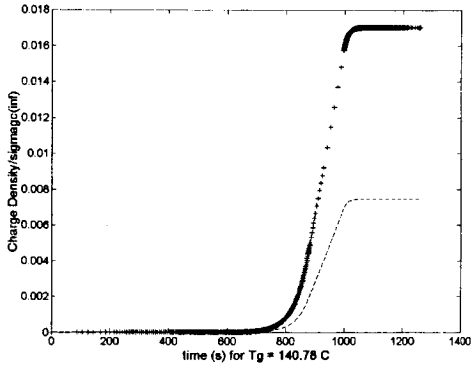

Figure 5.42 Die 931-3 Modeled Poling Charge Density

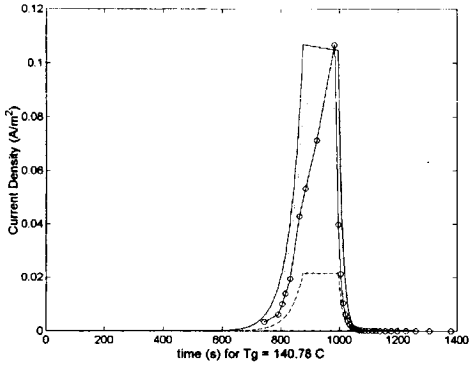

Figure 5.43 Die 931-3 Modeled and Measured Poling Current Density

Die 931-1 was poled at 1000 V. Figures 5.44 and 5.45 show the poling charge and current densities for this wafer. The total measured current density in Figure 5.45

also shows significant drift during the poling which is attributed to the estimation of the α_r and E_A for the modeled current density and the thermal considerations discussed above. Die 929-2 and 932-1 were also poled at 1000. Plots for these Die are presented in Appendix B.

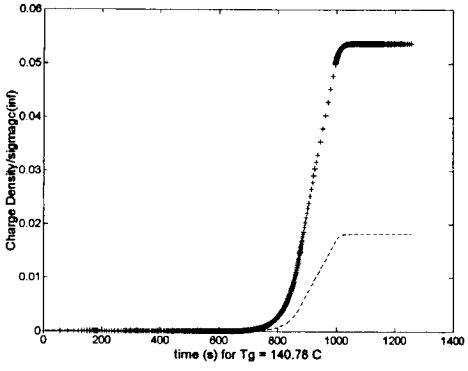

Figure 5.44 Die 931-1 Modeled Poling Charge Density

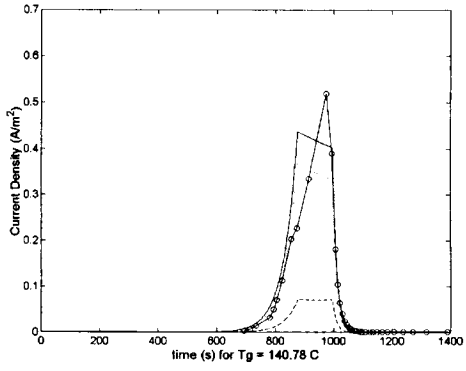

Figure 5.45 Die 931-1 Modeled and Measured Poling Current Density

There are some interesting conclusions that can be drawn from the charge density values given in Table 5.11. The boundary charge and polarization charge densities clearly show an increase with V_p. However, the magnitude of the change is small as compared with the values achieved with poling time. Poling at a 1000 V produced the same polarization charge density as poling for 10 minutes or for poling at 155 °C. Much larger charge values are achievable by poling at 30 minutes. This indicates that poling at higher temperatures and voltages can reduce the poling time, but poling time will still be in the 10 – 20 minute range. Assuming 1000 V at 155 °C, a poling time of approximately 10 minutes is expected. However, this may not be optimal as poling at 750 V or above tends to produce arcing which damages device electrodes.

Table 5.11 also shows that poling voltage tends to increase the dipole relaxation frequency. As the poling voltage increases, α_r also tends to increase. This is a calculated value, so experimental chemical studies of poled relaxation frequencies are needed to confirm this. Note also that as ar increases so do both charge densities. However, comparing charge densities for die with similar α_r and different poling voltages confirm that charge densities do increase with increasing V_p. Figure 5.46 illustrates the increase in charge densities with poling voltage using values from wafer 929.

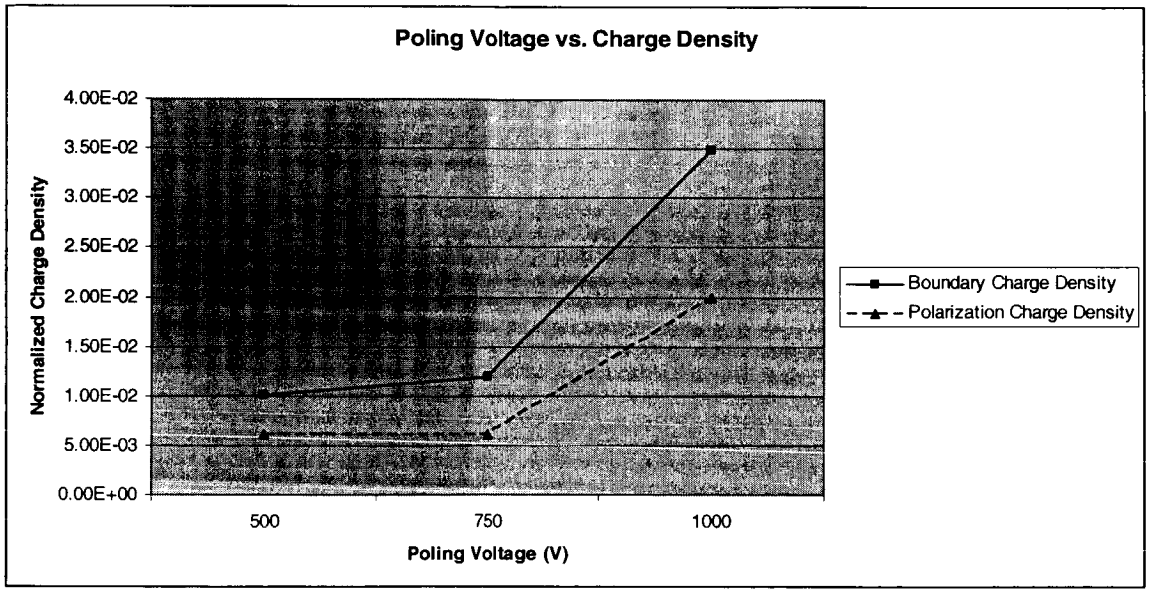

Figure 5.46 Wafer 929 Charge Density Change versus Poling Voltage

Following the statistical analysis for a 3x3 Latin Square as presented in Section 4.1.5, these results can be statistically analyzed. Table 5.12 presents the Analysis of Variance Table for the poling voltage experimental data.

Table 5.12 Poling Voltage Experiment Analysis of Variance Table

Source of Variation	Sum of Squares	Degrees of Freedom	Mean Square	Expected Value Mean Square	Ratio of Mean Squares
Grand Average (G)	294.0082	1	294.0082	-	-
Wafers (β_{929})	0.509781	2	0.254891	0.499044	0.50855
Wafers (β_{931})	0.007837	2	0.003919	0.985244	0.007818
Wafers (β_{932})	0.391204	2	0.195602	1.810244	0.390258
Die (β_1)	0.194226	2	0.097113	1.798578	0.193757
Die (β_2)	0.00107	2	0.000535	0.664111	0.001068
Die (β_3)	0.166459	2	0.08323	0.284778	0.166057
Treatments (τ_{500})	1.391737	2	0.695869	2.332944	1.388374
Treatments (τ_{750})	0.01867	2	0.009335	1.284244	0.018625
Treatments (τ_{1000})	1.088015	2	0.544007	1.266944	1.085386
Residuals (R)	1.002422	2	0.501211	0.596428	-
Total	298.7796	21			

The data in this table show that the V_π averages close to 750 V. This shows that the data is fairly evenly distributed with the values of V_π at 500 V being higher than those for 750 V while this average is offset by the reduction in V_π at 1000 V. The values of the Ratios of Mean Squares is very low since the value of the Residual Mean Square is on the same order or larger than the wafer, die, and treatment Mean Squares. This is a function of the small number of samples resulting in a low Degree of freedom for the Residuals. Replicating these experiment 3 or 4 times would greatly increase the available Residual Degrees of Freedom and provide a better statistical base from which to evaluate the experimental error. The data, as seen in the Mean Square Values in Table 5.12 and the

data trends plotted in Figure 5.46 support the conclusion that increasing poling voltage improves the wafer V_π.

5.5 Electrical Transfer Function

The electrical transfer function can be determined from the optical response of the modulation system. [58] The change in the core voltage and the associated optical response can be modeled using Equations (2.66), (3.62), and (2.86). Equation (3.62) defines the level of core voltage fixed by the boundary and polarization charge densities and the poling field. In the absence of the poling field, $V_p = 0$, the voltage induced by the boundary charge is given by:

$$V_{charge}(t) = \frac{\sigma_{cg}(t) - P_s(t)}{\left(\frac{\varepsilon_0 \varepsilon_g}{h_g} + \frac{\varepsilon_c}{h_c \varepsilon_g}\Gamma_{cs}(T)\right)}. \tag{5.8}$$

Equation (5.8) can be treated as an initial condition and combined with Equation (2.86) so the core voltage can then be written as:

$$V_{core}(t) = \int H_{wg}(j\omega) V_{applied}(j\omega) e^{-j\omega t} dt + V_{charge}(t). \tag{5.9}$$

The r_{33} values can then be calculated by solving Equation (2.73) for a TM wave and determining V_π as the maximum change in core voltage, $\Delta V_{core}(t)$, divided by the number of modulation half periods in the experimental data. These equations were programmed in Matlab to produce plots of these quantities with the modulating voltage, V_m. The Matlab programs are listed in Appendix C. To determine the electrical characteristics, 3 responses of the model were evaluated: transient response to a square wave modulation, modulation response to a saw tooth modulation, and the frequency response. The model components and values were set to match the experimental data.

Most experiments conducted in Phase 1 were done before the Labview program was updated for the optical measurement bench as discussed in Section 4.2. Thus, computer based matching of boundary layer capacitance and resistance could not be readily accomplished. However, 3 wafers were measured with the new system to produce the required data. Data was taken for a square wave modulation to measure transient response and saw tooth modulation to measure V_{π}. Wafer 791-1, a CLDX/APC photobleached wafer; wafer 809-1, a CLDX/APC rib waveguide wafer; and wafer 685-3, a TP7 waveguide wafer were measured. TP7 is an attached side chain polymer. [59],[60],[61]

Table 5.13 gives the resistance and capacitance values for the electrical transfer function corresponding to the model shown in Figure 2.10. Since NOA71 is used as both the upper and lower cladding, the upper and lower interface resistance values were assumed to be equal. Table 5.13 gives the resistance and capacitance values for all 3 waveguides measured experimentally. The resistances were calculated by multiplying the material resistivity with the electrode area divided by the fabricated film thickness. Similarly, the capacitances were calculated as a function of the material dielectric constant, film thickness, and electrode area. C_{core} for the rib waveguide was calculated as a series capacitance of upper cladding and planar core capacitance combined with a parallel capacitance of core material scaled for the width of the rib. R_{core} represents the parallel combination of bleached and unbleached (waveguide core) areas of the core layer. The bleached area resistance is taken as equal to R_{host}. The unbleached area is the parallel combination of R_{host} and R_{chr} for the guest/host material. Measured values were used for R_{core}, and R_{host} in the CLD/APC material. R_{chr} was then derived from these values. Measured values for R_{core} were also used for the TP7 device but separate values

for the R_{host} and R_{chr} were not available. The resistance of the bleached and unbleached areas of the TP7 core were assumed to be the same since the resistance is primarily due to the backbone in the side chain attached material. Values for the boundary layer resistance and capacitance were determined by matching the model with the experimental data. The modeled plots were produced by optimizing the boundary capacitance and resistance to produce the best match in both the square wave and sawtooth modulation optical response.

Table 5.13 Waveguide Electrical Transfer Function Values

Parameter	CLDX/APC PB	CLDX/APC Rib	TP7
R_{uc}	3.933×10^{17} Ω	3.82×10^{17} Ω	2.29×10^{18} Ω
C_{uc}	14.38 pF	27.52 pF	23.96 pF
R_{host}	3.703×10^{19} Ω	3.631×10^{19} Ω	N/A
R_{chr}	1.825×10^{17} Ω	1.79×10^{17} Ω	N/A
R_{core}	1.673×10^{17} Ω	1.64×10^{17} Ω	8.41×10^{15} Ω
C_{core}	10.55 pF	15.64 pF	20.51 pF
R_B	100 KΩ	10 KΩ	5 KΩ
C_B	17.74 pF	47.32 pF	709.74 pF
$R_{electrode}$	0.1 Ω	0.1 Ω	0.1 Ω
R_{lc}	5.167×10^{17} Ω	4.13×10^{17} Ω	2.52×10^{18} Ω
C_{lc}	10.94 pF	25.41 pF	21.73 pF

This CLDX/APC modulator has $V_{charge} = 0.283$ V and $r_{33} = 52.02$ pm/V. This value of r_{33} corresponds to a V_π value across the core of 2.1 V or a stack V_π of 5.48 V. Figure 5.47 shows the calculated core voltage and square wave modulation voltage for the CLDX/APC rib waveguide modulator. Note, that due to computer memory limitations in executing the Matlab models, the frequency content of the calculated values was clipped at 0.64 MHz. Thus, Gibbs Phenomena creates a large overshoot in the calculated core voltage when translated back to the time domain. This overshoot is

clearly shown in Figure 5.48. This creates a large ringing and phase offset error in the optical cosine transfer function as can be seen by the transient square wave response in Figure 5.48.

Figure 5.48 shows the comparison of the model and experimental results with the core voltage superimposed on the bottom of the figure for reference. The y-axis scale is in volts for the core voltage and is in 20x volts for the optical response. The optical response is shown in the voltage units corresponding to the detector voltage signal measured. The left side of the figure shows the response when the square is a maximum (-235 V) and the right side shows the square wave when grounded. The Gibbs overshoot in the core voltage is clearly seen in the modeled optical response where the boundary responses have narrowed peaks. The Gibbs Phenomena also produces a rounding of the signal at the peaks which creates a phase error seen in the response at the center of each wave pattern. The rounding is especially significant when the modulation signal is grounded and causes a flattening of the phase changes as compared with the experimental data. This error reflects the slope error in the modeled core voltage.

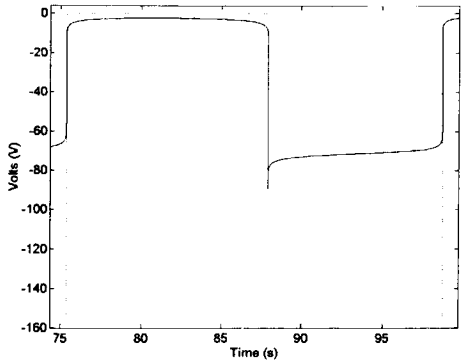

Figure 5.47 809-1 Modeled Square Wave Modulation Voltage and Core Voltage

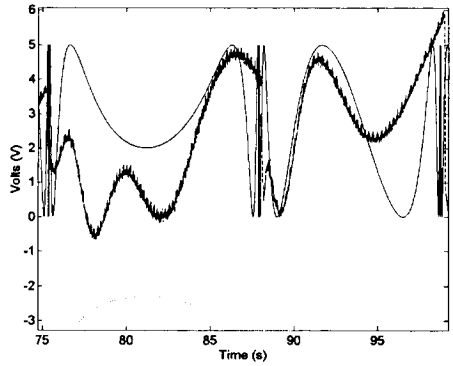

Figure 5.48 809-1 Modeled and Measured Square Wave Optical Response

Accounting for the Gibbs Phenomena errors, the model data matches the experimental data well. The same number of maximums and minimums are present, although shifted by the errors in the modeled core voltage.

Figure 5.49 shows the saw tooth modulation response with similar Gibbs effects. These effects show up as marked rounding of the core voltage just prior to the modulation signal returning to ground. This translates into both an optical response period error at the edge and a slight slope error that creates a small phase shift in the optical response modulation. The Gibbs effects are also apparent in the transient response when the modulating waveform returns to ground. In addition, the experimental modulation saw tooth wave had significant rounding at the boundaries which is not modeled. This affects the response at the boundaries. The model shows a single mode response and so does not reflect the multimode effects seen in the experimental data as well.

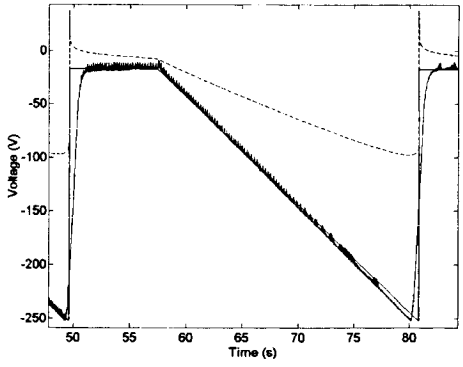

Figure 5.49 809-1 Modeled and Measured Sawtooth with Core Voltage Response

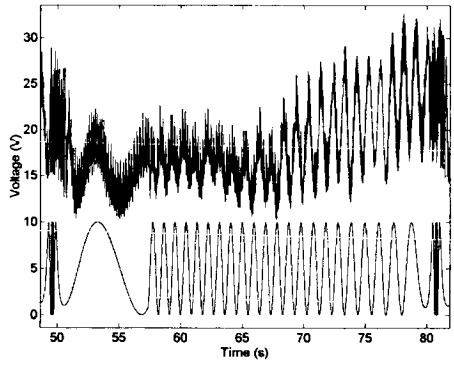

Figure 5.50 809-1 Modeled and Measured Sawtooth Modulation Response

Figure 5.50 shows the experimental and optical response to this wave form. The experimental response was scaled by 1000 V and the modeled response by 20 V for this plot. The difference in scale factor is related to the scaling performed by the optical meter when taking the experimental data. The core voltage overshoot is seen in the

smaller band of fast optical changes when the core voltage returns to ground. In addition the slight phase error in the optical response is due to the core voltage slope error as discussed above. Note, that a highly damped response is seen at the right boundary where the core voltage curves up due to Gibbs effects.

The effects of the RC circuit are clearly seen in the change in core voltage in Figures 5.47 and 5.49 and the resultant induced modulation of the optical response in Figures 5.46 and 5.48. The transient responses are driven by the values of the boundary capacitance and resistance. The boundary capacitance is notably higher than the layer capacitances and has the most significant effect on the transient responses. Raising or lowering this capacitance by more than a few pF can dampen the transient responses significantly while leaving the response to the saw tooth ramp unchanged. In addition, C_B has a significant effect on the value of r_{33}. As C_B is reduced, the core voltage increases. This leads to a decrease in the value of r_{33} to achieve the same number of periods to the saw tooth ramp response. The large value of C_B is due to the large boundary charge densities that exist between the layers. The capacitance increases with decreasing layer separation, which lower the interface impedance.

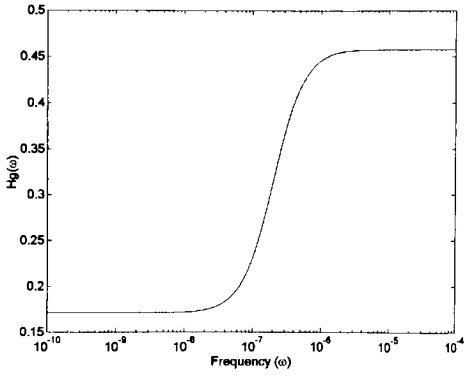

Figure 5.51 809-1 Low Frequency Response

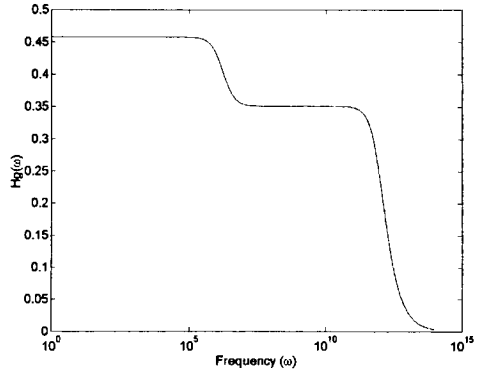

Figure 5.52 809-1 High Frequency Response

An additional characteristic of the circuit is the frequency response. Figures 5.51 and 5.52 show the low and high frequency response modulator 809-1. Note the step in the frequency response at 1 MHz. This is due to the value of the boundary capacitance. As the capacitance is increased, the right plateau of the response increases. However, this also dampens the transient response. So, C_B is chosen to minimize the frequency response step while still providing for the transient responses. The modulator 809-1 was tested to 30 MHz using sine wave modulation and did not show any detectable degradation in the response as expected from the model results.

A curious feature of the low frequency response is the DC response at $\omega = 0$ (a characteristic of a series RC circuit) shown in Figure 5.51. The value of the transfer function at this point is 0.17 which is the ratio of the stack resistance. However, this value is not approached until the frequency is below 10^{-6} Hz. Thus a true DC response is not achieved with waveguide modulators unless the voltage is stable for over 1000 hours. This corresponds well with relaxation time values known for glassy polymer materials. This means that the stack reactance is the most significant characteristic in determining the core voltage. Changing the layer resistances does not have a significant effect on the reactance, and therefore the core voltage. Changing the capacitance, however, has a large effect on the magnitude of the core voltage. This is significant in not only modulation efficiency, but poling efficiency as well. Thus, to increase the core voltage for a given modulation or poling voltage value, the dielectric constants must be considered for not only their optical effects but also their effect on the stack reactance.

For wafer 791-1, an $r_{33} = 52.14$ was calculated very similar to that of wafer 809-1. This value of r_{33} corresponds to a V_π value across the core of 2.0 V or a stack V_π of 6.3 V. Figure 5.53 shows the modeled and actual square wave form. Figure 5.54 shows the

modeled and measured square wave modulation response wave form. Note the strong Gibbs overshoot at the square wave edges. This causes a significant error at the edges and leads to rounding of the waveform in the middle of the period. This results in errors in matching the modeled and measured data in Figure 5.54. The edge errors create faster responses in the modeled data, while the rounding of the function produces slope errors which change the modulation periods of the optical response.

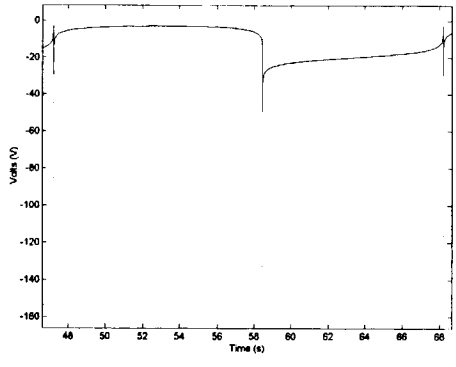

Figure 5.53 791-1 Modeled Square Wave and Core Voltage Response

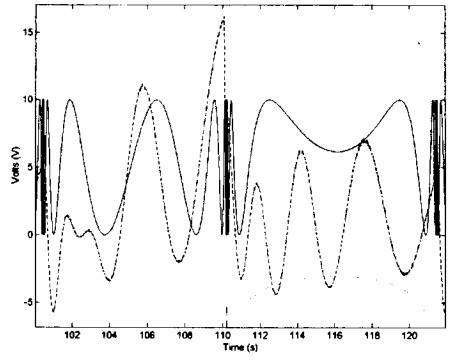

Figure 5.54 791-1 Modeled and Measured Square Wave Modulation Response

Figure 5.55 shows the calculated and measured square wave response. Figure 5.56 shows the calculated and measured saw tooth wave response.

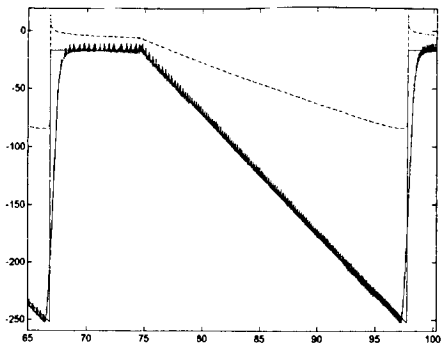

Figure 5.55 791-1 Modeled and Measured Sawtooth with Core Voltage Response

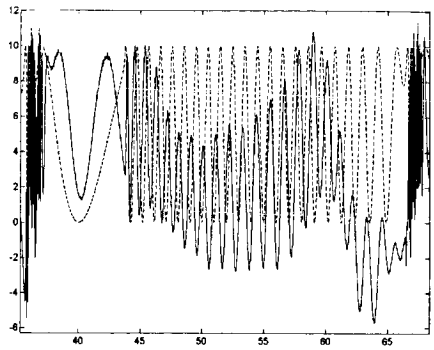

Figure 5.56 791-1 Modeled and Measured Sawtooth Modulation Response

Figures 5.57 and 5.58 show the low frequency and high frequency response of the waveguide stack. The high frequency response is set by the electrode resistance, $R_{electrode}$, and is shown to be greater than 100 GHz for the values used in Table 5.13.

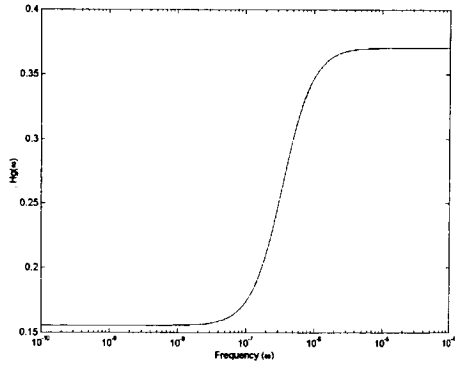

Figure 5.57 791-1 Low Frequency Response

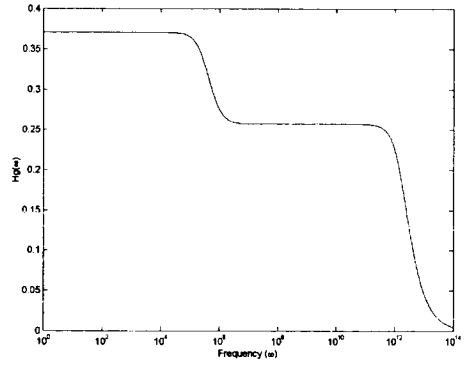

Figure 5.58 791-1 High Frequency Response

A side chain attached material, TP7, was used as the core for the 3rd waveguide modulator which was fabricated by photobleaching. TP7 has r_{33} = 10.105 pm/V. This value of r_{33} corresponds to a V_π value across the core of 6.25 V or a stack V_π of 18.07 V. Figure 5.59 shows the calculated core voltage and modulation voltage for the TP7 photobleached waveguide modulator. Note the core voltage follows the modulation

voltage very well, but some Gibbs overshoot still exists. Figure 5.60 shows the experimental and optical response with the core voltage superimposed again for reference. The experimental response was scaled by 100 V and the modeled response by 20 V for this plot. The difference in scale factor is related to the scaling performed by the optical meter when taking the experimental data. The experimental and model data match well. Note the core voltage follows the modulation voltage very well. Figure 5.61 shows the saw tooth modulation and core voltage response and Figure 5.62 shows the corresponding optical response. Again, note the very good fit produced by the model for this data. The model for the TP7 has less transient content and so has less error induced by Gibbs overshoots and therefore fits the experimental data very well.

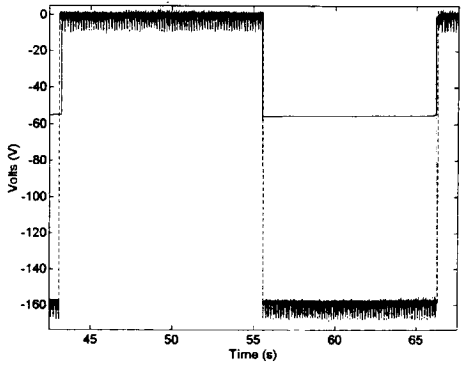

Figure 5.59 685-3 Modeled Square Wave Modulation Voltage and Core Voltage

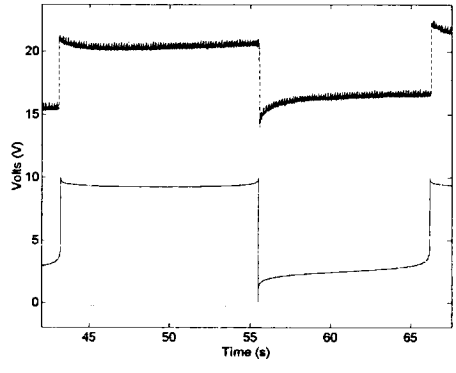

Figure 5.60 685-3 Modeled and Measured Square Wave Optical Response

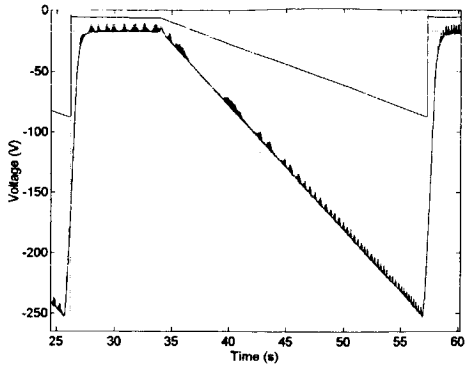

Figure 5.61 685-3 Modeled and Measured Sawtooth with Core Voltage Response

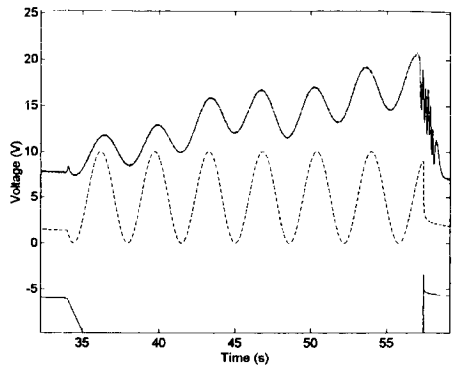

Figure 5.62 685-3 Modeled and Measured Sawtooth Modulation Response

Figures 5.63 and 5.64 show the high and low frequency response for the TP7 modulator. The modulator has responses similar to the CLDX/APC modulators. For the high frequency response, the TP7 has higher interface capacitance and, therefore, a significantly smaller step at 1 MHz.

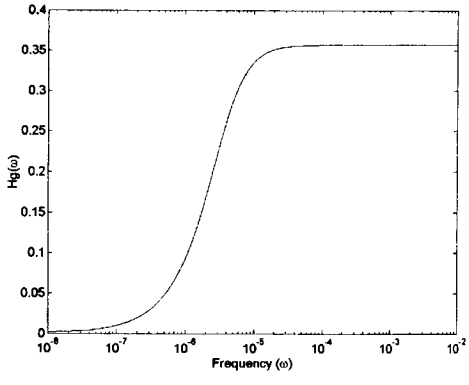

Figure 5.63 685-3 Low Frequency Response

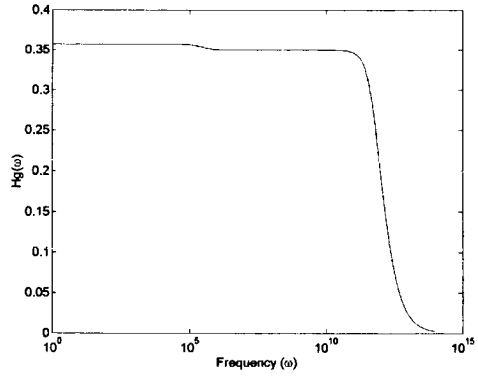

Figure 5.64 685-3 High Frequency Response

In considering the data for the CLDX/APC and the TP7 modulators, the largest difference is in the interface resistances and capacitances. All other variations are functions of the differences in the layer thickness between the 3 devices and the differences in core resistivity and dielectric constant. The core capacitances are not

significantly different while there is an almost order of magnitude difference in the core resistance. Varying the resistance values, however, did not show a significant change in the electrical response. So, the boundary interface characteristics are the most significant factor. Varying these parameters effect both the transient response and the frequency response knee. As adhesion of the layers improves, the layers have better bonding (lower resistance) and smaller separations (higher capacitance). Thus, the boundary electrical characteristics are strongly affected by adhesion. This is illustrated in Table 5.13 for the 3 modulators evaluated. These electrical differences are clearly seen in the optical response of the system. The optical response is not only a measure of the electro-optic coefficient, but also reflects the systems electrical response as can be seen from Equation (2.77). Thus, calculation of r_{33} from V_π measurements must consider the stack electrical response as well.

These experiments have verified the performance predicted by the theoretical developments. The poling time experiments show that 30 minutes is the optimal poling time at 145 C and 500 V. Both poling temperature and poling voltage show improvements with increasing temperature/voltage. These increases, however, are much smaller than the improvements realized through the poling time. Poling time then is the most influential in dipole alignments, but the time can be reduced by increasing temperature, voltage, or both. In all cases, electrostriction is induced as the poling charge increases, as can be seen most vividly by the increased optical losses with poling time. Thus, there is a tradeoff between improved dipole alignment and optical losses. Because electrostriction results in an increased chromophore density, dipoles can interfere with each other as the density increases resulting in a decrease in V_π. Statistical experimental analysis showed a need to replicate experiments 3 or 4 times to create enough degrees of

freedom to make the statistical analysis meaningful. This is not an invalidation of experimental results, but rather a mathematical limitation in the statistical analysis.

Experiments to verify the electrical transfer function were also successful, demonstrating the effects of the boundary capacitance and resistance in the low frequency response. These experiments also provide verification that capacitance effects must be considered even at near DC conditions.

Thus, this dissertation has successfully derived 3 layer waveguide stack electrical transfer function and poling mechanisms. These results enable future endeavors to characterize poling of various material systems and define optimal poling conditions and expected electrical performance of electro optic polymer modulators.

CHAPTER 6

Summary and Conclusions

Poling of nonlinear optical (NLO) polymers has evolved from early work on charge storage using electrets. This work concentrated primarily on single layer studies and quantum chemical studies of polymer dipole alignments in complex material systems. While these studies have provided a molecular level theoretical understanding of dipole orientations, they focused on molecular rather than macroscopic effects. Macroscopic studies have used poling and thermally stimulated discharge (TSD) current studies to evaluate charge buildup and dipole orientation in single layer films. For optical waveguide applications, these techniques required extension from single layer to three layer systems. This work has been performed for this dissertation providing the first poling charge and current density models for a 3 layer optical waveguide stack.

A theoretical poling model was initially developed to describe charge and current densities during poling and TSD for a 3 layer waveguide system following the approach used for single layer electrets. The development of this model revealed that the boundary charge density formed at the Maxwell-Wagner boundary between the core and cladding layers was significant. This large charge density is an indication of poling efficiency as dipole alignment produces a polarization current density. The boundary and polarization charge densities were shown to limits for infinite poling time. These limits are directly proportional to the poling voltage showing that the maximum charge density achievable is controlled by the poling voltage. The boundary charge was shown to contribute to dipole alignment and also shown to be responsible for electrostriction as the charge layer

builds during poling. Thus, there is an optimal charge density below which the dipoles are not fully aligned and above which electrostriction begins to significantly increase optical losses. These effects lead to a translation of the chromophore which compacts the chromophores increasing the chromophore density with in the host system. This leads then to interference in dipole alignment as chromophore misalignment with the poling field are induced and the poling efficiency decreases.

A theoretical model of the 3 layer waveguide electrical transfer function was also developed to accurately determine the core voltage responsible for dipole alignment. This model showed that the effects of the boundary charge density is significant and leads to a transient response in the core voltage and therefore the optical response. The boundary charge produces a large capacitance value at the interface and along with the resistance of the interface leads to a parallel Resistive Capacitive (RC) circuit at each interface boundary in series with the bulk layer RC circuits. Being a series connection of RC circuits, the high pass frequency was shown to be limited only by the contact resistance of the electrodes. The low pass response for this circuit was extremely interesting. This showed that the capacitance of the circuit is significant down to 10-6 Hz. Thus, the circuit does not relax to a pure DC response unless the voltage is stable for 1000 hours! The core voltage is much more sensitive to capacitance values than resistance values. Thus, layer and boundary capacitance are significant quantities even at low frequency operation indicating dielectric constant values play a more significant role in the magnitude of the core voltage than resistance values.

Poling of 3 layer optical waveguide systems were investigated by poling Mach-Zehnder modulators. Exploratory experiments were conducted to investigate various poling parameters and verify the theoretical predictions.

The experiments focused on poling time, temperature, and voltage. The experimental data matched the modeled data extremely well. The poling current was measured for each experiment and compared to modeled data. The curves matched extremely well with errors attributed to temperature drift and time conversion accuracies with the experimental data. As suggested by the theory, poling time were shown to be significant parameters in poling efficiency. Increasing poling times allows a continuous charge density build-up within the waveguide stack that improves the dipole alignments. Poling times greater than 30 minutes showed significantly increased optical losses and reduced V_π as predicted by theory for electrostriction effects. Poling voltage also showed increase charge densities with increasing voltage as predicted by theory. Poling temperature was limited to 160 °C by the maximum temperature of the chromophore. Both poling voltage and poling temperature increases had much smaller effects on polarization charge density build-up. Poling at 155 °C or 1000 V produce charge densities similar to poling for 10 minutes. Thus, poling time may be used to offset reduced poling temperature (due to chromophore stability limitations) or reduced poling voltage (to eliminate arcing damage to electrodes and polymer layers which occur at higher voltages). If poling time is desired to be optimized, the data indicate a poling voltage of 1000 V and poling temperature of 155 °C would minimize optimal poling time to 10 minutes. This is compared to 30 minutes at 500 V and 145 °C. Increasing poling voltage also appears to increase the dipole relaxation frequency. Further chemical studies of poled polymer relaxation frequencies are required to verify this.

The electrical response of the modulators was also investigated in the experiments. Experiments were conducted with a square wave and saw tooth modulation wave form. Matching the model to the experiment data showed that the electrical transfer

function theoretical model accurately predicted the transient and modulation response. This effort also showed that the measured value of r_{33} which is dependent on the actual value of the core voltage was sensitive to the boundary interface capacitance and resistance. Thus, accounting for these values is crucial to calculating an accurate value for r_{33}. The experiments showed that as the boundary resistance and capacitance decreased, the transient response of the modulator was attenuated. No transient response was seen for a boundary resistance $\pm$ 1 KΩ (good interface contact) or a boundary capacitance > 10 nF (small layer separation).

This work has significantly contributed to investigating and understanding various effects in poled waveguide devices. The poling theory and electrical transfer function developments provide key insight into device electrical and optical behavior. These theories can be applied to future studies in device thermal stability, a key factor in practical device applications. These theories also provide a basis from which to determine the manner in which space radiation may effect device operation and can be applied to explanations of radiation test results. These also indicate the need for chemical studies to determine the separate values of μ, α, and β_{33}. New device applications may also be realized through the combination of electret charge storage and NLO effects. Radiation sensors can be envisioned which optically detect the change in electret charge layers. By providing an understanding of the charge densities and their role in the NLO activity and electrical response this work has moved the field of electro-optic polymer devices forward significantly, provided the basis for understanding many experimentally observed phenomena, and opened the door for future application developments.

APPENDICES

APPENDIX A

MATERIAL SYSTEMS REVIEW

In this Appendix, material systems reported in the literature is surveyed. Section A.1 discusses results for Guest Host Systems reported in the literature. Section A.2 discusses results for Attached Systems (both side chain polymers (A.2.1) and main chain polymers (A.2.2))

Various material systems have been investigated over the years. There are 3 main systems: guest/host polymers, side chain polymers, and main chain polymers. Guest/host systems are a mixture of NLO chromophore molecules in a polymer host material. Side chain polymers have the NLO chromophore attached to the main polymer backbone as a side chain. Main chain polymers have the NLO chromophore directly attached as part of the main polymer backbone. Side chain and main chain polymers can be grouped together as attached materials.

A.1 Guest Host Systems

Guest Host polymers systems involve a guest chromophore mixed with a polymer host matrix. The chromophores are not attached to the polymer chains, only dispersed within the polymer matrix. There are various chromophores and host matrices that have been investigated for their nonlinear optical properties. The following paragraphs address these chromophores and polymer hosts separately. Section A.1.3 then provides the overall NLO properties for these systems.

A.1.1 Chromophores

Chromophores are the primary source of NLO properties for a polymer material system. Various chromophores have been explored recently including Disperse Red dyes, DANS, FTC, and CLD.

A lot of early NLO polymer systems where investigated using Disperse Red (DR) optical dye. Several varieties of DR exist, designated by their number. DR1 has been extensively investigated and has a $\mu\beta$ product of 580 x 10^{-48} esu. [62]

In the quest to see improved r_{33} coefficients over those provided by the various dye compounds, a new set of chromophores were developed based on optimization of the $\mu\beta$ product. FTC and CLD are the recent results of these efforts. FTC (Furan derivative ring incorporated into a TriCyanobutadiene acceptor) was one of the first of these chromophores to be characterized and used to fabricate modulators. FTC has a $\mu\beta$ product of 15000 x 10^{-48} esu, significantly larger than DR1. [62]

A.1.2 Polymer Hosts

Various hosts have been reported in the literature. The most predominate are Poly methyl(methacrylate) (PMMA), Polycarbonate (PC), Polystyrene (PS), and Polyimide.

PMMA is a readily available material, but has a low T_g (120 C). PMMA shows no dipole effects on poling, but does show large build up of space charges. Studies show that space charge build-up in PMMA is strongly dependant on poling temperature, with T_p = 90 C showing the highest level of charge build up for samples poled from 40 C to 90 C. Poling voltage (corona) has a smaller, but still significant effect on charge build-up. In this case, samples poled at 15 kV showed a larger charge build up than those at 5kV or 2 kV. Poling times also show increases in space charge as the poling time is increased.

Dipole effects are seen in the charge distributions near the anode and cathode. However, these effects are believed to be caused by a surface charge layer countering the space charge in the bulk material. No molecular dipoles are said to be formed. [63] Polycarbonate (PC) is a polarizable host with a high T_g (205 C). Studies have shown that PC has an r_{33} of 0.10 pm/V when poled under the conditions given in Table A.1. Thus, PC enhances the electro-optic response of the chromophore in the guest/host system. [64] Thermal stability of PC based systems has been shown to be very good. This is attributed to the high T_g and dipole characteristics of PC. Under a poling field, the Carbonyl groups will align to the field. This alignment process is slower than the chromophore alignment and thus requires longer poling. [39] Amorphous polycarbonate (APC) has been shown to be one of the best host materials evaluated to date.

Table A.1: Polycarbonate Poling Characteristics

Polymer System	T_g	Poling Voltage (V_p)	Poling Temp. (T_p)	Poling time (t_p)	r_{33}	λ
Polycarbonate	NR	8.5 V/μm	127 C	15 min	0.10 pm/V	.633 μm

Polystyrene is another readily available polymer, but, like PMMA, has a low T_g (100 C). Although some work has been done with PS, it is not suitable has a high temperature material.

Polyimides are a promising new host material that may rival APC. They have a fairly high T_g (220 C– 270 C) and show promise as a low optical loss host material.

A.1.3 System Properties

Guest/host systems involve the mixing of a guest chromophore in a host polymer matrix. As the %wt. of the guest increases, the spacing between host chains increases and

the material T_g decreases below that of the host material with no guest molecules. Thus, guest/host systems tend to have lower T_g and therefore thermal stability temperatures are lower. One study of bisphenal-A polycarbonate (BPA-PC) doped with 35% wt. DAN showed a reduction of T_g from 155 C to 85 C. Another polycarbonate based host, BPTMC-PC, showed a reduction of T_g from 239 C to 117 C for the same DAN doping level. [39]

Many studies of electro-optic and nonlinear optical effects have been done with PMMA doped with DR1. The absorption band of a system consisting of the DR1 chromophore dispersed in PMMA has been investigated. The system was corona poled at 10kV with a grid voltage of 800 V at a poling temperature of 90 C. Absorption band studies showed that relaxation of the dipoles occur at room temperature over a period of a few days. During poling, the host chains can interfere with the chromophore orientation resulting in a deformation of the π electron configuration. This can destroy the chromophore or lead to a relaxation of the dipole orientation as the chromophore seeks an equilibrium state. [65]

Various loadings of chromophore in PMMA have been investigated in different studies. PMMA doped with 12% DR1 have shown electro-optic characteristics at 1.55 μm. The material was corona poled in the triode configuration and cooled slowly (rate not reported). Results showed thermal stability only up to around 50 C. [66] Other studies of PMMA-DR1 have investigated chromophore loadings of 4% to 10%. These samples where poled with a constant current (I = 3 nA) corona in a triode configuration also. The material dielectric constant, ε, increased linearly with dye concentration and followed the shape of the undoped PMMA curves with increasing temperature. In

addition, the results showed dipole orientation (measured by the pyroelectric coefficient) improved with increased poling field and increased chromophore loading. Optimal poling conditions are given in Table A.2. [67]

Thermal stability has been measured in samples of PMMA-DR1. Loading was not specified but, the material system showed thermal stability up to 105 C for both corona poled and electron beam poled samples. [44]

Studies of PMMA and PC doped with 20% DANS chromophore have been made. The PC-DANS system has a much higher r_{33} due to the polarizability of the PC backbone. Note, that the PC-DANS was poled below the T_g due to increasing current flows with temperature. The electro-optic response may have been higher had the poling been performed closer to the T_g, but concerns for film breakdown due to high current flows limited the poling temperature. The PMMA-DANS electro-optic response may have also been reduced during fabrication. A bake out of 150 C is required to cure the film possibly damaging the chromophore. [64]

Table A.2: Guest/Host NLO Polymer Poling Characteristics

Polymer System	Host T_g	Poling Voltage (V_p)	Poling Temp. (T_p)	Poling time (t_p)	Cooling Rate	r_{33}	r_{13}	λ
PMMA-DR1	NR		90	NR	NR	NR	NR	NR
PMMA-DR1 (4%)	90 C	80 MV/m	80 C	30 min	NR	NR	NR	NR
PMMA-DR1 (6%)	90 C	80 MV/m	80 C	30 min	NR	NR	NR	NR
PMMA-DR1 (8%)	90 C	80 MV/m	80 C	30 min	NR	NR	NR	NR
PMMA-DR1 (12%)	80 C	NR	NR	NR	NR	.3 pm/V	NR	1.55 μm
PMMA-DANS (20%)	105 C	1.7 V/μm	100 C	15 min	NR	.17 pm/V	NR	.633 μm
PC-DANS (20%)	150 C	1.7 V/μm	110 C	15 min	NR	1.20 pm/V	NR	.633 μm
PMMA-CLD1	90 C	8 kV	95 C	30 min	NR	85 pm/V	NR	1.3 μm
APC-CLD1	145 C	8 kV	150 C	30 min	NR	92 pm/V	NR	1.3 μm

CLD1 was initially studied with a PMMA host. By corona poling a 30% wt system at 95 C, an r_{33} of 85 pm/V was obtained. This represents a significant improvement over previous material systems, but the thermal stability was good only to 75 C. To address the low thermal stability temperature limit, amorphous polycarbonate (APC) was used as a host material. CLD1/APC in a 25% wt mixture was corona poled at 8 kV for 30 minutes at a temperature of 150 C. An r_{33} of 92 pm/V was measured with a thermal stability temperature limit of 115 C. Clearly, APC proved to be a better host material providing better thermal stability with a slight improvement of the NLO properties. No T_g could be measured indicating the chromophore/host mixture is highly amorphous. TM mode Optical losses in planar samples were measured at both 1.3 μm and 1.55 μm. These measurements yielded losses of 1.0 dB/cm and 1.2 dB/cm,

respectively, in unpoled films. After poling, an index of refraction change was noted. n_{TM} changed from 1.625 to 1.655 while n_{TE} decreased from 1.637 to 1.626. This indicates a shift of chromophore alignment from in plane to perpendicular to the plane of propagation. Thus, the index increases as better alignment of the chromophores is achieved and decreases as dipoles become less aligned. [9] More recent reports have also measured pre and post poling index changes in CLD1/APC. Pre poling index numbers were 1.60 (TM) and 1.62 (TE). After poling these values changed to 1.625 (TM) and 1.595 (TE). [68]

Thermal stability studies have been conducted at 60 °C for 65 days. These results show a 25% decrease in r_{33} (based on modulator V_π measurements at 1.55 μm) over a 20 day period followed by stable values for the remaining 45 days. [9] Subsequent studies conducted over 40 days compared modulator systems held at 60 °C and at room temperature in air. Again, a decrease in r_{33} of 25% (increase in V_π) was noted for the device at 60 °C, but no change was noted for the device at room temperature. Measurements were made at 1.55 μm. [5]

Oxygen has been shown to cause serious NLO degradation for CLD samples. Photostability studies using a 10 mW laser diode in the TM mode at 1.55 μm showed a 67% decrease in r_{33} over a 24 hour period. However, r_{13} did not decrease in a similar fashion. Thus, bleaching of the chromophore aligned in the r_{33} (i.e. TM mode) direction is attributed to the decrease. Performing a similar test in an Ar atmosphere showed no degradation in r_{33}. Thus, the results seen in air show that photoinduced oxidation of the chromophore is responsible for the bleaching. [9] Subsequent studies of the effect showed that the core is significantly bleached at the input facet causing a lowering of the

index of refraction and a loss of TM mode confinement. The TE mode was much less affected. The bleaching is believed to be a photochemical reaction where a single oxygen atom attacks the carbon double bonds or the nitrogen bonds in the chromophore. Two-photon absorption may also cause degradation through 1.5 μm light exciting the 0.7 μm absorption peak. Oxygen induced loss effects have also been noted in both corona and electrode poling. Electrode poling at 600 V in air resulted in optical loss increases of 2 – 3.5 dB/cm versus no loss increases when poled in a nitrogen environment. Similarly, samples heated to poling temperatures, but without a poling field, showed no optical loss increases. Thus, these losses where determined to be due to the presence of oxygen at high temperatures and high currents during poling. [5]

Optimal electrode poling procedures have been developed for the CLD1/APC system. Poling is performed in a nitrogen environment due to oxygen sensitivity. In addition, a nitrogen purge is performed at 120 C for 30 minutes to remove dissolved oxygen trapped in the core at room temperature. Poling is then performed at 145 C for 30 minutes with a field of 400 V applied across the electrodes. The poling field is applied at the end of the purge cycle and left on until the sample is cooled back to room temperature. An r_{33} = 43 pm/V has been measured using this poling method. [5]

A.2 Attached Systems

Attached polymers systems include both side chain and main chain attached chromophores. In side chain polymers, the chromophores are attached to the polymer main chain or backbone. The chromophore is then oriented by the poling field, though the motion is somewhat limited by the attachment site. Side chain polymers provide better long term stability as the backbone limits the motion of the chromophore and thus

limits the ability of the chromophore to re-orient or relax. In main chain polymers, the chromophore is incorporated directly into the polymer backbone. The entire backbone must then be oriented in poling to produce a noncentrosymmetric structure. Main chain polymers provide the best long-term stability as the chromophore cannot re-orient or relax freely. Most of the attached polymer systems investigated for their nonlinear optical properties have been side chain polymers. The following paragraphs address side chain and main chain polymer systems separately.

A.2.1 Side Chain Polymers

A side chain system consisting of DR 13 attached to a methyl methacrylate forming (MMA)-DR13. Table A.3 gives the characteristics of the poled system. The system was corona poled at constant current using a needle configuration (see Figure 3.1). Three levels of chromophore loading were used: 4%, 9%, and 43%. Poling studies indicated 120 C as the optimum poling temperature and 30 minutes as the optimum poling time. Poling above 120 C led to reduced values of the electro-optic coefficients. Extremely long poling times led to degradation from corona induce chemical breakdown. Optimum poling voltage was 100MV/m or 1MV/cm. Optimum poling conditions were determined by measuring r_{13} as each parameter (V_p, T_p, t_p) was varied individually. Cooling rate was best at 0.2 C/min. Faster rates showed quick degradation in r_{13}. Thus, slow cooling rates led to better thermal stability. Increased space between the polymer backbones correspond to faster relaxation times. Thus, low chromophore content, which allows a tighter spacing of backbone segments, produced the most stable material system. However, there is also some indication that thermal history of the sample plays an important role in thermal stability. Samples cooled quickly do not have sufficient orientation time to allow the backbones to achieve the optimal packing density. Thus, in

samples that were cooled quickly during fabrication and prior to poling, thermal stability numbers were always lower. So, thermal history of the samples is an area noted for additional investigation of poling effectiveness. [69]

Table A.3: Side-Chain NLO Polymer Poling Characteristics

Polymer System	T_g	Poling Voltage (V_p)	Poling Temp. (T_p)	Poling time (t_p)	Cooling Rate	r_{33}	r_{13}	λ
(MMA)-DR13 (4%)	117 C	100 MV/m	120 C	30 min		6 pm/V*	2 pm/V	.633 μm
(MMA)-DR13 (9%)	117 C	100 MV/m	120 C	30 min		9 pm/V*	3 pm/V	.633 μm
(MMA)-DR13 (43%)	117 C	100 MV/m	120 C	30 min		27 pm/V*	9 pm/V	.633 μm
PMMA-azoviolet	120 C		100 C	5 min		NR	NR	.3 - .7 μm
PC-azoviolet	145 C		155 C	5 min		NR	NR	.3 - .7 μm
PS-azoviolet	100 C		120 C	5 min		NR	NR	.3 - .7 μm
PMMA-MMA amino nitro azobenzene	150 C	NR	150	NR	NR	14 pm/V	NR	1.3 μm
Polyimide – DR	205 C	NR	220C-250C	NR	NR	11 pm/V	NR	1.3 μm
Sol-Gel amino-sulfone	NR	NR	NR	NR	NR	Small	NR	1.3 μm
PMDA-DR19	110 C	NR	140 C	120 min	NR	NR	NR	NR
POA-DR1	165 C	NR	NR	NR	NR	NR	NR	NR

* Calculated as $r_{33} = 3r_{13}$
NR = Not Reported

Side chain polymers have been investigated by attaching an azoviolet dye to 3 different backbone materials: PMMA, Polycarbonate, and Polystyrene. Each material system was needle corona poled at -12 kV, but without the voltage control grid. The

samples were poled for 5 minutes near the T_g and then cooled to room temperature in 10 minutes. Absorption studies showed a slight relaxation of each system at room temperature over 6 hours. Partial recovery of the absorption value was obtained by depoling the PMMA-azodye sample. However, the PC-azodye and PS-azodye showed a further drop in absorption. This was caused by destruction of the dye chromophore while poling above the T_g. [70]

Thermal stability of various side chain polymers have been reported. PMMA-DR1 was thermally stable to 120 C for a corona poled sample. This is an improvement over the guest/host PMMA-DR1 system that was stable to 105 C. This illustrates the improved thermal stability of side chain systems over guest/host systems. [44]

Work has also been done with different attachment mechanisms in side-chain polymers. An amino nitro azobenzene chromophore has been attached to a PMMA-MMA polymer. The chromophore was crosslinked for added stability and showed a 30 C improvement in thermal stability due to crosslinking. This system has a high T_g, an estimated r_{33} of 14 pm/V (d_{33} = 110 pm/V at 1.06 μm) and showed good thermal stability to approximately 130 C. The r_{33} estimate was obtained by extrapolating the d_{33} coefficient measured at 1.06 μm. A Disperse Red (DR) chromophore was also attached to a polyimide. This system has a high T_g, an estimated r_{33} of 11 pm/V (d_{33} = 112 pm/V at 1.06 μm) and showed good thermal stability to 190 C. Finally, a sol-gel was investigated with an amino-sulfone dye attached. This system had poor nonlinearity (r_{33} not estimated, d_{33} = 10 – 13 pm/V at 1.06 μm) and the thermal stability trailed off slowly starting near 130 C. This system had 9 crosslinking sites to hold the chromophores tightly. [71]

Poling dynamics of two different aromatic polyimide films have been investigated with Disperse Red chromophores attached: poly(pyromelliticdianhydride) – DR 19 (PMDA-DR19) and poly(pyromelliticdianhydride)-4,4'-diaminodiphenyl ether – DR1 (POA-DR1). These studies measured the second harmonic generation signal during the poling process. For PMDA-DR19 the SHG increased sporadically during corona poling due to randomly oriented potential wells in the polymer films. After poling for > 30 minutes, the sample SHG response became consistent and leveled off to a constant value as the sample was cooled below the T_g. Theoretical curves matching the free-rotor model of the polymer backbone to the experimental data showed good correlation for long poling durations (120 minutes) and less correlation for poling at 30 minutes. SHG response was also higher for longer poling durations indicating better orientation of the chromophore dipoles. In addition, IR absorption measurements indicated that chemical reactions with functional groups on the polymer chains occur and these reactions reduce the spacing of the backbones. Thus, long poling durations create a more thermally stable molecule as reactions reduce the backbone spacing and the chromophore orientations have less opportunity to re-orient after cool down. [72]

An MO3ONS (oxynitrostibene attached to poly-acrylate) was also studied. The electro-optic coefficient is similar to that of PC-DANS (20%) when the results are scaled by the size of the poling fields. Another side-chain polymer (poly 4-vinylpyridine, [P-4VP]) was also studied. MO3ONS showed long term thermal stability (1000 days) after a settling period of 10 days where r_{33} dropped to 70% of the original value at room temperature. P-4VP showed a smaller r_{33} and continued degradation over time. [64]

The FTC chromophore has been attached to a polyurethane (PU-FTC) to produce an intensity modulator. Modulator structures were needle corona poled at 8 kV before

application of the top electrodes. A pre-curing was added to allow partial crosslinking of the material so that the material can with stand the surface potential applied during poling. If pre-curing was allowed to proceed to long, then the crosslinking prevents efficient chromophore orientation to the electric field. In addition, polymerization and poling orientation were found to be effective by maximum poling temperature. If the poling temperature was too high, then polymerization occurred faster than the chromophore orientation. Optimal poling conditions then were found to be pre-cure 3 minutes at 120 C followed by poling for 60 minutes at 100 C. Optical losses of 2 dB/cm were measured at 1.3 μm. This produced an r_{33} of 40 pm/V at 1.06 μm that corresponds to 25 pm/V at 1.3 μm. [62]

A.2.2 Main Chain Polymers

Polyurea (PU) polymers have been prepared separately with the monomer 4,4'-Diamino Diphenyl methane (DDM) or the monomer p-Diamino nitro benzene (DNB). The monomers (DDM or DNB) serve as the chromophore segment in the PU backbone. Planar films of PU(DDM) and PU(DNB) were prepared by vapor deposition polymerization and then corona poled without a control grid. The control grid was omitted to avoid interference with the SHG measurements during poling. Films were also prepared by Electric filed VDP, but the results where poor. Table A.4 shows the poling parameters for each film fabricated by VDP and then corona poled. In these films, polymerization continued during the poling process. Thus, a thermally stable configuration was polymerized during the poling process. When films where heat treated prior to poling, poor poling results were noted. This was attributed to the polymerization being completed before poling, locking in the random orientation of the polymer chains. For PU(DNB), the poling field was determined to interfere with polymerization, reducing

the reactivity of some groups that in turn limits the poling effectiveness. Note, that the index of refraction of these films was not measured, so a calculation of r_{33} using Equation (3.22) is not possible. [73]

Table A.4: Main Chain Polymer Poling Characteristics

Polymer System	T_g	Poling Voltage (V_p)	Poling Temp. (T_p)	Poling time (t_p)	Cooling Rate	d_{33}	λ
PU(DDM)		+ 4 kV	200 C	No Dwell	NR	5 pm/V	1.064 μm
PU(DNB)		+ 4.4 kV	200 C	No Dwell	NR	15 pm/V	1.064 μm

Although main chain polymers provide mechanisms to enhance thermal stability, these same mechanisms may also hinder chromophore alignment in the poling electric field. A lot of polymer engineering is still required to identify promising candidate main chain materials. Therefore, only guest/host and side chain systems will be considered in the dissertation work.

A.3 Reported Modulators Results

Mach Zehnder modulators have been demonstrated in a variety of different material systems. Table A.5 lists the reported performance achieved for these systems.

A MZ modulator was produced in a side chain PU-FTC core material using the corona poling process discussed in Section A.2.1. The lower cladding was Epoxylite 9653 (n = 1.54 at 1.3 μm) and the upper cladding was NOA73 (n = 1.54 at 1.3 μm). The waveguide was 6 μm wide and 1.5 μm thick. The core was etched back 0.3 μm in the field to produce a rib guide as illustrated in Figure 2.4. The lower cladding was 3.0 μm and the upper cladding 3.5 μm thick, giving a total stack height of 8.0 μm. The

modulator electrodes were 2.0 cm long. A Vπ of 4.5 V was measured corresponding to r_{33} = 25 pm/V at 1.3 μm. The optical loss was measured to be 2.5 dB/cm at this same wavelength. [62]

A CLD1/PMMA (30% wt.) modulator was produced the results listed in Table A.5. An electrode length of 2.5 cm was used and the modulator was operated in the push-pull configuration. [74] PMMA, however, was abandoned as a host due to low thermal stability and modulators were subsequently fabricated from CLD1/APC.

CLD1/APC (25% wt.) modulators were produced by corona poling and results for both 1.3 μm and 1.55 μm are indicated in Table A.5. The rib waveguides were formed by O_2 RIE. The modulator electrodes were 2 cm long. The total stack thickness was 9.0 μm, though the thickness of the upper and lower cladding layers was not reported. By taking into account the optical loss data for the cladding, the optical loss due only to the CLD1/APC core was extrapolated to be 1.4 dB/cm at 1.3 mm and 1.3 dB/cm at 1.55 μm. Table A.5 reflects the actual measured optical loss of the modulator stack that is of more practical concern when comparing the modulator performance of various material systems. [9]

CLD1/APC (25% wt.) modulators have also been produced by electrode poling. The rib waveguides were formed by O_2 RIE. The waveguides were 6 μm wide. Optical loss measurements were made for both 3 μm and 5 μm thick waveguides using the cut-back method at 1.55 μm. The 3 μm waveguides has losses of 1.7 dB/cm while the 5 μm waveguides has losses of 1.2 dB/cm indicating better mode matching with the input fiber. The V_π numbers reported in Table A.5 have been converted to non push-pull values. The

numbers reported were actually 1.4 V at 1.3 μm and 2.1 V at 1.55 μm for push-pull modulation (induced by push-pull poling). [5]

Table A.5: Reported Modulator Experimental Results

Layer	Material	Planar Thickness	Waveguide Thickness	V_p	T_p	t_p	Optical Loss	V_π	λ
LC	Epoxylite 9653	3.3 μm	3.0 μm	8kV	100 C	60 min	2.5 dB/cm	4.5V	
Corona Poled Core	PU-FTC	1.2 μm	1.5 μm						
UC	NOA73	3.5 μm							
LC				8kV	95 C	30 min	0.8 dB/cm	0.8V	1.3 μm
Corona Poled Core	CLD1/PMMA								
UC									
LC	UV15	NR		8kV	150 C	30 min	1.7 dB/cm	2.4V	1.3 μm
Corona Poled Core	CLD1/APC	1.8 μm	2.4 μm						
UC	UFC-170	NR							
LC	UV15	NR		8kV	150 C	30 min	1.7 dB/cm	3.7V	1.55 μm
Corona Poled Core	CLD1/APC	1.8 μm	2.4 μm						
UC	UFC-170	NR							
LC	UV15	3.0 μm	2.5 μm	400 V	145 C	30 min	NR	2.8V	
Electrode Poled Core	CLD1/APC	2.5 μm	3.0 μm						1.3 μm
UC	UFC-170	2.5 μm	2.5 μm						
LC	UV15	3.0 μm	2.5 μm	400 V	145 C	30 min	1.7 dB/cm	4.2V	
Electrode Poled Core	CLD1/APC	2.5 μm	3.0 μm						1.55 μm
UC	UFC-170	2.5 μm	2.5 μm						
LC	UV15	2.5 μm	2.5 μm	500 V	150 C	30 min	1.3 dB/cm	3.5V	
Poling Induced Core	CLD1/APC	3.0 μm	3.0 μm						1.55 μm
UC	UFC-170	2.5 μm	2.5 μm						
LC	UV15	2.5 μm	2.5 μm	500 V	150 C	30 min	NR	5.4V	
Photo Bleached Core	CLD1/APC	3.0 μm	3.0 μm						1.3 μm
UC	UFC-170	2.5 μm	2.5 μm						
LC	UV15	2.5 μm	2.5 μm	400 V	145 C	30 min	NR	7.5V	
Photo Bleached Core	CLD1/APC	3.0 μm	3.0 μm						1.55 μm
UC	UFC-170	2.5 μm	2.5 μm						

Modulator waveguides have also been fabricated by poling. This process is similar to photobleaching, but the waveguide channels are defined by the poling field creating a change in index as compared to the unpoled field. 7 mm wide channels were fabricated producing the results in Table A.5. Note the increase in poling voltage and temperature over earlier efforts. The modulating electrodes were 3 cm long. [68]

Photobleached modulators in CLD1/APC have also been measured. These devices give a V_π of 7.5 V at 1.55 μm and 5.4 V at 1.3 μm. [75]

APPENDIX B

Modulator Data

This Appendix provides additional data plots covered by the discussions in Chapter 5. Plots are provided for the theoretical poling calculations in B.1 and the modeled and measured plots for poling experiments in B.2.

B.1 Wafer Theoretical Data Plots

These plots are the theoretical poling and TSD plots supporting the discussion in Section 5.2 The polarization charge density plots show the boundary charge density as a solid line and the polarization charge density as a dashed line. The poling current density plots show the total current density as a solid line, the boundary charge current density as a dotted line, the polarization charge density as a dashed line, and the conduction current density as a dot-dash line. The TSD charge density plots show the boundary charge density as a solid line and the polarization charge density as a dashed line. The TSD current density plots show the total current density as a solid line, the boundary charge current density as a dotted line, and the polarization charge density as a dashed line.

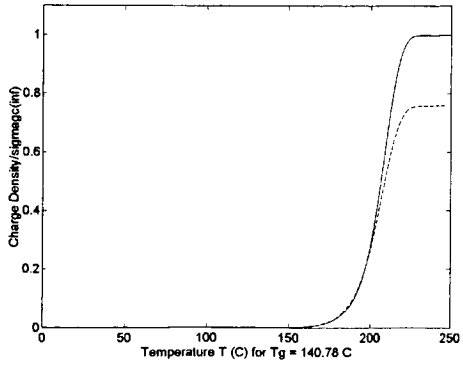

Figure A.1 Wafer 761 Theoretical Poling Charge Densities

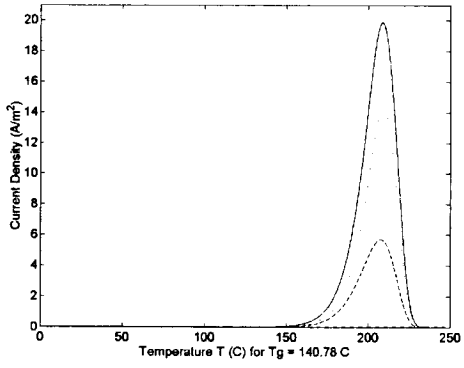

Figure A.2 Wafer 761 Theoretical Poling Current Densities

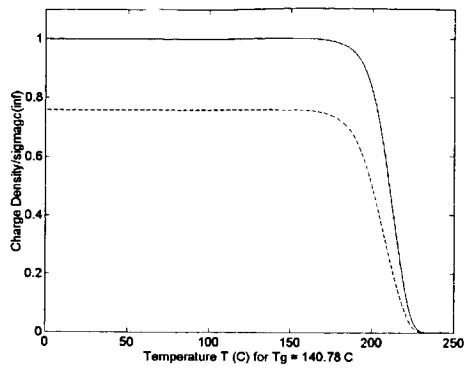

Figure A.3 Wafer 761 Theoretical TSD Charge Densities

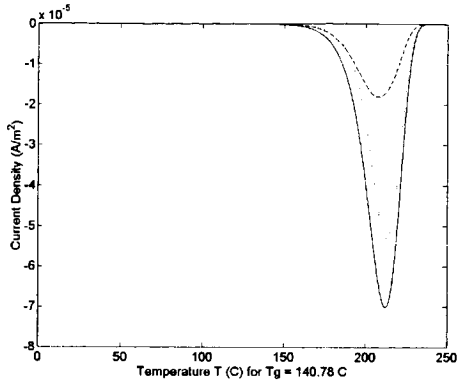

Figure A.4 Wafer 761 Theoretical TSD Current Densities

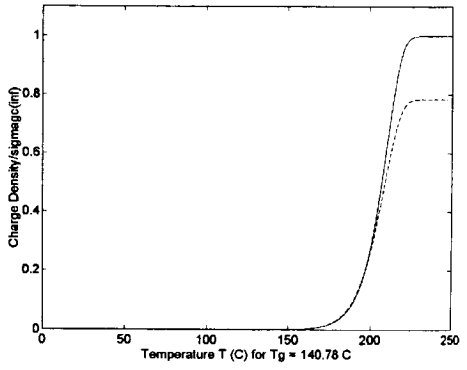

Figure A.5 Wafer 775 Theoretical Poling Charge Densities

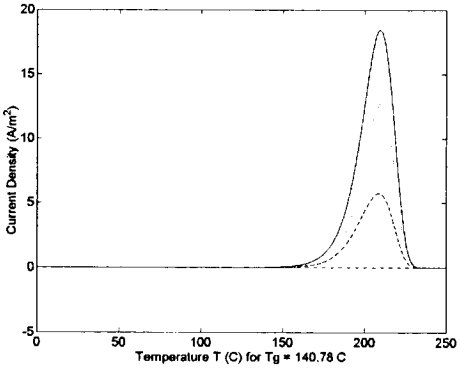

Figure A.6 Wafer 775 Theoretical Poling Current Densities

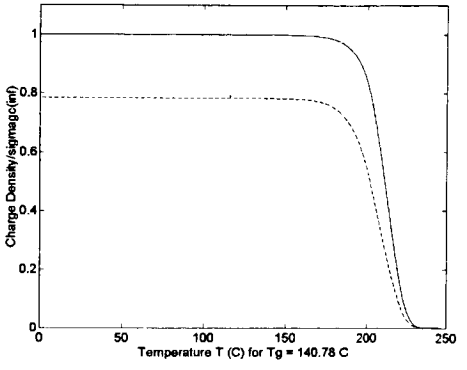

Figure A.7 Wafer 775 Theoretical TSD Charge Densities

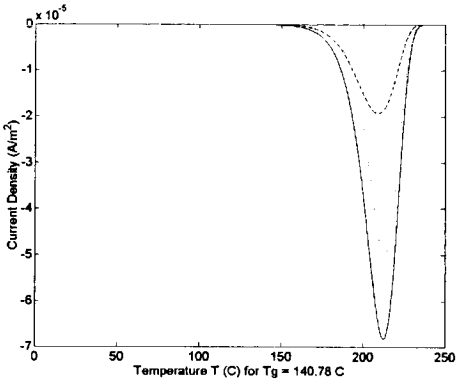

Figure A.8 Wafer 775 Theoretical TSD Current Densities

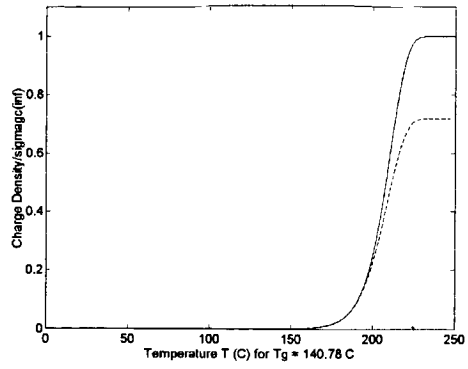

Figure A.9 Wafer 782 Theoretical Poling Charge Densities

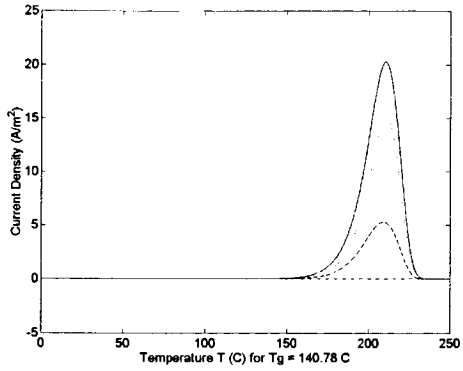

Figure A.10 Wafer 782 Theoretical Poling Current Densities

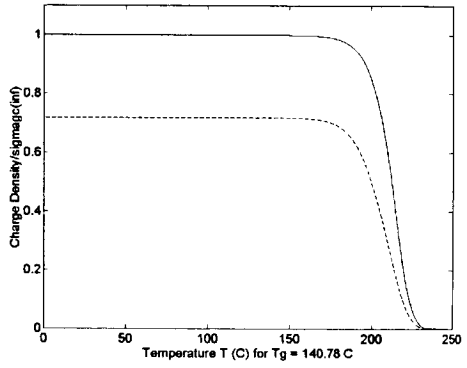

Figure A.11 Wafer 782 Theoretical TSD Charge Densities

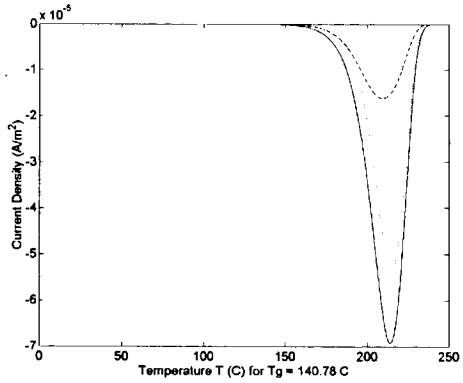

Figure A.12 Wafer 782 Theoretical TSD Current Densities

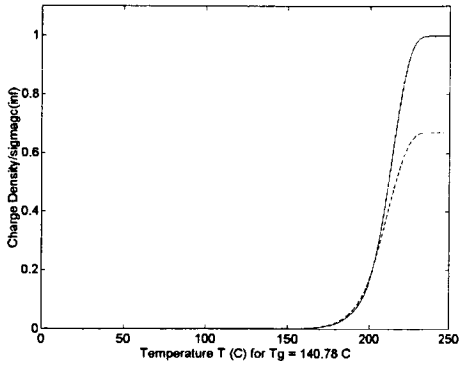

Figure A.13 Wafer 783 Theoretical Poling Charge Densities

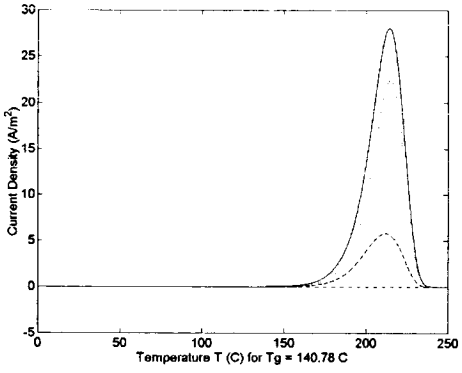

Figure A.14 Wafer 783 Theoretical Poling Current Densities

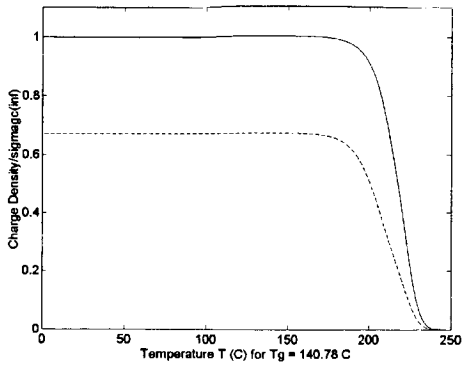

Figure A.15 Wafer 783 Theoretical TSD Charge Densities

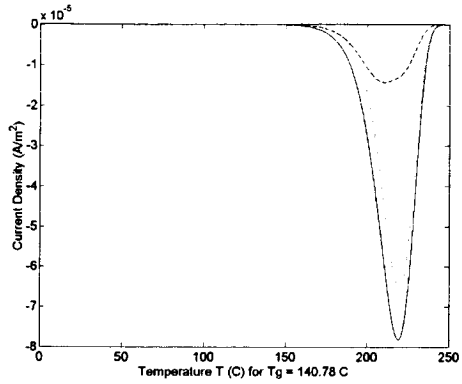

Figure A.16 Wafer 782 Theoretical TSD Current Densities

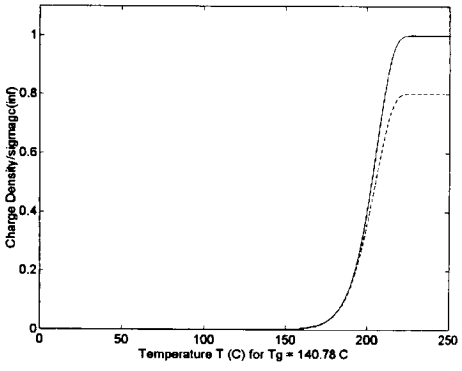

Figure A.17 Wafer 790 Theoretical Poling Charge Densities

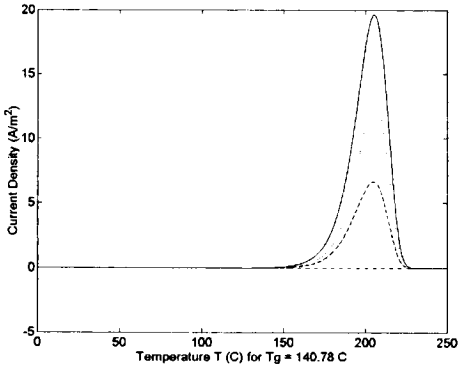

Figure A.18 Wafer 790 Theoretical Poling Current Densities

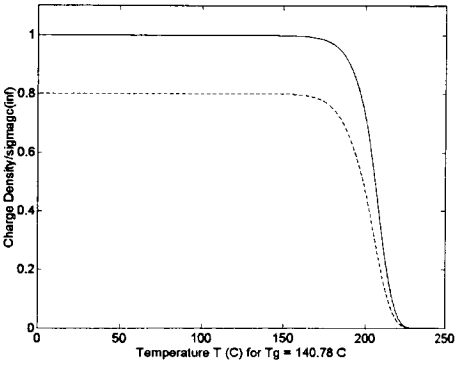

Figure A.19 Wafer 790 Theoretical TSD Charge Densities

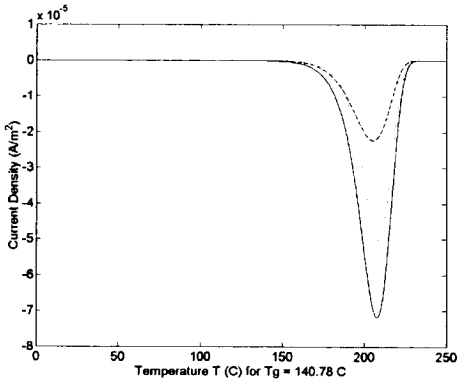

Figure A.20 Wafer 790 Theoretical TSD Current Densities

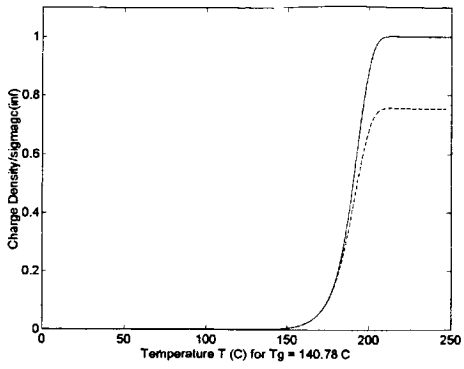

Figure A.21 Wafer 812 Theoretical Poling Charge Densities

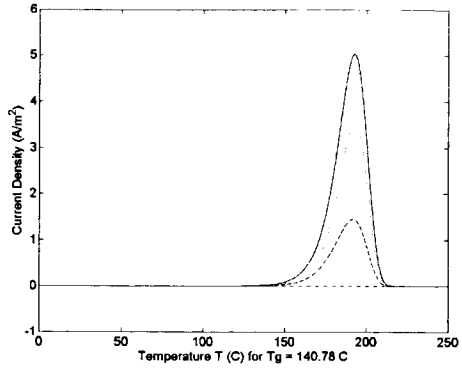

Figure A.22 Wafer 812 Theoretical Poling Charge Densities

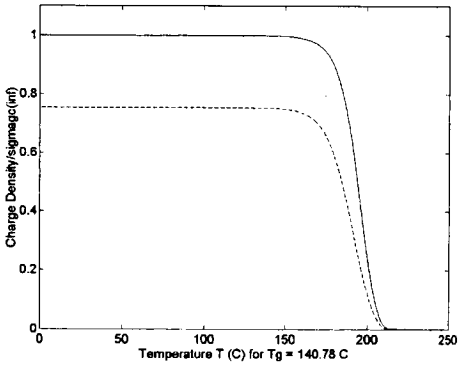

Figure A.23 Wafer 812 Theoretical TSD Charge Densities

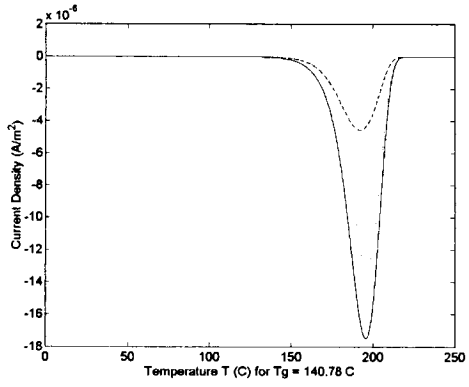

Figure A.24 Wafer 812 Theoretical TSD Current Densities

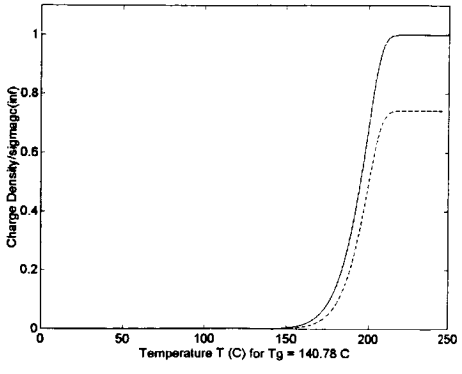

Figure A.25 Wafer 929 Theoretical 500 V Poling Charge Densities

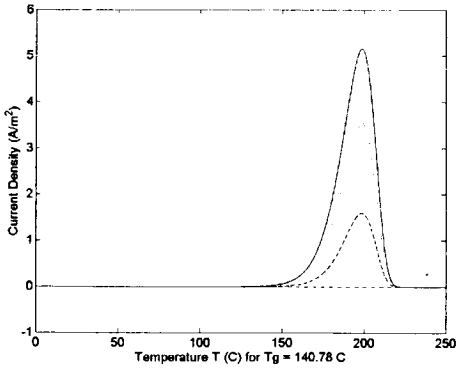

Figure A.26 Wafer 929 Theoretical 500 V Poling Current Densities

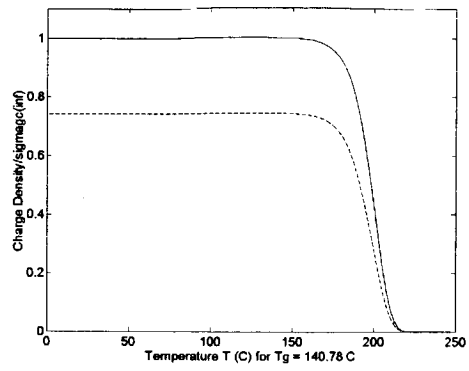

Figure A.27 Wafer 929 Theoretical 500 V TSD Charge Densities

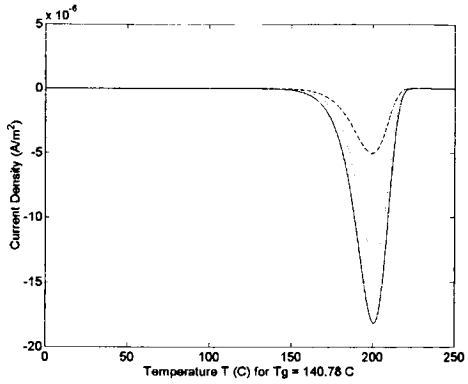

Figure A.28 Wafer 929 Theoretical 500 V TSD Current Densities

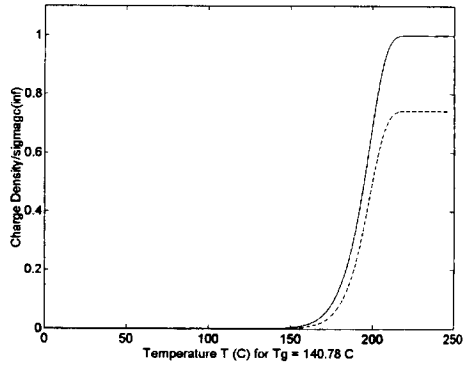

Figure A.29 Wafer 929 Theoretical 750 V Poling Charge Densities

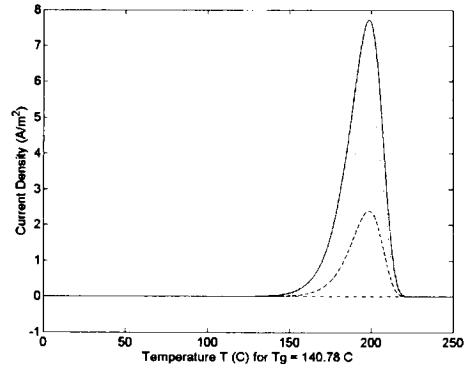

Figure A.30 Wafer 929 Theoretical 750 V Poling Current Densities

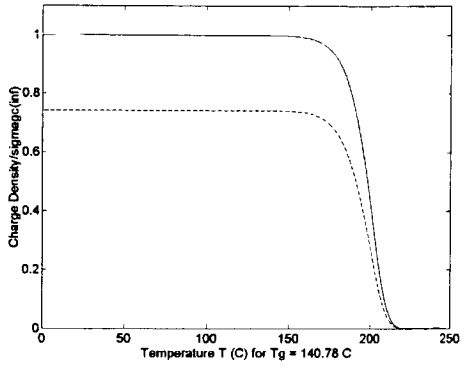

Figure A.31 Wafer 929 Theoretical 750 V TSD Charge Densities

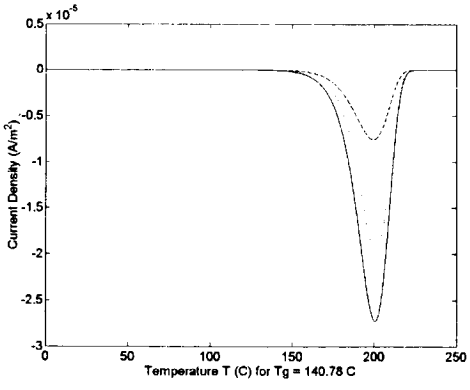

Figure A.32 Wafer 929 Theoretical 750 V TSD Current Densities

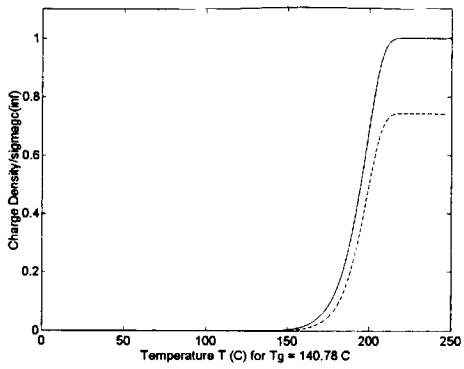

Figure A.33 Wafer 929 Theoretical 1000 V Poling Charge Densities

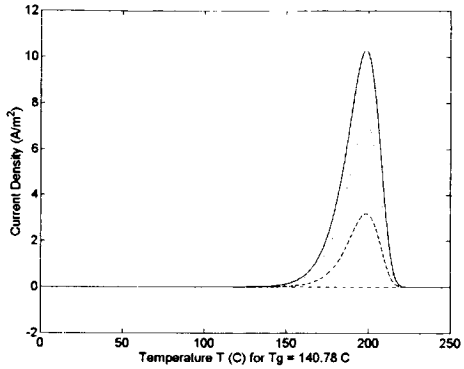

Figure A.34 Wafer 929 Theoretical 1000 V Poling Current Densities

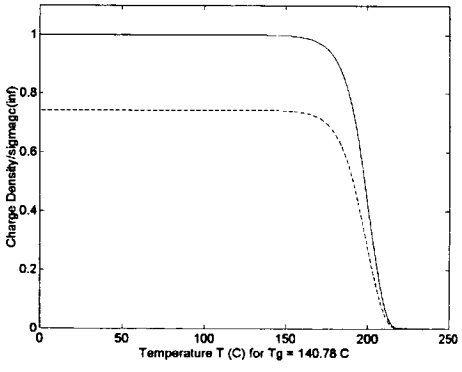

Figure A.35 Wafer 929 Theoretical 1000 V TSD Charge Densities

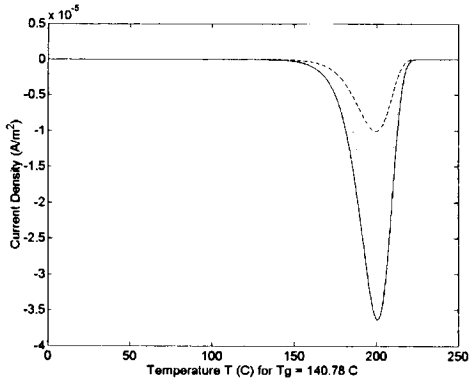

Figure A.36 Wafer 929 Theoretical 1000 V TSD Current Densities

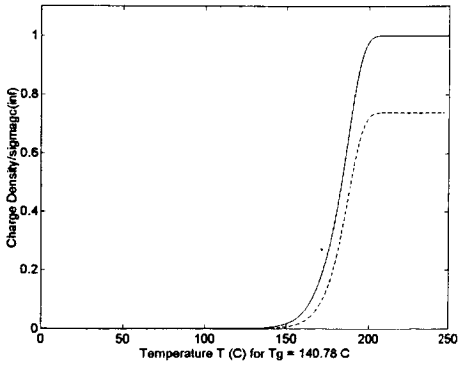

Figure A.37 Wafer 932 Theoretical 500 V Poling Charge Densities

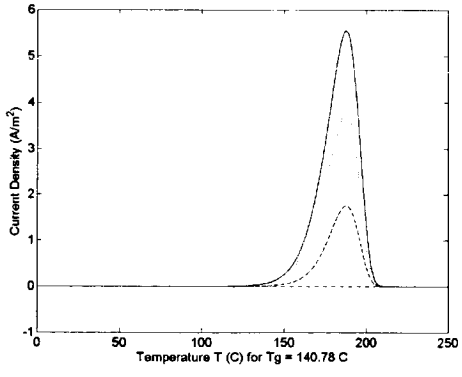

Figure A.38 Wafer 932 Theoretical 500 V Poling Current Densities

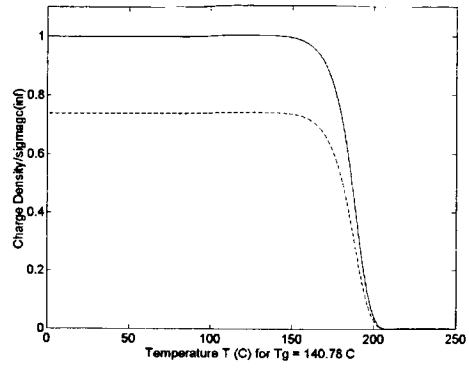

Figure A.39 Wafer 932 Theoretical 500 V TSD Charge Densities

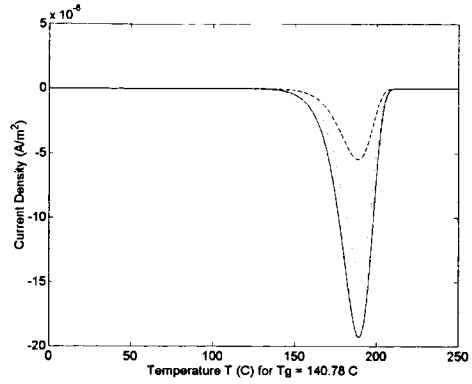

Figure A.40 Wafer 932 Theoretical 500 V TSD Current Densities

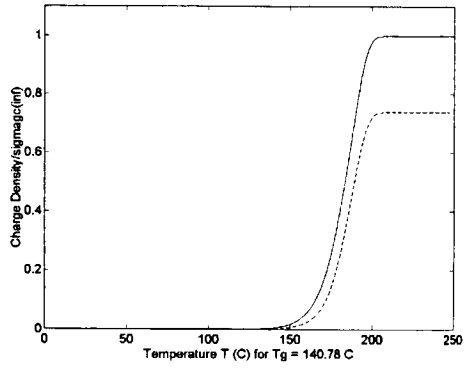

Figure A.41 Wafer 932 Theoretical 750 V Poling Charge Densities

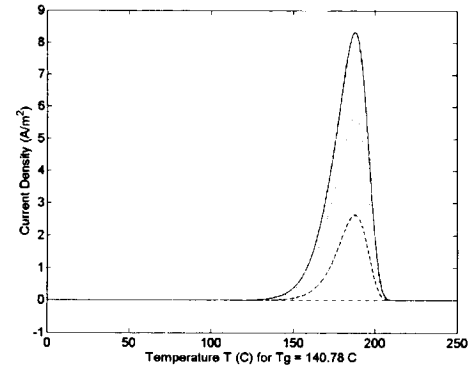

Figure A.42 Wafer 932 Theoretical 750 V Poling Current Densities

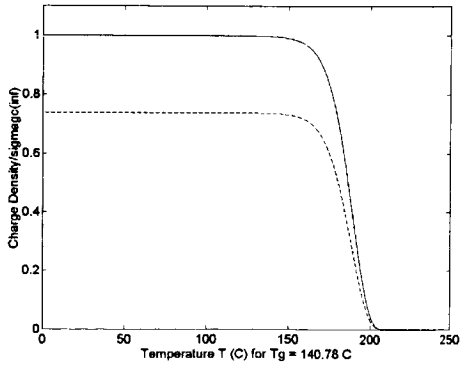

Figure A.43 Wafer 932 Theoretical 750 V TSD Charge Densities

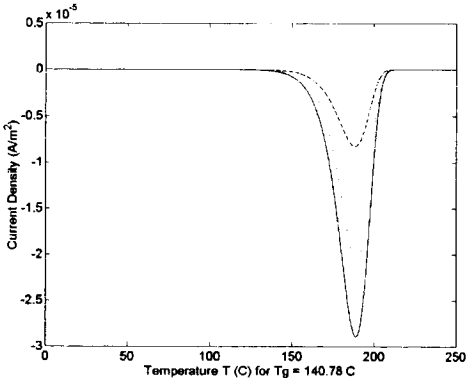

Figure A.44 Wafer 932 Theoretical 750 V TSD Current Densities

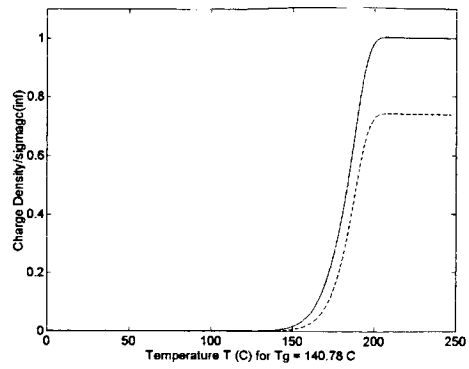

Figure A.45 Wafer 932 Theoretical 1000 V Poling Charge Densities

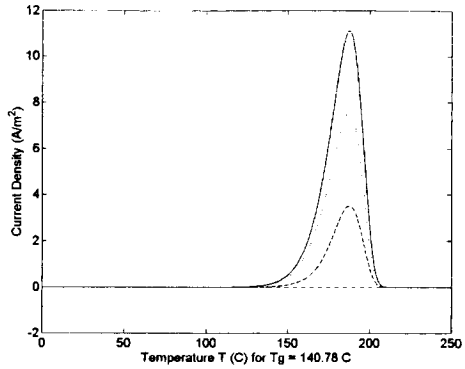

Figure A.46 Wafer 932 Theoretical 1000 V Poling Current Densities

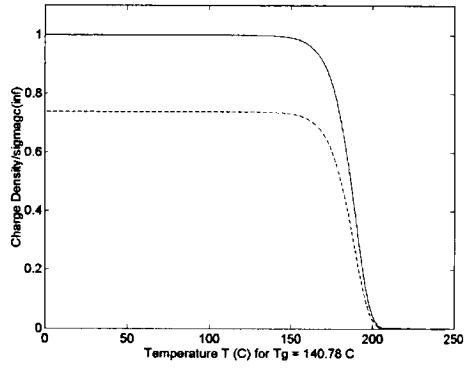

Figure A.47 Wafer 932 Theoretical 1000 V Poling Charge Densities

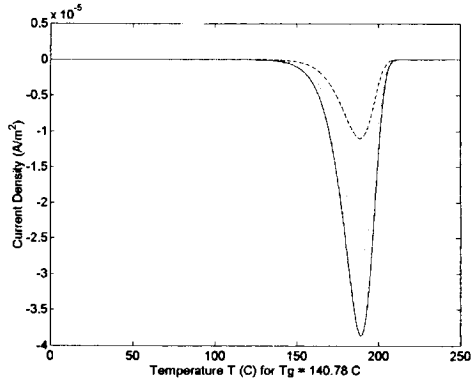

Figure A.48 Wafer 932 Theoretical 1000 V Poling Current Densities

B.2 Die Experimental Data Plots

This section presents the modeled and measured data plots for the poling time and temperature studies discussed in Section 5.2. Figures B.49 – B.86 are the additional plots for the poling time Phase 1 poling experiments. Figures B.32 – B.38 are the additional plots for the poling temperature phase 1 poling experiments. The charge density plots show the modeled charge densities for the poling experiment with the boundary charge density shown by the + symbols and the polarization charge density shown by the dashed line. The charge densities are plotted as the ratios to the boundary charge infinite value. The current density plots show the modeled and measured poling current density with the

total modeled current density shown as a solid line, the modeled boundary charge current density shown as a dashed line, the modeled polarization charge current density shown as a dotted line, and the measured total current density shown as a solid line with circles marking the measured data points. Tables 5.4 and 5.5 contain the relevant poling information for these plots.

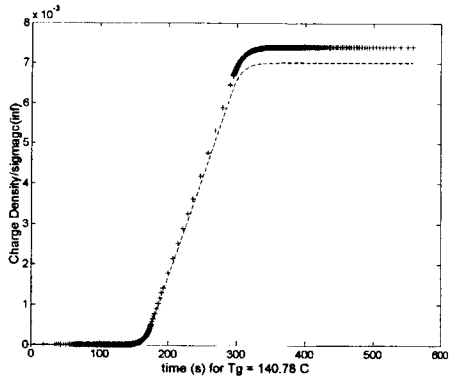

Figure A.49 Die 761-2 Modeled Poling Charge Density

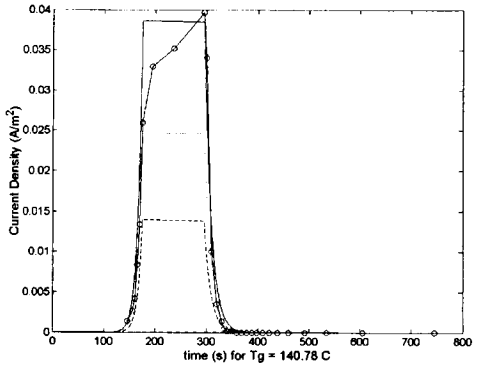

Figure A.50 Die 761-2 Modeled and Measured Poling Current Density

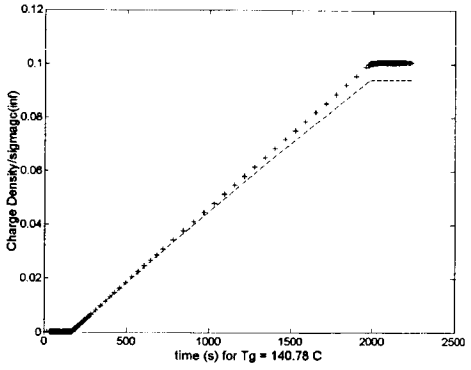

Figure A.51 Die 761-3 Modeled Poling Charge Density

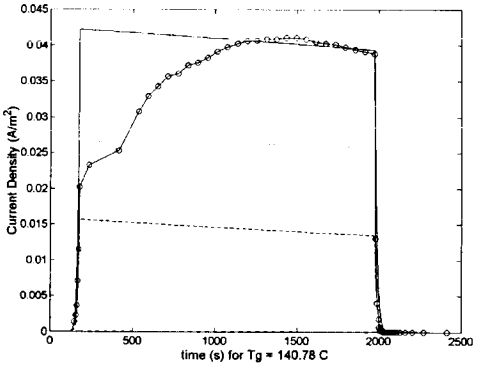

Figure A.52 Die 761-3 Modeled and Measured Poling Current Density

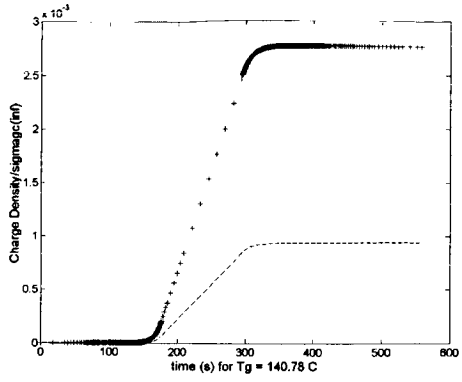

Figure A.53 Die 775-3 Modeled Poling Charge Density

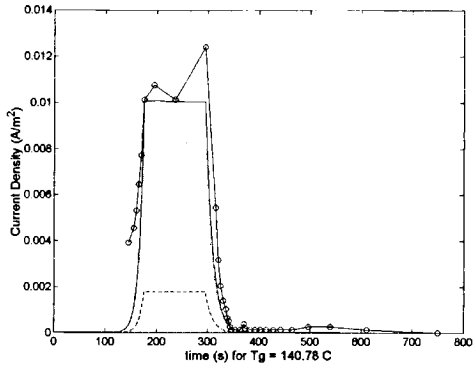

Figure A.54 Die 775-3 Modeled and Measured Poling Current Density

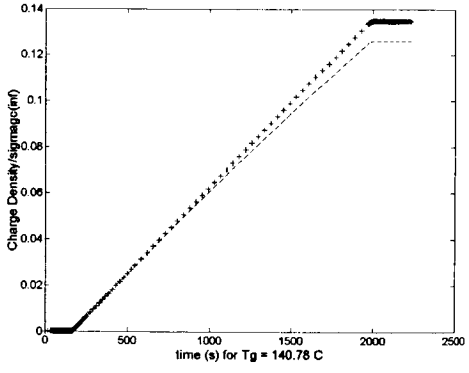

Figure A.55 Die 790-1 Modeled Poling Charge Density

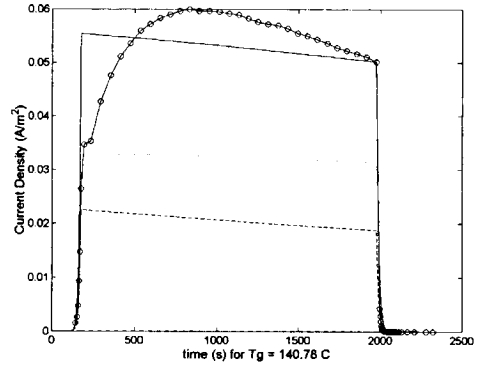

Figure A.56 Die 790-1 Modeled and Measured Poling Current Density

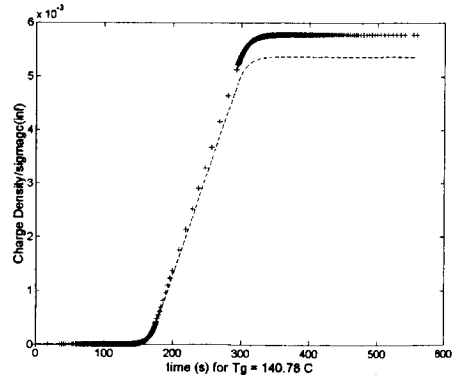

Figure A.57 Die 790-2 Modeled Poling Charge Density

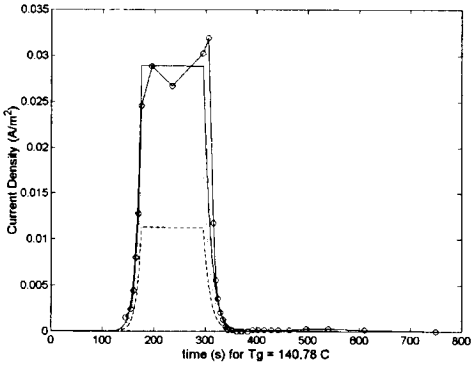

Figure A.58 Die 790-2 Modeled and Measured Poling Current Density

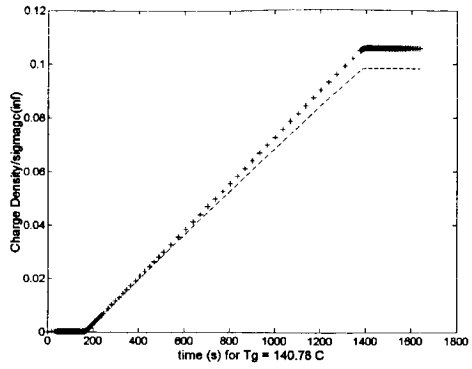

Figure A.59 Die 790-3 Modeled Poling Charge Density

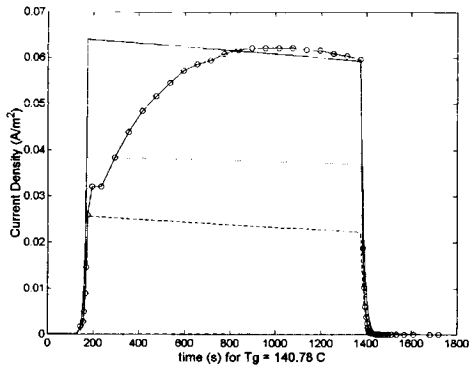

Figure A.60 Die 790-3 Modeled and Measured Poling Current Density

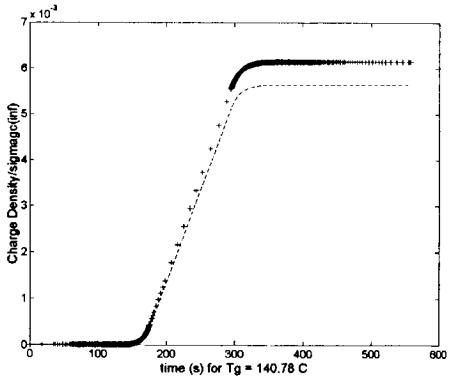

Figure A.61 Die 782-1 Modeled Poling Charge Density

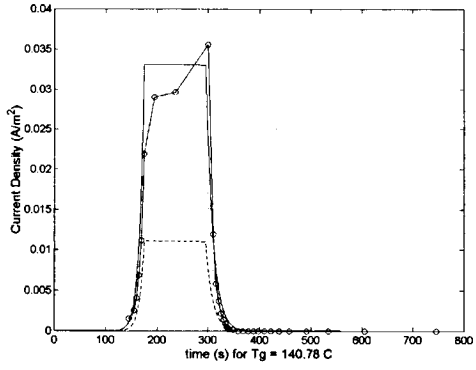

Figure A.62 Die 782-1 Modeled and Measured Poling Current Density

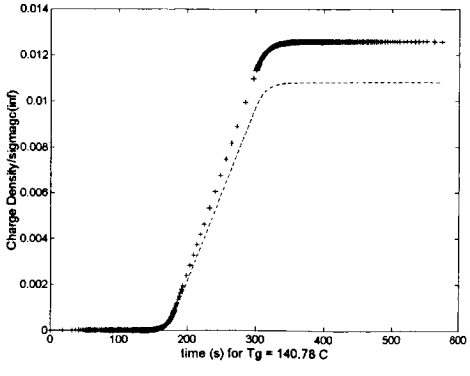

Figure A.63 Die 782-3 Modeled Poling Charge Density

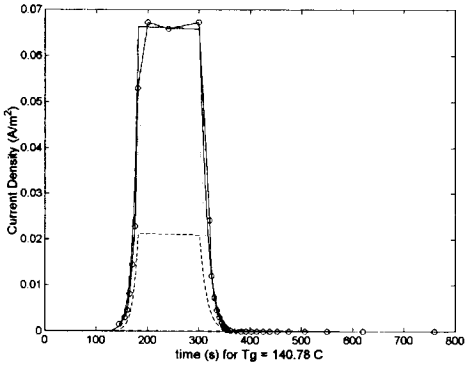

Figure A.64 Die 782-3 Modeled and Measured Poling Current Density

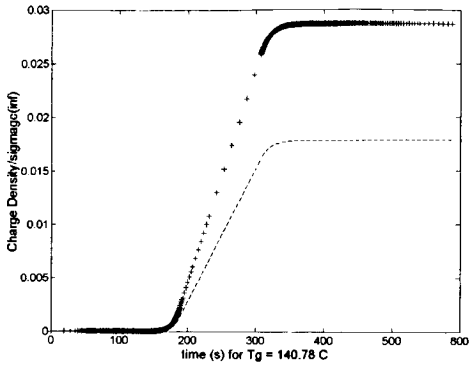

Figure A.65 Die 783-1 Modeled Poling Charge Density

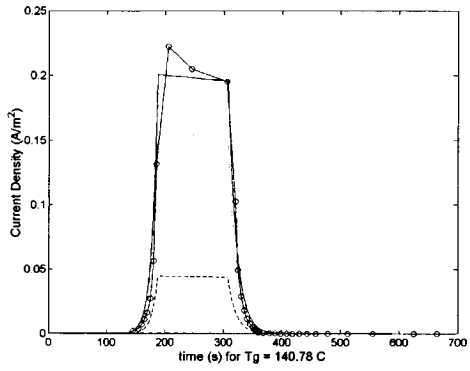

Figure A.66 Die 783-1 Modeled and Measured Poling Current Density

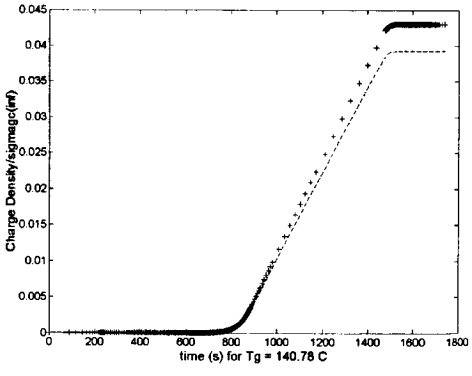

Figure A.67 Die 812-1 Modeled Poling Charge Density

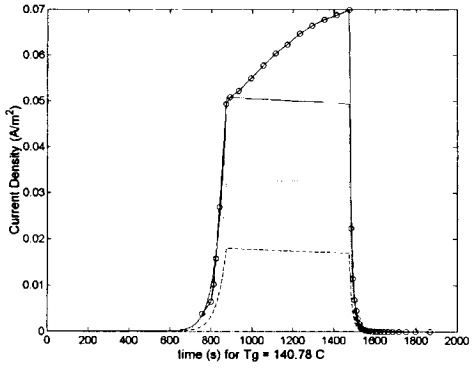

Figure A.68 Die 812-1 Modeled and Measured Poling Current Density

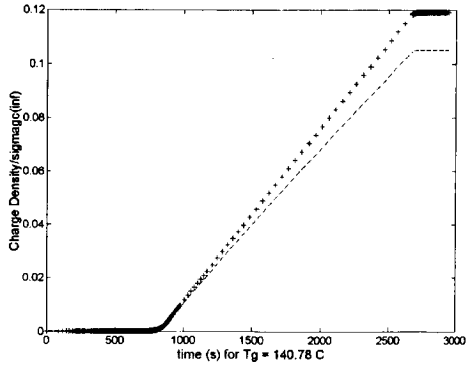

Figure A.69 Die 812-2 Modeled Poling Charge Density

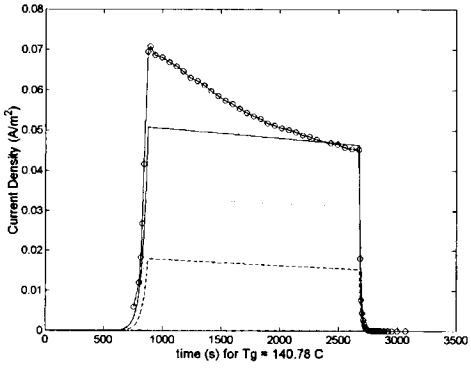

Figure A.70 Die 812-2 Modeled and Measured Poling Current Density

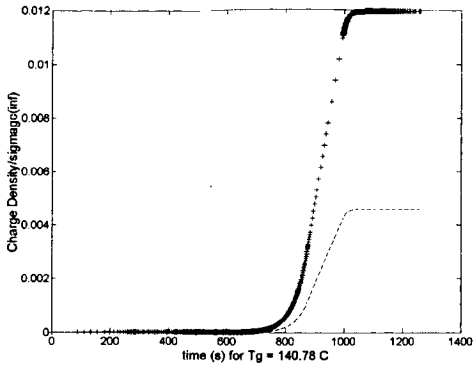

Figure A.71 Die 929-1 Modeled Poling Charge Density

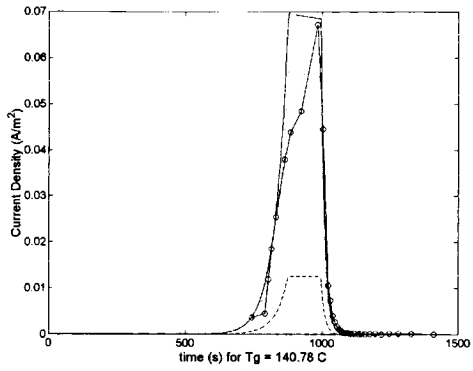

Figure A.72 Die 929-1 Modeled and Measured Poling Current Density

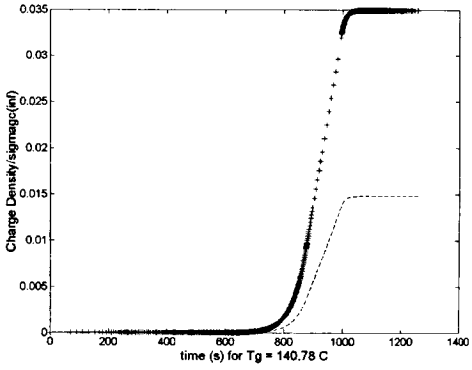

Figure A.73 Die 929-2 Modeled Poling Charge Density

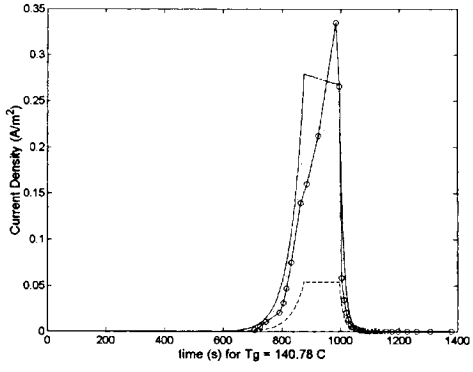

Figure A.74 Die 929-2 Modeled and Measured Poling Current Density

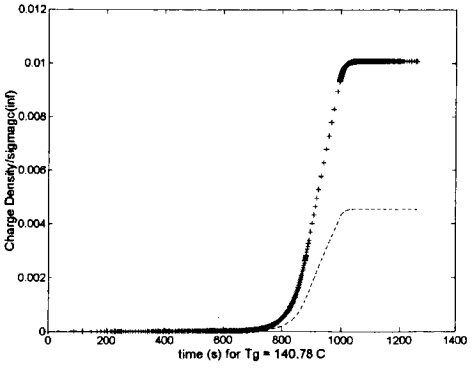

Figure A.75 Die 929-3 Modeled Poling Charge Density

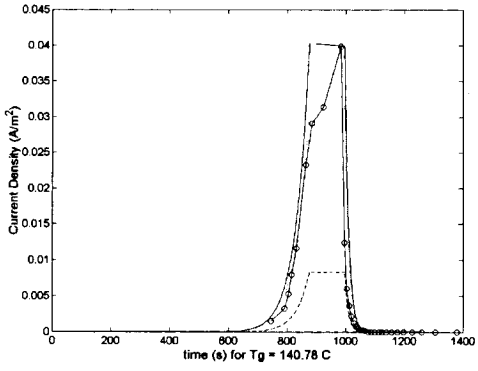

Figure A.76 Die 929-3 Modeled and Measured Poling Current Density

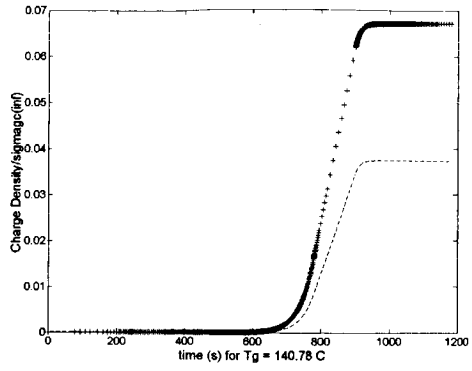

Figure A.77 Die 930-2 Modeled Poling Charge Density

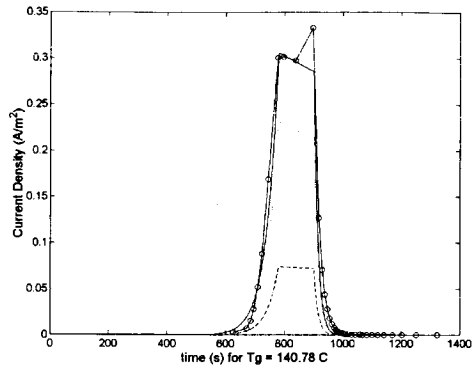

Figure A.78 Die 930-2 Modeled and Measured Poling Current Density

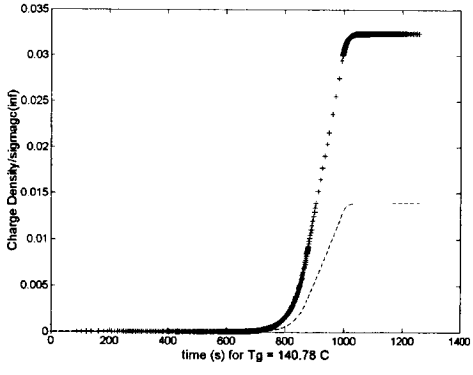

Figure A.79 Die 930-3 Modeled Poling Charge Density

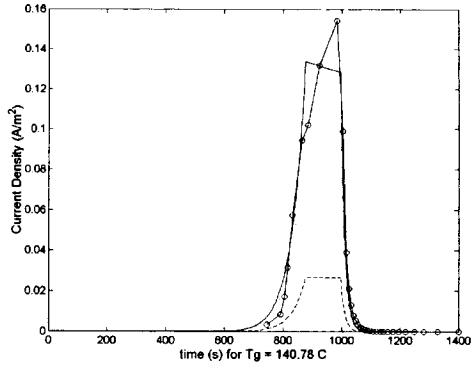

Figure A.80 Die 930-3 Modeled and Measured Poling Current Density

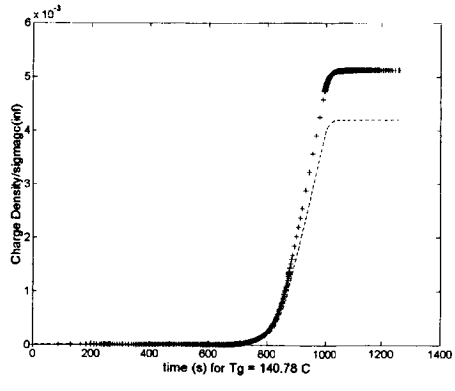

Figure A.81 Die 932-1 Modeled Poling Charge Density

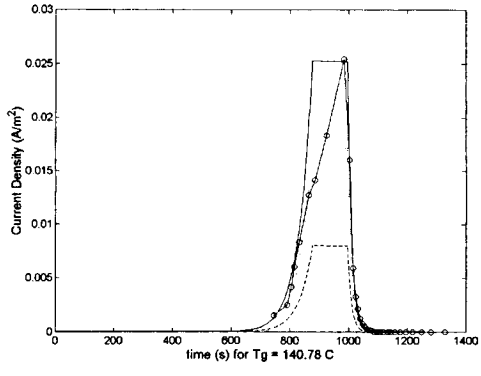

Figure A.82 Die 932-1 Modeled and Measured Poling Current Density

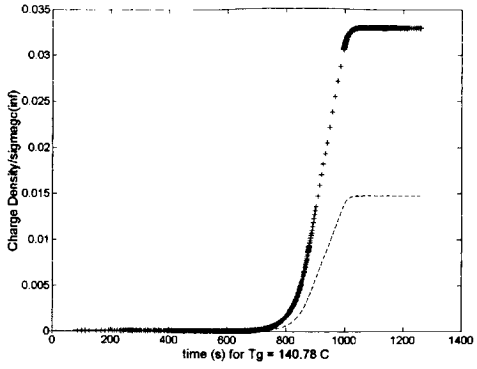

Figure A.83 Die 932-2 Modeled Poling Charge Density

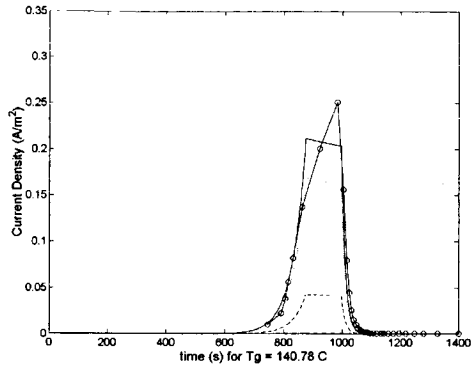

Figure A.84 Die 932-2 Modeled and Measured Poling Current Density

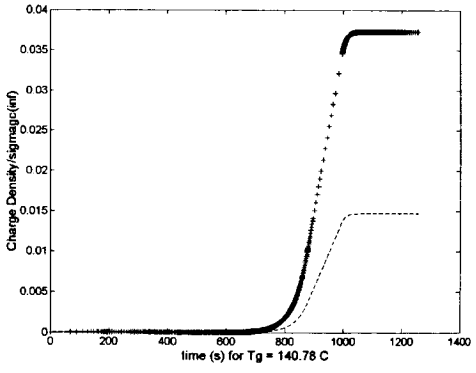

Figure A.85 Die 932-3 Modeled Poling Charge Density

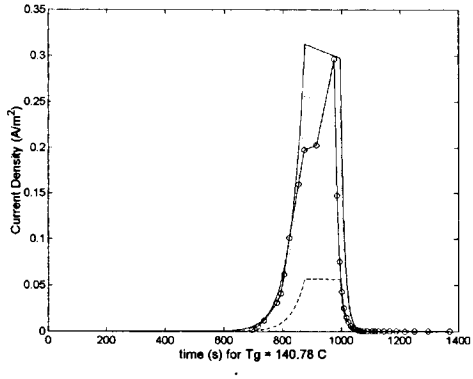

Figure A.86 Die 932-3 Modeled and Measured Poling Current Density

Appendix C

Matlab Programs

This Appendix contains the Matlab programs written to produce the theoretical data and plots and the experimental data plots shown in combination with the theoretical plots presented in Chapter 5. There are 5 main programs written to produce these plots. These plots are:

- Polar Current Theory – produces the theoretical data and plots showing the poling charge densities and poling current densities for unlimited poling temperature.
- Polar Current Experiment – produces the theoretical data values and plots for an experimental poling run and plots the experimental data with the theoretical data.
- Modulation Model – produces the theoretical data (including V_{core} and r_{33} values) and plots for a saw tooth modulation waveform and plots the experimental data with the theoretical data.
- Modulation Model SqWv– produces the theoretical data (including V_{core} value) and plots for a square wave modulation waveform and plots the experimental data with the theoretical data.
- Mod Transfer Function – produces the theoretical data and plots for the high and low frequency response.

In addition to these main programs there were several functions written to support the calculations used in these main programs. There are 5 functions supporting both Polar Current programs. There are:

- arrenhius – calculates the arrenhius function.
- dsdP – calculates the change in the boundary charge density and polarization charge density with time during the heating ramp of the temperature. Used by the ODE solver in the Polar Current programs.
- dsdPdwell – calculates the change in the boundary charge density and polarization charge density with time during the poling temperature dwell. Used by the ODE solver in the Polar Current programs.
- dsdPcool – calculates the change in the boundary charge density and polarization charge density with time during the cooling ramp of the temperature. Used by the ODE solver in the Polar Current programs.
- dsdPTSD – calculates the change in the boundary charge density and polarization charge density with time during the heating ramp of the temperature for TSD (zero poling voltage). Used by the ODE solver in the Polar Current programs.

The Modulation Model program was supported by a single function:

- Sawtoothmodulation – produces the saw tooth modulation wave form for the theoretical plots.

The main programs were tailored for the waveguide dimensions, optical indexes, resistances, and capacitances for each wafer and die. Thus, each wafer and die has a version of the program which contains information on the model used to produce these programs. All programs were used in the analysis of Wafer 791-1. These programs were used for other Wafers be updating the values contained in Tables 5.3, 5.5, 5.6, 5.8, 5.9, 5.11 and C.1 for the Polar Current programs and Table 5.12 for the Modulation Model, Modulation Model SqWv, and Modulation

Transfer function programs. The functions are generic and are listed at the end in the order presented above.

Table C.1 Upper and Lower Conductivity Coefficients used in Polar Current Programs

Wafer-Die#	Upper and Lower Cladding Conductivity (gc0 = gs0)
761 Theory	$0.4x10^9$
761-1	$0.4x10^9$
761-2	$0.43x10^9$
775 theory	$0.4x10^9$
775-1	$0.4x10^9$
775-2	$0.5x10^9$
775-3	$0.16x10^9$
782 theory	$0.33x10^9$
782-1	$0.3x10^9$
782-3	$0.33x10^9$
783 Theory	$0.2x10^9$
783-1	$0.4x10^9$
783-2	$0.35x10^9$
783-3	$0.25x10^9$
790 theory	$0.7x10^9$
790-1	$0.65x10^9$
790-2	$0.35x10^9$
790-3	$0.76x10^9$
791 theory	$0.5x10^9$
791-1	$0.5x10^9$
791-2	$0.7x10^9$
791-3	$0.5x10^9$
812 theory	$0.5x10^9$
812-1	$0.5x10^9$
812-2	$0.5x10^9$
812-3	$0.7x10^9$
929 theory	$0.42x10^9$
929-1	$0.5x10^9$
929-2	$1.5x10^9$
929-3	$0.42x10^9$
930 theory	$0.9x10^9$
930-1	$0.9x10^9$
930-2	$0.9x10^9$
930-3	$1.4x10^9$
931 theory	$0.72x10^9$
931-1	$2.4x10^9$
931-2	$0.35x10^9$
931-3	$0.72x10^9$
932 theory	$1.6x10^9$
932-1	$0.21x10^9$
932-2	$1.4x10^9$
932-3	$1.6x10^9$

791 Polar Current Theory

```
%Script File:  PolarCurrent 791 Theory
%Solves for the polarization and boundary charge in Poling and TSD current
density Theoretical equations
%Wafer #791 (NOA71-CLDX/APC-NOA71)
%
close all
% index of refraction values (lambda = 1.55 microns, TM)
nc = 1.546;
ng = 1.638;
ns = 1.546;
%
% height values
%
hc = 2.79e-6;
hg = 3.61e-6;
hs = 3.1e-6;
height = [ hc hg hs ];
%
% gamma (conductance)
%
gg0 = 1e20;
gc0 = .5e9;
gs0 = gc0;
gamma = [ gc0 gg0 gs0 ];
%
% epsilon (permitivity)
%
e0 = 8.854e-12;
ec = nc^2;          % High Frequency Dielectric Constant
eg = ng^2;          % High Frequency Dielectric Constant
eslow = 4.6;        % Low Frequency Dielectric Constant for core
es = ns^2;
epsilon = [ ec eg es e0 eslow ];
%
% Poling Voltage
%
Vp = 500;
%
% Dipole relaxation frequency and conduction activation energy
%
ar = 1.1e20;                %
Ea = 2;                     %in eV
Ec = 1.9;                   %in eV
AKT = 56;
Tm = Ea*(1.6e-19)/((1.381e-23)*AKT);    %Tm in K; Baseline:  A/kT = 55
```

```
CKTc = AKT*(1.13);              % Upper Cladding Conductance activation
energy
CKTg = AKT*(1.5);               % Core Conductance activation energy
CKTs = CKTc;                    % Lower Cladding Conductance activation energy
Tcc = Ec*(1.6e-19)/((1.381e-23)*CKTc);      %Norlund Tg is 50 - 100 C
depending on crosslinking.
Tcg = Tm/.85;                   %Tm/Tc = .85
Tcs = Tcc;
CKT = [ CKTc CKTg CKTs ];
Tc = [ Tcc Tcg Tcs ];
%
% Time (seconds) and heating rate
%
Tg = 520;                       % Degrees Kelvin
T0 = 273;                       % Initial temperature in Kelvin
s = 44/60;                      % Celsius per seconds  Baseline:  44/60
t = [ 0 (Tg-T0)/s];             % time in seconds to go from T0 to Tg
%
% Solve for Ps(t) during charging
%
%
% ODE solver
%
% Calculate Current Density, J, based on Ps and sigmacg
%
PsC = 0;        % no polarization (random orientation) initially
sigmacg = 0;    % no boundary charge initially
y0 = [ sigmacg PsC ];
options = odeset('RelTol',3e-14,'AbsTol',1e-15);
[t1,Y1] =
ode15s(@dsdP,t,y0,options,s,T0,epsilon,gamma,height,Vp,ar,AKT,CKT,Tm,Tc);
%
% Initialize values for current calculation
%
Bw = zeros(length(Y1),1);
dpsdt = zeros(length(Y1),1);
dsgcdt = zeros(length(Y1),1);
gc = zeros(length(Y1),1);
gg = zeros(length(Y1),1);
gs = zeros(length(Y1),1);
Ggc = zeros(length(Y1),1);
Gcs = zeros(length(Y1),1);
PsC = zeros(length(Y1),1);
sigmagcC = zeros(length(Y1),1);
Vg = zeros(length(Y1),1);
Eg = zeros(length(Y1),1);
jt = zeros(length(Y1),1);
```

```
jp = zeros(length(Y1),1);
jb = zeros(length(Y1),1);
jc = zeros(length(Y1),1);
%
% Current Density Calculation during Charging (jt)
%
PsC(1:length(Y1),1) = Y1(1:length(Y1),2);
sigmagcC(1:length(Y1),1) = Y1(1:length(Y1),1);
gc(1:length(Y1)) = arrenhius(t1*s+273,gc0,CKTc,Tcc);        %273 sets temp =
273 at time = 0
gg(1:length(Y1)) = arrenhius(t1*s+273,gg0,CKTg,Tcg);        %273 sets temp =
273 at time = 0
gs(1:length(Y1)) = arrenhius(t1*s+273,gs0,CKTs,Tcs);        %273 sets temp =
273 at time = 0
Ggc(1:length(Y1)) = 1+(hc*gg)./(hg*gc);
Gcs(1:length(Y1)) = 1./(1+gc./gs);
Bw(1:length(Y1)) = gc./(hc*(e0*ec*Gcs/hc + e0*eg/hg));
dsgcdt(1:length(Y1)) = Ggc.*Bw.*(PsC -
sigmagcC)+Bw.*Gcs.*((e0*eg/hg)+(e0*ec/hc).*(Gcs-Ggc))*Vp;
dpsdt(1:length(t1)) = (arrenhius(t1*s+273,ar,AKT,Tm)).*(((eslow-
eg)*(e0*Vp+(hc/ec)*sigmagcC))-
(hg*Gcs+(hc*eslow/ec)).*PsC)./(hg*Gcs+(hc*eg/ec));
Vg(1:length(t1)) = ((e0*ec*Gcs*Vp/hc)+sigmagcC-
PsC)./((e0*eg/hg)*(1+Gcs*ec*hg/(hc*eg)));
jt(1:length(t1)) = (gg.*(sigmagcC - PsC + e0*ec*Gcs*Vp/hc) + e0*eg*dsgcdt/hg
+ e0*ec*Gcs.*dpsdt/hc)./(hg*(e0*eg/hg + e0*ec*Gcs/hc));  % total current
density
jp(1:length(t1)) =(gg.*(-PsC) + e0*ec*Gcs.*dpsdt/hc)./(hg*(e0*eg/hg +
e0*ec*Gcs/hc));      % Polar current density
jb(1:length(t1)) =(gg.*(sigmagcC) + e0*eg*dsgcdt/hg)./(hg*(e0*eg/hg +
e0*ec*Gcs/hc));   % Conduction current density
jc(1:length(t1)) =(gg.*(e0*ec*Gcs*Vp/hc))./(hg*(e0*eg/hg + e0*ec*Gcs/hc));   %
Conduction current density
scginf = e0*Vp*((eslow-eg) +
(Gcs./Ggc).*(hg*Gcs+hc*eslow/ec).*(eg/hg+(ec/hc)*(Gcs-
Ggc)))./(hg*Gcs+hc*eg/ec);  % Infinite value of boundary charge
q0 = scginf;                                    % q0 is maximum charge density
Psinf = e0*(eslow-eg)*((1 + (Gcs./Ggc).*(eg*hc/(ec*hg)+Gcs-Ggc))./(hg*Gcs +
hc*eg/ec))*Vp;  % Infinite value of Polarization Charge
Vgmod(1:length(t1)) = ((e0*ec*Gcs*235/hc)+sigmagcC-
PsC)./((e0*eg/hg)*(1+Gcs*ec*hg/(hc*eg)));
%
% Note:  sigmagcC, PsC, jp, jc, jt are all calculated interms of K, NOT C, so plot
scale must put ratios
%        in K.  s = C/sec = K/sec.
t1celcius = (t1*s);          %Celcius Temperatures
t1relative = (t1*s+273)/Tm;    %Relative Kelvin values
```

```
figure(1)
axes('fontsize',14)
plot(t1celcius,sigmagcC/q0(1),'k',t1celcius,PsC/q0(1),'--k')
axis([ 0 250 0 1.1 ])
%legend('boundary charge density (sigmagc)','polarization charge density (Ps)',0)
%title (sprintf('Polarization and Boundary Charge Densities during Thermal
Charging for Vp = %3d V',Vp))
ylabel('Charge Density/sigmagc(inf)','fontsize',14), xlabel(sprintf('Temperature T
(C) for Tg = %3.2f C',Tm-273),'fontsize',14)
figure(2)
axes('fontsize',14)
plot(t1celcius,jt,'k',t1celcius,jp,'--k',t1celcius,jb,':k',t1celcius,jc,'-.k')
% legend('Total Current Density (jt)','Polarization Current Density (jp)','Boundary
Charge Current Density (jb)','Conduction Current Density (jc)',0)
% title (sprintf('Total, Polarization, and Conduction Current Density during
Thermal Charging for Vp = %3d V',Vp))
ylabel('Current Density (A/m^2)','fontsize',14), xlabel(sprintf('Temperature T (C)
for Tg = %3.2f C',Tm-273),'fontsize',14)
%
%  TSD Current Calculation
%
tTSD = 0;
YTSD = 0;
PsCstorage = 0;
sigmagcCstorage = 0;
PsCstorage = PsC(length(Y1));          % Polarization charge initialized at max
temperature
sigmagcCstorage = sigmagcC(length(Y1));   % Polarization charge initialized at
max temperature
ystorage = [ sigmagcCstorage PsCstorage ];
tstorage= [ 0 (Tg-T0)/s ];             % Time to get from T0 to Tg
% options = [];
[tTSD,YTSD] =
ode15s(@dsdPTSD,tstorage,ystorage,options,s,T0,epsilon,gamma,height,0,ar,AK
T,CKT,Tm,Tc);
%
% TSD Current Calculation
% Initialize values for TSD current calculation
%
sigmagcTSD = zeros(length(YTSD),1);
PsCTSD = zeros(length(YTSD),1);
dpsdtTSD = zeros(length(YTSD),1);
dsgcdtTSD = zeros(length(YTSD),1);
BwTSD = zeros(length(YTSD),1);
gcTSD = zeros(length(YTSD),1);
ggTSD = zeros(length(YTSD),1);
gsTSD = zeros(length(YTSD),1);
```

```
GgcTSD = zeros(length(YTSD),1);
GcsTSD = zeros(length(YTSD),1);
VgTSD = zeros(length(YTSD),1);
EgTSD = zeros(length(YTSD),1);
jrTSD = zeros(length(YTSD),1);
jpTSD = zeros(length(YTSD),1);
jbTSD = zeros(length(YTSD),1);
%
% Current Density Calculation during TSD (jr)
%
PsCTSD(1:length(YTSD),1) = YTSD(1:length(YTSD),2);
sigmagcTSD(1:length(YTSD),1) = YTSD(1:length(YTSD),1);
gcTSD(1:length(YTSD)) = arrenhius(tTSD*s+273,gc0,CKTc,Tcc);      % 273
sets temp = 273 at time = 0
ggTSD(1:length(YTSD)) = arrenhius(tTSD*s+273,gg0,CKTg,Tcg);      % 273
sets temp = 273 at time = 0
gsTSD(1:length(YTSD)) = arrenhius(tTSD*s+273,gs0,CKTs,Tcs);      % 273 sets
temp = 273 at time = 0
GcsTSD(1:length(YTSD)) = 1./(1+gcTSD./gsTSD);
GgcTSD(1:length(YTSD)) = 1./(e0*eg/hg + e0*ec*GcsTSD/hc);
%GgcTSD solved for Vp=0
BwTSD(1:length(YTSD)) = (ggTSD/hg + gcTSD.*GcsTSD/hc)./(e0*eg/hg +
e0*ec*GcsTSD/hc);  %BwTSD solved for Vp=0
dsgcdtTSD(1:length(YTSD)) = BwTSD.*(PsCTSD-sigmagcTSD);
dpsdtTSD(1:length(YTSD)) =
(arrenhius(tTSD*s+273,ar,AKT,Tm)).*((e0/hg)*(eslow - eg)*sigmagcTSD -
((e0/hg)*(eslow - eg)+(e0*eg/hg +
e0*ec*GcsTSD/hc)).*PsCTSD)./(e0*eg/hg+e0*ec*GcsTSD/hc);
VgTSD(1:length(YTSD)) = (sigmagcTSD-
PsCTSD)./(e0*eg/hg+e0*ec*GcsTSD/hc);
jrTSD(1:length(YTSD)) = (e0*eg*GgcTSD/hg).*dsgcdtTSD + (1-
e0*eg*GgcTSD/hg).*dpsdtTSD + ggTSD.*GgcTSD/hg.*(sigmagcTSD -
PsCTSD);        % total current density
jpTSD(1:length(YTSD)) = (1-e0*eg*GgcTSD/hg).*dpsdtTSD+
ggTSD.*GgcTSD/hg.*(-PsCTSD);   % Polarization charge current density
jbTSD(1:length(YTSD)) = (e0*eg*GgcTSD/hg).*dsgcdtTSD +
ggTSD.*GgcTSD/hg.*(sigmagcTSD);   % Boundary Charge current density
%
% Note:  sigmagcC, PsC, jp, jc, jt are all calculated interms of K, NOT C, so plot
scale must put ratios
%         in K.  s = C/sec = K/sec.
tTSDcelcius = (tTSD*s);            %Celcius Temperatures
tTSDrelative = (tTSD*s+273)/Tm;     %Relative Kelvin values
figure(3)
axes('fontsize',14)
plot(tTSDcelcius,sigmagcTSD/q0(1),'k',tTSDcelcius,PsCTSD/q0(1),'--k')
axis([ 0 250 0 1.1 ])
```

```
% legend('boundary charge density (sigmagc)','polarization charge density (Ps)',0)
% title ('Polarization Charge Density and Boundary Charge Density during TSD')
ylabel('Charge Density/sigmagc(inf)','fontsize',14), xlabel(sprintf('Temperature T
(C) for Tg = %3.2f C',Tm-273),'fontsize',14)
figure(4)
axes('fontsize',14)
plot(tTSDcelcius,jrTSD,'k',tTSDcelcius,jpTSD,'--k',tTSDcelcius,jbTSD,':k')
% legend('Released Current Density (jr)','Polarization Current Density
(jp)','Boundary Current Density (jb)',0)
% title ('Total, Polarization, and Conduction Current Density during TSD')
ylabel('Current Density (A/m^2)','fontsize',14), xlabel(sprintf('Temperature T (C)
for Tg = %3.2f C',Tm-273),'fontsize',14)
```

791-1 Polar Current Experiment

```
%Script File:  PolarCurrent 791_1 Experiment
%Solves for the polarization and boundary charge in Poling and TSD current
density equations to match Experimental Data
%Wafer #791-1 (NOA71-CLDX/APC-NOA71)
%
close all
% index of refraction values
nc = 1.546;
ng = 1.638;
ns = 1.546;
%
% height values
%
hc = 2.79e-6;
hg = 3.61e-6;
hs = 3.1e-6;
height = [ hc hg hs ];
%
% gamma (conductance)
%
gg0 = 1e20;
gc0 = .5e9;
gs0 = gc0;
gamma = [ gc0 gg0 gs0 ];
%
% epsilon (permitivity)
%
e0 = 8.854e-12;
ec = nc^2;          % High Frequency Dielectric Constant
eg = ng^2;          % High Frequency Dielectric Constant
eslow = 4.6;        % Low Frequency Dielectric Constant for core
es = ns^2;
epsilon = [ ec eg es e0 eslow ];
%
% Poling Voltage
%
Vp = 500;
%
% Dipole relaxation frequency and conduction activation energy
%
ar =1.e20;                  % Dipole Natural Relaxation Frequency in 1/seconds
Ea = 2;                     % in eV
Ec = 1.9;                   % in eV
AKT = 56;
Tm = Ea*(1.6e-19)/((1.381e-23)*AKT);    %Tm in K; Baseline:  A/kT = 55
```

```
CKTc = AKT*(1.13);              % Upper Cladding Conductance activation
energy
CKTg = AKT*(1.5);               % Core Conductance activation energy
CKTs = CKTc;                    % Lower Cladding Conductance activation energy
Tcc = Ec*(1.6e-19)/((1.381e-23)*CKTc);      %Norlund Tg is 50 - 100 C
depending on crosslinking.
Tcg = Tm/.85;                   %Tm/Tc = .85
Tcs = Tcc;
CKT = [ CKTc CKTg CKTs ];
Tc = [ Tcc Tcg Tcs ];
%
% Time (seconds) and heating rate
%
Tg = 419;                       % Degrees Kelvin
T0 = 273;                       % Initial temperature in Kelvin
s = 50/60;                      % Celsius per seconds  Baseline:  44/60
t = [ 0 (Tg-T0)/s];             % time in seconds to go from T0 to Tg
%
% Solve for Ps(t) during charging
%
%
% ODE solver
%
% Calculate Current Density, J, based on Ps and sigmacg
%
PsC = 0;        % no polarization (random orientation) initially
sigmacg = 0;    % no boundary charge initially
y0 = [ sigmacg PsC ];
options = odeset('RelTol',3e-14,'AbsTol',1e-15);
[t1,Y1] =
ode15s(@dsdP,t,y0,options,s,T0,epsilon,gamma,height,Vp,ar,AKT,CKT,Tm,Tc);
%
% Initialize values for current calculation
%
Bw = zeros(length(Y1),1);
dpsdt = zeros(length(Y1),1);
dsgcdt = zeros(length(Y1),1);
gc = zeros(length(Y1),1);
gg = zeros(length(Y1),1);
gs = zeros(length(Y1),1);
Ggc = zeros(length(Y1),1);
Gcs = zeros(length(Y1),1);
PsC = zeros(length(Y1),1);
sigmagcC = zeros(length(Y1),1);
Vg = zeros(length(Y1),1);
Eg = zeros(length(Y1),1);
jt = zeros(length(Y1),1);
```

```
jp = zeros(length(Y1),1);
jb = zeros(length(Y1),1);
jc = zeros(length(Y1),1);
%
% Current Density Calculation during Charging (jt)
%
PsC(1:length(Y1),1) = Y1(1:length(Y1),2);
sigmagcC(1:length(Y1),1) = Y1(1:length(Y1),1);
gc(1:length(Y1)) = arrenhius(t1*s+273,gc0,CKTc,Tcc);        %273 sets temp =
273 at time = 0
gg(1:length(Y1)) = arrenhius(t1*s+273,gg0,CKTg,Tcg);        %273 sets temp =
273 at time = 0
gs(1:length(Y1)) = arrenhius(t1*s+273,gs0,CKTs,Tcs);        %273 sets temp =
273 at time = 0
Ggc(1:length(Y1)) = 1+(hc*gg)./(hg*gc);
Gcs(1:length(Y1)) = 1./(1+gc./gs);
Bw(1:length(Y1)) = gc./(hc*(e0*ec*Gcs/hc + e0*eg/hg));
dsgcdt(1:length(Y1)) = Ggc.*Bw.*(PsC -
sigmagcC)+Bw.*Gcs.*((e0*eg/hg)+(e0*ec/hc).*(Gcs-Ggc))*Vp;
dpsdt(1:length(t1)) = (arrenhius(t1*s+273,ar,AKT,Tm)).*(((eslow-
eg)*(e0*Vp+(hc/ec)*sigmagcC))-
(hg*Gcs+(hc*eslow/ec)).*PsC)./(hg*Gcs+(hc*eg/ec));
Vg(1:length(t1)) = ((e0*ec*Gcs*Vp/hc)+sigmagcC-
PsC)./((e0*eg/hg)*(1+Gcs*ec*hg/(hc*eg)));
jt(1:length(t1)) = (gg.*(sigmagcC - PsC + e0*ec*Gcs*Vp/hc) + e0*eg*dsgcdt/hg
+ e0*ec*Gcs.*dpsdt/hc)./(hg*(e0*eg/hg + e0*ec*Gcs/hc));  % total current
density
jp(1:length(t1)) =(gg.*(-PsC) + e0*ec*Gcs.*dpsdt/hc)./(hg*(e0*eg/hg +
e0*ec*Gcs/hc));      % Polar current density
jb(1:length(t1)) =(gg.*(sigmagcC) + e0*eg*dsgcdt/hg)./(hg*(e0*eg/hg +
e0*ec*Gcs/hc));   % Conduction current density
jc(1:length(t1)) =(gg.*(e0*ec*Gcs*Vp/hc))./(hg*(e0*eg/hg + e0*ec*Gcs/hc));   %
Conduction current density
scginf = e0*Vp*((eslow-eg) +
(Gcs./Ggc).*(hg*Gcs+hc*eslow/ec).*(eg/hg+(ec/hc)*(Gcs-
Ggc)))./(hg*Gcs+hc*eg/ec);  % Infinite value of boundary charge
q0 = scginf;                                % q0 is maximum charge density
Psinf = e0*(eslow-eg)*((1 + (Gcs./Ggc).*(eg*hc/(ec*hg)+Gcs-Ggc))./(hg*Gcs +
hc*eg/ec))*Vp;  % Infinite value of Polarization Charge
%
% Experimental Charging
%
Data = xlsread('D:\Projects\Avionics\Phd\Wafer791PolingData', 'Sheet2');
ElectrodeArea = 79e-6;              % Electrode area in m^2
jtexp = Data(14:20,3)/ElectrodeArea;    % Poling current densities in A/m^2
Tcexp = Data(14:20,1)+273;          % Poling current temperatures adjusted to
Kelvin
```

```
tcexp = Data(14:20,2)-1800;                % Poling time in seconds
%
% Note:  sigmagcC, PsC, jp, jc, jt are all calculated interms of K, NOT C, so plot
scale must put ratios
%          in K.  s = C/sec = K/sec.
t1celcius = (t1*s);            %Celcius Temperatures
t1relative = (t1*s+273)/Tm;     %Relative Kelvin values
figure(1)
axes('fontsize',12)
plot(t1celcius,sigmagcC/q0(1),'k',t1celcius,PsC/q0(1),'--k')
%legend('boundary charge density (sigmagc)','polarization charge density (Ps)',0)
%title (sprintf('Polarization and Boundary Charge Densities during Thermal
Charging for Vp = %3d V',Vp))
ylabel('Charge Density/sigmagc(inf)','fontsize',14), xlabel(sprintf('Temperature T
(C) for Tg = %3.2f C',Tm-273),'fontsize',14)
figure(2)
axes('fontsize',12)
plot(t1celcius,jt,'k',t1celcius,jp,'--kD',t1celcius,jb,':k',t1celcius,jc,'-.k')
% legend('Total Current Density (jt)','Polarization Current Density (jp)','Boundary
Charge Current Density (jb)','Conduction Current Density (jc)',0)
% title (sprintf('Total, Polarization, and Conduction Current Density during
Thermal Charging for Vp = %3d V',Vp))
ylabel('Current Density (A/m^2)','fontsize',14), xlabel(sprintf('Temperature T (C)
for Tg = %3.2f C',Tm-273),'fontsize',14)
figure(3)
axes('fontsize',12)
plot(t1celcius,jt,'k',Tcexp-273,jtexp,'--ko')
% legend('Total Current Density (jt)','Experimental Total Current Density
(jtexp)',0)
% title (sprintf('Total Modeled and Experimental Current Density during Poling
for Vp = %3d V',Vp))
ylabel('Current Density (A/m^2)','fontsize',14), xlabel(sprintf('Temperature T (C)
for Tg = %3.2f C',Tm-273),'fontsize',14)
%
%  Dwell Time
%
Td = Tg;          %dwell temperature:  145 C
tdwellmax = 120;    %maximum dwell time in seconds
sdwell = 0;
PsCmax = PsC(length(Y1));              % Polarization charge initialized at max
temperature
sigmagcCmax = sigmagcC(length(Y1));    % Boundary charge initialized at max
temperature
ymax = [ sigmagcCmax PsCmax ];
tdwell = [ t1(length(t1)) t1(length(t1))+tdwellmax ];          %Initial conditions set
the value properly, time should start at zero sec with time to go from Tg to T0
```

```
[t1d,Ydwell] =
ode15s(@dsdPdwell,tdwell,ymax,options,sdwell,Td,epsilon,gamma,height,Vp,ar,
AKT,CKT,Tm,Tc);
%
% Initialize values for current calculation
%
Bwdwell = zeros(length(Ydwell),1);
dpsdtdwell = zeros(length(Ydwell),1);
dsgcdtdwell = zeros(length(Ydwell),1);
gcdwell = zeros(length(Ydwell),1);
ggdwell = zeros(length(Ydwell),1);
gsdwell = zeros(length(Ydwell),1);
Ggcdwell = zeros(length(Ydwell),1);
Gcsdwell = zeros(length(Ydwell),1);
PsCdwell = zeros(length(Ydwell),1);
sigmagcdwell = zeros(length(Ydwell),1);
Vgdwell = zeros(length(Ydwell),1);
Egdwell = zeros(length(Ydwell),1);
jtdwell = zeros(length(Ydwell),1);
jpdwell = zeros(length(Ydwell),1);
jbdwell = zeros(length(Ydwell),1);
jcdwell = zeros(length(Ydwell),1);
%
% Current Density Calculation during Dwell (jt)
%
PsCdwell(1:length(Ydwell),1) = Ydwell(1:length(Ydwell),2);
sigmagcdwell(1:length(Ydwell),1) = Ydwell(1:length(Ydwell),1);
gcdwell(1:length(Ydwell)) = arrenhius(Td,gc0,CKTc,Tcc);
ggdwell(1:length(Ydwell)) = arrenhius(Td,gg0,CKTg,Tcg);
gsdwell(1:length(Ydwell)) = arrenhius(Td,gs0,CKTs,Tcs);
Ggcdwell(1:length(Ydwell)) = 1+(hc*ggdwell)./(hg*gcdwell);
Gcsdwell(1:length(Ydwell)) = 1./(1+gcdwell./gsdwell);
Bwdwell(1:length(Ydwell)) = gcdwell./(hc*(e0*ec*Gcsdwell/hc + e0*eg/hg));
dsgcdtdwell(1:length(Ydwell)) = Ggcdwell.*Bwdwell.*(PsCdwell -
sigmagcdwell)+Bwdwell.*Gcsdwell.*((e0*eg/hg)+(e0*ec/hc).*(Gcsdwell-
Ggcdwell))*Vp;
dpsdtdwell(1:length(t1d)) = (arrenhius(t1d*sdwell+Td,ar,AKT,Tm)).*(((eslow-
eg)*(e0*Vp+(hc/ec)*sigmagcdwell))-
(hg*Gcsdwell+(hc*eslow/ec)).*PsCdwell)./(hg*Gcsdwell+(hc*eg/ec));
Vgdwell(1:length(t1d)) = ((e0*ec*Gcsdwell*Vp/hc)+sigmagcdwell-
PsCdwell)./((e0*eg/hg)*(1+Gcsdwell*ec*hg/(hc*eg)));
jtdwell(1:length(t1d)) = (ggdwell.*(sigmagcdwell - PsCdwell +
e0*ec*Gcsdwell*Vp/hc) + e0*eg*dsgcdtdwell/hg +
e0*ec*Gcsdwell.*dpsdtdwell/hc)./(hg*(e0*eg/hg + e0*ec*Gcsdwell/hc));  %
total current density
```

```
jpdwell(1:length(t1d)) =(ggdwell.*(-PsCdwell) +
e0*ec*Gcsdwell.*dpsdtdwell/hc)./(hg*(e0*eg/hg + e0*ec*Gcsdwell/hc));      %
Polar current density
jbdwell(1:length(t1d)) =(ggdwell.*(sigmagcdwell) +
e0*eg*dsgcdtdwell/hg)./(hg*(e0*eg/hg + e0*ec*Gcsdwell/hc));   % Conduction
current density
jcdwell(1:length(t1d)) =(ggdwell.*(e0*ec*Gcsdwell*Vp/hc))./(hg*(e0*eg/hg +
e0*ec*Gcsdwell/hc));   % Conduction current density
%
figure(4)
axes('fontsize',12)
plot(t1d,sigmagcdwell/q0(1),'+k',t1d,PsCdwell/q0(1),'--k')
% legend('boundary charge density (sigmagc)','polarization charge density (Ps)',0)
% title (sprintf('Polarization and Boundary Charge Densities Thermal Charging
Dwell for Vp = %3d V',Vp))
ylabel('Charge Density/sigmagc(inf)','fontsize',14), xlabel(sprintf('Time (s) for
Tdwell = %3.2f C',Td-273),'fontsize',14)
figure(5)
axes('fontsize',12)
plot(t1d,jtdwell,'k',t1d,jpdwell,'--k',t1d,jbdwell,':k',t1d,jcdwell,'-.k')
% legend('Total Current Density (jt)','Polarization Current Density (jp)','Boundary
Charge Current Density (jb)','Conduction Current Density (jc)',0)
% title (sprintf('Total, Polarization, and Conduction Current Density during
Thermal Charging Dwell for Vp = %3d V',Vp))
ylabel('Current Density (A/m^2)','fontsize',14), xlabel(sprintf('Time (s) for Tdwell
= %3.2f C',Td-273),'fontsize',14)
%
% Cool Down Current (too calculate TSD initial point)
%
PsCmaxd = PsCdwell(length(Ydwell));          % Polarization charge initialized
at max temperature
sigmagcCmaxd = sigmagcdwell(length(Ydwell));   % Boundary charge initialized
at max temperature
ymaxd = [ sigmagcCmaxd PsCmaxd ];
Tmax = Tg;                              % in Kelvin
scool = 33.3/60;                          % Cool down rate  C/min = C/(60 sec)=
K/(60 sec)
tc = [ t1d(length(t1d)) t1d(length(t1d))+(Tmax-T0)/scool ];        %Initial
conditions set the value properly, time should start at zero sec with time to go
from Tg to T0
options1 = odeset('RelTol',3e-14,'AbsTol',1e-15);
[tcool,Ycool] =
ode15s(@dsdPcool,tc,ymaxd,options1,scool,Tmax,epsilon,gamma,height,Vp,ar,A
KT,CKT,Tm,Tc,t1d(length(t1d)));
%
% Initialize values for current calculation
%
```

```
tcoolrev = zeros(length(tcool),1);
sigmagccool = zeros(length(Ycool),1);
PsCcool = zeros(length(Ycool),1);
dpsdtcool = zeros(length(Ycool),1);
dsgcdtcool = zeros(length(Ycool),1);
Bwcool = zeros(length(Ycool),1);
gccool = zeros(length(Ycool),1);
ggcool = zeros(length(Ycool),1);
gscool = zeros(length(Ycool),1);
Ggccool = zeros(length(Ycool),1);
Gcscool = zeros(length(Ycool),1);
Vgcool = zeros(length(Ycool),1);
Egcool = zeros(length(Ycool),1);
jtcool = zeros(length(Ycool),1);
jpcool = zeros(length(Ycool),1);
jbcool = zeros(length(Ycool),1);
jccool = zeros(length(Ycool),1);
sigmagccoolmax = 0;
PsCcoolmax = 0;
dwellcharge = [ 0 0 0 ];
%
% Current Density Calculation during Charging (jt)
%
PsCcool(1:length(Ycool),1) = Ycool(1:length(Ycool),2);
sigmagccool(1:length(Ycool),1) = Ycool(1:length(Ycool),1);
gccool(1:length(Ycool)) = arrenhius(Tmax-(tcool-
min(tcool))*scool,gc0,CKTc,Tcc);  % Initialize Temperature to Tmax-
(max(tcool)-tcool)*scool to adjust for time shift from start
ggcool(1:length(Ycool)) = arrenhius(Tmax-(tcool-
min(tcool))*scool,gg0,CKTg,Tcg);  % Initialize Temperature to Tmax-
(max(tcool)-tcool)*scool to adjust for time shift from start
gscool(1:length(Ycool)) = arrenhius(Tmax-(tcool-
min(tcool))*scool,gs0,CKTs,Tcs);  % Initialize Temperature to Tmax-
(max(tcool)-tcool)*scool to adjust for time shift from start
Ggccool(1:length(Ycool)) = 1+(hc*ggcool)./(hg*gccool);
Gcscool(1:length(Ycool)) = 1./(1+gccool./gscool);
Bwcool(1:length(Ycool)) = gccool./(hc*(e0*ec*Gcscool/hc + e0*eg/hg));
dsgcdtcool(1:length(Ycool)) = Ggccool.*Bwcool.*(PsCcool -
sigmagccool)+Bwcool.*Gcscool.*((e0*eg/hg)+(e0*ec/hc).*(Gcscool-
Ggccool))*Vp;
dpsdtcool(1:length(tcool)) = (arrenhius(Tmax-(tcool-
min(tcool))*scool,ar,AKT,Tm)).*(((eslow-eg)*(e0*Vp+(hc/ec)*sigmagccool))-
(hg*Gcscool+(hc*eslow/ec)).*PsCcool)./(hg*Gcscool+(hc*eg/ec));
Vgcool(1:length(tcool)) = ((e0*ec*Gcscool*Vp/hc)+sigmagccool-
PsCcool)./((e0*eg/hg)*(1+Gcscool*ec*hg/(hc*eg)));
jtcool(1:length(tcool)) =(ggcool.*(sigmagccool - PsCcool +
e0*ec*Gcscool*Vp/hc) + e0*eg*dsgcdtcool/hg +
```

```
e0*ec*Gcscool.*dpsdtcool/hc)./(hg*(e0*eg/hg + e0*ec*Gcscool/hc));  % total
current density
jpcool(1:length(tcool)) =(ggcool.*(-PsCcool) +
e0*ec*Gcscool.*dpsdtcool/hc)./(hg*(e0*eg/hg + e0*ec*Gcscool/hc));      %
Polar current density
jbcool(1:length(tcool)) =(ggcool.*(sigmagccool) +
e0*eg*dsgcdtcool/hg)./(hg*(e0*eg/hg + e0*ec*Gcscool/hc));   % Boundary
Charge current density
jccool(1:length(tcool)) =(ggcool.*(e0*ec*Gcscool*Vp/hc))./(hg*(e0*eg/hg +
e0*ec*Gcscool/hc));   % Conduction current density
Vgcharge(1:length(tcool)) = (sigmagccool-
PsCcool)./((e0*eg/hg)*(1+Gcscool*ec*hg/(hc*eg)));
%
% Experimental Cool Down
%
ElectrodeArea1 = 79e-6;                                    %Electrode area in
m^2
jcoolexp = Data(20:47,3)/ElectrodeArea;    % Poling current densities in A/m^2
Tcoolexp = Data(20:47,1)+273;          % Poling current temperatures adjusted
to Kelvin
tccoolexp = Data(20:47,2)-1800;              % Poling time in seconds
%
% Note:  sigmagcC, PsC, jp, jc, jt are all calculated interms of K, NOT C, so plot
scale must put ratios
%          in K.  s = C/sec = K/sec.
tcoolcelcius = Tmax-(max(tcool)-tcool)*scool-273;          %Celcius
Temperatures
tcoolrelative = (Tmax-(max(tcool)-tcool)*scool+273)/Tm;    %Relative Kelvin
values
plotrange = 10:length(tcool);
sigmagccoolmax = sigmagccool(length(Ycool),1)/q0(1);
PsCcoolmax = PsCcool(length(Ycool),1)/Psinf(1);
dwellcharge = [ tdwellmax sigmagccoolmax PsCcoolmax ];
%
% Write maximum normalized charge to file to produce charge vs. dwell time
plots
%
% fid = fopen('d:/projects/avionics/phd/dwelltemp.txt','a');      % If file exists, use
'w' to write over, then switch to append 'a'
% fprintf(fid,'%8d %2.4f %2.4f',tdwellmax, sigmagccoolmax, PsCcoolmax);
% fclose(fid);
figure(6)
axes('fontsize',12)
plot(tcoolcelcius,sigmagccool/q0(1),'+k',tcoolcelcius,PsCcool/q0(1),'--k')
% legend('boundary charge density (sigmagc)','polarization charge density (Ps)',0)
% title (sprintf('Polarization and Boundary Charge Densities during Cool down
for Vp = %3d V',Vp))
```

```
ylabel('Charge Density/sigmagc(inf)','fontsize',14), xlabel(sprintf('Temperature T
(C) for Tg = %3.2f C',Tm-273),'fontsize',14)
prangemin = 55;
prangemax = length(Ycool);
figure(7)
axes('fontsize',12)
plot(tcoolcelcius(prangemin:prangemax),jtcool(prangemin:prangemax),'+k',tcoolc
elcius(prangemin:prangemax),jpcool(prangemin:prangemax),'--
k',tcoolcelcius(prangemin:prangemax),jbcool(prangemin:prangemax),':k',tcoolcelc
ius(prangemin:prangemax),jccool(prangemin:prangemax),'-.k')
% legend('Total Current Density (jt)','Polarization Current Density (jp)','Boundary
Charge Current Density (jb)','Conduction Current Density (jc)',0)
% title (sprintf('Total, Polarization, and Conduction Current Density during Cool
Down for Vp = %3d V',Vp))
ylabel('Current Density (A/m^2)','fontsize',14), xlabel(sprintf('Temperature T (C)
for Tg = %3.2f C',Tm-273),'fontsize',14)
figure(8)
axes('fontsize',12)
plot(tcoolcelcius,jtcool,'k',tccoolexp-273,jcoolexp,'--ko')
% legend('Total Current Density (jt)','Experimental Total Current Density
(jtexp)',0)
% title (sprintf('Total Modeled and Experimental Current Density during Cool
Down for Vp = %3d V',Vp))
ylabel('Current Density (A/m^2)','fontsize',14), xlabel(sprintf('Temperature T (C)
for Tg = %3.2f C',Tm-273),'fontsize',14)
%
% Full Plots
%
jexp = Data(14:47,3)/(ElectrodeArea);    % Poling current densities in A/m^2
Texp = Data(14:47,1)+273;              % Poling current temperatures adjusted to
Kelvin
texp = Data(14:47,2)-1800;               % Poling time in seconds adjusted to
remove 30 min purge
figure(9)
axes('fontsize',12)
plot(t1,sigmagcC/q0(1),'+k',t1d,sigmagcdwell/q0(1),'+k',tcool,sigmagccool/q0(1),'
+k',t1,PsC/q0(1),'--k',t1d,PsCdwell/q0(1),'--k',tcool,PsCcool/q0(1),'--k')
% legend('boundary charge density (sigmagc)','polarization charge density (Ps)',0)
% title (sprintf('Polarization and Boundary Charge Densities during Cool down
for Vp = %3d V',Vp))
ylabel('Charge Density/sigmagc(inf)','fontsize',14), xlabel(sprintf('time (s) for Tg
= %3.2f C',Tm-273),'fontsize',14)
figure(10)
axes('fontsize',12)
%plot(t1,jt,'k',t1d,jtdwell,'k',tcool,jtcool,'k')
```

```
plot(t1,jt,'k',t1,jp,'--k',t1,jb,':k',t1,jc,'-.k',t1d,jtdwell,'k',t1d,jpdwell,'--
k',t1d,jbdwell,':k',t1d,jcdwell,'-.k',tcool,jtcool,'k',tcool,jpcool,'--
k',tcool,jbcool,':k',tcool,jccool,'-.k',texp,jexp,'-ko')
% legend('Total Current Density (jt)','Experimental Total Current Density
(jtexp)',0)
% title (sprintf('Total Modeled and Experimental Current Density during Cool
Down for Vp = %3d V',Vp))
ylabel('Current Density (A/m^2)','fontsize',14), xlabel(sprintf('time (s) for Tg =
%3.2f C',Tm-273),'fontsize',14)
%
%  TSD Current Calculation
%
tTSD = 0;
YTSD = 0;
PsCstorage = 0;
sigmagcCstorage = 0;
PsCstorage = PsCcool(length(Ycool));          % Polarization charge initialized at
max temperature
sigmagcCstorage = sigmagccool(length(Ycool));   % Polarization charge
initialized at max temperature
ystorage = [ sigmagcCstorage PsCstorage ];
tstorage= [ 0 (Tg-T0)/s ];                    % Time to get from T0 to Tg
% options = [];
[tTSD,YTSD] =
ode15s(@dsdPTSD,tstorage,ystorage,options,s,T0,epsilon,gamma,height,0,ar,AK
T,CKT,Tm,Tc);
%
% TSD Current Calculation
% Initialize values for TSD current calculation
%
sigmagcTSD = zeros(length(YTSD),1);
PsCTSD = zeros(length(YTSD),1);
dpsdtTSD = zeros(length(YTSD),1);
dsgcdtTSD = zeros(length(YTSD),1);
BwTSD = zeros(length(YTSD),1);
gcTSD = zeros(length(YTSD),1);
ggTSD = zeros(length(YTSD),1);
gsTSD = zeros(length(YTSD),1);
GgcTSD = zeros(length(YTSD),1);
GcsTSD = zeros(length(YTSD),1);
VgTSD = zeros(length(YTSD),1);
EgTSD = zeros(length(YTSD),1);
jrTSD = zeros(length(YTSD),1);
jpTSD = zeros(length(YTSD),1);
jbTSD = zeros(length(YTSD),1);
%
% Current Density Calculation during TSD (jr)
```

```
%
PsCTSD(1:length(YTSD),1) = YTSD(1:length(YTSD),2);
sigmagcTSD(1:length(YTSD),1) = YTSD(1:length(YTSD),1);
gcTSD(1:length(YTSD)) = arrenhius(tTSD*s+273,gc0,CKTc,Tcc);      % 273
sets temp = 273 at time = 0
ggTSD(1:length(YTSD)) = arrenhius(tTSD*s+273,gg0,CKTg,Tcg);      % 273
sets temp = 273 at time = 0
gsTSD(1:length(YTSD)) = arrenhius(tTSD*s+273,gs0,CKTs,Tcs);      % 273 sets
temp = 273 at time = 0
GcsTSD(1:length(YTSD)) = 1./(1+gcTSD./gsTSD);
GgcTSD(1:length(YTSD)) = 1./(e0*eg/hg + e0*ec*GcsTSD/hc);
%GgcTSD solved for Vp=0
BwTSD(1:length(YTSD)) = (ggTSD/hg + gcTSD.*GcsTSD/hc)./(e0*eg/hg +
e0*ec*GcsTSD/hc);  %BwTSD solved for Vp=0
dsgcdtTSD(1:length(YTSD)) = BwTSD.*(PsCTSD-sigmagcTSD);
dpsdtTSD(1:length(YTSD)) =
(arrenhius(tTSD*s+273,ar,AKT,Tm)).*((e0/hg)*(eslow - eg)*sigmagcTSD -
((e0/hg)*(eslow - eg)+(e0*eg/hg +
e0*ec*GcsTSD/hc)).*PsCTSD)./(e0*eg/hg+e0*ec*GcsTSD/hc);
VgTSD(1:length(YTSD)) = (sigmagcTSD-
PsCTSD)./(e0*eg/hg+e0*ec*GcsTSD/hc);
jrTSD(1:length(YTSD)) = (e0*eg*GgcTSD/hg).*dsgcdtTSD + (1-
e0*eg*GgcTSD/hg).*dpsdtTSD + ggTSD.*GgcTSD/hg.*(sigmagcTSD -
PsCTSD);        % total current density
jpTSD(1:length(YTSD)) = (1-e0*eg*GgcTSD/hg).*dpsdtTSD+
ggTSD.*GgcTSD/hg.*(-PsCTSD);   % Polarization charge current density
jbTSD(1:length(YTSD)) = (e0*eg*GgcTSD/hg).*dsgcdtTSD +
ggTSD.*GgcTSD/hg.*(sigmagcTSD);   % Boundary Charge current density
%
% Note:  sigmagcC, PsC, jp, jc, jt are all calculated interms of K, NOT C, so plot
scale must put ratios
%         in K.  s = C/sec = K/sec.
tTSDcelcius = (tTSD*s);            %Celcius Temperatures
tTSDrelative = (tTSD*s+273)/Tm;    %Relative Kelvin values
figure(11)
axes('fontsize',12)
plot(tTSDcelcius,sigmagcTSD/q0(1),'k',tTSDcelcius,PsCTSD/q0(1),'--k')
% legend('boundary charge density (sigmagc)','polarization charge density (Ps)',0)
% title ('Polarization Charge Density and Boundary Charge Density during TSD')
ylabel('Charge Density/sigmagc(inf)','fontsize',14), xlabel(sprintf('Temperature T
(C) for Tg = %3.2f C',Tm-273),'fontsize',14)
figure(12)
axes('fontsize',12)
plot(tTSDcelcius,jrTSD,'k',tTSDcelcius,jpTSD,'--k',tTSDcelcius,jbTSD,':k')
% legend('Released Current Density (jr)','Polarization Current Density
(jp)','Boundary Current Density (jb)',0)
% title ('Total, Polarization, and Conduction Current Density during TSD')
```

```
ylabel('Current Density (A/m^2)','fontsize',14), xlabel(sprintf('Temperature T (C)
for Tg = %3.2f C',Tm-273),'fontsize',14)
```

791-2 Polar Current Experiment

```
%Script File:  PolarCurrent 791_2 Experiment
%Solves for the polarization and boundary charge in Poling and TSD current
density equations to match Experimental Data
%Wafer #791-2 (NOA71-CLDX/APC-NOA71)
%
close all
% index of refraction values
nc = 1.546;
ng = 1.638;
ns = 1.546;
%
% height values
%
hc = 2.79e-6;
hg = 3.61e-6;
hs = 3.1e-6;
height = [ hc hg hs ];
%
% gamma (conductance)
%
gg0 = 1e20;
gc0 = .7e9;
gs0 = gc0;
gamma = [ gc0 gg0 gs0 ];
%
% epsilon (permitivity)
%
e0 = 8.854e-12;
ec = nc^2;          % High Frequency Dielectric Constant
eg = ng^2;          % High Frequency Dielectric Constant
eslow = 4.6;        % Low Frequency Dielectric Constant for core
es = ns^2;
epsilon = [ ec eg es e0 eslow ];
%
% Poling Voltage
%
Vp = 500;
%
% Dipole relaxation frequency and conduction activation energy
%
ar =1.5e20;                 % Dipole Natural Relaxation Frequency in 1/seconds
Ea = 2;                     % in eV
Ec = 1.9;                   % in eV
AKT = 56;
Tm = Ea*(1.6e-19)/((1.381e-23)*AKT);   %Tm in K; Baseline:  A/kT = 55
```

```
CKTc = AKT*(1.13);              % Upper Cladding Conductance activation
energy
CKTg = AKT*(1.5);               % Core Conductance activation energy
CKTs = CKTc;                    % Lower Cladding Conductance activation energy
Tcc = Ec*(1.6e-19)/((1.381e-23)*CKTc);      %Norlund Tg is 50 - 100 C
depending on crosslinking.
Tcg = Tm/.85;                   %Tm/Tc = .85
Tcs = Tcc;
CKT = [ CKTc CKTg CKTs ];
Tc = [ Tcc Tcg Tcs ];
%
% Time (seconds) and heating rate
%
Tg = 419;                       % Degrees Kelvin
T0 = 273;                       % Initial temperature in Kelvin
s = 50/60;                      % Celsius per seconds  Baseline:  44/60
t = [ 0 (Tg-T0)/s];             % time in seconds to go from T0 to Tg
%
% Solve for Ps(t) during charging
%
%
% ODE solver
%
% Calculate Current Density, J, based on Ps and sigmacg
%
PsC = 0;        % no polarization (random orientation) initially
sigmacg = 0;    % no boundary charge initially
y0 = [ sigmacg PsC ];
options = odeset('RelTol',3e-14,'AbsTol',1e-15);
[t1,Y1] =
ode15s(@dsdP,t,y0,options,s,T0,epsilon,gamma,height,Vp,ar,AKT,CKT,Tm,Tc);
%
% Initialize values for current calculation
%
Bw = zeros(length(Y1),1);
dpsdt = zeros(length(Y1),1);
dsgcdt = zeros(length(Y1),1);
gc = zeros(length(Y1),1);
gg = zeros(length(Y1),1);
gs = zeros(length(Y1),1);
Ggc = zeros(length(Y1),1);
Gcs = zeros(length(Y1),1);
PsC = zeros(length(Y1),1);
sigmagcC = zeros(length(Y1),1);
Vg = zeros(length(Y1),1);
Eg = zeros(length(Y1),1);
jt = zeros(length(Y1),1);
```

```
jp = zeros(length(Y1),1);
jb = zeros(length(Y1),1);
jc = zeros(length(Y1),1);
%
% Current Density Calculation during Charging (jt)
%
PsC(1:length(Y1),1) = Y1(1:length(Y1),2);
sigmagcC(1:length(Y1),1) = Y1(1:length(Y1),1);
gc(1:length(Y1)) = arrenhius(t1*s+273,gc0,CKTc,Tcc);        %273 sets temp =
273 at time = 0
gg(1:length(Y1)) = arrenhius(t1*s+273,gg0,CKTg,Tcg);        %273 sets temp =
273 at time = 0
gs(1:length(Y1)) = arrenhius(t1*s+273,gs0,CKTs,Tcs);        %273 sets temp =
273 at time = 0
Ggc(1:length(Y1)) = 1+(hc*gg)./(hg*gc);
Gcs(1:length(Y1)) = 1./(1+gc./gs);
Bw(1:length(Y1)) = gc./(hc*(e0*ec*Gcs/hc + e0*eg/hg));
dsgcdt(1:length(Y1)) = Ggc.*Bw.*(PsC -
sigmagcC)+Bw.*Gcs.*((e0*eg/hg)+(e0*ec/hc).*(Gcs-Ggc))*Vp;
dpsdt(1:length(t1)) = (arrenhius(t1*s+273,ar,AKT,Tm)).*(((eslow-
eg)*(e0*Vp+(hc/ec)*sigmagcC))-
(hg*Gcs+(hc*eslow/ec)).*PsC)./(hg*Gcs+(hc*eg/ec));
Vg(1:length(t1)) = ((e0*ec*Gcs*Vp/hc)+sigmagcC-
PsC)./((e0*eg/hg)*(1+Gcs*ec*hg/(hc*eg)));
jt(1:length(t1)) = (gg.*(sigmagcC - PsC + e0*ec*Gcs*Vp/hc) + e0*eg*dsgcdt/hg
+ e0*ec*Gcs.*dpsdt/hc)./(hg*(e0*eg/hg + e0*ec*Gcs/hc));  % total current
density
jp(1:length(t1)) =(gg.*(-PsC) + e0*ec*Gcs.*dpsdt/hc)./(hg*(e0*eg/hg +
e0*ec*Gcs/hc));      % Polar current density
jb(1:length(t1)) =(gg.*(sigmagcC) + e0*eg*dsgcdt/hg)./(hg*(e0*eg/hg +
e0*ec*Gcs/hc));   % Conduction current density
jc(1:length(t1)) =(gg.*(e0*ec*Gcs*Vp/hc))./(hg*(e0*eg/hg + e0*ec*Gcs/hc));   %
Conduction current density
scginf = e0*Vp*((eslow-eg) +
(Gcs./Ggc).*(hg*Gcs+hc*eslow/ec).*(eg/hg+(ec/hc)*(Gcs-
Ggc)))./(hg*Gcs+hc*eg/ec);  % Infinite value of boundary charge
q0 = scginf;                                    % q0 is maximum charge density
Psinf = e0*(eslow-eg)*((1 + (Gcs./Ggc).*(eg*hc/(ec*hg)+Gcs-Ggc))./(hg*Gcs +
hc*eg/ec))*Vp;  % Infinite value of Polarization Charge
%
% Experimental Charging
%
Data = xlsread('D:\Projects\Avionics\Phd\Wafer791PolingData', 'Sheet2');
ElectrodeArea = 79e-6;              % Electrode area in m^2
jtexp = Data(13:19,7)/ElectrodeArea;    % Poling current densities in A/m^2
Tcexp = Data(13:19,5)+273;          % Poling current temperatures adjusted to
Kelvin
```

```
tcexp = Data(13:19,6)-1800;                % Poling time in seconds
%
% Note:  sigmagcC, PsC, jp, jc, jt are all calculated interms of K, NOT C, so plot
scale must put ratios
%          in K.  s = C/sec = K/sec.
t1celcius = (t1*s);            %Celcius Temperatures
t1relative = (t1*s+273)/Tm;    %Relative Kelvin values
figure(1)
axes('fontsize',12)
plot(t1celcius,sigmagcC/q0(1),'k',t1celcius,PsC/q0(1),'--k')
%legend('boundary charge density (sigmagc)','polarization charge density (Ps)',0)
%title (sprintf('Polarization and Boundary Charge Densities during Thermal
Charging for Vp = %3d V',Vp))
ylabel('Charge Density/sigmagc(inf)','fontsize',14), xlabel(sprintf('Temperature T
(C) for Tg = %3.2f C',Tm-273),'fontsize',14)
figure(2)
axes('fontsize',12)
plot(t1celcius,jt,'k',t1celcius,jp,'--kD',t1celcius,jb,':k',t1celcius,jc,'-.k')
% legend('Total Current Density (jt)','Polarization Current Density (jp)','Boundary
Charge Current Density (jb)','Conduction Current Density (jc)',0)
% title (sprintf('Total, Polarization, and Conduction Current Density during
Thermal Charging for Vp = %3d V',Vp))
ylabel('Current Density (A/m^2)','fontsize',14), xlabel(sprintf('Temperature T (C)
for Tg = %3.2f C',Tm-273),'fontsize',14)
figure(3)
axes('fontsize',12)
plot(t1celcius,jt,'k',Tcexp-273,jtexp,'--ko')
% legend('Total Current Density (jt)','Experimental Total Current Density
(jtexp)',0)
% title (sprintf('Total Modeled and Experimental Current Density during Poling
for Vp = %3d V',Vp))
ylabel('Current Density (A/m^2)','fontsize',14), xlabel(sprintf('Temperature T (C)
for Tg = %3.2f C',Tm-273),'fontsize',14)
%
%  Dwell Time
%
Td = Tg;        %dwell temperature:  145 C
tdwellmax = 1800;   %maximum dwell time in seconds
sdwell = 0;
PsCmax = PsC(length(Y1));          % Polarization charge initialized at max
temperature
sigmagcCmax = sigmagcC(length(Y1));   % Boundary charge initialized at max
temperature
ymax = [ sigmagcCmax PsCmax ];
tdwell = [ t1(length(t1)) t1(length(t1))+tdwellmax ];        %Initial conditions set
the value properly, time should start at zero sec with time to go from Tg to T0
```

```
[t1d,Ydwell] =
ode15s(@dsdPdwell,tdwell,ymax,options,sdwell,Td,epsilon,gamma,height,Vp,ar,
AKT,CKT,Tm,Tc);
%
% Initialize values for current calculation
%
Bwdwell = zeros(length(Ydwell),1);
dpsdtdwell = zeros(length(Ydwell),1);
dsgcdtdwell = zeros(length(Ydwell),1);
gcdwell = zeros(length(Ydwell),1);
ggdwell = zeros(length(Ydwell),1);
gsdwell = zeros(length(Ydwell),1);
Ggcdwell = zeros(length(Ydwell),1);
Gcsdwell = zeros(length(Ydwell),1);
PsCdwell = zeros(length(Ydwell),1);
sigmagcdwell = zeros(length(Ydwell),1);
Vgdwell = zeros(length(Ydwell),1);
Egdwell = zeros(length(Ydwell),1);
jtdwell = zeros(length(Ydwell),1);
jpdwell = zeros(length(Ydwell),1);
jbdwell = zeros(length(Ydwell),1);
jcdwell = zeros(length(Ydwell),1);
%
% Current Density Calculation during Dwell (jt)
%
PsCdwell(1:length(Ydwell),1) = Ydwell(1:length(Ydwell),2);
sigmagcdwell(1:length(Ydwell),1) = Ydwell(1:length(Ydwell),1);
gcdwell(1:length(Ydwell)) = arrenhius(Td,gc0,CKTc,Tcc);
ggdwell(1:length(Ydwell)) = arrenhius(Td,gg0,CKTg,Tcg);
gsdwell(1:length(Ydwell)) = arrenhius(Td,gs0,CKTs,Tcs);
Ggcdwell(1:length(Ydwell)) = 1+(hc*ggdwell)./(hg*gcdwell);
Gcsdwell(1:length(Ydwell)) = 1./(1+gcdwell./gsdwell);
Bwdwell(1:length(Ydwell)) = gcdwell./(hc*(e0*ec*Gcsdwell/hc + e0*eg/hg));
dsgcdtdwell(1:length(Ydwell)) = Ggcdwell.*Bwdwell.*(PsCdwell -
sigmagcdwell)+Bwdwell.*Gcsdwell.*((e0*eg/hg)+(e0*ec/hc).*(Gcsdwell-
Ggcdwell))*Vp;
dpsdtdwell(1:length(t1d)) = (arrenhius(t1d*sdwell+Td,ar,AKT,Tm)).*(((eslow-
eg)*(e0*Vp+(hc/ec)*sigmagcdwell))-
(hg*Gcsdwell+(hc*eslow/ec)).*PsCdwell)./(hg*Gcsdwell+(hc*eg/ec));
Vgdwell(1:length(t1d)) = ((e0*ec*Gcsdwell*Vp/hc)+sigmagcdwell-
PsCdwell)./((e0*eg/hg)*(1+Gcsdwell*ec*hg/(hc*eg)));
jtdwell(1:length(t1d)) = (ggdwell.*(sigmagcdwell - PsCdwell +
e0*ec*Gcsdwell*Vp/hc) + e0*eg*dsgcdtdwell/hg +
e0*ec*Gcsdwell.*dpsdtdwell/hc)./(hg*(e0*eg/hg + e0*ec*Gcsdwell/hc));  %
total current density
```

```
jpdwell(1:length(t1d)) =(ggdwell.*(-PsCdwell) +
e0*ec*Gcsdwell.*dpsdtdwell/hc)./(hg*(e0*eg/hg + e0*ec*Gcsdwell/hc));      %
Polar current density
jbdwell(1:length(t1d)) =(ggdwell.*(sigmagcdwell) +
e0*eg*dsgcdtdwell/hg)./(hg*(e0*eg/hg + e0*ec*Gcsdwell/hc));   % Conduction
current density
jcdwell(1:length(t1d)) =(ggdwell.*(e0*ec*Gcsdwell*Vp/hc))./(hg*(e0*eg/hg +
e0*ec*Gcsdwell/hc));   % Conduction current density
%
figure(4)
axes('fontsize',12)
plot(t1d,sigmagcdwell/q0(1),'+k',t1d,PsCdwell/q0(1),'--k')
% legend('boundary charge density (sigmagc)','polarization charge density (Ps)',0)
% title (sprintf('Polarization and Boundary Charge Densities Thermal Charging
Dwell for Vp = %3d V',Vp))
ylabel('Charge Density/sigmagc(inf)','fontsize',14), xlabel(sprintf('Time (s) for
Tdwell = %3.2f C',Td-273),'fontsize',14)
figure(5)
axes('fontsize',12)
plot(t1d,jtdwell,'k',t1d,jpdwell,'--k',t1d,jbdwell,':k',t1d,jcdwell,'-.k')
% legend('Total Current Density (jt)','Polarization Current Density (jp)','Boundary
Charge Current Density (jb)','Conduction Current Density (jc)',0)
% title (sprintf('Total, Polarization, and Conduction Current Density during
Thermal Charging Dwell for Vp = %3d V',Vp))
ylabel('Current Density (A/m^2)','fontsize',14), xlabel(sprintf('Time (s) for Tdwell
= %3.2f C',Td-273),'fontsize',14)
%
% Cool Down Current (too calculate TSD initial point)
%
PsCmaxd = PsCdwell(length(Ydwell));          % Polarization charge initialized
at max temperature
sigmagcCmaxd = sigmagcdwell(length(Ydwell));   % Boundary charge initialized
at max temperature
ymaxd = [ sigmagcCmaxd PsCmaxd ];
Tmax = Tg;                                % in Kelvin
scool = 33.3/60;                           % Cool down rate  C/min = C/(60 sec)=
K/(60 sec)
tc = [ t1d(length(t1d)) t1d(length(t1d))+(Tmax-T0)/scool ];        %Initial
conditions set the value properly, time should start at zero sec with time to go
from Tg to T0
options1 = odeset('RelTol',3e-14,'AbsTol',1e-15);
[tcool,Ycool] =
ode15s(@dsdPcool,tc,ymaxd,options1,scool,Tmax,epsilon,gamma,height,Vp,ar,A
KT,CKT,Tm,Tc,t1d(length(t1d)));
%
% Initialize values for current calculation
%
```

```
tcoolrev = zeros(length(tcool),1);
sigmagccool = zeros(length(Ycool),1);
PsCcool = zeros(length(Ycool),1);
dpsdtcool = zeros(length(Ycool),1);
dsgcdtcool = zeros(length(Ycool),1);
Bwcool = zeros(length(Ycool),1);
gccool = zeros(length(Ycool),1);
ggcool = zeros(length(Ycool),1);
gscool = zeros(length(Ycool),1);
Ggccool = zeros(length(Ycool),1);
Gcscool = zeros(length(Ycool),1);
Vgcool = zeros(length(Ycool),1);
Egcool = zeros(length(Ycool),1);
jtcool = zeros(length(Ycool),1);
jpcool = zeros(length(Ycool),1);
jbcool = zeros(length(Ycool),1);
jccool = zeros(length(Ycool),1);
sigmagccoolmax = 0;
PsCcoolmax = 0;
dwellcharge = [ 0 0 0 ];
%
% Current Density Calculation during Charging (jt)
%
PsCcool(1:length(Ycool),1) = Ycool(1:length(Ycool),2);
sigmagccool(1:length(Ycool),1) = Ycool(1:length(Ycool),1);
gccool(1:length(Ycool)) = arrenhius(Tmax-(tcool-
min(tcool))*scool,gc0,CKTc,Tcc);  % Initialize Temperature to Tmax-
(max(tcool)-tcool)*scool to adjust for time shift from start
ggcool(1:length(Ycool)) = arrenhius(Tmax-(tcool-
min(tcool))*scool,gg0,CKTg,Tcg);  % Initialize Temperature to Tmax-
(max(tcool)-tcool)*scool to adjust for time shift from start
gscool(1:length(Ycool)) = arrenhius(Tmax-(tcool-
min(tcool))*scool,gs0,CKTs,Tcs);  % Initialize Temperature to Tmax-
(max(tcool)-tcool)*scool to adjust for time shift from start
Ggccool(1:length(Ycool)) = 1+(hc*ggcool)./(hg*gccool);
Gcscool(1:length(Ycool)) = 1./(1+gccool./gscool);
Bwcool(1:length(Ycool)) = gccool./(hc*(e0*ec*Gcscool/hc + e0*eg/hg));
dsgcdtcool(1:length(Ycool)) = Ggccool.*Bwcool.*(PsCcool -
sigmagccool)+Bwcool.*Gcscool.*((e0*eg/hg)+(e0*ec/hc).*(Gcscool-
Ggccool))*Vp;
dpsdtcool(1:length(tcool)) = (arrenhius(Tmax-(tcool-
min(tcool))*scool,ar,AKT,Tm)).*(((eslow-eg)*(e0*Vp+(hc/ec)*sigmagccool))-
(hg*Gcscool+(hc*eslow/ec)).*PsCcool)./(hg*Gcscool+(hc*eg/ec));
Vgcool(1:length(tcool)) = ((e0*ec*Gcscool*Vp/hc)+sigmagccool-
PsCcool)./((e0*eg/hg)*(1+Gcscool*ec*hg/(hc*eg)));
jtcool(1:length(tcool)) =(ggcool.*(sigmagccool - PsCcool +
e0*ec*Gcscool*Vp/hc) + e0*eg*dsgcdtcool/hg +
```

```
e0*ec*Gcscool.*dpsdtcool/hc)./(hg*(e0*eg/hg + e0*ec*Gcscool/hc));  % total
current density
jpcool(1:length(tcool)) =(ggcool.*(-PsCcool) +
e0*ec*Gcscool.*dpsdtcool/hc)./(hg*(e0*eg/hg + e0*ec*Gcscool/hc));       %
Polar current density
jbcool(1:length(tcool)) =(ggcool.*(sigmagccool) +
e0*eg*dsgcdtcool/hg)./(hg*(e0*eg/hg + e0*ec*Gcscool/hc));   % Boundary
Charge current density
jccool(1:length(tcool)) =(ggcool.*(e0*ec*Gcscool*Vp/hc))./(hg*(e0*eg/hg +
e0*ec*Gcscool/hc));   % Conduction current density
%
% Experimental Cool Down
%
ElectrodeArea1 = 79e-6;                                    %Electrode area in
m^2
jcoolexp = Data(19:73,7)/ElectrodeArea;    % Poling current densities in A/m^2
Tcoolexp = Data(19:73,5)+273;              % Poling current temperatures adjusted
to Kelvin
tccoolexp = Data(19:73,6)-1800;                % Poling time in seconds
%
% Note:  sigmagcC, PsC, jp, jc, jt are all calculated interms of K, NOT C, so plot
scale must put ratios
%         in K.  s = C/sec = K/sec.
tcoolcelcius = Tmax-(max(tcool)-tcool)*scool-273;          %Celcius
Temperatures
tcoolrelative = (Tmax-(max(tcool)-tcool)*scool+273)/Tm;    %Relative Kelvin
values
plotrange = 10:length(tcool);
sigmagccoolmax = sigmagccool(length(Ycool),1)/q0(1);
PsCcoolmax = PsCcool(length(Ycool),1)/Psinf(1);
dwellcharge = [ tdwellmax sigmagccoolmax PsCcoolmax ];
%
% Write maximum normalized charge to file to produce charge vs. dwell time
plots
%
% fid = fopen('d:/projects/avionics/phd/dwelltemp.txt','a');       % If file exists, use
'w' to write over, then switch to append 'a'
% fprintf(fid,'%8d %2.4f %2.4f',tdwellmax, sigmagccoolmax, PsCcoolmax);
% fclose(fid);
figure(6)
axes('fontsize',12)
plot(tcoolcelcius,sigmagccool/q0(1),'+k',tcoolcelcius,PsCcool/q0(1),'--k')
% legend('boundary charge density (sigmagc)','polarization charge density (Ps)',0)
% title (sprintf('Polarization and Boundary Charge Densities during Cool down
for Vp = %3d V',Vp))
ylabel('Charge Density/sigmagc(inf)','fontsize',14), xlabel(sprintf('Temperature T
(C) for Tg = %3.2f C',Tm-273),'fontsize',14)
```

```
prangemin = 55;
prangemax = length(Ycool);
figure(7)
axes('fontsize',12)
plot(tcoolcelcius(prangemin:prangemax),jtcool(prangemin:prangemax),'+k',tcoolc
elcius(prangemin:prangemax),jpcool(prangemin:prangemax),'--
k',tcoolcelcius(prangemin:prangemax),jbcool(prangemin:prangemax),':k',tcoolcelc
ius(prangemin:prangemax),jccool(prangemin:prangemax),'-.k')
% legend('Total Current Density (jt)','Polarization Current Density (jp)','Boundary
Charge Current Density (jb)','Conduction Current Density (jc)',0)
% title (sprintf('Total, Polarization, and Conduction Current Density during Cool
Down for Vp = %3d V',Vp))
ylabel('Current Density (A/m^2)','fontsize',14), xlabel(sprintf('Temperature T (C)
for Tg = %3.2f C',Tm-273),'fontsize',14)
figure(8)
axes('fontsize',12)
plot(tcoolcelcius,jtcool,'k',tccoolexp-273,jcoolexp,'--ko')
% legend('Total Current Density (jt)','Experimental Total Current Density
(jtexp)',0)
% title (sprintf('Total Modeled and Experimental Current Density during Cool
Down for Vp = %3d V',Vp))
ylabel('Current Density (A/m^2)','fontsize',14), xlabel(sprintf('Temperature T (C)
for Tg = %3.2f C',Tm-273),'fontsize',14)
%
% Full Plots
%
jexp = Data(13:73,7)/(ElectrodeArea);    % Poling current densities in A/m^2
Texp = Data(13:73,5)+273;              % Poling current temperatures adjusted to
Kelvin
texp = Data(13:73,6)-1800;               % Poling time in seconds adjusted to
remove 30 min purge
figure(9)
axes('fontsize',12)
plot(t1,sigmagcC/q0(1),'+k',t1d,sigmagcdwell/q0(1),'+k',tcool,sigmagccool/q0(1),'
+k',t1,PsC/q0(1),'--k',t1d,PsCdwell/q0(1),'--k',tcool,PsCcool/q0(1),'--k')
% legend('boundary charge density (sigmagc)','polarization charge density (Ps)',0)
% title (sprintf('Polarization and Boundary Charge Densities during Cool down
for Vp = %3d V',Vp))
ylabel('Charge Density/sigmagc(inf)','fontsize',14), xlabel(sprintf('time (s) for Tg
= %3.2f C',Tm-273),'fontsize',14)
figure(10)
axes('fontsize',12)
%plot(t1,jt,'k',t1d,jtdwell,'k',tcool,jtcool,'k')
plot(t1,jt,'k',t1,jp,'--k',t1,jb,':k',t1,jc,'-.k',t1d,jtdwell,'k',t1d,jpdwell,'--
k',t1d,jbdwell,':k',t1d,jcdwell,'-.k',tcool,jtcool,'k',tcool,jpcool,'--
k',tcool,jbcool,':k',tcool,jccool,'-.k',texp,jexp,'-ko')
```

```
% legend('Total Current Density (jt)','Experimental Total Current Density
(jtexp)',0)
% title (sprintf('Total Modeled and Experimental Current Density during Cool
Down for Vp = %3d V',Vp))
ylabel('Current Density (A/m^2)','fontsize',14), xlabel(sprintf('time (s) for Tg =
%3.2f C',Tm-273),'fontsize',14)
%
%  TSD Current Calculation
%
tTSD = 0;
YTSD = 0;
PsCstorage = 0;
sigmagcCstorage = 0;
PsCstorage = PsCcool(length(Ycool));          % Polarization charge initialized at
max temperature
sigmagcCstorage = sigmagccool(length(Ycool));   % Polarization charge
initialized at max temperature
ystorage = [ sigmagcCstorage PsCstorage ];
tstorage= [ 0 (Tg-T0)/s ];                    % Time to get from T0 to Tg
% options = [];
[tTSD,YTSD] =
ode15s(@dsdPTSD,tstorage,ystorage,options,s,T0,epsilon,gamma,height,0,ar,AK
T,CKT,Tm,Tc);
%
% TSD Current Calculation
% Initialize values for TSD current calculation
%
sigmagcTSD = zeros(length(YTSD),1);
PsCTSD = zeros(length(YTSD),1);
dpsdtTSD = zeros(length(YTSD),1);
dsgcdtTSD = zeros(length(YTSD),1);
BwTSD = zeros(length(YTSD),1);
gcTSD = zeros(length(YTSD),1);
ggTSD = zeros(length(YTSD),1);
gsTSD = zeros(length(YTSD),1);
GgcTSD = zeros(length(YTSD),1);
GcsTSD = zeros(length(YTSD),1);
VgTSD = zeros(length(YTSD),1);
EgTSD = zeros(length(YTSD),1);
jrTSD = zeros(length(YTSD),1);
jpTSD = zeros(length(YTSD),1);
jbTSD = zeros(length(YTSD),1);
%
% Current Density Calculation during TSD (jr)
%
PsCTSD(1:length(YTSD),1) = YTSD(1:length(YTSD),2);
sigmagcTSD(1:length(YTSD),1) = YTSD(1:length(YTSD),1);
```

```
gcTSD(1:length(YTSD)) = arrenhius(tTSD*s+273,gc0,CKTc,Tcc);      % 273
sets temp = 273 at time = 0
ggTSD(1:length(YTSD)) = arrenhius(tTSD*s+273,gg0,CKTg,Tcg);      % 273
sets temp = 273 at time = 0
gsTSD(1:length(YTSD)) = arrenhius(tTSD*s+273,gs0,CKTs,Tcs);      % 273 sets
temp = 273 at time = 0
GcsTSD(1:length(YTSD)) = 1./(1+gcTSD./gsTSD);
GgcTSD(1:length(YTSD)) = 1./(e0*eg/hg + e0*ec*GcsTSD/hc);
%GgcTSD solved for Vp=0
BwTSD(1:length(YTSD)) = (ggTSD/hg + gcTSD.*GcsTSD/hc)./(e0*eg/hg +
e0*ec*GcsTSD/hc);  %BwTSD solved for Vp=0
dsgcdtTSD(1:length(YTSD)) = BwTSD.*(PsCTSD-sigmagcTSD);
dpsdtTSD(1:length(YTSD)) =
(arrenhius(tTSD*s+273,ar,AKT,Tm)).*((e0/hg)*(eslow - eg)*sigmagcTSD -
((e0/hg)*(eslow - eg)+(e0*eg/hg +
e0*ec*GcsTSD/hc)).*PsCTSD)./(e0*eg/hg+e0*ec*GcsTSD/hc);
VgTSD(1:length(YTSD)) = (sigmagcTSD-
PsCTSD)./(e0*eg/hg+e0*ec*GcsTSD/hc);
jrTSD(1:length(YTSD)) = (e0*eg*GgcTSD/hg).*dsgcdtTSD + (1-
e0*eg*GgcTSD/hg).*dpsdtTSD + ggTSD.*GgcTSD/hg.*(sigmagcTSD -
PsCTSD);        % total current density
jpTSD(1:length(YTSD)) = (1-e0*eg*GgcTSD/hg).*dpsdtTSD+
ggTSD.*GgcTSD/hg.*(-PsCTSD);   % Polarization charge current density
jbTSD(1:length(YTSD)) = (e0*eg*GgcTSD/hg).*dsgcdtTSD +
ggTSD.*GgcTSD/hg.*(sigmagcTSD);   % Boundary Charge current density
%
% Note:  sigmagcC, PsC, jp, jc, jt are all calculated interms of K, NOT C, so plot
scale must put ratios
%         in K.  s = C/sec = K/sec.
tTSDcelcius = (tTSD*s);            %Celcius Tempcratures
tTSDrelative = (tTSD*s+273)/Tm;     %Relative Kelvin values
figure(11)
axes('fontsize',12)
plot(tTSDcelcius,sigmagcTSD/q0(1),'k',tTSDcelcius,PsCTSD/q0(1),'--k')
% legend('boundary charge density (sigmagc)','polarization charge density (Ps)',0)
% title ('Polarization Charge Density and Boundary Charge Density during TSD')
ylabel('Charge Density/sigmagc(inf)','fontsize',14), xlabel(sprintf('Temperature T
(C) for Tg = %3.2f C',Tm-273),'fontsize',14)
figure(12)
axes('fontsize',12)
plot(tTSDcelcius,jrTSD,'k',tTSDcelcius,jpTSD,'--k',tTSDcelcius,jbTSD,':k')
% legend('Released Current Density (jr)','Polarization Current Density
(jp)','Boundary Current Density (jb)',0)
% title ('Total, Polarization, and Conduction Current Density during TSD')
ylabel('Current Density (A/m^2)','fontsize',14), xlabel(sprintf('Temperature T (C)
for Tg = %3.2f C',Tm-273),'fontsize',14)
```

791-3 Polar Current Experiment

```
%Script File:  PolarCurrent 791_3 Experiment
%Solves for the polarization and boundary charge in Poling and TSD current
density equations to match Experimental Data
%Wafer #791-3 (NOA71-CLDX/APC-NOA71)
%
close all
% index of refraction values
nc = 1.546;
ng = 1.638;
ns = 1.546;
%
% height values
%
hc = 2.79e-6;
hg = 3.61e-6;
hs = 3.1e-6;
height = [ hc hg hs ];
%
% gamma (conductance)
%
gg0 = 1e20;
gc0 = .5e9;
gs0 = gc0;
gamma = [ gc0 gg0 gs0 ];
%
% epsilon (permitivity)
%
e0 = 8.854e-12;
ec = nc^2;          % High Frequency Dielectric Constant
eg = ng^2;          % High Frequency Dielectric Constant
eslow = 4.6;        % Low Frequency Dielectric Constant for core
es = ns^2;
epsilon = [ ec eg es e0 eslow ];
%
% Poling Voltage
%
Vp = 500;
%
% Dipole relaxation frequency and conduction activation energy
%
ar =1.1e20;                 % Dipole Natural Relaxation Frequency in 1/seconds
Ea = 2;                     % in eV
Ec = 1.9;                   % in eV
AKT = 56;
Tm = Ea*(1.6e-19)/((1.381e-23)*AKT);   %Tm in K; Baseline:  A/kT = 55
```

```
CKTc = AKT*(1.13);              % Upper Cladding Conductance activation
energy
CKTg = AKT*(1.5);               % Core Conductance activation energy
CKTs = CKTc;                    % Lower Cladding Conductance activation energy
Tcc = Ec*(1.6e-19)/((1.381e-23)*CKTc);      %Norlund Tg is 50 - 100 C
depending on crosslinking.
Tcg = Tm/.85;                   %Tm/Tc = .85
Tcs = Tcc;
CKT = [ CKTc CKTg CKTs ];
Tc = [ Tcc Tcg Tcs ];
%
% Time (seconds) and heating rate
%
Tg = 419;                       % Degrees Kelvin
T0 = 273;                       % Initial temperature in Kelvin
s = 50/60;                      % Celsius per seconds  Baseline:  44/60
t = [ 0 (Tg-T0)/s];             % time in seconds to go from T0 to Tg
%
% Solve for Ps(t) during charging
%
%
% ODE solver
%
% Calculate Current Density, J, based on Ps and sigmacg
%
PsC = 0;        % no polarization (random orientation) initially
sigmacg = 0;    % no boundary charge initially
y0 = [ sigmacg PsC ];
options = odeset('RelTol',3e-14,'AbsTol',1e-15);
[t1,Y1] =
ode15s(@dsdP,t,y0,options,s,T0,epsilon,gamma,height,Vp,ar,AKT,CKT,Tm,Tc);
%
% Initialize values for current calculation
%
Bw = zeros(length(Y1),1);
dpsdt = zeros(length(Y1),1);
dsgcdt = zeros(length(Y1),1);
gc = zeros(length(Y1),1);
gg = zeros(length(Y1),1);
gs = zeros(length(Y1),1);
Ggc = zeros(length(Y1),1);
Gcs = zeros(length(Y1),1);
PsC = zeros(length(Y1),1);
sigmagcC = zeros(length(Y1),1);
Vg = zeros(length(Y1),1);
Eg = zeros(length(Y1),1);
jt = zeros(length(Y1),1);
```

```
jp = zeros(length(Y1),1);
jb = zeros(length(Y1),1);
jc = zeros(length(Y1),1);
%
% Current Density Calculation during Charging (jt)
%
PsC(1:length(Y1),1) = Y1(1:length(Y1),2);
sigmagcC(1:length(Y1),1) = Y1(1:length(Y1),1);
gc(1:length(Y1)) = arrenhius(t1*s+273,gc0,CKTc,Tcc);        %273 sets temp =
273 at time = 0
gg(1:length(Y1)) = arrenhius(t1*s+273,gg0,CKTg,Tcg);        %273 sets temp =
273 at time = 0
gs(1:length(Y1)) = arrenhius(t1*s+273,gs0,CKTs,Tcs);        %273 sets temp =
273 at time = 0
Ggc(1:length(Y1)) = 1+(hc*gg)./(hg*gc);
Gcs(1:length(Y1)) = 1./(1+gc./gs);
Bw(1:length(Y1)) = gc./(hc*(e0*ec*Gcs/hc + e0*eg/hg));
dsgcdt(1:length(Y1)) = Ggc.*Bw.*(PsC -
sigmagcC)+Bw.*Gcs.*((e0*eg/hg)+(e0*ec/hc).*(Gcs-Ggc))*Vp;
dpsdt(1:length(t1)) = (arrenhius(t1*s+273,ar,AKT,Tm)).*(((eslow-
eg)*(e0*Vp+(hc/ec)*sigmagcC))-
(hg*Gcs+(hc*eslow/ec)).*PsC)./(hg*Gcs+(hc*eg/ec));
Vg(1:length(t1)) = ((e0*ec*Gcs*Vp/hc)+sigmagcC-
PsC)./((e0*eg/hg)*(1+Gcs*ec*hg/(hc*eg)));
jt(1:length(t1)) = (gg.*(sigmagcC - PsC + e0*ec*Gcs*Vp/hc) + e0*eg*dsgcdt/hg
+ e0*ec*Gcs.*dpsdt/hc)./(hg*(e0*eg/hg + e0*ec*Gcs/hc));  % total current
density
jp(1:length(t1)) =(gg.*(-PsC) + e0*ec*Gcs.*dpsdt/hc)./(hg*(e0*eg/hg +
e0*ec*Gcs/hc));      % Polar current density
jb(1:length(t1)) =(gg.*(sigmagcC) + e0*eg*dsgcdt/hg)./(hg*(e0*eg/hg +
e0*ec*Gcs/hc));   % Conduction current density
jc(1:length(t1)) =(gg.*(e0*ec*Gcs*Vp/hc))./(hg*(e0*eg/hg + e0*ec*Gcs/hc));   %
Conduction current density
scginf = e0*Vp*((eslow-eg) +
(Gcs./Ggc).*(hg*Gcs+hc*eslow/ec).*(eg/hg+(ec/hc)*(Gcs-
Ggc)))./(hg*Gcs+hc*eg/ec); % Infinite value of boundary charge
q0 = scginf;                                % q0 is maximum charge density
Psinf = e0*(eslow-eg)*((1 + (Gcs./Ggc).*(eg*hc/(ec*hg)+Gcs-Ggc))./(hg*Gcs +
hc*eg/ec))*Vp;  % Infinite value of Polarization Charge
%
% Experimental Charging
%
Data = xlsread('D:\Projects\Avionics\Phd\Wafer791PolingData', 'Sheet2');
ElectrodeArea = 79e-6;              % Electrode area in m^2
jtexp = Data(14:20,11)/ElectrodeArea;    % Poling current densities in A/m^2
Tcexp = Data(14:20,9)+273;          % Poling current temperatures adjusted to
Kelvin
```

```
tcexp = Data(14:20,10)-1800;                % Poling time in seconds
%
% Note:  sigmagcC, PsC, jp, jc, jt are all calculated interms of K, NOT C, so plot
scale must put ratios
%          in K.  s = C/sec = K/sec.
t1celcius = (t1*s);            %Celcius Temperatures
t1relative = (t1*s+273)/Tm;     %Relative Kelvin values
figure(1)
axes('fontsize',12)
plot(t1celcius,sigmagcC/q0(1),'k',t1celcius,PsC/q0(1),'--k')
%legend('boundary charge density (sigmagc)','polarization charge density (Ps)',0)
%title (sprintf('Polarization and Boundary Charge Densities during Thermal
Charging for Vp = %3d V',Vp))
ylabel('Charge Density/sigmagc(inf)','fontsize',14), xlabel(sprintf('Temperature T
(C) for Tg = %3.2f C',Tm-273),'fontsize',14)
figure(2)
axes('fontsize',12)
plot(t1celcius,jt,'k',t1celcius,jp,'--kD',t1celcius,jb,':k',t1celcius,jc,'-.k')
% legend('Total Current Density (jt)','Polarization Current Density (jp)','Boundary
Charge Current Density (jb)','Conduction Current Density (jc)',0)
% title (sprintf('Total, Polarization, and Conduction Current Density during
Thermal Charging for Vp = %3d V',Vp))
ylabel('Current Density (A/m^2)','fontsize',14), xlabel(sprintf('Temperature T (C)
for Tg = %3.2f C',Tm-273),'fontsize',14)
figure(3)
axes('fontsize',12)
plot(t1celcius,jt,'k',Tcexp-273,jtexp,'--ko')
% legend('Total Current Density (jt)','Experimental Total Current Density
(jtexp)',0)
% title (sprintf('Total Modeled and Experimental Current Density during Poling
for Vp = %3d V',Vp))
ylabel('Current Density (A/m^2)','fontsize',14), xlabel(sprintf('Temperature T (C)
for Tg = %3.2f C',Tm-273),'fontsize',14)
%
%  Dwell Time
%
Td = Tg;          %dwell temperature:  145 C
tdwellmax = 3600;    %maximum dwell time in seconds
sdwell = 0;
PsCmax = PsC(length(Y1));              % Polarization charge initialized at max
temperature
sigmagcCmax = sigmagcC(length(Y1));    % Boundary charge initialized at max
temperature
ymax = [ sigmagcCmax PsCmax ];
tdwell = [ t1(length(t1)) t1(length(t1))+tdwellmax ];          %Initial conditions set
the value properly, time should start at zero sec with time to go from Tg to T0
```

```
[t1d,Ydwell] =
ode15s(@dsdPdwell,tdwell,ymax,options,sdwell,Td,epsilon,gamma,height,Vp,ar,
AKT,CKT,Tm,Tc);
%
% Initialize values for current calculation
%
Bwdwell = zeros(length(Ydwell),1);
dpsdtdwell = zeros(length(Ydwell),1);
dsgcdtdwell = zeros(length(Ydwell),1);
gcdwell = zeros(length(Ydwell),1);
ggdwell = zeros(length(Ydwell),1);
gsdwell = zeros(length(Ydwell),1);
Ggcdwell = zeros(length(Ydwell),1);
Gcsdwell = zeros(length(Ydwell),1);
PsCdwell = zeros(length(Ydwell),1);
sigmagcdwell = zeros(length(Ydwell),1);
Vgdwell = zeros(length(Ydwell),1);
Egdwell = zeros(length(Ydwell),1);
jtdwell = zeros(length(Ydwell),1);
jpdwell = zeros(length(Ydwell),1);
jbdwell = zeros(length(Ydwell),1);
jcdwell = zeros(length(Ydwell),1);
%
% Current Density Calculation during Dwell (jt)
%
PsCdwell(1:length(Ydwell),1) = Ydwell(1:length(Ydwell),2);
sigmagcdwell(1:length(Ydwell),1) = Ydwell(1:length(Ydwell),1);
gcdwell(1:length(Ydwell)) = arrenhius(Td,gc0,CKTc,Tcc);
ggdwell(1:length(Ydwell)) = arrenhius(Td,gg0,CKTg,Tcg);
gsdwell(1:length(Ydwell)) = arrenhius(Td,gs0,CKTs,Tcs);
Ggcdwell(1:length(Ydwell)) = 1+(hc*ggdwell)./(hg*gcdwell);
Gcsdwell(1:length(Ydwell)) = 1./(1+gcdwell./gsdwell);
Bwdwell(1:length(Ydwell)) = gcdwell./(hc*(e0*ec*Gcsdwell/hc + e0*eg/hg));
dsgcdtdwell(1:length(Ydwell)) = Ggcdwell.*Bwdwell.*(PsCdwell -
sigmagcdwell)+Bwdwell.*Gcsdwell.*((e0*eg/hg)+(e0*ec/hc).*(Gcsdwell-
Ggcdwell))*Vp;
dpsdtdwell(1:length(t1d)) = (arrenhius(t1d*sdwell+Td,ar,AKT,Tm)).*(((eslow-
eg)*(e0*Vp+(hc/ec)*sigmagcdwell))-
(hg*Gcsdwell+(hc*eslow/ec)).*PsCdwell)./(hg*Gcsdwell+(hc*eg/ec));
Vgdwell(1:length(t1d)) = ((e0*ec*Gcsdwell*Vp/hc)+sigmagcdwell-
PsCdwell)./((e0*eg/hg)*(1+Gcsdwell*ec*hg/(hc*eg)));
jtdwell(1:length(t1d)) = (ggdwell.*(sigmagcdwell - PsCdwell +
e0*ec*Gcsdwell*Vp/hc) + e0*eg*dsgcdtdwell/hg +
e0*ec*Gcsdwell.*dpsdtdwell/hc)./(hg*(e0*eg/hg + e0*ec*Gcsdwell/hc));  %
total current density
```

```
jpdwell(1:length(t1d)) =(ggdwell.*(-PsCdwell) +
e0*ec*Gcsdwell.*dpsdtdwell/hc)./(hg*(e0*eg/hg + e0*ec*Gcsdwell/hc));      %
Polar current density
jbdwell(1:length(t1d)) =(ggdwell.*(sigmagcdwell) +
e0*eg*dsgcdtdwell/hg)./(hg*(e0*eg/hg + e0*ec*Gcsdwell/hc));   % Conduction
current density
jcdwell(1:length(t1d)) =(ggdwell.*(e0*ec*Gcsdwell*Vp/hc))./(hg*(e0*eg/hg +
e0*ec*Gcsdwell/hc));   % Conduction current density
%
figure(4)
axes('fontsize',12)
plot(t1d,sigmagcdwell/q0(1),'+k',t1d,PsCdwell/q0(1),'--k')
% legend('boundary charge density (sigmagc)','polarization charge density (Ps)',0)
% title (sprintf('Polarization and Boundary Charge Densities Thermal Charging
Dwell for Vp = %3d V',Vp))
ylabel('Charge Density/sigmagc(inf)','fontsize',14), xlabel(sprintf('Time (s) for
Tdwell = %3.2f C',Td-273),'fontsize',14)
figure(5)
axes('fontsize',12)
plot(t1d,jtdwell,'k',t1d,jpdwell,'--k',t1d,jbdwell,':k',t1d,jcdwell,'-.k')
% legend('Total Current Density (jt)','Polarization Current Density (jp)','Boundary
Charge Current Density (jb)','Conduction Current Density (jc)',0)
% title (sprintf('Total, Polarization, and Conduction Current Density during
Thermal Charging Dwell for Vp = %3d V',Vp))
ylabel('Current Density (A/m^2)','fontsize',14), xlabel(sprintf('Time (s) for Tdwell
= %3.2f C',Td-273),'fontsize',14)
%
% Cool Down Current (too calculate TSD initial point)
%
PsCmaxd = PsCdwell(length(Ydwell));          % Polarization charge initialized
at max temperature
sigmagcCmaxd = sigmagcdwell(length(Ydwell));   % Boundary charge initialized
at max temperature
ymaxd = [ sigmagcCmaxd PsCmaxd ];
Tmax = Tg;                                % in Kelvin
scool = 33.3/60;                           % Cool down rate  C/min = C/(60 sec)=
K/(60 sec)
tc = [ t1d(length(t1d)) t1d(length(t1d))+(Tmax-T0)/scool ];       %Initial
conditions set the value properly, time should start at zero sec with time to go
from Tg to T0
options1 = odeset('RelTol',3e-14,'AbsTol',1e-15);
[tcool,Ycool] =
ode15s(@dsdPcool,tc,ymaxd,options1,scool,Tmax,epsilon,gamma,height,Vp,ar,A
KT,CKT,Tm,Tc,t1d(length(t1d)));
%
% Initialize values for current calculation
%
```

```
tcoolrev = zeros(length(tcool),1);
sigmagccool = zeros(length(Ycool),1);
PsCcool = zeros(length(Ycool),1);
dpsdtcool = zeros(length(Ycool),1);
dsgcdtcool = zeros(length(Ycool),1);
Bwcool = zeros(length(Ycool),1);
gccool = zeros(length(Ycool),1);
ggcool = zeros(length(Ycool),1);
gscool = zeros(length(Ycool),1);
Ggccool = zeros(length(Ycool),1);
Gcscool = zeros(length(Ycool),1);
Vgcool = zeros(length(Ycool),1);
Egcool = zeros(length(Ycool),1);
jtcool = zeros(length(Ycool),1);
jpcool = zeros(length(Ycool),1);
jbcool = zeros(length(Ycool),1);
jccool = zeros(length(Ycool),1);
sigmagccoolmax = 0;
PsCcoolmax = 0;
dwellcharge = [ 0 0 0 ];
%
% Current Density Calculation during Charging (jt)
%
PsCcool(1:length(Ycool),1) = Ycool(1:length(Ycool),2);
sigmagccool(1:length(Ycool),1) = Ycool(1:length(Ycool),1);
gccool(1:length(Ycool)) = arrenhius(Tmax-(tcool-
min(tcool))*scool,gc0,CKTc,Tcc);  % Initialize Temperature to Tmax-
(max(tcool)-tcool)*scool to adjust for time shift from start
ggcool(1:length(Ycool)) = arrenhius(Tmax-(tcool-
min(tcool))*scool,gg0,CKTg,Tcg);  % Initialize Temperature to Tmax-
(max(tcool)-tcool)*scool to adjust for time shift from start
gscool(1:length(Ycool)) = arrenhius(Tmax-(tcool-
min(tcool))*scool,gs0,CKTs,Tcs);  % Initialize Temperature to Tmax-
(max(tcool)-tcool)*scool to adjust for time shift from start
Ggccool(1:length(Ycool)) = 1+(hc*ggcool)./(hg*gccool);
Gcscool(1:length(Ycool)) = 1./(1+gccool./gscool);
Bwcool(1:length(Ycool)) = gccool./(hc*(e0*ec*Gcscool/hc + e0*eg/hg));
dsgcdtcool(1:length(Ycool)) = Ggccool.*Bwcool.*(PsCcool -
sigmagccool)+Bwcool.*Gcscool.*((e0*eg/hg)+(e0*ec/hc).*(Gcscool-
Ggccool))*Vp;
dpsdtcool(1:length(tcool)) = (arrenhius(Tmax-(tcool-
min(tcool))*scool,ar,AKT,Tm)).*(((eslow-eg)*(e0*Vp+(hc/ec)*sigmagccool))-
(hg*Gcscool+(hc*eslow/ec)).*PsCcool)./(hg*Gcscool+(hc*eg/ec));
Vgcool(1:length(tcool)) = ((e0*ec*Gcscool*Vp/hc)+sigmagccool-
PsCcool)./((e0*eg/hg)*(1+Gcscool*ec*hg/(hc*eg)));
jtcool(1:length(tcool)) =(ggcool.*(sigmagccool - PsCcool +
e0*ec*Gcscool*Vp/hc) + e0*eg*dsgcdtcool/hg +
```

```
e0*ec*Gcscool.*dpsdtcool/hc)./(hg*(e0*eg/hg + e0*ec*Gcscool/hc));  % total
current density
jpcool(1:length(tcool)) =(ggcool.*(-PsCcool) +
e0*ec*Gcscool.*dpsdtcool/hc)./(hg*(e0*eg/hg + e0*ec*Gcscool/hc));      %
Polar current density
jbcool(1:length(tcool)) =(ggcool.*(sigmagccool) +
e0*eg*dsgcdtcool/hg)./(hg*(e0*eg/hg + e0*ec*Gcscool/hc));   % Boundary
Charge current density
jccool(1:length(tcool)) =(ggcool.*(e0*ec*Gcscool*Vp/hc))./(hg*(e0*eg/hg +
e0*ec*Gcscool/hc));   % Conduction current density
%
% Experimental Cool Down
%
ElectrodeArea1 = 79e-6;                                    %Electrode area in
m^2
jcoolexp = Data(20:103,11)/ElectrodeArea;    % Poling current densities in
A/m^2
Tcoolexp = Data(20:103,9)+273;            % Poling current temperatures adjusted
to Kelvin
tccoolexp = Data(20:103,10)-1800;              % Poling time in seconds
%
% Note:  sigmagcC, PsC, jp, jc, jt are all calculated interms of K, NOT C, so plot
scale must put ratios
%         in K.  s = C/sec = K/sec.
tcoolcelcius = Tmax-(max(tcool)-tcool)*scool-273;          %Celcius
Temperatures
tcoolrelative = (Tmax-(max(tcool)-tcool)*scool+273)/Tm;    %Relative Kelvin
values
plotrange = 10:length(tcool);
sigmagccoolmax = sigmagccool(length(Ycool),1)/q0(1);
PsCcoolmax = PsCcool(length(Ycool),1)/Psinf(1);
dwellcharge = [ tdwellmax sigmagccoolmax PsCcoolmax ];
%
% Write maximum normalized charge to file to produce charge vs. dwell time
plots
%
% fid = fopen('d:/projects/avionics/phd/dwelltemp.txt','a');      % If file exists, use
'w' to write over, then switch to append 'a'
% fprintf(fid,'%8d %2.4f %2.4f',tdwellmax, sigmagccoolmax, PsCcoolmax);
% fclose(fid);
figure(6)
axes('fontsize',12)
plot(tcoolcelcius,sigmagccool/q0(1),'+k',tcoolcelcius,PsCcool/q0(1),'--k')
% legend('boundary charge density (sigmagc)','polarization charge density (Ps)',0)
% title (sprintf('Polarization and Boundary Charge Densities during Cool down
for Vp = %3d V',Vp))
```

```
ylabel('Charge Density/sigmagc(inf)','fontsize',14), xlabel(sprintf('Temperature T
(C) for Tg = %3.2f C',Tm-273),'fontsize',14)
prangemin = 55;
prangemax = length(Ycool);
figure(7)
axes('fontsize',12)
plot(tcoolcelcius(prangemin:prangemax),jtcool(prangemin:prangemax),'+k',tcoolc
elcius(prangemin:prangemax),jpcool(prangemin:prangemax),'--
k',tcoolcelcius(prangemin:prangemax),jbcool(prangemin:prangemax),':k',tcoolcelc
ius(prangemin:prangemax),jccool(prangemin:prangemax),'-.k')
% legend('Total Current Density (jt)','Polarization Current Density (jp)','Boundary
Charge Current Density (jb)','Conduction Current Density (jc)',0)
% title (sprintf('Total, Polarization, and Conduction Current Density during Cool
Down for Vp = %3d V',Vp))
ylabel('Current Density (A/m^2)','fontsize',14), xlabel(sprintf('Temperature T (C)
for Tg = %3.2f C',Tm-273),'fontsize',14)
figure(8)
axes('fontsize',12)
plot(tcoolcelcius,jtcool,'k',tccoolexp-273,jcoolexp,'--ko')
% legend('Total Current Density (jt)','Experimental Total Current Density
(jtexp)',0)
% title (sprintf('Total Modeled and Experimental Current Density during Cool
Down for Vp = %3d V',Vp))
ylabel('Current Density (A/m^2)','fontsize',14), xlabel(sprintf('Temperature T (C)
for Tg = %3.2f C',Tm-273),'fontsize',14)
%
% Full Plots
%
jexp = Data(14:103,11)/(ElectrodeArea);    % Poling current densities in A/m^2
Texp = Data(14:103,9)+273;              % Poling current temperatures adjusted to
Kelvin
texp = Data(14:103,10)-1800;              % Poling time in seconds adjusted to
remove 30 min purge
figure(9)
axes('fontsize',12)
plot(t1,sigmagcC/q0(1),'+k',t1d,sigmagcdwell/q0(1),'+k',tcool,sigmagccool/q0(1),'
+k',t1,PsC/q0(1),'--k',t1d,PsCdwell/q0(1),'--k',tcool,PsCcool/q0(1),'--k')
% legend('boundary charge density (sigmagc)','polarization charge density (Ps)',0)
% title (sprintf('Polarization and Boundary Charge Densities during Cool down
for Vp = %3d V',Vp))
ylabel('Charge Density/sigmagc(inf)','fontsize',14), xlabel(sprintf('time (s) for Tg
= %3.2f C',Tm-273),'fontsize',14)
figure(10)
axes('fontsize',12)
%plot(t1,jt,'k',t1d,jtdwell,'k',tcool,jtcool,'k')
```

```
plot(t1,jt,'k',t1,jp,'--k',t1,jb,':k',t1,jc,'-.k',t1d,jtdwell,'k',t1d,jpdwell,'--
k',t1d,jbdwell,':k',t1d,jcdwell,'-.k',tcool,jtcool,'k',tcool,jpcool,'--
k',tcool,jbcool,':k',tcool,jccool,'-.k',texp,jexp,'-ko')
% legend('Total Current Density (jt)','Experimental Total Current Density
(jtexp)',0)
% title (sprintf('Total Modeled and Experimental Current Density during Cool
Down for Vp = %3d V',Vp))
ylabel('Current Density (A/m^2)','fontsize',14), xlabel(sprintf('time (s) for Tg =
%3.2f C',Tm-273),'fontsize',14)
%
%  TSD Current Calculation
%
tTSD = 0;
YTSD = 0;
PsCstorage = 0;
sigmagcCstorage = 0;
PsCstorage = PsCcool(length(Ycool));          % Polarization charge initialized at
max temperature
sigmagcCstorage = sigmagccool(length(Ycool));   % Polarization charge
initialized at max temperature
ystorage = [ sigmagcCstorage PsCstorage ];
tstorage= [ 0 (Tg-T0)/s ];                    % Time to get from T0 to Tg
% options = [];
[tTSD,YTSD] =
ode15s(@dsdPTSD,tstorage,ystorage,options,s,T0,epsilon,gamma,height,0,ar,AK
T,CKT,Tm,Tc);
%
% TSD Current Calculation
% Initialize values for TSD current calculation
%
sigmagcTSD = zeros(length(YTSD),1);
PsCTSD = zeros(length(YTSD),1);
dpsdtTSD = zeros(length(YTSD),1);
dsgcdtTSD = zeros(length(YTSD),1);
BwTSD = zeros(length(YTSD),1);
gcTSD = zeros(length(YTSD),1);
ggTSD = zeros(length(YTSD),1);
gsTSD = zeros(length(YTSD),1);
GgcTSD = zeros(length(YTSD),1);
GcsTSD = zeros(length(YTSD),1);
VgTSD = zeros(length(YTSD),1);
EgTSD = zeros(length(YTSD),1);
jrTSD = zeros(length(YTSD),1);
jpTSD = zeros(length(YTSD),1);
jbTSD = zeros(length(YTSD),1);
%
% Current Density Calculation during TSD (jr)
```

```
%
PsCTSD(1:length(YTSD),1) = YTSD(1:length(YTSD),2);
sigmagcTSD(1:length(YTSD),1) = YTSD(1:length(YTSD),1);
gcTSD(1:length(YTSD)) = arrenhius(tTSD*s+273,gc0,CKTc,Tcc);      % 273
sets temp = 273 at time = 0
ggTSD(1:length(YTSD)) = arrenhius(tTSD*s+273,gg0,CKTg,Tcg);      % 273
sets temp = 273 at time = 0
gsTSD(1:length(YTSD)) = arrenhius(tTSD*s+273,gs0,CKTs,Tcs);      % 273 sets
temp = 273 at time = 0
GcsTSD(1:length(YTSD)) = 1./(1+gcTSD./gsTSD);
GgcTSD(1:length(YTSD)) = 1./(e0*eg/hg + e0*ec*GcsTSD/hc);
%GgcTSD solved for Vp=0
BwTSD(1:length(YTSD)) = (ggTSD/hg + gcTSD.*GcsTSD/hc)./(e0*eg/hg +
e0*ec*GcsTSD/hc);  %BwTSD solved for Vp=0
dsgcdtTSD(1:length(YTSD)) = BwTSD.*(PsCTSD-sigmagcTSD);
dpsdtTSD(1:length(YTSD)) =
(arrenhius(tTSD*s+273,ar,AKT,Tm)).*((e0/hg)*(eslow - eg)*sigmagcTSD -
((e0/hg)*(eslow - eg)+(e0*eg/hg +
e0*ec*GcsTSD/hc)).*PsCTSD)./(e0*eg/hg+e0*ec*GcsTSD/hc);
VgTSD(1:length(YTSD)) = (sigmagcTSD-
PsCTSD)./(e0*eg/hg+e0*ec*GcsTSD/hc);
jrTSD(1:length(YTSD)) = (e0*eg*GgcTSD/hg).*dsgcdtTSD + (1-
e0*eg*GgcTSD/hg).*dpsdtTSD + ggTSD.*GgcTSD/hg.*(sigmagcTSD -
PsCTSD);        % total current density
jpTSD(1:length(YTSD)) = (1-e0*eg*GgcTSD/hg).*dpsdtTSD+
ggTSD.*GgcTSD/hg.*(-PsCTSD);   % Polarization charge current density
jbTSD(1:length(YTSD)) = (e0*eg*GgcTSD/hg).*dsgcdtTSD +
ggTSD.*GgcTSD/hg.*(sigmagcTSD);   % Boundary Charge current density
%
% Note:  sigmagcC, PsC, jp, jc, jt are all calculated interms of K, NOT C, so plot
scale must put ratios
%         in K.  s = C/sec = K/sec.
tTSDcelcius = (tTSD*s);            %Celcius Temperatures
tTSDrelative = (tTSD*s+273)/Tm;     %Relative Kelvin values
figure(11)
axes('fontsize',12)
plot(tTSDcelcius,sigmagcTSD/q0(1),'k',tTSDcelcius,PsCTSD/q0(1),'--k')
% legend('boundary charge density (sigmagc)','polarization charge density (Ps)',0)
% title ('Polarization Charge Density and Boundary Charge Density during TSD')
ylabel('Charge Density/sigmagc(inf)','fontsize',14), xlabel(sprintf('Temperature T
(C) for Tg = %3.2f C',Tm-273),'fontsize',14)
figure(12)
axes('fontsize',12)
plot(tTSDcelcius,jrTSD,'k',tTSDcelcius,jpTSD,'--k',tTSDcelcius,jbTSD,':k')
% legend('Released Current Density (jr)','Polarization Current Density
(jp)','Boundary Current Density (jb)',0)
% title ('Total, Polarization, and Conduction Current Density during TSD')
```

```
ylabel('Current Density (A/m^2)','fontsize',14), xlabel(sprintf('Temperature T (C)
for Tg = %3.2f C',Tm-273),'fontsize',14)
```

791-1B Mod Transfer Function

```
%Script File:  ModTransferFunction791_1B
%Solves for the frequency response of a poled film during signal modulation
%This version has a separate boundary interface RC circuit (4 total boundaries
UC ->AP->core->AP->LC)
%
close all
RC = zeros(1,5);
% index of refraction values
nc = 1.546;
ng = 1.638;  %CLD42A
ns = 1.546;
%
% height values
%
hc = 2.36e-6;
hg = 3.61e-6;
hs = 3.1e-6;
height = [ hc hg hs ];

%
% epsilon (permitivity)
%
e0 = 8.854e-12;
ec = nc^2;
eg = ng^2;
eslow = 4.7;
es = ns^2;
epsilon = [ ec eg es e0 eslow ];
%
% Capacitance
%
Length = .0136-.24e-3;          % in meters  .0136 - .24e-3 (2 X .12e-3 for break
width)
ElectrodeWidth = 120e-6;     % in meters
Cc = e0*ec*(Length*ElectrodeWidth)/hc;
Cg = e0*eg*(Length*ElectrodeWidth)/hg;
Cs = e0*es*(Length*ElectrodeWidth)/hs;
CB = e0*(Length*ElectrodeWidth)/(8e-7); %.8e-7
%CBs = CBc;
Cap = e0*(Length*ElectrodeWidth)/(1e-9);  %1e-9
CMW = e0*eg*(Length*ElectrodeWidth)/(3.61e-6);
Cstack = e0*((eg+ec+es)/3)*(Length*ElectrodeWidth)/(1.3e-5);
%
% Resistance
%
```

```
Rc = 3e15*(100*hc)/(120e-6*15e-3);  % hc/arrenhius(293,gc0,CKTc,Tcc);
%Upper Cladding Resistance
%
RB = 1e5;  %.8e5
%Rap = 5e3;  %9e3
%
Rgm = 1e16*(100*hg)/(6.5e-6*15e-3); %hg/arrenhius(293,gg0,CKTg,Tcg);
%Core Main Chain Resistance (1e16 for APC)
Rgc = 4.93e13*(100*hg)/(6.5e-6*15e-3); %hg/arrenhius(293,gg0,AKT,Tm);
%Core chromophore Resistance
Rgb = .5*(1e16*(100*hg)/(56.75e-6*15e-3));    %Bleached core layer resistance
same as the host resistance.  This is the parallel combination of the 2 bleached
regions.
% Rgion = 1.005e14/(100*hg);   %hg/arrenhius(293,gg0,AKT,Tm);        %Core
Ion Resistance (conductive particles in the bleached area)
Rgu = Rgm*Rgc/(Rgm + Rgc);   %Unbleached Core Resistance
Rg = Rgu*Rgb/(Rgu + Rgb);   %Total Core Resistance
%
Rs = 3e15*(100*hs)/(120e-6*15e-3);  %hs/arrenhius(293,gs0,CKTs,Tcs);
%Lower Cladding Resistance%
%
%  Frequency Response
%
% w = 1:1e4:1e8;
% w2 = 1e8:1e8:1e14;
w = 1e-10:1e-10:1e-6;
w2 = 1e-6:1e-8:1e-4;
Zc = (Rc- j*w.*(Rc^2)*Cc)./(1 + (w*Rc*Cc).^2);
ZB = (RB- j*w.*(RB^2)*CB)./(1 + (w*RB*CB).^2);
Zg = (Rg- j*w.*(Rg^2)*Cg)./(1 + (w*Rg*Cg).^2);
Zs = (Rs- j*w.*(Rs^2)*Cs)./(1 + (w*Rs*Cs).^2);
Zelectrode = .1;
Hgw = Zg./(Zc+Zg+Zs+2*ZB+2*Zelectrode);
Zc2 = (Rc- j*w2.*(Rc^2)*Cc)./(1 + (w2*Rc*Cc).^2);
ZB2 = (RB- j*w2.*(RB^2)*CB)./(1 + (w2*RB*CB).^2);
Zg2 = (Rg- j*w2.*(Rg^2)*Cg)./(1 + (w2*Rg*Cg).^2);
Zs2 = (Rs- j*w2.*(Rs^2)*Cs)./(1 + (w2*Rs*Cs).^2);
Hgw2 = Zg2./(Zc2+Zg2+Zs2+2*ZB2+2*Zelectrode);
figure(1)
%plot(w,abs(Hgw),'k',w,abs(Zc),w,abs(Zg),w,abs(ZBg),w,abs(Zs))
semilogx(w,abs(Hgw),'k',w2,abs(Hgw2),'k')
%legend('Hgw','Zc','Zg','ZBg','Zs')
ylabel('Hg(\omega)'), xlabel('Frequency (\omega)')
% figure(2)
%
%semilogx(w,abs(Zg./(Zc+Zg+2*ZB+Zap)),w,abs(Zg./(Zs+Zg+2*ZB+Zap)),w,ab
s(Zg./(Zc+Zg+Zs+2*ZB+Zap)))
```

```
% semilogx(w,abs(Zg./(Zc+Zg+Zs+2*Zelectrode)))
% legend('Zg/(Zc+Zg)','Zg/(Zg+Zs)','Zg/(Zc+Zg+Zs)')
% ylabel('Hg(\omega)'), xlabel('Frequency (\omega)')
```

791-1B Modulation Model

```
%Script File:  ModulationModel
%Solves for the frequency response of a poled film during signal modulation
%
close all
RC = zeros(1,5);
% index of refraction values
nc = 1.546;
ng = 1.638;  %CLD42A
ns = 1.546;
%
% height values
%
hc = 2.36e-6;
hg = 3.61e-6;
hs = 3.1e-6;
height = [ hc hg hs ];
%
% gamma (conductance)
%
gg0 = 1e20;
gc0 = 1e9;
gs0 = gc0;
gamma = [ gc0 gg0 gs0 ];
%
% epsilon (permitivity)
%
e0 = 8.854e-12;
ec = nc^2;          % 2
eg = ng^2;          % 3
eslow = 4.6;          % 7
es = ns^2;
epsilon = [ ec eg es e0 eslow ];
%
% dipole relaxation frequency and conduction activation energy
%
ar = 2.4e20;                  % Baseline: 1e13
Ea = 2;                     %in eV  Baseline: 2
Ec = 1.9;                     %in eV  Baseline: 2
AKT = 56;
Tm = Ea*(1.6e-19)/((1.381e-23)*AKT);    %Tm in K; Baseline:  A/kT = 55
CKTc = AKT*(1.13);              % Upper Cladding Conductance activation
energy
CKTg = AKT*(1.5);             % Core Conductance activation energy
CKTs = CKTc;                  % Lower Cladding Conductance activation energy
```

```
Tcc = Ec*(1.6e-19)/((1.381e-23)*CKTc);      %Norlund Tg is 50 - 100 C
depending on crosslinking.
Tcg = Tm/.85;                  %Tm/Tc = .95  Baseline:  .95
Tcs = Tcc;
CKT = [ CKTc CKTg CKTs ];
Tc = [ Tcc Tcg Tcs ];
%
% Capacitance
%
Length = .0136-.24e-3;          % in meters  .0136 - .24e-3 (2 X .12e-3 for break
width)
ElectrodeWidth = 120e-6;     % in meters
Cc = e0*ec*(Length*ElectrodeWidth)/hc;
Cg = e0*eg*(Length*ElectrodeWidth)/hg;
Cs = e0*es*(Length*ElectrodeWidth)/hs;
CB = e0*(Length*ElectrodeWidth)/(8e-7); %.8e-7
%CBs = CBc;
Cap = e0*(Length*ElectrodeWidth)/(1e-9);  %1e-9
CMW = e0*eg*(Length*ElectrodeWidth)/(3.61e-6);
Cstack = e0*((eg+ec+es)/3)*(Length*ElectrodeWidth)/(1.3e-5);
%
% Resistance
%
Rc = 3e15*(100*hc)/(120e-6*15e-3);  % hc/arrenhius(293,gc0,CKTc,Tcc);
%Upper Cladding Resistance
%
RB = 1e5;  %.8e5
%Rap = 5e3;  %9e3
%
Rgm = 1e16*(100*hg)/(6.5e-6*15e-3); %hg/arrenhius(293,gg0,CKTg,Tcg);
%Core Main Chain Resistance (1e16 for APC)
Rgc = 4.93e13*(100*hg)/(6.5e-6*15e-3); %hg/arrenhius(293,gg0,AKT,Tm);
%Core chromophore Resistance
Rgb = .5*(1e16*(100*hg)/(56.75e-6*15e-3));    %Bleached core layer resistance
same as the host resistance.  This is the parallel combination of the 2 bleached
regions.
% Rgion = 1.005e14/(100*hg);   %hg/arrenhius(293,gg0,AKT,Tm);       %Core
Ion Resistance (conductive particles in the bleached area)
Rgu = Rgm*Rgc/(Rgm + Rgc);   %Unbleached Core Resistance
Rg = Rgu*Rgb/(Rgu + Rgb);   %Total Core Resistance
%
Rs = 3e15*(100*hs)/(120e-6*15e-3);  %hs/arrenhius(293,gs0,CKTs,Tcs);
%Lower Cladding Resistance%
% Experimental Data
%
%  791-1B
%
```

```
fid = fopen('d:projects\avionics\phd\791_1B 072904p.txt');
a = fscanf(fid,'%g %g %g',[3 inf]); % It has three rows now.
a = a';
fclose(fid);
t = a(:,1);
OP = a(:,2);
Vm = a(:,3);
duration = t(length(t));
%
% Modulation Voltage
%
% Vmt1 = 1+sawtooth(2*pi*(tm-2.8)*1/31.2); % 2.8 sec offset to match
experimental waveform;  31.2 sec period
% Vmt2 = 1+square(2*pi*(tm-2.8)*1/31.2,75);  %2.8 sec offset to match
experimental waveform; 31.2 sec period; 75% duty cycle
% Vmt = -78.4*(Vmt1.*Vmt2);  %-78.4*3 is the maximum voltage
period = 30.9;  %seconds
offset = 12.8;  %seconds
amplitude = -78.4;  %volts
dutycycle = 75;  %percent
step = .001;  %to make sawtooth modulation have a variable step size
tm = 0:step:duration;
Vmt = sawtoothmodulation(period, offset, amplitude, dutycycle, duration, step)-
17;
%
%  Search Algorithm
%
% r33 = 80.7e-12;          % in m/V
opticaloffset = 0*pi;  %optical offset representing interference with no voltage
applied
% options = [];
% [RC, fmin] = fminsearch(@ORerror, [RBc, CBc, r33, opticaloffset], options,
Rc, Cc, Rg, Cg, Rs, Cs, duration, ng, hg, Vmt, OP);
% RBc = RC(1);
% CBc = RC(2);
% r33 = RC(3);
% opticaloffset = RC(4);
%
%  Frequency Response
%
w = -duration/2*(1/step):1:duration/2*(1/step);
Vmw = fft(Vmt);
Zc = (Rc- j*w.*(Rc^2)*Cc)./(1 + (w*Rc*Cc).^2);
ZB = (RB- j*w.*(RB^2)*CB)./(1 + (w*RB*CB).^2);
Zg = (Rg- j*w.*(Rg^2)*Cg)./(1 + (w*Rg*Cg).^2);
Zs = (Rs- j*w.*(Rs^2)*Cs)./(1 + (w*Rs*Cs).^2);
Zelectrode = .1;
```

```
% Zap = (Rap- j*w.*(Rap^2)*Cap)./(1 + (w*Rap*Cap).^2);
%ZBg = (Zap + 2*ZB + Zg)./((j*w*CMW).*(Zap + Zg + 2*ZB) + 1);
%Zstack =  Zc + ZBg + Zs + Zap;
Hgw = Zg./(Zc+Zg+Zs+2*ZB+2*Zelectrode);
Vgw = Vmw.*Hgw;
Vgt = ifft(Vgw)+.283;  % .283 V is charge density induced voltage from poling
%
% Modulation Transfer Function
%
lambda = 1.55e-6;       % in meters
r33 = hg*lambda./(Length*(ng^3)*((84.6-6)/43));  %43 is the number of periods
of the experimental data
k = 2*pi/lambda;
DeltaGamma = k*Length*(0.5*(ng^3*r33)*(1/hg)*(abs(Vgt)));
Im = .5*cos(DeltaGamma/2+opticaloffset/2).^2;
Vpi = hg*lambda/(Length*(ng^3)*r33);
%
% Plots
%
% figure(1)
% plot(tm,Vmt,tm,Vgt,tm,20*Im)
% figure(2)
% plot(tm,Im)
% figure(3)
% plot(tm,Vmt,tm,Vmt2)
figure(2)
plot(tm,20*Im,'--k',t,20*OP-13,'k')  %magnify optical power by 20 to see on
graph; shift voltage up 17V to 0
figure(1)
plot(tm,Vmt,'k',t,Vm,'k',tm,Vgt,'--k')
```

791-1B Modulation Model SqWv

```
%Script File:  ModulationModel
%Solves for the frequency response of a poled film during signal modulation
%
close all
RC = zeros(1,5);
% index of refraction values
nc = 1.546;
ng = 1.638;  %CLD42A
ns = 1.546;
%
% height values
%
hc = 2.36e-6;
hg = 3.61e-6;
hs = 3.1e-6;
height = [ hc hg hs ];
%
% gamma (conductance)
%
gg0 = 1e20;
gc0 = 1e9;
gs0 = gc0;
gamma = [ gc0 gg0 gs0 ];
%
% epsilon (permitivity)
%
e0 = 8.854e-12;
ec = 4.44;          % based on exerimental measurements
eg = 3.59;          % based on exerimental measurements
es = ec;
%
% Capacitance
%
Length = .0136-.24e-3;          % in meters  .0136 - .24e-3 (2 X .12e-3 for break
width)
ElectrodeWidth = 120e-6;     % in meters
Cc = e0*ec*(Length*ElectrodeWidth)/hc;
%Cg = e0*eg*(Length*ElectrodeWidth)/hg;
Cs = e0*es*(Length*ElectrodeWidth)/hs;
CB = e0*(Length*ElectrodeWidth)/(8e-7);  %6e-7
Cap = e0*(Length*ElectrodeWidth)/(1e-5);
Ribwidth = 6e-6;
Cg = e0*ec*(Length*ElectrodeWidth)/(1.54e-6);
CMW = Cg;  %.25Cgbulk
RMW = 1e9;
```

```
% CMW = e0*eg*(Length*ElectrodeWidth)/hg;
%
% Resistance
%
Rc = 3e15*(100*hc)/(ElectrodeWidth*15e-3); %
hc/arrenhius(293,gc0,CKTc,Tcc);       %Upper Cladding Resistance
%
RB = 1e5; %.8e5
%Rap = 5e3; %9e3
%
Rgm = 1e16*(100*hg)/(6.5e-6*15e-3); %hg/arrenhius(293,gg0,CKTg,Tcg);
%Core Main Chain Resistance (1e16 for APC)
Rgc = 4.93e13*(100*hg)/(6.5e-6*15e-3); %hg/arrenhius(293,gg0,AKT,Tm);
%Core chromophore Resistance
Rgb = .5*(1e16*(100*hg)/(56.75e-6*15e-3));   %Bleached core layer resistance
same as the host resistance. This is the parallel combination of the 2 bleached
regions.
% Rgion = 1.005e14/(100*hg);  %hg/arrenhius(293,gg0,AKT,Tm);       %Core
Ion Resistance (conductive particles in the bleached area)
Rgu = Rgm*Rgc/(Rgm + Rgc);  %Unbleached Core Resistance
Rg = Rgu*Rgb/(Rgu + Rgb);  %Total Core Resistance
%
Rs = 3e15*(100*hs)/(ElectrodeWidth*15e-3);
%hs/arrenhius(293,gs0,CKTs,Tcs);       %Lower Cladding Resistance%
%
% Experimental Data
%
%  791-1B
%
fid = fopen('d:projects\avionics\phd\791_1B 081704 SqWv p.txt');
a = fscanf(fid,'%g %g %g',[3 inf]); % It has three rows now.
a = a';
fclose(fid);
t = a(:,1);
OP = a(:,2);
Vm = a(:,3);
duration = t(length(t));
%
% Modulation Voltage
%
% Vmt1 = 1+sawtooth(2*pi*(tm-2.8)*1/31.2); % 2.8 sec offset to match
experimental waveform;  31.2 sec period
% Vmt2 = 1+square(2*pi*(tm-2.8)*1/31.2,75);  %2.8 sec offset to match
experimental waveform; 31.2 sec period; 75% duty cycle
% Vmt = -78.4*(Vmt1.*Vmt2);  %-78.4*3 is the maximum voltage
period = 21;  %seconds
offset = -4.55;  %seconds
```

```
amplitude = -79;  %volts
dutycycle = 46.5;  %percent
%duration = 215;  %seconds
tm = 0:.0001:duration;
Vmt = amplitude*(1+square(2*pi*(tm-offset)*1/period,dutycycle));
%Vmt = sin(50e3*tm);
%
%  Search Algorithm
%
% r33 = 80.7e-12;          % in m/V
opticaloffset = 0*pi;  %optical offset representing interference with no voltage
applied
% options = [];
% [RC, fmin] = fminsearch(@ORerror, [RBc, CBc, r33, opticaloffset], options,
Rc, Cc, Rg, Cg, Rs, Cs, duration, ng, hg, Vmt, OP);
% RBc = RC(1);
% CBc = RC(2);
% r33 = RC(3);
% opticaloffset = RC(4);
%
%  Frequency Response
%
w = -duration/2*1e4:1:duration/2*1e4;
%w = -duration/2*1e12:1e8:duration/2*1e12;
Vmw = fft(Vmt);
Zc = (Rc- j*w.*(Rc^2)*Cc)./(1 + (w*Rc*Cc).^2);
ZB = (RB- j*w.*(RB^2)*CB)./(1 + (w*RB*CB).^2);
Zg = (Rg- j*w.*(Rg^2)*Cg)./(1 + (w*Rg*Cg).^2);
Zs = (Rs- j*w.*(Rs^2)*Cs)./(1 + (w*Rs*Cs).^2);
%ZMW = RMW./(1+j*w*CMW*RMW);
%Zap = (Rap- j*w.*(Rap^2)*Cap)./(1 + (w*Rap*Cap).^2);
Zelectrode = .1;
%ZBg = (2*ZB + Zg)./((j*w*CMW).*(Zg + 2*ZB) + 1);
%ZBg2 = (j*w*RMW*CMW + 1).*(Zap + 2*ZB + Zg)./((j*w*CMW).*(Zap +
Zg + 2*ZB) + 1 + j*w*RMW*CMW);  %series
%ZBg3 = ZMW.*(2*ZB + Zg)./(Zg + 2*ZB + ZMW);
%Zstack =  Zc + ZBg3 + Zs + Zelectrode;
%Hgw = (ZBg3.*Zg)./(Zstack.*(Zelectrode + 2*ZB + Zg));
Hgw2 = Zg./(Zc+Zg+Zs+2*ZB+2*Zelectrode);
Vgw = Vmw.*Hgw2;
Vgt = ifft(Vgw)+.283;  % .283 V is charge density induced voltage from poling
%
% Modulation Transfer Function
%
lambda = 1.55e-6;       % in meters
r33 = 49.443e-12; %46.433 was calculated for 809-1 rib, adjusted slightly for
transient response in 791-1
```

```
k = 2*pi/lambda;
DeltaGamma = k*Length*(0.5*(ng^3*r33)*(1/hg)*(-abs(Vgt)));
Im = .5*cos(DeltaGamma/2+opticaloffset/2).^2;
Vpi = hg*lambda/(Length*(ng^3)*r33);
%
% Plots
%
% figure(1)
% plot(tm,Vmt,tm,-abs(Vgt),tm,10*Im,t,50*OP-35,t,Vm)  %magnify optical
power by 20 to see on graph;
figure(2)
plot(tm,Vmt,':k',tm,-abs(Vgt),'k')
axis([0,110,-150,100])
ylabel('Volts (V)'), xlabel('Time (s)')
figure(3)
plot(tm,20*(Im),'k',t,20*(OP-.7),'--k',tm,-abs(Vgt),':k')  %magnify optical power
by 20 to see on graph;
ylabel('Volts (V)'), xlabel('Time (s)')
figure(4)
semilogx(w,abs(Hgw2),'k')
ylabel('Hg(\omega)'), xlabel('Frequency (\omega)')
```

arrenhius

```
function aT = arrenhius(T,ar,EKT,Tm)
% Function to calculate the distribution of relaxation frequencies using an
arrenhius function
%
% TK = T+273;
aT = ar*exp(-EKT./(T./Tm));   % T and Tm in K
```

dsdP

```
function TSDdata =
dsdP(t,y,s,Tin,epsilon,gamma,height,Vp,ar,AKT,CKT,Tm,Tc)
% Function to calculate the coupled values of dsigmacg/dt and dPs/dt.
% y(1) are the sigmacg values.
% y(2) are the Ps values.
% TSDdata is a column vector returning dsigmacg/dt in row 1 and dPs/dt in row
2.
%
T1 = Tin+s*t;
% if Tin+s*t <= 145
%    T1 = Tin+s*t;
% else
%    T1 = 145;
% end
gc = arrenhius(T1,gamma(1),CKT(1),Tc(1));
gg = arrenhius(T1,gamma(2),CKT(2),Tc(2));
gs = arrenhius(T1,gamma(3),CKT(3),Tc(3));
Ggc = 1+(height(1)*gg)./(height(2)*gc);
Gcs = 1./(1+(gc./gs));
Bw = gc./(height(1)*(epsilon(4)*epsilon(1)*Gcs/height(1) +
epsilon(4)*epsilon(2)/height(2)));
TSDdata = [ Ggc*Bw*(y(2) -
y(1))+Bw*Gcs*((epsilon(4)*epsilon(2)/height(2))+(epsilon(4)*epsilon(1)/height(
1))*(Gcs-Ggc))*Vp
        arrenhius(T1,ar,AKT,Tm)*(((epsilon(5)-
epsilon(2))*(epsilon(4)*Vp+(height(1)/epsilon(1))*y(1)))-
(height(2)*Gcs+(height(1)*epsilon(5)/epsilon(1)))*y(2))/(height(2)*Gcs+(height(
1)*epsilon(2)/epsilon(1))) ];
```

dsdPdwell

```
function TSDdata =
dsdPdwell(t,y,s,Tin,epsilon,gamma,height,Vp,ar,AKT,CKT,Tm,Tc)
% Function to calculate the coupled values of dsigmacg/dt and dPs/dt.
% y(1) are the sigmacg values.
% y(2) are the Ps values.
% TSDdata is a column vector returning dsigmacg/dt in row 1 and dPs/dt in row
2.
%
T1 = Tin;
% if Tin+s*t <= 145
%    T1 = Tin+s*t;
% else
%    T1 = 145;
% end
gc = arrenhius(T1,gamma(1),CKT(1),Tc(1));
gg = arrenhius(T1,gamma(2),CKT(2),Tc(2));
gs = arrenhius(T1,gamma(3),CKT(3),Tc(3));
Ggc = 1+(height(1)*gg)./(height(2)*gc);
Gcs = 1./(1+(gc./gs));
Bw = gc./(height(1)*(epsilon(4)*epsilon(1)*Gcs/height(1) +
epsilon(4)*epsilon(2)/height(2)));
TSDdata = [ Ggc*Bw*(y(2) -
y(1))+Bw*Gcs*((epsilon(4)*epsilon(2)/height(2))+(epsilon(4)*epsilon(1)/height(
1))*(Gcs-Ggc))*Vp
        arrenhius(T1,ar,AKT,Tm)*(((epsilon(5)-
epsilon(2))*(epsilon(4)*Vp+(height(1)/epsilon(1))*y(1)))-
(height(2)*Gcs+(height(1)*epsilon(5)/epsilon(1)))*y(2))/(height(2)*Gcs+(height(
1)*epsilon(2)/epsilon(1))) ];
```

dsdPcool

```
function TSDdata =
dsdPcool(t,y,s,Tin,epsilon,gamma,height,Vp,ar,AKT,CKT,Tm,Tc,tmin)
% Function to calculate the coupled values of dsigmacg/dt and dPs/dt.
% y(1) are the sigmacg values.
% y(2) are the Ps values.
% TSDdata is a column vector returning dsigmacg/dt in row 1 and dPs/dt in row
2.
%
T1 = Tin-s*(t-tmin);
% if Tin+s*t <= 145
%    T1 = Tin+s*t;
% else
%    T1 = 145;
```

```
% end
gc = arrenhius(T1,gamma(1),CKT(1),Tc(1));
gg = arrenhius(T1,gamma(2),CKT(2),Tc(2));
gs = arrenhius(T1,gamma(3),CKT(3),Tc(3));
Ggc = 1+(height(1)*gg)./(height(2)*gc);
Gcs = 1./(1+(gc./gs));
Bw = gc./(height(1)*(epsilon(4)*epsilon(1)*Gcs/height(1) +
epsilon(4)*epsilon(2)/height(2)));
TSDdata = [ Ggc*Bw*(y(2) -
y(1))+Bw*Gcs*((epsilon(4)*epsilon(2)/height(2))+(epsilon(4)*epsilon(1)/height(
1))*(Gcs-Ggc))*Vp
        arrenhius(T1,ar,AKT,Tm)*(((epsilon(5)-
epsilon(2))*(epsilon(4)*Vp+(height(1)/epsilon(1))*y(1)))-
(height(2)*Gcs+(height(1)*epsilon(5)/epsilon(1)))*y(2))/(height(2)*Gcs+(height(
1)*epsilon(2)/epsilon(1))) ];
```

dsdPTSD

```
function TSDdata =
dsdPTSD(t,y,s,Tin,epsilon,gamma,height,Vp,ar,AKT,CKT,Tm,Tc)
% Function to calculate the coupled values of dsigmacg/dt and dPs/dt.
% y(1) are the sigmacg values.
% y(2) are the Ps values.
% TSDdata is a column vector returning dsigmacg/dt in row 1 and dPs/dt in row
2.
%
T1 = Tin+s*t;
gc = arrenhius(T1,gamma(1),CKT(1),Tc(1));
gg = arrenhius(T1,gamma(2),CKT(2),Tc(2));
gs = arrenhius(T1,gamma(3),CKT(3),Tc(3));
Gcs = 1/(1+gc/gs);
Ggc = 1/(epsilon(4)*epsilon(2)/height(2) + epsilon(4)*epsilon(1)*Gcs/height(1));
%GgcTSD solved for Vp=0
Bw = (gg/height(2) + gc*Gcs/height(1))./(epsilon(4)*epsilon(2)/height(2) +
epsilon(4)*epsilon(1)*Gcs/height(1));  %BwTSD solved for Vp=0
TSDdata = [ Bw.*(y(2) - y(1))
(arrenhius(T1,ar,AKT,Tm)).*((epsilon(4)/height(2))*(epsilon(5) -
epsilon(2))*y(1)-((epsilon(4)/height(2))*(epsilon(5) -
epsilon(2))+(epsilon(4)*epsilon(2)/height(2) +
epsilon(4)*epsilon(1)*Gcs/height(1)))*y(2))./(epsilon(4)*epsilon(2)/height(2)+eps
ilon(4)*epsilon(1)*Gcs/height(1)) ];
```

sawtoothmodulation

```
function Vmt = sawtoothmodulation(period, offset, amplitude, dutycycle,
duration, step)
%
% Produces a chirped sawtooth waveform
%  period is the period of the waveform in seconds (31.2 sec typical)
%  offset is the time offset to match the start with the experimental data (varies
with experiment)
%  amplitude is the amplitude of the waveform in volts to match the experimental
data (80 V typical)
%  duty cycle is the duty cylce of the square wave to create the chirp (75%
typical)
%  duration is the total measurement time
%
tm = 0:step:duration;
Vmt1 = 1+sawtooth(2*pi*(tm-offset)*1/period); % 2.8 sec offset to match
experimental waveform;  31.2 sec period
Vmt2 = 1+square(2*pi*(tm-offset)*1/period,dutycycle);  %2.8 sec offset to match
experimental waveform; 31.2 sec period; 75% duty cycle
Vmt = amplitude*(Vmt1.*Vmt2);  %-78.4*3 is the maximum voltage
```

REFERENCES

[1] S. Bauer-Gogonea and R. Gerhard-Multhaupt, "Nonlinear Optical Polymer Electrets Current Practice", *IEEE Transactions on Dielectrics and Electrical Insulation*, Vol. 3, No. 5, October 1996, pp 677 – 705.

[2] H. Lefevre, *Fiber Optic Gyroscopes*, Artech House, Boston, 1993, ppp. 46-58.

[3] L. R. Dalton (2003, Jan.). Organic Electro-Optic Materials: Present and Future, Presented at NSF Organic 2003 Workshop, [Online]. Available: www.mrc.utexas.edu/NSFWorkshop/Abstracts/dalton2.pdf.

[4] Inrad Data Sheet on Lithium Niobate, [Online]. Available: www.inrad.com.

[5] M. C. Oh, H. Zhang, C. Zhang, H. Erlig, Y. Chang, B. Tsap, D. Chang, A. Szep, W. H. Steier, H. R. Fetterman, and L. R. Dalton, "Recent Advances in Electrooptic Polymer Modulators Incorporating Highly Nonlinear Chromophore", *IEEE Journal on Selected Topics in Quantum Electronics*, Vol. 7, No. 5, September 2001, pp. 826 – 835.

[6] M. C. Oh, H. Zhang, A. Szep, V. Chuyanov, W. H. Steier, C. Zhang, and L. R. Dalton, "Practical electro-optic polymer modulators using PC/CLD", *Organic Thin Films for Photonic Applications*, September 1999.

[7] D. H. Chang, H. Erlig, M. C. Oh, C. Zhang, W. H. Steier, L. R. Dalton, , and H. R. Fetterman, "Time Stretching of 102-GHz Millimeter Waves Using Novel 1.55-μm Polymer Electrooptic Modulator", *IEEE Photonics Technology Letters*, Vol. 12, No. 5, pp 537 – 539, May 2000.

[8] H. Zhang, M. C. Oh, A. Szep, W. H. Steier, C. Zhang, L. R. Dalton, H. Erlig, Y. Chang, D. H. Chang, and H. R. Fetterman, "Push-pull electrooptic polymer modulators with low half-wave voltage and low loss at both 1310 nm and 1550 nm", *Applied Physics Letters*, Vol. 78, pp 3136 - 3138, May 2001.

[9] C. Zhang, L. R. Dalton, M.C. Oh, H. Zhang, and W. Steier, "Low Vpi Electrooptic Modulators from CLD-1: Chromophore Design and Synthesis, Material Processing, and Characterization", Chem. Mater., 2001, 13, pp. 3043-3050.

[10] G. M. Sessler, ed., *Electrets*, 2nd ed., Springer-Verlag, Berlin, 1987.

[11] P. N. Prasad and D. J. Williams, *Introduction to Nonlinear Optical Effects in Molecules and Polymers*, Wiley, NY, 1991.

[12] D. S. Chemla and J. Zyss, *Nonlinear Optical Properties of Organic Molecules and Crystals*, Volume 1, Academic Press, Orlando, 1987, pp. 31-105.

[13] J. Turnhout, *Thermally Stimulated Discharge of Polymer Electrets*, NY, Elsevier, 1975, pg. 27, 40, 138 - 149.

[14] G. Chen, Z. Zia, T. Zhang, and H. Zhang, "Preparing and Polarizing Stability of Teflon AF Nonlinear Optical Polymer Electret Double Layer Film System", IEEE Transactions on Dielectrics and Electrical Insulation, Vol 6, No. 6, December 1999, pp 831-834.

[15] G. M. Sessler, "Charge Dynamics in Irradiated Polymers", IEEE 9th International Symposium on Electrets (ISE9), 1996, pp. 23 – 42.

[16] G. M. Sessler, M., T. Figueiredo, and G. F. L. Ferreira, "Models of Charge Transport in Electron-Beam Irradiated Insulators", IEEE 11th International Symposium on Electrets (ISE11), 2002, pp. 23 – 42.

[17] S. Bauer-Gogonea, Z.-Y. Cheng, W. Wirges, S. Bauer, R. Gerhard-Multhaupt, and D. K. Das-Gupta, "Dielectric Investigation of Thermally-induced Chromophore Degradation in Nonlinear Optical Polymer Electrets", *IEEE Trans. Dielec. Elec. Ins.*, vol. 5, no. 1, Feb 1998, pp. 21 - 25.

[18] S. Bauer and S. Bauer-Gogonea, "Current Practice in Space Charge and Polarization Profile Measurements Using Thermal Techniques", *IEEE Trans. Dielec. Elec. Ins.*, vol. 10, no. 5, Oct 2003, pp. 883-902.

[19] G. M. Sessler, "Charge Distribution and Transport in Polymers", *IEEE Trans. Dielec. Elec. Ins.*, vol. 4, no. 5, Oct 1997, pp. 614 – 628.

[20] S. Bauer, W. Ren, S. Bauer-Gogonea, R. Gerhard-Multhaupt, J. Liang, J. Zyss, M. Ahlheim, M. Stahelin, and B. Zysset, "Thermal Stability of the Dipole Orientation in Nonlinear Optical Guest-Host, Side-Chain and Cross-Linked Polymer Electrets", IEEE, 1994, pp. 800 – 805.

[21] M. E. Borisova and M. S. Marchenko, "Influence of Irradiation on the Thermally Stimulated Depolarization Currents of Polyimide Films", *10th International Symposium on Electrets, IEEE*, 1999, pp. 781 – 784.

[22] S. N. Koykov and Y. A. Panteleev, "Computer Simulation of TSP and TSD Current in Dielectrics on the Basis of Some Physical Models of Charge Relaxation", *10th International Symposium on Electrets, IEEE*, 1999, pp. 423 – 426.

[23] J. Arentoft, K. Pedersen, S. I. Bozhevolnyi, M. Kristensen, P. Yu, and C. B. Nielsen, "Second-harmonic imaging of poled silica waveguides", Applied Physics Letters, 76 (1), 2000, pp. 25-27.

[24] K. Pedersen, S. I. Bozhevolnyi, J. Arentoft, M. Kristensen, and C. Laurent-Lund, "Second-harmonic scanning optical microscopy of poled silica waveguides", Journal of Applied Physics, 88(7), 2000, pp. 3872-3878.

[25] J. Beermann, S. I. Bozhevolnyi, K. Pederson, and J. Fage-Pederson, "High-resolution second-harmonic microscopy of poled silica waveguides", Optics Communications, 221, 2003, pp. 295-300.

[26] B. Kippelen, K., Meerholz, and N. Peyghambarian, "An Introduction of Photorefractive Polymers", in Nonlinear Optics of Organic Molecules and Polymers, H. S. Nalwa and S. Miyata, ed., CRC Press, NY, 1997, pp. 465 – 513.

[27] J. G. Grote, J. S. Zetts, R. L. Nelson, F. K. Hopkins, L. R. Dalton, C. Zhang, and W. H. Steier, "Effect of Conductivity and Dielectric Constant on the Modulation Voltage for Optoelectronic devices based on nonlinear optical polymers", *Opt. Eng.*, No. 40, Vol 11, Nov. 2001, pp. 2464-2473.

[28] M. C. Oh, S. Ura, T. Suhara, and H. Nishihara, "Integrated-Optic Focal-Spot intensity Modulator Using Electrooptic Polymer Waveguide", Journal of Lightwave Technology, Vol. 12, No. 9, September 1994, pp. 1569–1576.

[29] J. W. Wu, "Birefringent and electro-optic effects in poled polymer films: steady-state and transient properties" J. Opt. Soc. Am. B., vol. 8, no. 1, January 1991, pp. 142 - 152.

[30] D. M. Gill and A. Chowdhury, "Electro-optic Polymer-Based Modulator Design and Performance for 40 Gb/s System Applications", Journal of Lightwave Technology, vol. 20, no. 12, December 2002, pp. 2145-2153.

[31] D. H. Chang, H. R. Fetterman, H. Erlig, H. Zhang, M. C. Oh, C. Zhang, and W. H. Steier, "39-GHz Optoelectronic Oscillator Using Broad-Band Polymer Electrooptic Modulator", IEEE Photonics Technology Letters, Vol. 14, No. 2, February 2002, pp. 191-193.

[32] D. H. Chang, H. Erlig, M. C. Oh, C. Zhang, W. H. Steier, L. R. Dalton, and H. R. Fetterman, "Time Stretching of 102-GHz Millimeter Waves Using Novel 1.55-μm Polymer Electrooptic Modulator", IEEE Photonics Technology Letters, Vol. 12, No. 5, May 2000, pp. 537–539.

[33] D. Chen, H. R. Fetterman, A. Chen, W. H. Steier, L. R. Dalton, W. Wang, and Y. Shi, "Demonstration of 110 GHz electro-optic polymer modulators", Appl. Phys. Lett., vol. 70,. No. 25, pp. 3335-3337, 1997.

[34] Y. Shi, D. J. Olson, L. Weiping, and J. H. Bechtel, "Push-Pull Poled Polymer Mach-Zehnder Modulators with a Single Microstrip Line Electrode", IEEE Photonics Technology Letters, vol. 11, no. 1, January 1999, pp 51-53.

[35] D. Chen, D. Bhattacharya, A. Udupa, B. Tsap, H. R. Fetterman, A. Chen, S. S. Lee, J. Chen, W. H. Steier, L. R. Dalton, "High-Frequency Polymer Modulators with Integrated Finline Transitions and Low V_π", IEEE Photonics Technology Letters, vol. 11, no. 1, January 1999, pp. 54-56.

[36] K. Okamoto, *Fundamentals of Optical Waveguides*, Academic Press, San Diego, 2000, pp 26-30.

[37] Optical Waveguide Mode Solvers (OWMS) Suite Reference Manual, Apollo Photonics Inc., Waterloo, Ontario, version 1.2, pp 7-9.

[38] A. Yariv and P. Yeh, *Optical Waves in Crystals*, John Wiley and Sons, NY, 1984, pp 70, 222-3.

[39] D. Healy, G. H. Cross, D. Bloor, "Guest-Host Polymeric Systems as Non-Linear Optical Materials", IEEE, 1994, pp. 787 – 793.

[40] C. J. F. Bottcher, O. C. Van Belle, P. Bordewijk, and A. Rip, *Theory of Electric Polarization, Volume 1: Dielectrics in Static Fields*, Elsevier, New York, 1973, pp. 161–164.

[41] R. W. Boyd, *Nonlinear Optics*, Academic Press, San Diego, 1992, pg. 402.

[42] W. J. Tropf, M. E. Thomas, and T. J. Harris, *Properties of Crystals and Glasses, Handbook of Optics, Volume II*, M. Bass, E. W. Van Stryland, D. R. Williams, and W. L. Wolfe, McGraw-Hill, NY, 1995, pg. 33.29.

[43] R. Gerhard-Multhaupt, S. Bauer, S. G. Gogonea, W. Wirges, and S. Yilmaz, "Old and New Poling Techniques for Nonlinear Optical Polymer Electrets", Electrets, 1994. (ISE 8), 8th International Symposium on , 7-9 Sept. 1994, pp. 775 - 780.

[44] G. M. Yang, "Thermal Stability of NLO Effects in Polymers", Electrets, 1996. (ISE 9), 9th International Symposium on , 25-30 Sept. 1996, pp. 425 - 430.

[45] J. A. Giacometti and J. S. C. Campos, "Constant Current Corona Triode with Grid Voltage Control: Application to Polymer Foil Charging", Rev. Sci. Instrum. Vol. 61, No. 3, March 1990, pp. 1143 – 1150.

[46] K. Shindo, "Formation and Destruction of Polarization by Migration of Space Charge", Electrets, 1994. (ISE 8), 8th International Symposium on , 7-9 Sept. 1994, pp. 417 - 422.

[47] M. A. Sussi and G. R. G. Raju, "Depolarization Currents in Corona Charged Aromatic Polyamides", Proc. of the 3rd International Conf. on Properties and Applications of Dielectric Materials, Tokyo, Japan, July 1991, pp. 93 – 96.

[48] M. A. Sussi and G. R. G. Raju, "Thermally Stimulated Discharge and Polarization Currents in Aromatic Polyamides", Electrets, 1994. (ISE 8), 8th International Symposium on , 7-9 Sept. 1994, pp. 564 - 569.

[49] A. S. Deraggi and J. A. Giacometti, "Poling Kinetics in Polar Amorphous Polymers Containing Space Charge", Electrical Insulation and Dielectric Phenomena, 1994. IEEE 1994 Annual Report., Conference on , 23-26 Oct. 1994, pp. 286 - 291.

[50] M. D. Watson, P. R. Ashley, and M. A. G. Abushagur, "Modeling of Optical Waveguide Poling and Thermally Stimulated Discharge (TSD) Charge and Current Densities for Guest/Host Electro Optic Polymers" IEEE Journal of Quantum Electronics, Vol. 11, No. 4, November 2004, pp 1553 – 1561.

[51] A. J. Guenthner, U. S. Naval Air Warfare Center, China lake, CA., Private Communication, 2004.

[52] G. P. Box, W. G. Hunter, and J. S. Hunter, *Statistics for Experimenters*, John Wiley and Sons, NY, 1978, pp 1-279.

[53] D. C. Montgomery, *Design and Analysis of Experiments*, 5th edition, John Wiley and Sons, NY, 2001, pg. 154.

[54] H. Nishihara, M. Haruna, and T. Suhara, *Optical Integrated Circuits*, McGraw-Hill, NY, 1989, pp. 240.

[55] A. J. Guenthner, U. S. Naval Air Warfare Center, China lake, CA., Private Communication, 2004.

[56] R. F. Shi and A. F. Garito, "Introduction: Conventions and Standards for Nonlinear Optical Processes" in *Characterization Techniques and Tabulations for Organic Nonlinear Optical Materials*, M. G. Kuzyk and C. W. Dirk, Ed., New York: Marcel Dekker, 1998, pg 32.

[57] A. Chafin and A. J. Guenthner, U. S. Naval Air Warfare Center, China lake, CA., Private Communication, 2004.

[58] M. D. Watson, P. R. Ashley, A. J. Guenthner, and M. A. G. Abushagur, "Modeling of Electro Optic Polymer Electrical Characteristics in a 3 Layer Optical Waveguide Modulator", IEEE Journal of Quantum Electronics, to be published.

[59] S. E. Bales, D. J. Brennan, , R. J. Gulotty, A.P. Haag, and M.N. Insbasekaran, US Patent 5,208,299 (1993).

[60] D. J. Brennan, R. J. Gulotty, M. Inbasekaran, A. P. Haag, and M. A. Chartier, Polymer Preprints, 1995, 36(2), 37

[61] P.R. Ashley, G.A. Lindsay, W. M. Herman, and J. S. Cites, "Optical Waveguides and Modulators Based on Low-Loss Index-Tunable EO Polymers", PMSE, 83, 229 (2000).

[62] S. S. Lee, S. M. Garner, V. Chuyanov, H. Zhang, W. H. Steier, F. Wang, L. R. Dalton, A. H. Udupa, and H. R. Fetterman, Optical Intensity Modulator Based on a Novel Electrooptic Polymer Incorporating a High $\mu\beta$ Chromophore, IEEE Journal of Quantum Electronics, Vol. 36, No. 5, May 2000, pp. 527 – 532.

[63] J. B. Bernstein and C. M. Cooke, "Electric Poling Behavior of Polymethylmethacrylate", IEEE Trans. on Electrical Insulation, Vol. 26, No. 6, December 1991, pp. 1087 – 1093.

[64] Y. Karakus, D. Bloor, and G. H. Cross, "Electro-Optics in Moderately Doped Thermopoled Polymer Waveguides", IEEE, 1991, pp. 827 – 832.

[65] C. Gangjin, X. Zhongfu, and Z. Yewen, "Electrochromic Mechanism Study of Corona Poled Electro-Optic Polymer Films", Proc. of the IEEE 6th International Conf. On Properties and Applications of Dielectric Materials, June 2000, pp. 741 – 744.

[66] R. Gerhard-Multhaupt, S. Bauer, S. Yilmaz, W. Ren, and W. Wirges, "Poling Behavior of Electro-Optical Polymers", Electrical Insulation and Dielectric Phenomena, 1993. Annual Report., Conference on , 17-20 Oct. 1993, pp. 116 - 121.

[67] M. M. Costa, C. Wisiniewski, M. G. Miranda, and J. A. Giacometti, "Dielectric Relaxation and Polarization Phenomena in Poly(methyl methacrylate) with Disperse Red 1 Dye", IEEE Proc. of the 10th International Symposium on Electrets, 1999, pp. 99 – 102.

[68] S.-K. Kim, K. Geary, D. H. Chang, H. R. Fetterman, H. Zhang, C. Zhang, C. Wang, and W. H. Steier, "TM-pass Polymer Modulators with Poling-Induced Waveguides and Self-Aligned Electrodes", IEEE Electronics Letters, Vol. 39, No. 9, 1 May 2003, pp. 721 – 722.

[69] R. A. Ribeiro, D., T. Balogh, and J. A. Giacometti, "Corona Poling and Electroactivity in a Side-chain Methacrylate Copolymer", IEEE Trans. On Dielectrics and Electrical Insulation, Vol. 7, No. 4, August 2000, pp. 572 – 577.

[70] A. Wedel, R. Danz, W. Kunstler, K. Tauer, "Absorption Studies of Optically Nonlinear Side-Chain Polymer and Polymer-Dye Films Oriented by Corona Poling", Electrets, 1991. (ISE 7) Proceedings., 7th International Symposium on, 25-27 Sept. 1991, pp. 839 - 844.

[71] S. Kalluri, W. H. Steier, C. Xu, B. Wu, M. W. Becker, Z. Yang, L. R. Dalton, Y. Shi, and J. H. Bechtel, "Improved Second Order Nonlinear Optical Polymers by Covalent Attachment- Comparison of Four Different Thermally Stable Systems", Nonlinear Optics: Materials, Fundamentals, and Applications, 1994. NLO '94 IEEE , 25-29 July 1994, pp. 191 - 193.

[72] J. Y. Huang, C. L. Liao, C. J. Chang, and W. T. Whang, "Nonlinear Optical Properties and Poling Dynamics of a Side-Chain Polyimide/Disperse-Red Dye Film: In Situ Optical Second-Harmonic Generation Study", Nonlinear Optics: Materials, Fundamentals, and Applications, 1994. NLO '94 IEEE , 25-29 July 1994, pp. 126 - 128.

[73] T. Segi, T. Mizutani, Y. Suzuoki, A. Tabata, and K. Takagi, "Fabrication of Polyurea Thin Films for Optical Second-Harmonic Generation by Vapor Deposition Polymerization: Effects of Poling Field and Monomer Structure on Reactivity and SHG Performance", IEEE Trans. on Dielectrics and Electrical Insulation, Vol. 5, No. 1, February 1998, pp. 63 – 69.

[74] Y. Shi, W. Lin, D. J. Olson, J. H. Bechtel, H. Zhang, W. H. Steier, C. Zhang, L. R. Dalton, Appl. Phys. Lett., Vol. 77, 2000, pp. 1 – 3.

[75]Y.-H. Kuo, W. H. Steier, S. Dubovitsky, and B. Jalali, "Demonstration of Wavelength-Insensitive Biasing Using an Electrooptics Polymer Modulator", IEEE Photonics Technology Letters, Vol. 15, No. 6, June 2003, pp. 813 – 815.